Università degli Studi della Tuscia di Viterbo
Dipartimento di Scienze Agrarie e Forestali

Corso di Dottorato di Ricerca in
Ecosistemi e Sistemi Produttivi - XXIX ciclo

# Protective coatings for metallic interconnects in Solid Oxide Fuel Cells technology. An investigation on mixed oxide ceramic materials

s.s.d. ING-IND/09

**Tesi di dottorato di:**
Dott. Andrea Masi

**Coordinatore del corso**
Prof. Alessandro Sorrentino

**Tutore**
Prof. Maurizio Carlini

**Co-tutore**
Dr. Stephen J. McPhail

A.A. 2016/17

*Ad Eleonora,*
*per avermi accompagnato in questo percorso*

# Abstract

Solid Oxide Fuel Cells (SOFCs) are electrochemical devices characterized by high efficiency and fuel flexibility, and represent a suitable technology for the clean utilisation of fossil fuels. However, to achieve commercialization, corrosion issues giving rise to long term performance decay must be faced: in particular, the degradation of the metallic interconnects must be overcome through the deposition of ceramic protective coatings. Aim of this thesis is the development of cost-effective and environmental friendly methods for the synthesis of coating materials and for the production of coating layers.

The High Energy Ball Milling technique has been applied to metal oxides mixtures, verifying its effectiveness in the production of nanostructured mixed Mn-Co spinel powders. The influence of the composition on their chemico-physical properties has been studied to further optimize the materials for the application, assessing the advantages induced by a multiple compositional doping approach.

A novel molten carbonate dip-coating passivation method, suitable to produce dense La-Fe perovskite based coatings on stainless steels, has been successfully applied on SOFC interconnects alloys. The identification of opportune galvanic coupling phenomena occurring in the molten bath has allowed to further tune the process, resulting in the production of metal decorated composite structures. The stability of the obtained coatings has been assessed by means of high temperature oxidation experiments.

# Preface

The work described in this thesis was carried out in ENEA (Agenzia Nazionale per le Nuove Tecnologie, l'Energia e lo Sviluppo Economico Sostenibile) at the Casaccia Research Center under the supervision of Prof. Maurizio Carlini and Dr. Stephen J. McPhail.

The work has been carried out in the framework of the EU project SCORED 2:0 [1]. The project is predominantly of a technological nature, aiming to the evaluation of different coating materials and technologies to protect Solid Oxide Fuel Cells metallic interconnects. Four academic institutions and research centres and three industrial partners are involved at this aim. In this frame, the work here reported is related to the synthesis and optimization of Mn-Co based spinel powders described in chapter 3, subsequently evaluated as coating materials by other groups, and to the development of an innovative coating technique, based on the chemical conversion of the substrate, reported in chapters 4, 5 and 6.

This thesis is the result of my own work, and to the best of my knowledge does not contain material previously published or written by other authors, except where due reference is indicated in the text. This thesis does not contain any material which has been previously submitted for the award of a degree or other qualification to any university or institution.

Parts of the work presented in this thesis were published in the following works (in chronological order):

- A. Masi, S. Frangini, M. Carlini, A. Masci, S.J. McPhail, Evaluation of a Novel Perovskite-Based Conversion Coating for Corrosion Protection of 13Cr Ferritic Stainless Steels under Relevant SOFC Oxidizing Conditions, ECS Trans. 68 (2015) 1625–1632.

- A. Masi, M. Bellusci, M. Carlini, S.J. McPhail, F. Padella, P. Reale, Mechanochemical Processing of Mn and Co Oxides: An Alternative Way to Synthesize Mixed Spinels for Protective Coating, J. Am. Ceram. Soc. 99 (2016) 308–314.

- A. Masi, M. Bellusci, S.J. McPhail, F. Padella, P. Reale, J-E. Hong, R.

Steinberger-Wilckens, M. Carlini, Cu-Mn-Co oxides as protective materials in SOFC technology: The effect of chemical composition on mechanochemical synthesis, sintering behaviour, thermal expansion and electrical conductivity, J. Eur. Ceram. Soc. 37 (2017) 661–669.

- A. Masi, M. Bellusci, S.J. McPhail, F. Padella, P. Reale, J-E. Hong, R. Steinberger-Wilckens, M. Carlini, The Effect of Chemical Composition on High Temperature Behaviour of Fe and Cu Doped Mn-Co spinels, Ceram. International, 43 (2017) 2829–2835

- A.Masi, S. Frangini, P. Davide, L. Della Seta, A. Masci, S. J. McPhail, M. Carlini, $LaFeO_3$ perovskite conversion coatings grown on a 13Cr ferritic stainless steel: a corrosion degradation study in simulated Solid Oxide Fuel Cell (SOFC) interconnect conditions at 700°C, Mater. Corros. 68 (2017) 536–545.

- A. Masi, S. Frangini, L. Della Seta, S. J. McPhail, D. Pumiglia, M. Carlini, Composite Cu-LaFeO3 Coating on High Cr Ferritic Stainless Steels for IT-SOFC Interconnects, ECS Trans. 75 (2017) 77–86.

# Acknowledgements

I would like to acknowledge the FCH JU, for supporting this work within the project SCORED 2:0.

I would like to thank Prof. Maurizio Carlini, for the continuous support of my Ph.D study, and for pushing me to capitalize the results of my work.

My sincere gratitude goes to Dr. Stephen McPhail, for the acceptance in the SOFC group and for the assistance and guidance both in the mundane and academic matters.

I would like to thank Prof. Robert Steinberger-Wilckens and Prof. Jan Van Herle, for their precious assistance and the insightful comments.

A sincere thank goes to Dr. Franco Padella, for the continuous guidance, for pushing me towards my limits and for the animated but always honest and fruitful scientific discussions.

I would like to thank Dr. Stefano Frangini, for sharing his experience and for always assisting me along this journey.

I am really grateful to Dr. Jong-Eun Hong, for his kind help but most of all for the warm friendship.

I would like to thank Davide Pumiglia, for the constructive conversations and for sharing this path.

Finally, a special mention goes to Dr. Carlo Alvani, Dr. Mariangela Bellusci, Dr. Livia Della Seta, Dr. Aurelio La Barbera, Dr. Marzia Pentimalli, Dr. Priscilla Reale, Dr. Francesca Varsano, for their constant support and precious help during all of these years.

# Contents

**Abstract** i

**Preface** iii

**Acknowledgements** v

**Introduction** ix

**1 Solid Oxide Fuel Cells metallic interconnects: the need for protective coatings** 1

1.1 Solid Oxide Fuel Cells . . . . . 1

1.1.1 Working principles and geometries . . . . . 1

1.1.2 Planar SOFC interconnects . . . . . 7

1.2 Metallic interconnect coatings . . . . . 10

1.2.1 Reactive element oxides . . . . . 12

1.2.2 Perovskite materials . . . . . 12

1.2.3 Spinel compounds . . . . . 13

1.2.4 Composite coatings . . . . . 13

1.3 The Mn-Co oxides system . . . . . 15

1.3.1 High Energy Ball Milling as a synthesis process . . . . . 17

1.4 Lanthanum based perovskites . . . . . 20

1.4.1 La-Fe perovskite conversion coatings . . . . . 22

**2 Materials and methods** 29

**3 Mn-Co spinels by mechanical activation** 39

3.1 Mechanochemical processing of Co-Mn spinels . . . . . 40

3.1.1 Mechanochemical evolution of powder mixtures . . . . . 40

3.1.2 Powder morphology . . . . . 45

3.1.3 High-temperature phase behaviour . . . . . 47

3.2 Influence of the composition on processed powder properties . . . . . 49

3.2.1 Chemico-physical characterization . . . . . 50
3.2.2 Sintering Behaviour . . . . . 68
3.2.3 Thermal expansion . . . . . 82
3.2.4 Electrical conductivity . . . . . 85

**4 La-Fe perovskite coatings by chemical conversion of interconnect steels 89**
4.1 Thick coatings . . . . . 90
4.1.1 Considerations on the formation mechanism of thick perovskite coatings . . . . . 101
4.2 Thin coatings . . . . . 103
4.2.1 Considerations on the formation mechanism of thin perovskite coatings . . . . . 113
4.3 Economic evaluation of the passivation method . . . . . 114

**5 Metal decorated perovskite composite coatings 117**
5.1 Copper-dispersed composite . . . . . 117
5.2 Nickel-dispersed composite . . . . . 126
5.3 Silver-dispersed composite . . . . . 130
5.4 Formation mechanism of metal-perovskite composite coatings . . . . . 134

**6 Evaluation of the high temperature stability of coated steels 137**
6.1 Oxidation behaviour of La-Fe perovskite coated SS405 steel . . . . . 138
6.1.1 Corrosion mechanism in dual-atmosphere oxidation environments . . . . . 145
6.2 Oxidation behaviour of passivated K41 steel . . . . . 148
6.2.1 Thick perovskite coating . . . . . 148
6.2.2 Thin perovskite coating . . . . . 153
6.2.3 Cu-perovskite composite coating . . . . . 157
6.3 Concluding remarks on the oxidation behaviour of coated steels . . . 163

**Conclusions and outlook 167**

**References 176**

**List of Tables 178**

**List of Figures 186**

# Introduction

One of the current most challenging issues for the whole of mankind is represented by the constant growth of energy demand, driven by world population growth and increasing living standards [2]. With most of energy production (80% [3]) fulfilled by fossil fuels combustion, the release of $CO_2$ and other noxious gases in the atmosphere leads to significant environmental issues - remarkable is the Chinese example [4]. Among these, local and global climate change phenomena are relevant for the survival of the world as we know it, associated to greenhouse gas (GHG) emission. Anthropogenic climate change is obviously an intricate problem, arising from the complex interactions between three distinct parameters: energy, economics, and environment. Energy is essential for economic growth and society development, and on the other hand one of the major greenhouse gas sources. It is obviously difficult to balance the three factors, although a pathway towards environmental protection is now hypothesized, in particular by the agreements reached at the recent 2015 United Nations Climate Change Conference in Paris [5].

Representing nuclear energy a very controversial topic, the complete supply of energy demand by emission free renewable energies is the straightforward and more desirable strategy, not viable however in the short term principally due to the lack of sufficient and cost effective energy storage methods. The *efficient* exploitation of fossil fuel must therefore constitute the bridging strategy between the current unsustainable situation and a green energy production. Electrochemical devices such as fuel cells, characterized by high efficiency ratio (>50%) not limited by the Carnot principle, can represent a short-medium term solution. Their design furthermore contemplates the separation of fuels and oxidant streams, allowing to reach high levels of carbon capture without substantial additional cost.

Among fuel cells, Solid Oxide Fuel Cells (SOFCs) are characterized by some advantages exploitable in particular in stationary or low-mobility systems. Firstly, High grade exhaust heat is produced allowing high-efficiency combined cycle designs such as SOFC/gas turbine/steam turbine. Furthermore, SOFCs are characterized by high fuel flexibility, utilising conventional hydrocarbons. This opens two interesting

application scenarios: natural gas and syngas/biogas. For the first, SOFC may be the perfect technology to benefit from the recent global natural gas production rise, due to fracking technique development and to the recent increased production of natural gas from Gulf Cooperation Council (GCC) oil reservoirs [6]. The exploitation of SOFC as distributed power generators, with the possibility to use the existent natural gas distribution grid, could therefore represent a significant improvement in terms of efficiency and generated pollution. Regarding the second perspective, coupling SOFC with biomass gasification systems, as allowed by their high fuel flexibility, could result in a highly efficient and carbon neutral production of power and heat.

Development of SOFCs started in the seventies as niche application related to aerospace industry. In the last decades efforts have been directed in particular towards the development of kW systems suitable for distributed power generation. Economic viability of such systems is however dependent on costs and longevity. While the prices are related to the production scale, and expected to drop with mass-scale production, performance degradation associated with material corrosion is an issue that must be addressed at its basis. In particular, metallic interconnects corrosion with subsequent chromium diffusion and cathode deactivation is considered one of the major contributions to the degradation of SOFC systems. The application of protective coatings is therefore required to ensure long-term stability of the stack performance. Mn-Co Spinel and La-based perovskite oxides are commonly regarded as suitable materials, each characterized by strengths and drawbacks [7].

Aim of this thesis, with the need for large-scale application of the protective coatings, is the evaluation of cost-effective and environmental friendly methods for the synthesis of coating materials and for the production of effective coating layers. In order to achieve this aim, two main objectives were defined, consisting in the exploitation of mechanochemical techniques as synthesis method for mixed Mn-Co oxides and the application of a novel chemical conversion method on SOFC suitable ferritic alloys to produce effective La-Fe perovskite based coatings.

Regarding the first target, chemico-physical and processing properties of powders subjected to High Energy Ball Milling (HEBM) treatments have been studied to evaluate the effectiveness of the mechanochemical process. Furthermore, tailoring of the chemical composition has been carried out to further optimize the material. The results are reported in chapter 3.

The application of the molten carbonate chemical conversion technique, previously observed as suitable to produce dense and adherent La-Fe perovskite based coatings by a one-pot dip coating process in opportunely tailored molten carbonate alkali baths [8], to SOFC suitable alloys is described in chapter 4. To further tune

the coatings properties, the extension of the technique to obtain metal-perovskite composite coatings, exploiting advantageous galvanic coupling phenomena identified in opportunely tailored molten salts, is discussed in chapter 5. The effectiveness of the produced protective layers, evaluated by means of high-temperature exposure test, is finally reported in chapter 6.

# Chapter 1

# Solid Oxide Fuel Cells metallic interconnects: the need for protective coatings

## 1.1 Solid Oxide Fuel Cells

### 1.1.1 Working principles and geometries

A fuel cells is a device that promote the conversion of chemical energy in electricity. To produce the electricity, the *fuel* gets oxidized by the *oxidant*. Several fuels and oxidizing agents can be considered. However, the most promising combination involves the oxidation of hydrogen gas by oxygen with the formation of water:

$$H_2 + \frac{1}{2}O_2 \rightarrow H_2O \tag{1.1}$$

Fuel cells can therefore be clean devices, that do not imply a priori the formation or release of noxious gas in the atmosphere.

The direct product of the chemical reaction reported in equation (1.1), apart obviously from the water, is heat. To obtain electricity from this reaction, the process must proceed through several steps, with the formation of ions and the diffusion of ions and electrons - that constitute our electricity - through different paths.

To force the involved ions and electrons on different pathways, it must be provided an opportune media that separates the zones where fuel oxidation occurs (*anode*) and the oxidant reduction takes place (*cathode*). The *electrolyte* has therefore the role to allow the ions migration while representing a barrier to electrons

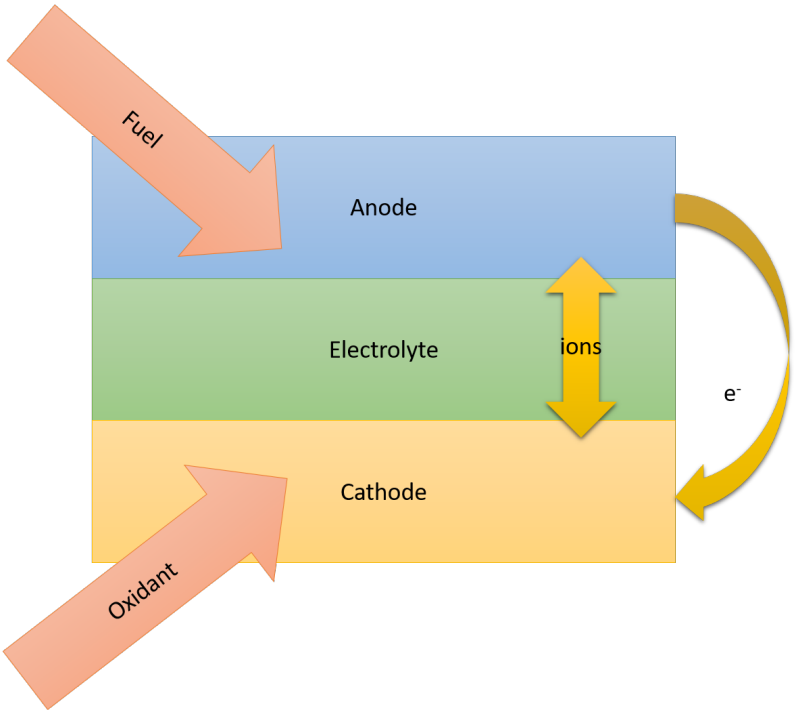



Figure 1.1: Schematic representation of a fuel cell.

diffusion, that takes place through and external circuit. The basic design of fuel cells comprises therefore 3 key parts: the anode, the cathode, and the electrolyte. A schematic representation is reported in figure 1.1.

With reduction of the oxidizing species occurring in the cathode and oxidation of the fuel in the anode, the electrolyte is responsible the physical separation of the anode and cathode, to avoid chemical short circuits. Furthermore, the electrolyte is responsible for the transport of the ions involved in the reaction, without allowing the electrons to migrate through. Considering the reaction of equation (1.1), the charge of the diffusing ions determines whether water production will occur at the anode or at the cathode side: if positive charges can diffuse through the electrolyte (e.g. $H^+$) cathode and anode reactions as reported respectively in equation (1.2) and (1.3) occur:

$$H_2 \rightarrow 2H^+ + 2e^- \tag{1.2}$$

$$\frac{1}{2}O_2 + 2H^+ + 2e^- \rightarrow H_2O \tag{1.3}$$

If the electrolyte is characterized instead by anion diffusion capability (e.g. $O^{2-}$ or $CO_3^{2-}$) the electrode reactions reported respectively in equation (1.4) and (1.5) will take place:

$$H_2 + O^{2-} \rightarrow H_2O + 2e^- \tag{1.4}$$

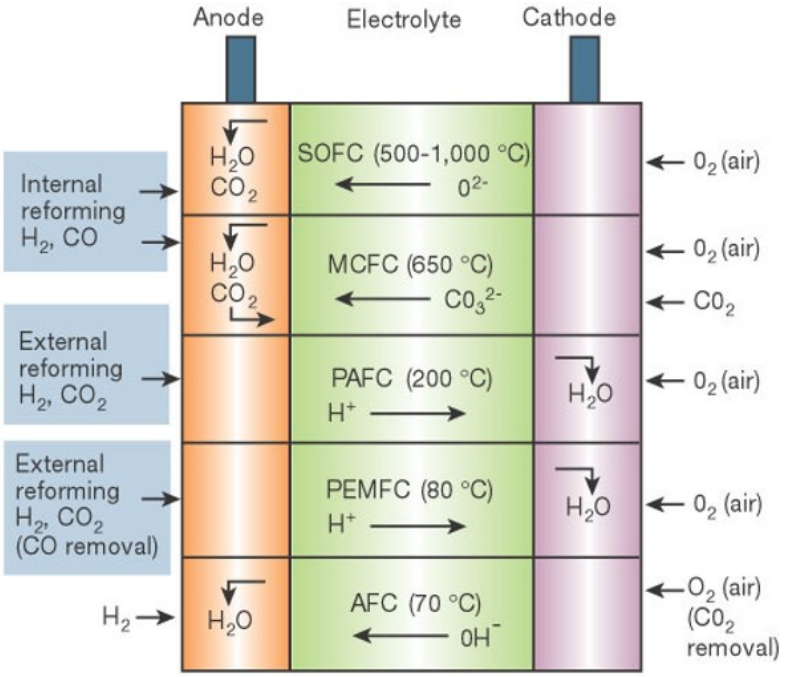



Figure 1.2: Common fuel cells and corresponding fuels, charge transport ions and oxidizers [9].

$$\frac{1}{2}O_2 + 2e^- \rightarrow O^{2-} \tag{1.5}$$

Cathodic and anodic reactions are therefore dependent on the electrolyte nature.

The large number of possible electrolytes gives rise to a high variety of viable fuel cells architectures, commonly divided in low temperature (T<250°C) and high temperature (T>500°C) devices. The most widespread and common fuel cell categories, namely Solid Oxide Fuel Cells (SOFC), Molten Carbonate Fuel Cells (MCFC), Phosphoric Acid Fuel Cells (PAFC), Proton Exchange Membrane Fuel Cells (PEMFC) and Alkaline Fuel Cells (AFC), are summarized in figure 1.2 [9]. The diversity among these cells arise from the electrolyte difference, with the different ion transport media and mechanisms involved and therefore different operating temperatures. Cathode and anode materials are accordingly linked, and the possibility to use different fuels and oxidizing agents is the consequence of electrodes materials and operating temperature combination.

Single cells generate however low amounts of power at low voltages.To obtain sufficient energy, multiple cells are connected in series with *interconnects* or bipolar plates to form cell *stacks*. The interconnect must be gas tight, and - contrary to electrolytes - a good electric and poor ionic conductor.

Regarding the efficiency of fuel cell systems, it is usually considered as the ratio of the output energy versus the energy stored in the fuel. The electrical efficiency of

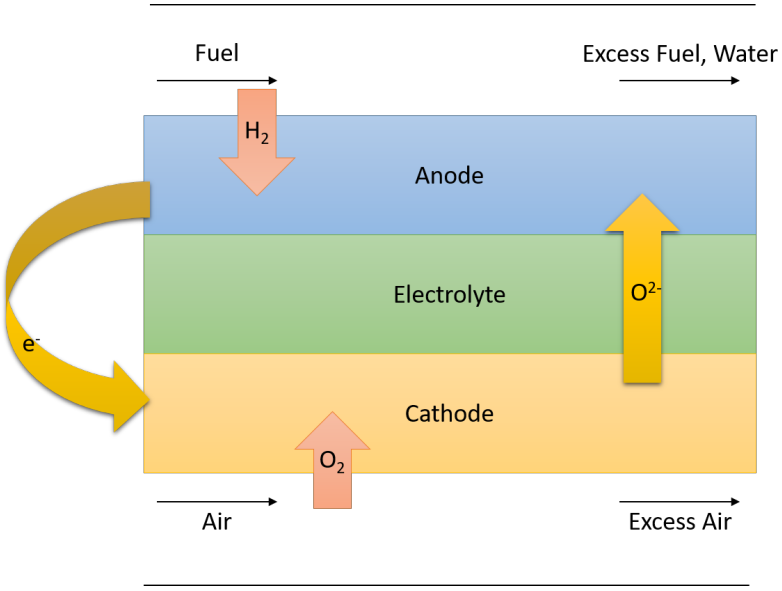



Figure 1.3: Schematic representation of a SOFC.

fuel cells is usually between 20-60% [10]. Furthermore, in certain fuel cell types, the thermal energy released in the chemical reactions occurring in the cell is released as high grade heat, and considering combined electrical energy and heat as output of Combined Heat and Power (CHP) systems (systems where both electrical energy and heat are obtained from the device) efficiencies up to 90% are achievable [10]. These values make fuel cells highly fascinating in several application fields (for comparison, internal combustion engines efficiency is approx. 25%). In particular, SOFCs attract interest being characterized by high efficiency within the different types of fuel cells (typically ∼40% electric efficiency and up to 90% CHP [10]), with application in fields involving relatively low system outputs (i.e. kW range) and stationary use, such as distributed power and heat generation for houses or buildings.

A schematic design of a SOFC is reported in figure 1.3. Air is injected at the cathode side, and oxygen is adsorbed and reduced. Oxygen ions diffuse through the electrolyte layer to the anode side, where they react with the fuel to form water and heat. The electrons involved in the oxygen reduction and in the fuel oxidation flow through an external circuit and generate the exploitable electrical current.

The electrolyte constitutes therefore a crucial part: it must provide gas tightness, low hydrogen permeability and high oxygen ionic conductivity. Several ceramic materials have been identified as suitable for the application, such as zirconium-based oxides, Lanthanum gallium perovskites and cerium-based oxides. Oxygen ions conductivity of these materials is highly dependent on temperature, and to promote significant diffusion phenomena these electrolytes need to work at temperatures higher than 600°C.

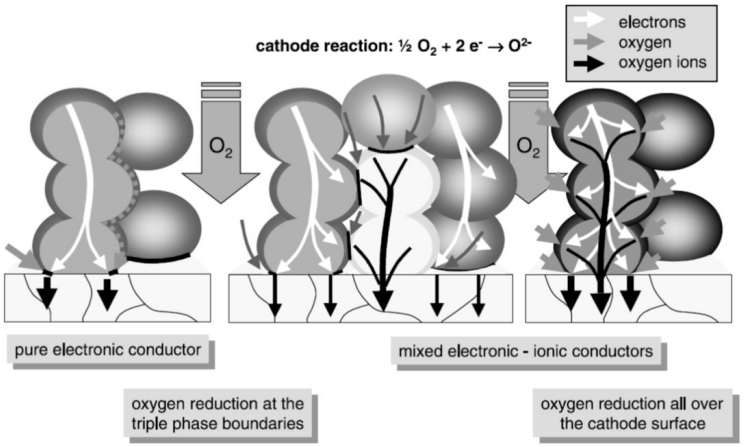



Figure 1.4: Oxygen reduction and diffusion mechanisms in pure electronic, ionic-electronic composite, mixed ionic-electronic conducting cathodes [13].

At the anode, the chemical reaction reported in equation (1.4) takes place preferentially at the *triple-phase boundaries*, the surface interfaces between the electrolyte, the electrode and the gas. In these sites, oxygen ions diffusing from the electrolyte encounter and react with hydrogen adsorbed on the anode material. This must be characterized by high electronic conductivity, to easily provide electrons to the external circuit, sufficient electrocatalytic activity, to facilitate hydrogen oxidation, and good thermal and chemical stability. Ni/YSZ cermets have been developed since the seventies [11], and currently represent the benchmark, even if some issue such as sulphur poisoning and carbon deposition still need to be fully addressed.

In the cathode, the oxygen is adsorbed on the surface and is reduced by the incoming electrons from the external circuit. Similarly as in the anode, cathode materials must be characterized by high electrical conductivity and high catalytic activity, in this case towards the Oxygen Reduction Reaction (ORR). In materials characterized by poor ionic conductivity, the effective process occurs commonly in the electrolyte proximity, in particular at the three-phase boundary (cathode/electrolyte/oxidant). In cathodes characterized by high ionic conductivity or composites cathodes, where the reduced oxygen ions can diffuse through the bulk of the cathode material, the reduction can occur on the whole surface, as depicted in figure 1.4.

Among cathode materials, Lanthanum-based perovskites, with common formula $A_x a_{1-x} B_y b_{1-y} O_3$, where A is lanthanum, a is a earth-alkaline ion (commonly Sr), B and b are transition metals (e.g. Mn, Fe, Co), have been exploited and developed since the seventies [12] and currently represent the benchmark materials.

Typical single SOFC cells produce low voltages (<1V) and are characterized by power densities in the W/cm$^2$ range. To raise the output, many cells are electrically

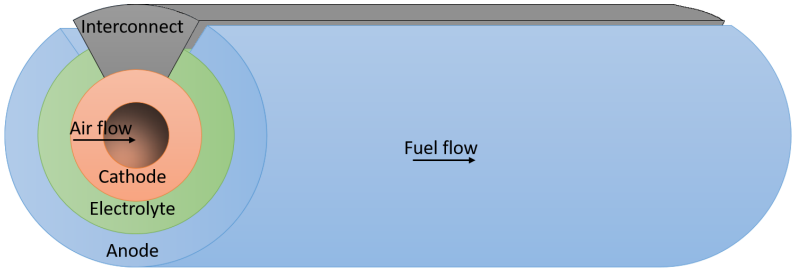



Figure 1.5: Schematic representation of a tubular SOFC.

connected together in a cell stack through interconnections. Two different strategies are commonly adopted to build SOFC stacks, exploiting different cell geometries, namely of tubular and planar shapes.

Tubular SOFCs, represented in figure 1.5, are built in a cylindrical shape, with the air flow channel in the center of the cell surrounded by the cathode material. On the cathode material the electrolyte and the interconnect are placed. The anode finally covers the electrolyte, without contact with the interconnect. The connection of the interconnect with the anode of a second cell links in series the two cells. Tubular SOFC may be of large (>15mm) or of much smaller diameter (<5mm) - the *microtubular* cells.

Among their advantages, they do not require high temperature seals, making their performances stable over long periods, and their geometry confers significant robustness towards thermal cycling. However, low power density is obtained (commonly approx. 0.2 W/cm$^2$) and the cell dimension scale up is not straightforward, limiting the overall power and therefore limiting their application to portable fields [14].

Planar SOFC, described in figure 1.6, are built as flat sheets of electrodes and electrolytes, tightly interrelated, with planar interconnects suitable to favour the gas flow. The side length is usually limited to approx 10-20 cm to avoid mechanical stresses arising when exposed to high temperature, that may cause cracks and faults.

The cell design and production are easier with respect to tubular SOFC. The energy density obtainable from planar SOFC is usually higher with respect to tubular cells (up to 2 W/cm$^2$) and the scale up is much easier, consisting in the assembly of a larger number of stacked cells.

The planar design introduces however a significant attention on the anode and cathode separation by the interconnect, described further in section 1.1.2. The requirements of this part may be the most severe of all cell components: high electronic conductivity, minimal ionic conductivity, stability in oxidizing and reducing atmospheres, low permeability to hydrogen and oxygen gases, thermal expansion

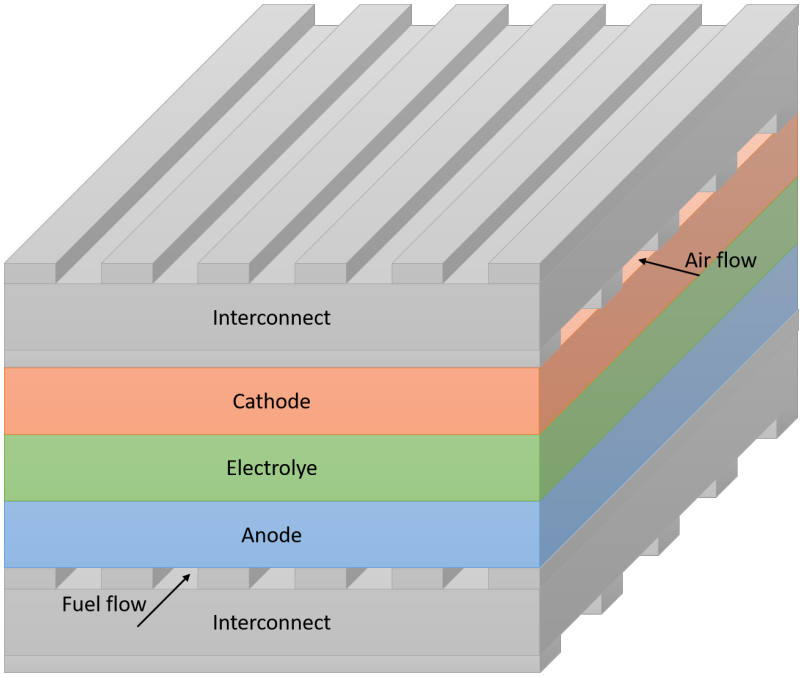



Figure 1.6: Schematic representation of a planar SOFC.

compatibility with the other cell materials, high chemical stability and low reactivity with the anode and cathode materials.

Furthermore, to avoid lateral leakage of gases, sealants are needed to connect two interconnects without electrical short circuits. Therefore, sealants must be hermetic, chemically stable and electrically insulating, characterized by a good thermal expansion match with the surrounding materials and good bonding adhesion and as well as the interconnects represent a crucial part in the stack design. These introduction of two elements in the stack design introduces therefore several new interfaces (electrode/interconnects, interconnects/sealant) that may give rise to instability and degradation issues in the long term.

### 1.1.2 Planar SOFC interconnects

As briefly introduced in section 1.1.1, interconnects play a key role in SOFCs. In particular, in planar SOFCs, interconnects separate adjacent anode and cathode ambients, characterized respectively by highly reducing and oxidizing atmospheres, providing electrical connection. Interconnect materials must therefore possess the following characteristics [15]:

- High bulk electrical conductivity;
- Low Area Specific Resistance (ASR), tipically less than 0.05 $\Omega \cdot cm^2$;

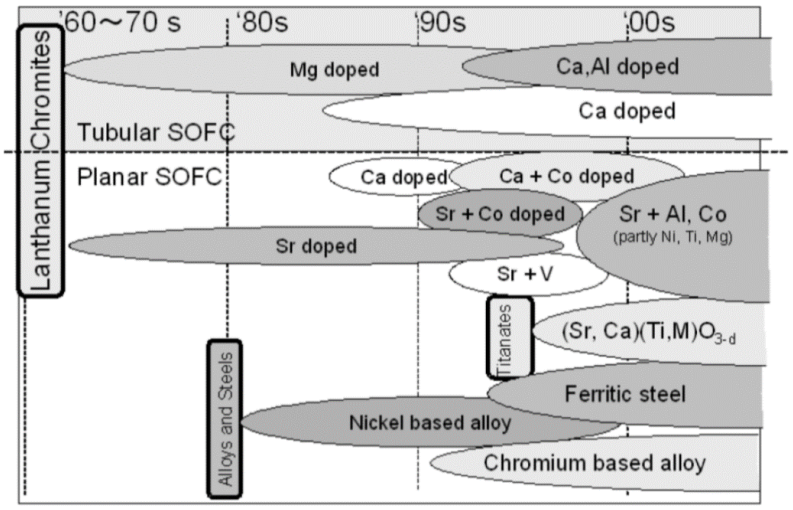



Figure 1.7: Trend of research and development on SOFC interconnect materials [16].

- structural and chemical stability in reducing and oxidizing atmospheres;
- gas imperviousness towards hydrogen and oxygen diffusion;
- Coefficient of Thermal Expansion (CTE) compatibility with the other cell components (CTE $\approx 11 \div 13 \cdot 10^{-6} \mathrm{K}^{-1}$);
- low chemical reactivity towards anode, cathode and sealant materials;
- good mechanical stress;
- low cost and ease of fabrication.

Research and development of interconnects materials has evaluated both ceramics and metal alloys. The trend of research on SOFC interconnect materials in the last 50 years is reported in figure 1.7 [16].

Regarding ceramic materials, research has focused on lanthanum chromite based perovskites ($LaCrO_3$). $LaCrO_3$ is a $p$-type semiconductor under oxidizing conditions [17], stable in low $P_{O_2}$ atmospheres [18], characterized by high compatibility with the other cell components. Being $LaCrO_3$ not characterized by sufficient electrical conductivity, compositional doping has been proved as an effective strategy to obtain sufficient conductivity in the high temperature range (T>800°C), making $LaCrO_3$-based materials suitable for the application. Among the drawback of ceramic interconnects, high costs and low processability, principally due to the high required sintering temperature (T>1450°C in reducing atmosphere), limit the large scale applicability of such materials [19].

On the contrary, metal alloys are characterized by significantly lower cost [20], high availability and ease of fabrication. A summary of the evaluated alloys is reported in table 1.1.

Table 1.1: Comparison of key properties of different alloy groups for SOFC applications [21]:

| Alloys | CTE ($\cdot 10^{-6}K^{-1}$) [800 °C] | Oxidation resistance | Mechanical strength | Manufacturability | Cost |
|---|---|---|---|---|---|
| Cr based | 11.0÷12.5 | Good | High | Difficult | Very high |
| Ferritic SS | 11.5÷14.0 | Good | Low | Fairly ready | Low |
| Austenitic SS | 18.0÷20.0 | Good | Fairly high | Ready | Low |
| Fe-Ni-Cr | 15.0÷20.0 | Good | High | Ready | Medium |
| Ni-Fe-Cr | 14.0÷19.0 | Good | High | Ready | High |

Among the reported alloys, the research trend developed in the last 20 years focused on the commercialization of SOFC (and therefore on the reduction of costs) and the development of Intermediate Temperature (T$\sim 600 \div 800$°C) suitable electrolytes made iron based alloys, in particular Fe-Cr ferritic stainless steels, particularly appealing.

Ferritic stainless steel are in fact characterized by good CTE match with the other cell components (CTE $\sim 11 \div 13 \cdot 10^{-6}K^{-1}$ [22]), high ductility, good workability, ease of processing and lower costs with respect to Ni and Cr based alloys [21].

With respect to their ceramic counterparts, these alloys suffer however from corrosion issues. When exposed to oxidizing conditions at high temperature, growth of superficial oxides is promoted. In the case of ferritic stainless steels, a dual layer oxide structure is commonly produced, with a inner protective chromia ($Cr_2O_3$) scale and an outer non-protective Mn-Cr spinel layer [23]. While steels can be considered excellent electrical conductors, the thermal oxide scales are characterized by high resistivity, that grows significantly when temperature is lowered towards 600°C. As a result, while acceptable at 800°C, the ASR of such scales has been found to increase to significantly high values under low operating temperatures (e.g. T$<$700°C) in spite of the very thin oxide scales forming on the surface in such conditions. Thus, for instance, an ASR value of $13.3 m\Omega \cdot cm^2$ is reported for an uncoated AISI 430 steel at 800 °C [24], which increases to 430 $m\Omega \cdot cm^2$ when temperature is decreased to 700 °C [25]. Proper additives (in particular Mn) are introduced in the alloy to enhance the scales electrical conductivity. The enhancement of electronic and

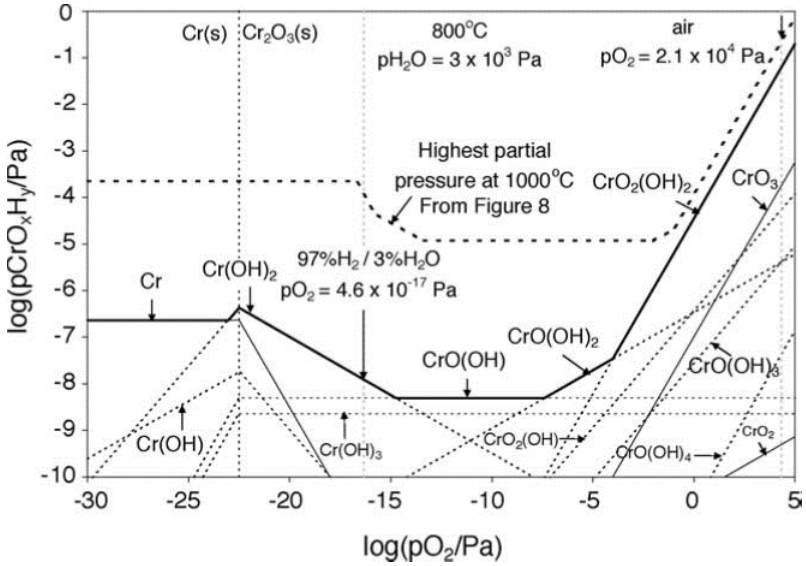



Figure 1.8: Equilibrium vapor pressures of chromium–oxygen–hydrogen gas species at 800 ∘C [27].

eventually ionic conductivity of the scales, however, may enhance the scale growth kinetic, favouring therefore the interconnect corrosion, and the right compromise must be found [21].

In addition to the conductivity issue, the use of ferritic stainless steels interconnects is responsible for the *chromium poisoning* phenomenon [26]. At operating temperature, especially in water rich environments, chromium tends to form volatile oxides and oxyhydroxides. In figure 1.8 the equilibrium gas pressures for $CrO_xH_y$ species calculated at 800°C [27] are reported. It can be observed that high pressures of chromium oxyhydroxides species are obtained both in the anode and cathode conditions, and that the phenomenon is enhanced in the oxygen rich side of the diagram, representing the cathode side. Volatile chromium species can migrate through the cathode, deposit and react with cathode materials, producing insulating compounds like $SrCrO_4$ and Cr-Mn spinels. Furthermore, these reactions commonly occur at the three-phase boundary (cathode/electrolyte/oxidant), reducing the active sites availability for the gaseous species. Furthermore, the reaction of chromium with elements of the active layers induces changes in the chemical composition of the electrodes, affecting its efficacy.

## 1.2 Metallic interconnect coatings

As highlighted in section 1.1.2, the use of ferritic stainless steel interconnects brings significant advantages over traditional ceramic parts if the degradation is reduced. One of the possible strategies to face this issue, developed in the last decade, is the

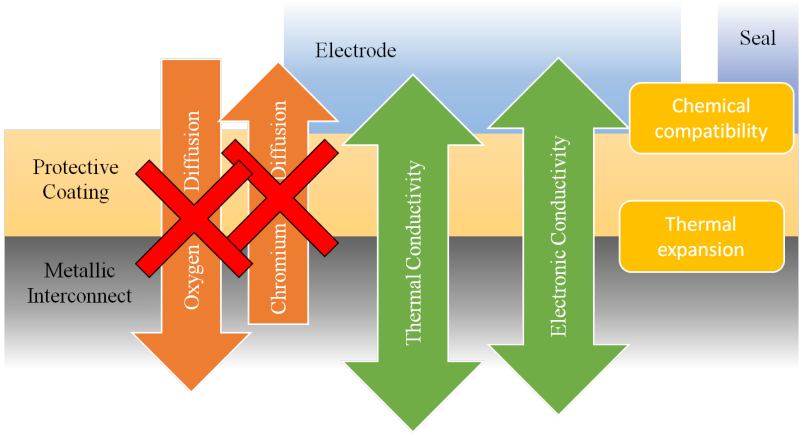



Figure 1.9: Schematic representation of the metallic interconnect coatings requirements.

application of protective coatings.

The application of a further layer in the stack geometry introduces however new interfaces, with related complications. To depict these new challenges, a schematic view of the coating interfaces is reported in fig 1.9.

As evident, the requirements of coating materials are demanding, and include:

- Low ionic conductivity and oxygen gas permeability, to avoid diffusion towards the substrate of oxygen species and substrate oxidation;
- Low Cr diffusion coefficient, to avoid chromium migration towards the surface and evaporation;
- Thermodynamically stability in the operating conditions, to ensure long term performance constancy;
- High chemical compatibility and stability towards the electrode materials and the sealants;
- Sufficient electrical conductivity, to avoid significant increase of the stack resistance;
- Good thermal expansion match with the substrate, to avoid detachment and spallation during thermal cycling;
- The possibility to be applied in dense and uniform layers with low cost and highly scalable techniques.

Various materials have been evaluated, focusing in particular on reactive element oxides, perovskite oxides and spinel oxides [**Shaigan2010;Mah2016**].

### 1.2.1 Reactive element oxides

The addition of small amounts of reactive elements (e.g. Y, La, Ce), also in the form of dispersed oxide particles, reduces the high temperature oxidation rate and improves the thermal oxide scale adhesion [28]. Their limited effectiveness has been related to the reactivity with impurities (e.g. S) that may segregate at the metal-scale interface, affecting the scale adhesion, or to the tendency for large reactive elements ions to segregate at the oxide scale grain boundary, where they block the fast diffusion paths for the transition metal cations that form the scale (i.e. Cr). The inhibition of the outward cation migration prevents vacancy injection at the interface, slowing therefore the oxide growth process.

Coatings of Rare Earth Oxides (REO) have shown to reduce oxidation rate and ASR growth, but do not represent an actual barrier to chromium evaporation, principally due to their morphology (thin and porous). REO coating are therefore considered as the first generation of protective coatings for steel interconnects, surpassed in effectiveness by spinel and perovskite oxides [7].

### 1.2.2 Perovskite materials

Perovskite oxides with general formula $ABO_3$, where A is a rare earth cation (typically La) and B is a transition metal, are considered as promising coating materials for for ferritic stainless steel protection for several reasons[7]:

- high p-Type electrical conductivity (composition dependent);
- good CTE match with the substrate;
- chemical compatibility with the electrode materials;

Among the perovskites, efforts have been focused on compositions already exploited as ceramic interconnects, such as lanthanum chromites and lanthanum strontium chromites (e.g. [25, 29, 30]), or similar to cathode materials, namely lantanum strontium manganites, lanthanum strontium cobaltites, lanthanum strontium ferrites (e.g. [31]). The stability of these materials in generally remarkably high in oxidizing conditions, while the composition, and in particular the B transition metal, influence greatly the behaviour in reducing atmospheres.

The effective use of perovskite coatings has proved to be particularly challenging. Firstly, such perovskites exhibit in fact mixed electronic and oxygen ion conductivity, raising doubts on the effectiveness in impeding oxygen diffusion and sub-coating scale growth [7]. In second place, deposition of fully dense perovskite coatings requires

the application of high firing temperatures or long sintering times, often in reducing conditions, with potential adverse effects on the substrates [32, 33]. Furthermore, perovskite layers exhibit usually poor adhesion strength on stainless steel substrates, potentially promoting premature failure during thermal cycles. Results reported in literature confirm these challenges, showing that the application of perovskite coatings does not suppress completely Cr migration, despite resulting effective in the enhancement of the oxide scale electrical conductivity and adhesion [7, 34].

### 1.2.3 Spinel compounds

Spinel oxides are characterized by the general formula $AB_2O_4$, where A and B are commonly transition metal cations. The chemico-physical properties of spinels are highly dependent on their composition, and the right metal choice can produce excellent CTE match with the substrate and other cell components, with sufficient electrical conductivity, as observed in particular in Mn-Co, Mn-Cu and Cu-Fe compounds [35].

Despite being characterized by lower chemical stability with respect to the perovskites competitors, in particular in reducing atmospheres, the low ionic conductivity of such spinels and the high compatibility with the substrates, with the formation of highly adhesive and coherent interfacial layers, make spinel oxides particularly attractive. Several studies have been published, focusing in particular on Mn-Co spinels and transition metal doped (e.g. Ni, Cu, Fe) Mn-Co spinels, demonstrating the effectiveness in the sub-coating scale growth inhibition and in chromium retention with the achievement of low ASR values in long-term tests [7].

### 1.2.4 Composite coatings

In the last years, results have been reported regarding composite coatings, in particular perovskite-spinel and rare earth oxides - spinel coatings. Regarding the first case, *Lacey* et al. [31] showed that the formation of a stable intermediate spinel layer formed under a thin perovskite outer layer can be highly effective in blocking outward Cr diffusion. More recently, low ASR values and no sign of Cr diffusion have been reported on a composite coating formed by a $LaCoO_3$ perovskite outer layer and an inner $Co_3O_4$ layer [36]. These works seem to suggest that the formation of an interfacial spinel layer could enhance the performance of thin perovskite coatings. The positive effect of a combined spinel/ perovskite thin coating approach is also supported by a very recent patent from Bloom Energy Co. that describes the use of double oxide film coatings composed of a perovskite oxide on top of the spinel layer

for best coating performance [37]. According to the patent, two main effects can be expected from a spinel-perovskite coating combination: firstly, the spinel layer prevents direct contact of the perovskite coating with the inner Cr-rich native oxide, which could lead to formation of unwanted and resistive phases; secondly, the top perovskite coating is an additional barrier against the transport of oxygen toward the inner Cr-rich native oxide.

Regarding the second case, the application of metallic Co thin layers ($<1\mu m$) and their thermal oxidation to form Co-rich spinels has been proved to produce coatings characterized by good barrier properties and low ASR [38]. The combination of such layer with a thin ($\approx$ 10 nm) cerium oxide interlayer improved furthermore the barrier efficacy, thanks to the enhancement of metal ion diffusions behaviour [39, 40]. Based on these studies, Sandvik Materials Technology has recently developed an industrially-designed physical vapour deposition method for high reliability and reproducibility of deposition conditions of Ce/Co conversion coatings. As a result of their efforts, Ce/Co precoated steel interconnects are considered today the best multi-functional coating technology available for IT-SOFC steel interconnects, although the commercial coated steels are still expensive and lower-cost solutions are still being actively pursued.

In table 1.2, a summary of the various coating material characteristics is reported.

Table 1.2: Comparison of the various coating materials:

| Coating material | Electronic conductivity | Cr diffusion inhibition | Oxidation resistance | Manufacturability |
|---|---|---|---|---|
| Reactive element oxide | Fair | Poor | Fair | Good |
| Rare earth perovskite | Good | Fair | Fair | Fair |
| Spinels | Good | Good | Good | Good |
| Composite coatings | Good | Good | Good | Fair |

Currently, Mn-Co spinel oxides represent the best compromise between ease of processing and effectiveness. Efforts are focused therefore in developing effective, highly scalable and cost effective spinel coatings ready for mass production [34]. Chemico-physical and processing properties of Mn-Co spinels have been further analysed and described in the next section.

The application of perovskite coatings, given the opportune combination of material and deposition technique to overcome the issues mentioned above, could represent an interesting solution due to their theoretical higher stability. La-based perovskite coatings are further examined in section 1.4.

## 1.3 The Mn-Co oxides system

Mn and Co are characterized by the existence of oxides with spinel structures, namely $Mn_3O_4$, Haussmanite, thermodynamically stable at high temperature (approx. in the 900 ÷ 1200 °C range), and $Co_3O_4$, thermodynamically stable below 900 °C. While cobalt spinel is characterized by a cubic simmetry, Haussmanite shows a tetragonal distortion due to Jhan-Teller effect induced by $Mn^{3+}$ in octahedral coordination.

In figure 1.10 the mixed oxide phase diagram in air is reported [41, 42]. The mixed oxide phases reflect the differences between the two metals. It can be observed that a wide stability region of the mixed cubic spinel phase exists at intermediate temperature, compatibly with the SOFC interconnect operating temperature. Cooling from the spinel stability region, oxidation of spinel phases and demixing of oxidized species ($Me_2^{(3+)}O_3^{(2-)}$) should occur. However, due to kinetic effects, the oxidized mixed phases are rarely observed [42], and the spinel phases are retained to room temperature. For Co rich $Mn_xCo_{3-x}O_4$ oxides (x<1.4) a single spinel phase is stable down to room temperature. When cooling intermediate compositions (1.4<x<2), in slow cooling treatments a mixture of a cobalt-rich cubic spinel and a manganese-rich tetragonal spinel is normally observed, while a single distorted tetragonal phase is obtained when quenching the same compositions. Single tetragonal spinel phases are obtained for Mn rich spinels (x>2) [43–45].

In intermediate compositions, distortion and de-mixing of the tetragonal phase from the cubic spinel is determined by different preferential occupations of lattice sites by Co and Mn ions. The lattice site occupation of Mn-Co spinels is quite complicated, due to the various possible oxidation states for both elements ($Mn^{2+}$, $Mn^{3+}$, $Mn^{4+}$, $Co^{2+}$, $Co^{III}$). $Mn^{3+}$, $Mn^{4+}$ and $Co^{III}$ tend to occupy preferentially octahedral sites, while $Mn^{2+}$ and $Co^{2+}$ show no preference at room temperature [46, 47]. The mixed spinel will therefore be characterized by the presence of cobalt as $Co^{2+}$ in tetrahedral sites and $Co^{III}$ and $Co^{2+}$ in ochtahedral sites, with manganese occupying octahedral sites with $Mn^3+$ ions and a certain amount of Mn ions oxidized to $Mn^{4+}$, to counterbalance $Co^{2+}$ in octahedral site maintaining electro-neutrality. If the ratio of octahedral sites occupied by $Mn^{3+}$ ions exceeds a certain amount (i.e. 0.55), Jahn Teller effect occurs, giving rise to phase lattice distortion and phase de-mixing. At high temperature, more disordered structures are formed, with $Co^{2+}$ ions occupation of octahedral sites and subsequent movement of $Mn^{3+}$ in tetrahedral sites, reducing lattice stress due to $Mn^{3+}$ Jahn Teller effect and allowing the existence of a single cubic spinel phase [48].

The chemico-physical properties are obviously linked to the spinel lattice struc-

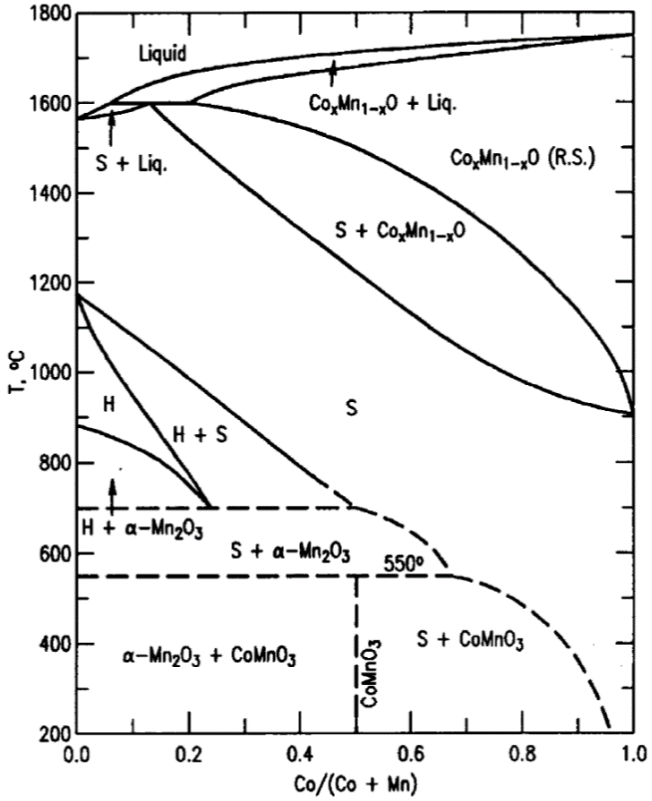



Figure 1.10: Phase diagram of the Mn-Co oxide system in air (S=spinel, H=Haussmanite, R.S. = rock salt) [41, 42].

ture. For example, electrical conductivity in such systems is associated to a small polaron hopping mechanism between $Mn^{3+}/Mn^{4+}$ and $Co^{2+}/Co^{3+}$ couples on octahedral sites of the spinel structures. While $Co_3O_4$ and $Mn_3O_4$ are characterized by low conductivity exhibiting insulating behaviour, intermediate compositions, characterized by high amount of $Mn^{3+}/Mn^{4+}$ and $Co^{2+}/Co^{3+}$ couples [48], are characterized by values of conductivity up to 80 S/cm at high temperature [49], making them suitable for the application as SOFC interconnects coating materials.

For what concerns thermal expansion behaviour, CTE of $Mn_xCo_{3-x}O_4$ intermediate composition spinels ($1<x<1.5$) is compatible with ferritic stainless steels [35, 50, 51]. The dependence of CTE with composition has been investigated on standard compositions (i.e. x=1, x=1.5, x=2) showing an increasing trend of CTE with Co content[52]. However, to the best of my knowledge, no systematic studies regarding intermediate composition spinels have been carried out.

The high stability of such oxides, their sufficiently high electrical conductivity, with low ionic conductivity, and the mechanical compatibility with ferritic alloys make therefore Mn-Co spinel suitable as coating materials for SOFC interconnects. First reports related to the effectiveness of Mn-Co spinel coatings have been pub-

lished in the mid-2000s, showing that electrical conductivity and oxidation resistance of ferritic alloys were enhanced by the coating application [50, 53]. Several studies have been carried out regarding the effectiveness of Mn-Co spinels coatings, producing the coatings with several techniques such as slurry coating methods, plasma spraying and metal electrodeposition followed by heat treatments, and a comprehensive review has been published recently [7].

The effectiveness of the coating layer is strictly related to an efficient sintering step. Mn-Co spinel powders require high sintering temperatures to achieve sufficient densification (e.g. >1000°C [54]), superior to the maximum acceptable temperatures for the steel substrates. To overcome this issue, sintering treatment of Mn-Co spinels coatings deposited on ferritic stainless steels include a thermal treatment in a reducing atmosphere. This step promotes spinel decomposition and allows to exploit the superior sintering properties of the metals, with respect to the spinel phase, and achieve high densities at temperature lower than 900°C. The reducing step is then followed by an oxidation treatment to produce again the spinel phase (e.g. [50]). The majority of published literature related to Mn-Co sintered coatings adopt this method (e.g. [55]). To the best of our knowledge, however, few studies have been conducted focusing on the sintering behaviour of Mn-Co systems in reducing conditions [56].

Modification of the Mn-Co spinel via chemical substitution through addition of dopant elements has been evaluated through the addition of transition metals (e.g. Fe, Ti, Ni, Cu) or rare earth elements (e.g. Y) to further tune the spinel properties, affecting the sintering, electrical and thermal expansion characteristics. Copper and nickel addition proved effective in enhancing sintering behaviour and electrical conductivity[57–61], iron addition can be effective in enhancing spinel stability [49]. The addition of further elements affect however the thermal expansion behaviour: the addition of Cu and Ni raises CTE [57–59], while Fe, Ti, or Cr lower CTE [52, 62]. No clear relation between CTE and dopant concentration can be however deduced from literature, mostly due to the high dispersion of results. Furthermore, the effect of simultaneous multiple doping has not been evaluated.

### 1.3.1 High Energy Ball Milling as a synthesis process

The spinel powders are usually produced by high-temperature solid state reactions between the oxides and/or carbonates of the metals, or through wet chemistry methods such as sol-gel technique or glycine-nitrate process [7]. High Energy Ball Milling (HEBM) is an alternative, well-consolidated and environmentally friendly powder processing technique applied in material science [63], cost-effectively scalable

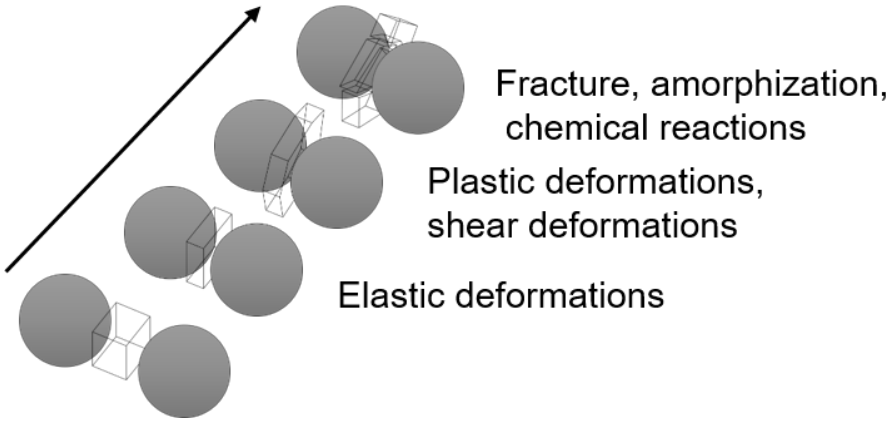



Figure 1.11: Schematic representation of the HEBM energy transfer mechanism.

through the exploitation of opportune milling equipment[64]. The process consists in exposing definite quantities of powder reactants to repeated energy transfer phenomena, realized by colliding balls. During the process, the colliding balls release their kinetic energy to the trapped powder, and a sequence of several physico-chemical phenomena can occur, as schematically depicted in figure 1.11.

The evolution during the HEBM process can be observed through the surface area development, as summarized in figure 1.12. At the beginning, the main effect is represented by the grinding of particles and the formation of new surfaces. The clean surfaces derived from particle fractures can interact with each other and an intimate mixing of the milled precursors is produced. Nanostructuration of the particles begins at this stage, and the powder mixture is highly activated toward possible reaction (Phase I). Particles are subjected to plastic deformations, and at increased processing time phenomena such as interdiffusion of species and atomic rearrangements, nucleation of new stable and metastable phases in nanostructured form, polymorphic transitions, amorphization or recrystallization transformations, and so on, can occur (Phase II). Providing further energy, homogenization and growth of particles in the milled mixture can occur (phase III). Although the process can also produce materials in their state of thermodynamic equilibrium, a HEBM process is mainly a "nonequilibrium" process, due to the impulsive nature of the mechanism of energy transfer, occurring at low temperature. Materials obtained in this way often show unique characteristics, not detectable using other processing techniques [65–67].

In view of large scale application of SOFCs, and therefore with the need for cost-effective deposition methods, cheap wet-powder coating techniques should be considered preferred. These methods consist in formulation of inks, application of the coating with techniques like spraying, slurry deposition, dip-coating or ink-jet

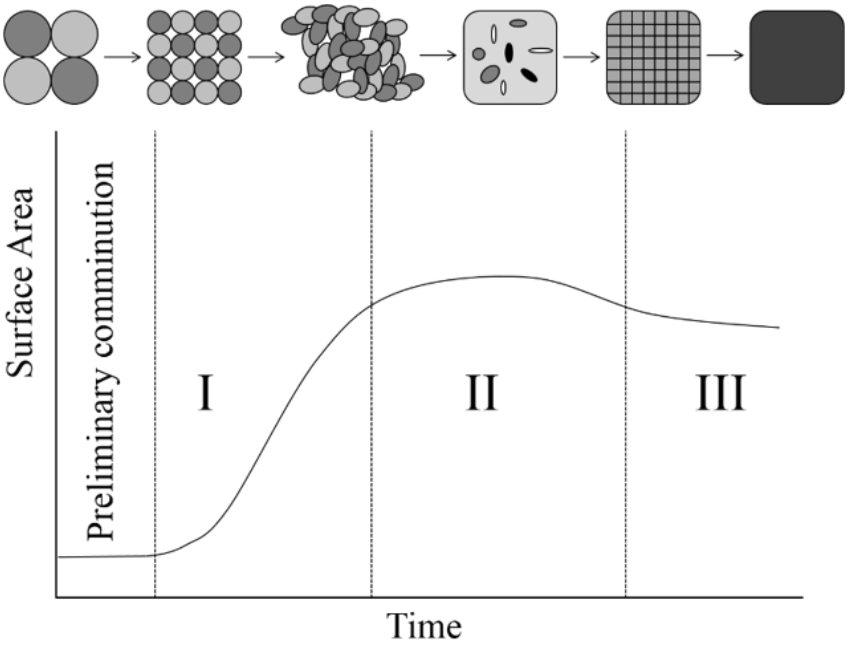



Figure 1.12: Schematic representation of a HEBM treatment evolution depicted as surface area development during the process.

printing, and a sintering step to densify the coating layer. In these cases, powder synthesis is critical to obtain compounds with the proper morphology, suitable for these cheap deposition techniques to realize at low sintering temperature the thin and dense layers requested for the protective activity. Nanostructuration of the compounds, obtained commonly through HEBM treatments, can be beneficial for the formulation of inks and the sintering steps [68]. HEBM was selected therefore as a cost-effective and environmentally friendly synthesis strategy in order to produce nanostructured oxide particles, evaluating the response of pristine oxide powders to the mechanochemical treatment and the chemico-physical properties of milled powders, to assess if HEBM could be effectively applied as synthetic method, and the results are reported in section 3.1.

After evaluating the behaviour of Mn-Co spinels subjected to a mechanochemical treatment, the dependence of chemico-physical properties of milled powder on the composition is studied evaluating several Mn:Co ratios and doping levels, focusing on Cu, Fe and simultaneous Cu+Fe doping. The results are reported in section 3.2.

## 1.4 Lanthanum based perovskites

As briefly introduced in section 1.2.2, an effective use of perovskite coatings for SOFC protection has proved to be particularly challenging for various reasons. Firstly, it is very difficult to obtain deposition of fully dense perovskite coatings without using high firing temperatures or long sintering times, that could adversely affect the mechanical properties of the stainless steel substrates [32, 33]. Secondly, $ABO_3$ perovskites may exhibit a mixed electronic and oxygen ion conductivity, which could raise doubts whether they could serve as effective ionic barriers to impede sub-coating oxide scale growth [7]. Besides this, ceramic perovskite layers usually exhibit poor adhesion strength on stainless steel substrates, which could promote premature failure of the coating layers. In this respect, it may be worth mentioning that recent studies report a simple sandblasting procedure with 320 mesh-size sands as an effective and simple way to enhance perovskite coating adhesion onto steel substrates[69].

A further issue, often ignored in the SOFC literature, is related to the fact that perovskite oxides do not have the same stability as other metal oxide systems when they are subjected to high electrical, electrochemical, thermal or oxygen chemical gradients [70, 71]. For instance, cation segregation and structural changes in the surface region are two important degradation issues that are commonly observed in thin perovskite membranes when exposed to steep oxygen chemical gradients [72]. Although the precise degradation mechanism is unclear, the influence of oxygen chemical gradients on perovskite surface stability is usually described in terms of kinetic demixing effects of mobile cations (kinetic instability). Likewise, it is believed that also SOFC perovskite coatings may be susceptible to kinetic instability as very steep chemical or electrical gradients could arise, especially across thin coating layers. All the aforementioned problems could explain, at least in part, why the published literature reports controversial and confusing results about the viability of perovskite coatings to suppress Cr diffusion and metal oxidation rates. For instance, Fu et al. [73] report the results of Sr-doped $LaFeO_3$ coatings (thickness about 70 μm) obtained by sintering at 900 °C for 10 h. The thick perovskite coating significantly reduces Cr diffusion and oxidation growth of a 430 ferritic stainless steel after 1000 h at 800 °C. A systematic study on the effect of various sintering conditions (3h in the range 800-1100 °C ) on the corrosion performance of perovskite coatings has been reported in a more recent study [69] by examining the behavior of a Sr-doped $LaMnO_3$ perovskite coated Crofer 22APU (coating thickness about 20 μm) exposed for nearly 8,000 h at 800 °C. Optimal Cr retention and minimal growth of oxide scales ($Cr_2O_3$ and $(Mn,Cr,Fe)_3O_4$ phases) could be obtained only with perovskite coated samples that

had been sintered at temperatures above 1000 °C, namely at 1100 °C in a $90N_2$-$10H_2$ atmosphere. However, these positive results are not in agreement with the findings of other authors. For instance, lanthanum-based perovskite coatings of $La_{0.8}Ca_{0.2}CrO_3$, $La_{0.8}Sr_{0.2}CrO_3$ and $La_{0.8}Sr_{0.2}MnO_3$ have been studied by Shong et al. [74] for SOFC corrosion protection of Crofer22APU samples. Thick coatings of about 20 µm were prepared by spin coating and then fired in air at 800 °C for 6 h for densification. The authors report that the perovskite coating protection was highly beneficial to improve electric conductivity of the oxide scale, but much less useful in preventing migration of Cr (and also Mn) species through the perovskite layers to the outer surface.

The protective properties of thin perovskite films have been also examined in some studies. Oddly enough, there is more consensus among the authors in reporting excellent protection performance of the perovskite coatings when in the form of thin films. For example, 1 µm coatings of La-based perovskites including $La_{0.8}Sr_{0.2}CoO_3$, $La_{0.6}Sr_{0.4}Co_{0.2}Fe_{0.8}O_3$ and $LaNi_{0.5}Fe_{0}.5O_3$ were applied by Lacey et al. [31] on Crofer22APU and 430 SS substrates by physical vapor deposition. Cr migration across the perovskite coatings was studied after firing at 1000 °C for 3 h followed by an oxidation treatment at 850 °C for 168 h. The authors report that an extensive chemical interdiffusion of the perovskite B-site cations and the transition metals from the steel substrates had occurred during the firing treatment resulting in rapid formation of a stable spinel intermediate layer below the perovskite film. The combination of perovskite and the spontaneously-formed spinel layer was claimed to be highly effective in blocking outward Cr diffusion during the following oxidation treatment. More recently, thin films of conductive $LaCoO_3$ perovskites have been prepared via a novel electrochemical route combined with thermal conversion in air [36]. Uniform, dense and adhesive films of $LaCoO_3$ with 1 µm thickness have been fabricated on Co-coated Crofer22APU steel substrates. After thermal conversion at 800 °C for 4h, an intermediate spinel $Co_3O_4$ layer, 2 µm thick, is also formed that provides additional protection against Cr diffusion. Results also indicate low and very stable ASR values (below 20 $m\Omega \cdot cm^2$) in the range 700-800 °C.

As introduced also in section 1.2.4, evidence from the last two works seems to suggest that an additional formation of an intermediate spinel layer could dramatically enhance the performance of thin perovskite coatings. Speculations could be made about the role of cation demixing in ensuring rapid interfacial cation transport for the spinel phase formation.The patent from Bloom Energy Co., describing the use of double oxide film coatings composed of a perovskite oxide on the top of spinel layer [37], suggests that the absence of a direct contact of the perovskite coating with the inner Cr-rich native oxide the spinel layer could prevents the formation of

unwanted and resistive phases. As a further yet not mentioned effect, it is also possible that the perovskite structure stability could be significantly improved by the intermediate spinel oxide layer. The spinel layer could, in fact, lead to an increased overall coating thickness, which means a lowered oxygen and electrochemical gradient across the perovskite layer. With a proper overall coating thickness, driving forces for cation pumping in perovskite structures should be minimized, including cation segregation and kinetic demixing effects.

### 1.4.1 La-Fe perovskite conversion coatings

As an alternative coating technique, a novel chemical surface treatment has been specifically developed in ENEA laboratories for the corrosion protection of Molten Carbonate Fuel Cell (MCFC) stainless steel bipolar plates. The method produces dense and adherent layers of perovskite coatings onto stainless steels substrates in molten alkali carbonate salt systems. For its novelty, this conversion coating method has been recently patented [75], using eutectic alkali carbonates as a suitable molten salt system. With respect to common deposition techniques (e.g. spray coating, plasma spray, PVD) this dip-coating process would be characterized by the relative absence of geometric constraints of the object to be coated (not line-of sight dependent), theoretically allowing to passivate objects of complex shapes. Research work on this novel chemical coating method has been also published by the inventors subsequent to the patent filing date (2010). Results described in literature are promising and show that the perovskite coating layers produced by the conversion treatment are stable and protective against corrosion of stainless steels in MCFC environments [8, 76]. Based on these previous studies, one purpose of this thesis is to verify the possibility to extend the application of this chemical conversion coating method to the SOFC protection technology which could place the basis for an efficient and highly versatile coating protection method to be used indifferently for any type of high temperature fuel cell systems.

In this molten salt method, a protective $LaFeO_3$ conversion coating is formed by reaction of a stainless steel surface with a lanthanum oxide reactant dissolved in the molten carbonate salt bath. Previous studies have clearly proven that perovskite oxide coatings on austenitic [76] and low-chromium ferritic [8] stainless steels can be produced with homogeneous and controlled structures at relatively low temperatures (approx. 600 °C). Under the oxidizing/basic conditions of the carbonate salt bath, iron is the only element sufficiently active to react with lanthanum to generate an iron oxide stabilized in a perovskite oxide structure, whereas chromium (and nickel, if present in the alloy) is selectively dissolved in the carbonate bath, thus resulting

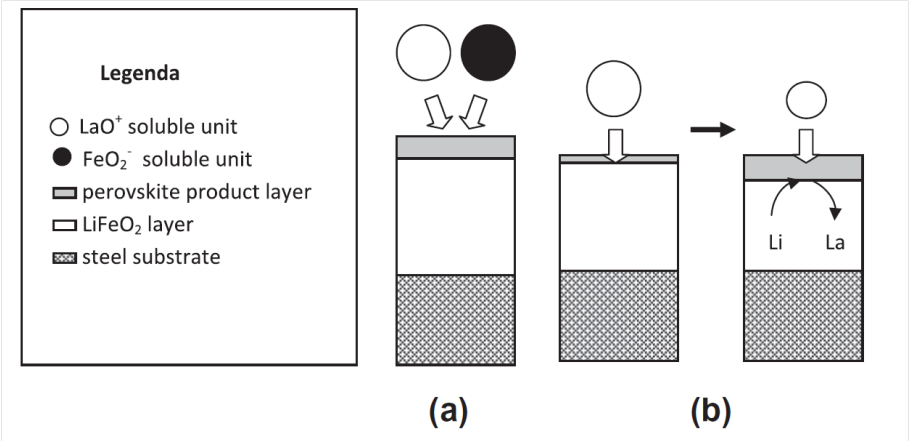



Figure 1.13: Schematic picture of the formation process of a La-Fe perovskite conversion coating by (a) dissolution-precipitation and (b) precursor-template processes [8].

in the formation of a Cr-free $LaFeO_3$–based perovskite coating layer. Morphology of the produced coatings can be controlled tailoring the bath composition. Thick layers (>10µm thickness) can be obtained in highly basic environments exploiting a dissolution-precipitation mechanism, while opportune additive addition will promote the formation of thin coatings (micron size thickness) through a template-conversion mechanism, as schematically reported in figure 1.13 [8].

With $LaFeO_3$ perovskites characterized by an opportune CTE value (approx. $10^{-6}K^{-1}$ between room temperature and 1000°C [77, 78]), the exploitation of the deposition method to SOFC suitable alloys could represent a promising strategy to obtain chromium free and dense perovskite coatings. Its application is discussed in chapter 4.

It is well known that electrical properties of lanthanum ferrite perovskites are highly influenced by defect chemistry of the material and significant variations can be obtained by partial substitution of both lanthanum and iron cations with alkali earth or transition metals. Thus, for instance, reported electronic conductivity of undoped $LaFeO_3$ material at 700°C is in the 0.1-1 S/cm range, which increases by several orders of magnitude upon partial Ca substitution on La site of the perovskite lattice, with a maximum conductivity of ca. 80 S/cm for a $La_0.85Ca_0.15FeO_3$ perovskite composition, or upon Fe substitution with divalent transition metals such as Co [77, 79].

In comparison to a direct perovskite lattice doping, secondary-phase addition could be a different way to increase electrical conductivity of a thick-film coating with a perovskite structure. Possibility of using a two-phase composite approach for enhancing electrical conductivity of perovskite materials is not a new concept

and it has been variously reported in literature. In particular, several studies on magnetoresistive properties of polycrystalline manganite perovskites indicate that electrical conductivity can be greatly enhanced by phase addition of transition metal or metal oxide particles of silver [80–83], copper [84, 85] or cobalt [86]. High conductivity of the added particles and their tendency to segregate at boundaries and surfaces of the perovskite grains have been reported as major factors leading to an improved electrical transport through a two-phase composite manganite perovskite structure.

The development of the molten carbonate method to produce metal-perovskite coatings, exploiting chemical equilibria described in next sections, is discussed in chapter 5.

### On chemical equilibria in molten alkali carbonates

**Acid-base properties of the melt** Molten alkali carbonates represent complex ionic systems. Several chemical equilibria affect acid-base and oxidizing properties of the melts. In particular, in equation (1.6) is reported an acid-base reaction (Lux-Flood acid-base model) involving oxide ion transfer between a base (carbonate anion) and the $CO_2$ gas, that behaves as the acidic component of the system (oxide ion acceptor). The equilibrium constant $K(1.6)$ is influenced by the temperature and the components of the melt.

$$CO_3^{2-} \rightleftharpoons CO_2 + O^{2-} \tag{1.6}$$

$$K_{(1.6)} = \frac{a_{O^{2-}} \cdot p_{CO_2}}{a_{CO_3^{2-}}} \tag{1.7}$$

Further important acid-base reactions influence the oxidizing power of the melt, such as the reactions involving the formation of $O_2^{2-}$ (peroxide) and $O_2^{-}$ (superoxide), as follows respectively from equations (1.8) and (1.9).

$$\frac{1}{2}O_2 + O^{2-} \rightleftharpoons O_2^{2-} \tag{1.8}$$

$$\frac{3}{4}O_2 + \frac{1}{2}O^{2-} \rightleftharpoons O_2^{-} \tag{1.9}$$

The two reactions can be related by the disproportion reaction of superoxide ion, as reported in equation (1.10).

$$2O_2^{-} \rightleftharpoons O_2^{2-} + O_2 \tag{1.10}$$

$$K_{(1.10)} = \frac{a_{O_2^{2-}} \cdot p_{O_2}}{a^2_{O_2^-}} \tag{1.11}$$

$K_{(1.10)}$ is reported to be ca. 0.11 at 723 °C for a binary lithium-sodium carbonate eutectic salt [87]. Therefore, with presence of appreciable amounts of oxygen in the supernate, oxide and peroxide ions are almost fully converted to superoxide, while in oxygen-lean atmospheres, oxide and peroxide are more important species than superoxide ions. The redox power of a carbonate melt is controlled by the amount of molecular oxygen and reactive oxides species dissolved in the melt. Since chemical stability of reactive oxide species greatly improves in basic melts, this implies that the oxidizing power of carbonate salts considerably increases along with melt basicity. Energetic considerations also indicate that stability of the peroxide compared with that of oxide and superoxide anions increases with decreasing the size of the alkali cations [88]. Thus, peroxide is largely predominant over superoxide concentration in lithium-sodium eutectic carbonate under basic conditions, namely $CO_2$-lean gases. At 750 °C, for instance, its concentration is of the order of $10^{-5}$ mol fractions, which is a value 100 to 1000 times higher than under acidic conditions [89]. The addition of further species to the molten carbonates can additionally influence the oxidizing property of the bath. In particular, it has been observed that the addition of magnesium oxide or lanthanum oxide in the melt can result in oxide buffering systems through the formation and dissociation phenomena of oxycarbonate species. This produces significant increase of peroxide and oxide ion concentration and therefore melt basicity [90, 91].

**Metals corrosion and solubility** Metal corrosion in molten salts is usually characterized by two steps: the oxidation of the metal and the dissolution of the oxide scales. The oxidation phenomena is obviously linked to the availability of oxidant species, that may have to diffuse through the melts or to develop by dissociation of oxides, and can be described by equation (1.12) [92, 93]:

$$Me + CO_3^{2-} \rightleftharpoons MeO + CO_2 + 2e \tag{1.12}$$

Solubility of the formed oxides is highly influenced by the acid-base chemistry of the molten carbonate melts. For instance, transition metal oxide solubility has been the subject of most previous studies because of its relevance to the development of NiO cathode materials in molten carbonate fuel cells [94–98]. Nickel oxide solubility is in general relatively low under typical fuel cell cathode condition, characterized by low basicity, although it may extensively vary depending on molten carbonate

composition, temperature and gas atmosphere. In particular, in oxide ions rich melts, basic dissolution modes prevail, meaning that metal oxides dissolve through the reaction with oxide ions to form soluble complex anions as indicated in equation (1.13) and (1.14):

$$NiO + O^{2-} \rightleftharpoons NiO_2^{2-} \tag{1.13}$$

$$2NiO + O^{2-} + \frac{1}{2}O_2 \rightleftharpoons 2NiO_2^{-} \tag{1.14}$$

Quantitative measurements indicate that NiO solubility may vary by two/three order of magnitude with melt basicity [95], and similar results have been reported also for copper or silver oxide, suggesting that high solubility of these metal ions can be obtained through opportune addition to the molten carbonate, allowing to hypothesize the exploitation of Ni, Cu and Ag as reactants in the above mentioned systems.

Regarding other elements, chromium tends to form highly soluble chromates. Several iron oxides can be formed in molten alkali carbonates, namely FeO, $Fe_3O_4$, $Fe_2O_3$ and lithiated species [99].

The exposure of complex alloys is characterized by several oxidation processes. Solubility of the oxidized species and further oxidation of the alloying elements are as expected well connected, due to the possible different solubility of the corrosion products. In ferritic stainless steels exposed to molten Li/Na carbonates, a dual-structured oxide scale is usually formed. An outer layer of lithiated iron oxide characterized by low solubility, left by chromate dissolution in the melt, acts as a protective layer for an inner layer composed by a chromium-rich oxide. The outer layer protects the sublayer from further carbonate attack, that would otherwise cause other chromate formation, while the corrosion of stainless steels is controlled by the stability of the chromium-rich layer, characterized by low diffusivity of metal ions to the surface [100].

The nature of the iron oxide is dependent on the environment: while a protective $LiFeO_2$ oxide is commonly formed in most of the conditions [100], lithiated spinel formation (e.g. $LiFe_5O_8$) seems promoted in oxygen-lean baths at low temperature (e.g. 580 °C) [101].

**Galvanic coupling in molten carbonates** Galvanic corrosion can be regarded as an electrochemical process in which one metal corrodes preferentially to another, occurring when both metals are in electrical contact in the presence of an electrolyte. The presence of several different metal ions in the molten carbonate bath leads

therefore to consider the occurrence of such phenomena. In particular, the reaction reported in equation (1.12) can be related to the following equilibrium potential:

$$E = E^0(MeO, CO_2/Me, CO_3^{2-}) - \frac{RT}{2F} ln \frac{a_{Me} \cdot a_{CO_3^{2-}}}{a_{MeO} \cdot P_{CO_2}} \tag{1.15}$$

In table 1.3 some oxidation reductions of metals evaluated in this work are reported with the standard redox potentials calculated at 600 °C versus the $CO_2/O_2$/Au electrode (as standard in molten carbonate environments). Nobility of the metals proceeds similarly as in more common environments (e.g. aqueous solutions), with chromium (a strong reducing agent) characterized by highly negative potential, and silver (a strong oxidant) slightly positive.

Table 1.3: Standard redox potentials for oxidation of various metals (vs. $CO_2/O_2$/Au SRE electrode) at 873 K

| Reaction | $E^0$ |
|---|---|
| $2Cr+\frac{3}{2}O_2 \rightleftharpoons Cr_2O_3$ | -1.65 |
| $Fe+\frac{1}{2}O_2 \rightleftharpoons FeO$ | -1.07 |
| $Ni + \frac{1}{2}O_2 \rightleftharpoons NiO$ | -0.82 |
| $Cu+\frac{1}{2}O_2 \rightleftharpoons CuO$ | -0.40 |
| $2Ag + \frac{1}{2}O_2 \rightleftharpoons Ag_2O$ | 0.12 |

It has been previously observed that accelerated corrosion of the less noble metal and reduction of the more oxidant can take place for instance in multi-phase Ni/Cu alloys [102]. The presence of several transition or noble metal ions in the molten carbonate melts may therefore give rise to the formation of galvanic couples, if their corrosion potentials in the melt are different. As shown in chapter 5, this may be exploited to promote the formation of metal/perovskite composite coatings.

# Chapter 2

# Materials and methods

## Mn-Co spinels

To study the mechanochemical behaviour of Mn-Co and Fe, Cu doped Mn-Co oxides, the compositions reported in table 2.1 have been evaluated. The samples were obtained mixing appropriate amounts of metal oxides, namely $Mn_3O_4$ (97%, Sigma Aldrich), $Co_3O_4$ (99%, Sigma Aldrich), CuO (99 %, Carlo Erba) and $Fe_2O_3$ (99 %, Carlo Erba). Approximately 8 g of powder were milled for each synthesis. The HEBM process was carried out in a SPEX 8000M mixer mill, using steel vials and steel balls in a 10:1 ball to powder weight ratio. To avoid oxidation of the powders, the milling vials were sealed in argon atmosphere. To evaluate the mechanochemical response, the HEBM treatment was carried out for different milling times, as explained in section 3.1.

For the results reported in section 3.2, the powders were subjected to 10 h of treatment. After the milling treatments, EDX analyses have been successfully carried out to exclude the presence of chromium that could highlight chemical contamination from the milling equipment.

Room temperature X-Ray diffraction analysis (XRD) was carried out on a SEIFERT PAD VI diffractometer equipped with Mo $K\alpha$ radiation source and a LiF monochromator on the diffracted beam, on an angular dispersion X-ray diffractometer (Italstructures, INEL curved position sensitive detector) using a Fe $K\alpha_1$ monochromatized source and on a Bruker D2 equipped with a Co $K\alpha$ source. The high temperature XRD analyses were carried out using the angular dispersion diffractometer coupled to a heating reactive chamber (Anton Paar Gmbh) in air (section 3.1- 3.2) and in $He/H_2$ 5% atmosphere, 50 ml/min flow (section 3.2).

Quantitative phase analysis (QPA) was carried out by means of Rietveld analysis. The full-profile Rietveld refinement method [103, 104], implemented into the MAUD software [105], permitted to perform numerical QPA. Preliminary structural data

Table 2.1: Sample nomenclature, metal composition, corresponding spinel composition and section of the thesis where the sample is described:

| Sample name | Metallic ratio | | | | Corresponding composition | Section |
|---|---|---|---|---|---|---|
| | Mn | Co | Fe | Cu | | |
| MnCo2 | 0.33 | 0.67 | 0 | 0 | $MnCo_2O_4$ | 3.1, 3.2 |
| Mn1.25Co1.75 | 0.42 | 0.58 | 0 | 0 | $Mn_{1.25}Co_{1.75}O_4$ | 3.2 |
| Mn1.5Co1.5 | 0.5 | 0.5 | 0 | 0 | $Mn_{1.5}Co_{1.5}O_4$ | 3.1, 3.2 |
| MnCo1.8Fe0.2 | 0.33 | 0.6 | 0.07 | 0 | $MnCo_{1.8}Fe_{0.2}O_4$ | 3.2 |
| MnCo1.6Fe0.4 | 0.33 | 0.53 | 0.14 | 0 | $MnCo_{1.6}Fe_{0.4}O_4$ | 3.2 |
| MnCo1.8Cu0.2 | 0.33 | 0.6 | 0 | 0.07 | $MnCo_{1.8}Cu_{0.2}O_4$ | 3.2 |
| MnCo1.6Fe0.2Cu0.2 | 0.33 | 0.53 | 0.07 | 0.07 | $MnCo_{1.6}Fe_{0.2}Cu_{0.2}O_4$ | 3.2 |
| Mn1.33Co1.17Cu0.5 | 0.44 | 0.39 | 0 | 0.17 | $Mn_{1.33}Co_{1.17}Cu_{0.5}O_4$ | 3.2 |
| Mn1.57Co0.93Cu0.5 | 0.52 | 0.31 | 0 | 0.17 | $Mn_{1.57}Co_{0.9}3Cu_{0.5}O_4$ | 3.2 |
| Mn2.05Co0.45Cu0.5 | 0.68 | 0.15 | 0 | 0.17 | $Mn_{2.05}Co_{0.45}Cu_{0.5}O_4$ | 3.2 |

were obtained by the ICSD database [106]. A well crystallised KCl standard sample [107] was prepared and utilised to calculate the instrumental broadening of the diffractometer.

The numerical goodness of the fits was evaluated with a weighted-profile parameter $R_{wp} = [\frac{\sum w_i(y_{0i}-y_i)^2}{\sum w_i(y_{0i}^2}]^{\frac{1}{2}}$, where for each $i^{th}$ point of the spectrum $y_{0i}$ and $y_i$ are respectively the observed and simulated intensity and $w_i$ is a weight factor. The parameters refinement procedure was iterated until $R_wp<0.15$.

Generally a Rietveld phase content analysis performed on well defined patterns coming from micro-crystalline powders (i.e. sharp and well defined peaks) produces quantitative data affected by relative error values as low as 1% [108]. However patterns coming from milled powder mixtures are composed of broad peak profiles, as normally expected by the nanosized crystalline domain. In addition the structural affinities of the examined oxides further affect the error evaluation due to significant overlapping of similar patterns. However, despite the non-ideality of the analysed patterns, obtained quantitative phase content results were characterized by maximum acceptable error values lower than 5%.

On the basis of the compounds previously identified by qualitative analysis, crystallographic models were properly chosen for every pattern. Pristine crystallographic models are reported in table 3.1. Starting from 2.5 h milled sample, cell parameters of phases and their relative content were calculated. Obtained results were utilised as input parameter for patterns coming from the successive milling time. Nucleation of new phases was taken into account when requested by qualitative pattern analysis results. High angle reflections permitted to avoid physically unacceptable numerical convergences in cell parameters, such as for $Co_3O_4$ and $MnCo_2O_4$ phases. Con-

cerning quantitative analysis performed on in situ XRD patterns collected during the thermal treatments, refined data obtained from room temperature experiments were used as starting structural data for the 200 °C pattern. For higher temperature spectra, refined output of the previous temperature step pattern was utilised as input data. Due to the presence of interfering reflection produced by the reactive chamber the analysed range was limited to the range $20°<2\Theta<60°$.

Morphology of the samples was evaluated by means of Scanning Electron Microscopy (SEM) equipped with Energy Dispersive X-ray microanalysis (EDX) and Nitrogen adsorption at 77K(Quantachrome Autosorb iQ). In the evaluation of the adsorption isotherms, BET method [109] was applied to calculate the specific surface area (SSA). The particle size $l$ was calculated as $l = \frac{6}{SSA \cdot \rho}$, where $\rho$ is the crystallographic density.

Thermogravimetric analysis was carried out using a Perkin Elmer thermobalance (Pyris Diamond TG/DTA, Perkin Elmer). The measurements were conducted with different procedures and atmospheres:

- From room temperature to 1200 °C with 60 minutes of dwell time and 5 °C/min heating and cooling rate, in air flow (50 ml/min), to evaluate the thermal behaviour in air atmosphere.

- From room temperature to 800 °C with 60 minutes of dwell time and 10 °C/min heating and cooling rate, in $Ar/H_2$ 5% flow (50 ml/min ), followed by a similar scan carried out in air flow (50 ml/min), to evaluate the behaviour of the powders during treatments in reducing atmosphere and subsequent reoxidation.

Peak fitting of DTG curves acquired in reducing atmosphere was carried out using the Fityk software [110] simulating the peaks by means of Fraser-Suzuki functions [111]. As explained later in section 3.1, each curve was simulated assuming one single peak for the spinel reduction phenomena and one single peak for Co, Fe and Cu reduction.

Dilatometric measurements were performed in a push-rod dilatometer (DIL 402C, NETZSCH). To evaluate sintering behaviour, consolidated pellets of about 6 mm diameter length were obtained by uniaxial cold pressing (3.5 $t/cm^2$). Sintering behaviour in air was evaluated up to 1200 °C with a heating and cooling rate of 5 °C/min. Sintering behaviour in reducing atmosphere and reoxidizing condition were carried out up to 800 °C with 1 h of dwell time with a heating rate of 5 °C/min, respectively in $N_2/H_2(5\%)$ flow (50 ml/min) and air atmosphere.

Thermal expansion measurements were carried out in air with a heating rate of 10 °C/min, on pellets of about 6 mm diameter and 2.5 mm height sintered as explained

Table 2.2: Nominal composition of the ferritic alloys used in this work:

| steel | 405 | 441/K41 | Sanergy HT | Crofer 22H | |
|---|---|---|---|---|---|
| element | avg. | avg. | avg. | min | max |
| Cr | 13.9 | 17.8 | 21.2 | 20 | 24 |
| Fe | bal | | | | |
| C | 0.06 | 0.018 | 0.04 | | 0.03 |
| Mn | 0.4 | 0.3 | 0.3 | | 0.8 |
| Si | 0.44 | 0.6 | 0.12 | 0.1 | 0.6 |
| Al | 0.25 | | 0.017 | | 0.1 |
| W | | | 0.1 | 1 | 3 |
| Nb | | Nb+Ti=0.65 | 0.71 | 0.2 | 1 |
| Ti | | | 0.09 | 0.02 | 0.2 |
| La | | | | 0.04 | 0.2 |
| P | 0.024 | | 0.01 | | 0.05 |
| Ni | 0.24 | | 0.8 | | 0.5 |
| Cu | | | 0.02 | | 0.5 |
| Mo | | | 0.96 | | |
| N | 0.027 | | | | |

late in section 3.2. Average CTE was calculated between room temperature and 800 °C as: CTE $= \frac{1}{L_0} \cdot \frac{\Delta L}{\Delta T}$, where $L_0$ is the initial length and $\Delta L$ represents the length change occurring in the $\Delta T$ temperature range.

To assess electrical conductivity, pellets of about 10 mm diameter and 0.5 mm height and were obtained by uniaxial cold pressing (3.5 T/cm2) and sintered similarly to thermal expansion samples. The conductivity was measured by applying the Van der Pauw method [112] (PAR273A potentiostat coupled to a HP 3457A multimeter) in the 500–800 °C temperature range. Activation energy Ea was calculated from the Arrhenius plot obtained using the formula: $\sigma = \frac{\sigma_0}{T} e^{-\frac{E_a}{kT}}$, where $\sigma$ is the conductivity, $T$ the temperature, $\sigma_0$ the pre-exponential factor, $E_a$ the activation energy and $k$ the Boltzmann's constant.

## La-Fe perovskites

Several commercial ferritic alloys have been used in this work, namely SS405, K41, Sandvik Sanergy HT (SSHT) and ThyssenKrupp Crofer 22H. The nominal composition of the alloys is reported in table 2.2. Before the molten carbonate treatment, steel samples of suitable dimensions were mechanically polished with SiC abrasive paper to 1200 grit finish and cleaned with ultrasound in acetone.

The molten carbonate dip coating treatments have been carried out using several salt formulations, based on a $LiCO_3$-$NaCO_3$ eutectic mixture (53:47). To the eutectic

mixture, 1 mol% of $La_2O_3$ was added as basicity regulator and as required for the formation of the La-Fe perovskite. Further additives were added as basicity regulators to promote the growth of thick or thin coatings. Furthermore, for the experiments reported in chapter 5, different amounts of metal oxides were added. A summary of the formulations utilized is reported in table 2.3.

Table 2.3: Summary of salt names and additives introduced in the eutectic $LiCO_3$ - $NaCO_3$ with 1 mol% $La_2O_3$, targeted coating morphology, level of basicity (with respect to the salts used in this work), metal additions and thesis section where the application is described:

| Name | Additives | Morphology | Basicity | Metal | Section |
|---|---|---|---|---|---|
| 10Mg | 10 mol% MgO | thick | high | | 4.1 |
| 3Mg | 3 mol% MgO | thick | low | | 4.1 |
| 10Mg0.25X | 10 mol% MgO<br>0.25 mol% additive X | thin | high | | 4.2 |
| 6Mg0.25X | 6 mol% MgO<br>0.25 mol% additive X | thin | medium | | 4.2 |
| 10Mg0.10X | 10 mol% MgO<br>0.1 mol% additive X | thin | high | | 4.2 |
| 3Mg2Cu | 3 mol% MgO<br>2 mol% CuO | thick | low | Cu | 5.1 |
| 3Mg4Cu | 3 mol% MgO<br>4 mol% CuO | thick | low | Cu | 5.1 |
| 10Mg1Cu | 10 mol% MgO<br>1 mol% CuO | thick | high | Cu | 5.1 |
| 3Mg3Ni | 3 mol% MgO<br>3 mol% NiO | thick | low | Ni | 5.2 |
| 6Mg1Ni | 6 mol% MgO<br>1 mol% NiO | thick | medium | Ni | 5.2 |
| 10Mg1Ni | 10 mol% MgO<br>1 mol% NiO | thick | high | Ni | 5.2 |
| 10Mg1Ag | 10 mol% MgO<br>0.5 mol% $Ag_2O$ | thick | high | Ag | 5.3 |

Different sample geometries have been adopted in this work. To study the passivation mechanisms and tailor the experimental conditions, small samples of approx. 1cm side were built as electrodes soldering a gold wire to one side of the sample and covering it with ceramic paste, as previously reported in [76, 113], allowing to follow the passivation kinetics in situ through electrochemical methods. A schematic view of the electrode geometry is reported in figure 2.1a, while the image of an electrode after the experiment is reported in figure 2.1b.

To obtain the full coated samples for the oxidation experiments described in sec-

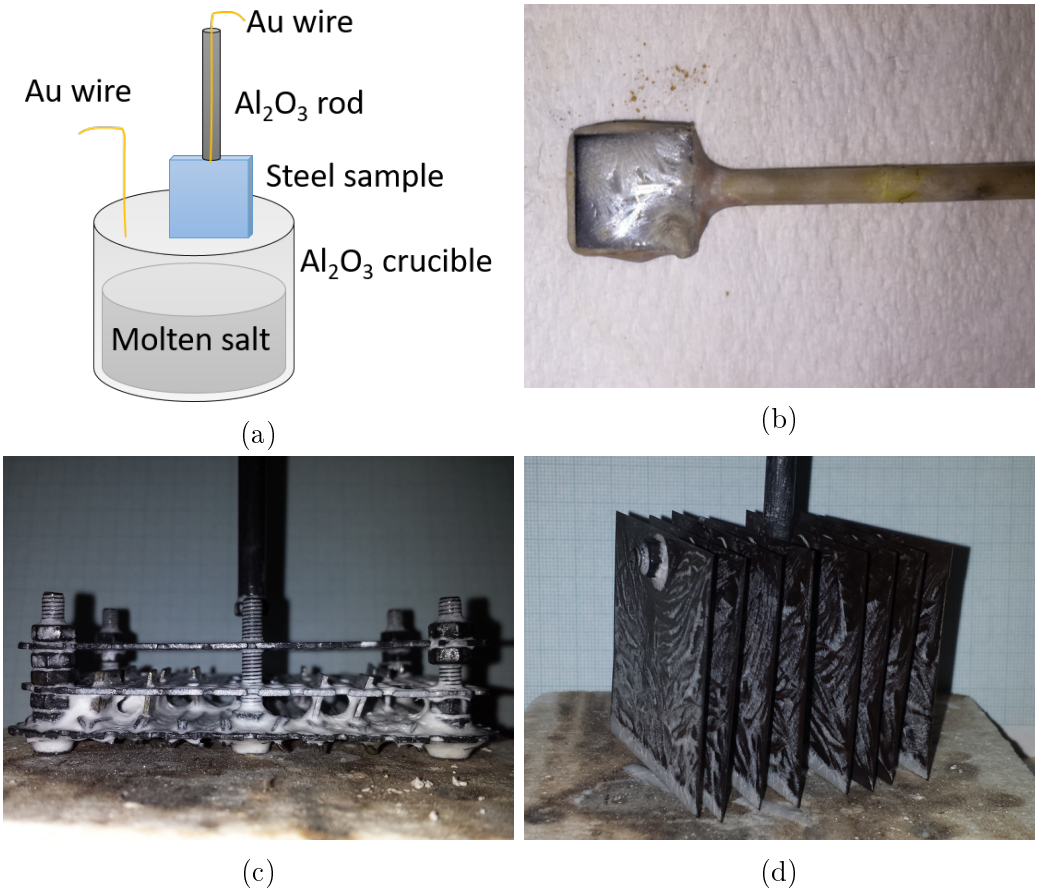



Figure 2.1: (a) Schematic view of the electrode samples processing geometry and pictures of (b) a steel electrode, (c) the sample cage used to obtain full coated steel samples and (d) steel foils after a passivation treatment.

tion 6.1, samples were enclosed in the steel cage reported in figure 2.1c and subjected to the passivation treatment. To produce the samples subjected to oxidation experiments described in section 6.2.1-6.2.2-6.2.3, steel foils were cut to approx. 50X50mm and suspended through a drilled hole as depicted in figure 2.1d.

The passivation treatment has been carried out in $Al_2O_3$ crucibles, reported in figure 2.2a. Preliminary experiments with electrode samples were carried out in the small crucibles, using approx. 50 g of salt. Scaled-up synthesis with foil samples were carried out in the larger crucibles, using approx. 800 g of salt.

The experiments were carried out at various temperatures, as explained later in the text, in the 550÷ 650 °C range. The tests were carried out with a $CO_2$ gas coverage, bubbling in the salt or flowing over the melt as explained later in the text.

To evaluate samples micro-structure, X-Ray Diffraction analysis has been carried out on a SEIFERT PAD VI diffractometer, equipped with Mo K$\alpha$ radiation and a LiF monochromator on the diffracted beam, and on an angular dispersion X-ray diffractometer (Italstructures, INEL curved position sensitive detector) using a Fe



(a) (b)

Figure 2.2: Picture of the $Al_2O_3$ crucibles used for the small scale experiments (a, left) and scaled up passivation process (a, right), the latter depicted during operation (b) with the $Al_2O_3$ rods used to insulate the thermocouple and to provide gas flow.

K$\alpha_1$ monochromatized source.

To evaluate samples morphology, Scanning Electron Microscopy coupled with Energy Dispersive X-ray microanalysis (EDX) was carried out on a JEOL JSM-5510LV instrument. Sample cross-sections for SEM analysis were conventionally prepared by sectioning, hot mounting with epoxy thermosetting resins and standard polishing procedures.

### Electrochemical characterization of perovskite conversion coatings

Standard electrochemical potentials reported in table 1.3 and in chapter 5 have been calculated with the HSC Chemistry for Windows (5.1) software with respect to the standard oxygen electrode, constituted by a gold electrode in an eutectic LiK salt under 1 atm of $CO_2(67\%)/O_2(33\%)$ gas, constituting the Standard Reference Electrode (SRE) in molten carbonates.

In the current work, a simple gold wire probe inserted directly in the same cell was used as a internal pseudo-reference electrode. As previously reported [76], this pseudo-reference electrode is characterized by stability and reversibility with respect to the SRE. The gold electrode immersed in a carbonate melt under a $CO_2$ gas, even with trace levels of $O_2$, can be in fact assumed to be thermodynamically equivalent to a very dilute oxygen electrode [87, 114], according to the following equilibrium:

$$CO_2 + \frac{1}{2}O_2 + 2e \rightleftharpoons CO_3^{2-} \tag{2.1}$$

The evaluation of the Open Circuit Potential (OCP) is commonly adopted in the analysis of conventional chemical conversion processes in water solution for several

purposes, such as the analysis of reaction mechanisms, of the passivation kinetic and of the influence of the process parameters (e.g. temperature, time, reactant concentration) on the interfaces. In this work, its measurement in the molten carbonate bath is carried out to evaluate the passivation degree of the steel samples. This can be evaluated in terms of the Mixed Potential corrosion theory: the passivation of an active surface can be considered as a form of inhibition of the anodic process, due to the drastic reduction of the rate of metal dissolution by the passivation film, and can be described by and increase of the Tafel anodic curve slope. The limitation of the anodic dissolution current will thus promote the shift of the corrosion potential (the meeting point of anodic and cathod curves) towards the cathodic compensation reaction potential [115]. The formation of an effective passive layer can be therefore suggested by the ennoblement of the OCP, as already seen in the case of a similar system in [8, 76].

## Oxidation experiments

Passivated samples have been subjected to oxidation tests to evaluate the coating layer stability, carrying out the experiments in air and in dual atmosphere (air/$H_2$) conditions.

Coupons exposed in air were placed in alumina vessels and inserted in furnace systems, performing the experiments at 700 °C in static ambient air (3vol% average moisture content).

Experiments carried out in dual atmosphere were conducted by exposing the coupons to simulated anode and cathode typical SOFC operating conditions. At the scope, a SOFC button cell test apparatus specifically adapted to allow ASR measurements during oxidation was adopted, reported in figure 2.3. A platinum gauze, 100 mesh, was used as cathode current collector, while a nickel one was employed as the anode current collector for measuring ASR. In this case, contact paste was not used to optimize the interfacial contact between steel coupons and current collectors, since purpose of these ASR measurements was detection of abrupt changes in surface resistivity rather than obtaining absolute values with high accuracy. Furthermore, the absence of the paste allowed an easy microscopic examination of the steel coupon surfaces after testing. The steel coupons were mounted on an alumina base and fixed to it by means of a high temperature refractory paste, which after being baked under the manufacturer's specified conditions plays two roles: to hold the sample in place and avoid gas leakages from air chamber to hydrogen chamber and vice-versa. Then the coupons were inserted in a high temperature furnace, to reach the operating temperature. A schematic overview of the experimental appa-

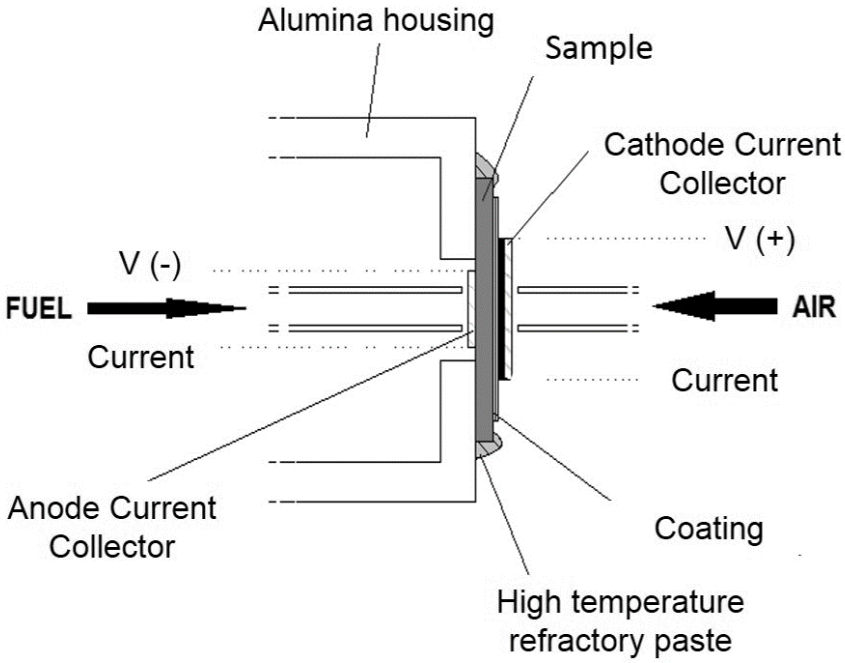



Figure 2.3: Schematic representation of the experimental set-up used for the dual atmosphere ASR measurements.

ratus is depicted in figure 2.3. ASR/dual atmosphere tests were conducted at 700 °C by exposing the coupons to typical SOFC operating conditions, according to the FCTESQA standard conditions [116] (anodic flow:$H_2$ 35 ml/min, gas humidity: 3%, cathodic flow: air 83 ml/min, gas humidity 3%) and the ASR was monitored by electrochemical impedance spectroscopy (EIS) measurements, carried out using a Solartron 1260 frequency response analyzer (FRA) module coupled with a Solartron 1287 Electrochemical Interface. ZView software for Windows was employed to process the EIS data. Impedance spectra were recorded imposing a frequency scan from 100 kHz to 0.1 Hz, with an amplitude of 10mV; measurements were repeated at regular intervals, typically at 24 h periods.

Exposed samples were characterized by means of XRD and SEM analysis similarly as reported in previous section.

# Chapter 3

# Mn-Co spinels by mechanical activation

Cobalt-manganese spinels have been widely identified in literature as promising coating materials for ferritic alloys to be adopted in SOFCs. These materials possess the requested stability in cathodic environments (highly oxidizing environments with water vapor at high temperature), sufficient electrical conductivity and compatible thermal expansion characteristics. Several studies have been reported in literature proving the effectiveness of Mn-Co coatings and the possibility to further enhance the coating properties through compositional tailoring. Most of the results reported in literature, however, are focused on the application and functional properties of coatings, rather than on the basic chemico-physical properties of such systems, leaving some uncovered areas such as the evaluation of the effect of composition on thermal expansion behaviour.

Considering however Mn-Co spinels as a *mature* material, and identifying the need for the large-scale application, focus of this chapter has been directed on the evaluation of cost-effective and environmentally friendly synthesis methods, such as the High Energy Ball Milling technique, and processing variables evaluation, such as sintering mechanisms in air and in reducing atmospheres, to further bring these materials and related coating technologies near to the final targets required for full SOFC market penetration.

In this chapter are therefore reported the results related to the mechanochemical processing of mixed Mn-Co oxides (section 3.1) and the properties of Mn-Co and Cu, Fe doped processed powders, focusing on high temperature spinel stability, sintering behaviour in air and in reducing atmospheres, thermal expansion and electrical conductivity (section 3.2).

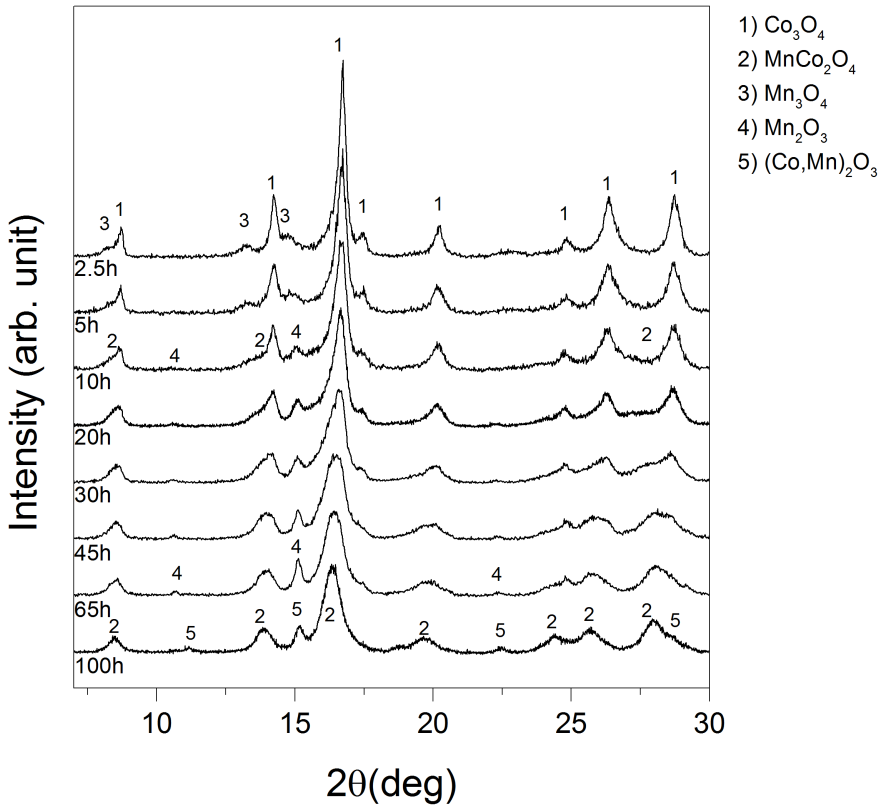



Figure 3.1: X-Ray Diffraction patterns (Mo source) of the Mn1.5Co1.5 powder mixture subjected to different milling times.

## 3.1 Mechanochemical processing of Co-Mn spinels

### 3.1.1 Mechanochemical evolution of powder mixtures

The energy transfer phenomena occurring between the colliding balls and the trapped powder, taking place during the HEBM treatment, give rise initially to significant comminution and intimate mixing of highly defective powders. This first activation step promotes solid-state reactions among the starting reactants at particles interfaces consisting in the nucleation and growth of new crystalline phases. In figure 3.1 and 3.2 the XRD patterns collected at different milling times are reported, respectively for Mn1.5Co1.5 and MnCo2 samples, while in figure 3.3 QPA results obtained from the patterns refinements are summarized.

Phase evolution observed in the HEBM treatment of Co-Mn mixed oxides clearly reflects both comminution and reaction phenomena. Starting from the Mn1.5Co1.5 composition, after 2.5 h of milling XRD patterns evidence the characteristic diffrac-

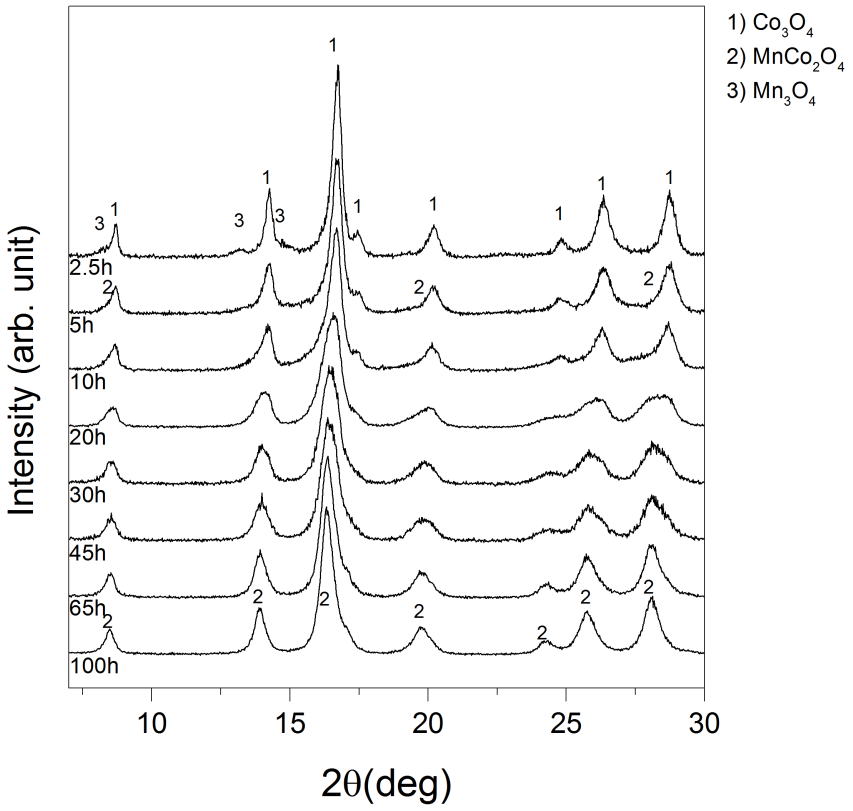



Figure 3.2: X-Ray Diffraction patterns (Mo source) of the MnCo2 powder mixture subjected to different milling times.

tion of the starting reactants, $Co_3O_4$ (JCPDS card N. 42-1467) and $Mn_3O_4$ (JCPDS card N. 24-0734). Significant peak broadening is visible, ascribable to nanostructuration and defectivity. After 10 h of milling, two new phases nucleate: a cubic spinel phase, identified as $Mn_xCo_{3-x}O_4$ with x$\sim$2, and a bixbyte-type phase, labeled as $Mn_{2-y}Co_yO_3$ with y$\sim$2, as identified by comparison with $MnCo_2O_4$ (JCPDS card N. 23-1237) and $Mn_2O_3$ (JCPDS card N. 24-0508) diffraction cards. After 20 h of milling time, peaks related to $Mn_3O_4$ are no more recognizable.

In the following milling steps a significant growth of the $Mn_xCo_{3-x}O_4$ and a slight growth of $Mn_{2-y}Co_yO_3$ phases is observed at the expenses of the $Co_3O_4$ precursor, fully consumed after 65 h of milling. After 100 h of milling, peaks ascribable to the bixbyite vanish, while appear peaks ascribable to the presence of an ilmenite-type oxide, identified as $Co_{1-z}Mn_zO_3$ in by comparison with $CoMnO_3$ 12-0476 JCPDS card. This phase is probably originated by the relevant insertion of Co ions in the cubic bixbyite-type oxide, causing a trigonal distortion in the lattice.

Regarding MnCo2 composition, XRD patterns and QPA evolution are simi-

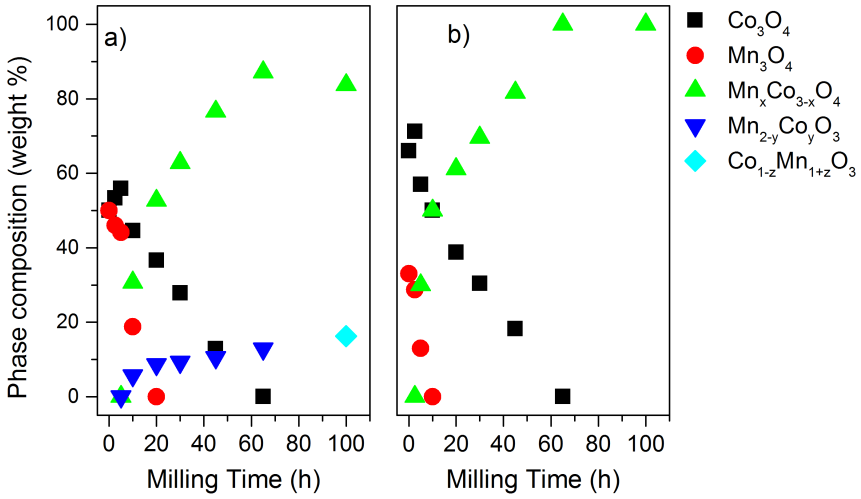



Figure 3.3: Quantitative phase analysis results (weight%) of (a) Mn1.5Co1.5 and (b) MnCo2 samples as a function of milling time.

lar to those described for Mn1.5Co1.5 composition. Nevertheless, a faster $Mn_3O_4$ disappearance is noted, and the only reaction product is the mixed cubic spinel $Mn_xCo_{3-x}O_4$ phase, with reaction complete after 65 h.

The qualitative analysis of the pattern sequence can help to gather further information on the compounds evolution during the milling process. As clearly highlighted by the 20 h and 30 h patterns in the 15-18 and 27-30 2Θ range, the cubic $Mn_xCo_{3-x}O_4$ phase co-exists with the cubic $Co_3O_4$ spinel, and the peaks of cobalt oxide do not show relevant shifts during the whole milling sequence.

This is particularly evident in the MnCo2 composition, and suggests a high mechanochemical stability of the $Co_3O_4$ precursor network with minimal (or negligible) solubilization of Mn ions. The $Co_3O_4$ network does not act as a template for the formation of the final cubic spinel, but as a source of metal ions for the mixed Mn-Co spinel growth. On the other hand, $Mn_3O_4$ appears to be poorly stable with respect to the mechanochemical process: in fact, during the first few steps of the milling process it can be observed the significant broadening of its peaks and a progressive decrease in its relative content, suggesting the occurrence of a fast nanometrization process.

In table 3.1 the starting crystallographic parameters of the phases adopted in the Rietveld analysis are reported. Table 3.2 reports crystallographic data obtained by the Rietveld full-pattern analysis of collected diffractograms both for Mn1.5Co1.5 and MnCo2 samples. The overview of these data reinforces previous considerations of the reactant stability to HEBM. The $Co_3O_4$ cubic cell exhibits a very small tendency to grow during the mechanochemical process for both mixtures, reaching

values of $\sim$ 8.10 Å. This growth suggests a noticeable but not massive Mn inclusion in the cubic lattice. On the contrary, $Mn_3O_4$ lattice parameters in all cases show significant distortions with respect to the theoretical values, confirming the low stability of the $Mn_3O_4$ lattice with respect to $Co_3O_4$ toward the HEBM treatment.

The cubic $Mn_xCo_{3-x}O_4$ spinel formed during the HEBM process in both treated composition is initially characterized by a large cell constant (close to 8.3 Å) and exhibits a decreasing trend during the process. The nucleation of this phase occurs in the first few milling steps, along with $Mn_3O_4$ disappearance. This suggests that the cubic spinel lattice initially formed could be rich in Mn content, and during the process enriches in cobalt, gathering metal ions from the $Co_3O_4$ reactant.

As expected from the higher Co content of the pristine mixture, in Co:Mn = 2:1 sample $Mn_xCo_{3-x}O_4$ spinel has a shorter lattice parameter than in the Co:Mn = 1:1 compound. Considering 100 h of milling in Co:Mn = 2:1 sample, a pure phase has been obtained, allowing us to assume the stoichiometry $MnCo_2O_4$ and compare its lattice parameter with literature data. This value is slightly lower than that reported in JCPDS library (i.e., a = 8.269 Å for JCPDS 23- 1237) but comparable to values reported in literature for analogue compounds [44]. A slight cell shrinking could be accounted to a partial oxidation of $Mn^{3+}$ ions to $Mn^{4+}$ ions in tetragonal sites eventually occurring during the HEBM.

Regarding sideways products of Mn1.5Co1.5 mixture process, cell constants of bixbyite and ilmenite phases slightly deviate from theoretical ones suggesting, respectively, Co inclusion in the first and Mn abundance in the latter, and further confirming the fact that the trigonal lattice is formed by Co diffusion in the cubic phase.

Finally, Rietveld data highlight the relevant comminution degree and lattice destabilization effects induced by the milling action (see crystallite size and microstrain results obtained from the microstructure analysis). Both 2:1 and 1:1 Co:Mn ratio samples exhibit crystallite domains within the nanometric range for all examined process time. As it appears, the mixed cubic spinel phase $Mn_xCo_{3-x}O_4$ possesses microstrain value greater than 2%. Further milling and reaction induce strain release and the values decrease down to about 1.2% and about 0.7% for Mn1.5Co1.5 and MnCo2 powders, respectively.

Table 3.1: Phases and crystallographic data of structural models used in Rietveld analysis:

| Nominal phase composition | ICSD code | Symmetry | Symmetry space group | | Starting lattice parameters | | | |
|---|---|---|---|---|---|---|---|---|
| | | | name | number | a (Å) | a' (Å) | c (Å) | $\alpha$ (deg) |
| $Co_3O_4$ | 9362 | cubic | F-43m | 216 | 8.065 | | | |
| $MnCo_2O_4$ | 201314 | cubic | Fd-3m | 227 | 8.28 | | | |
| $Mn_3O_4$ | 68174 | tetragonal | I41/amd | 141 | | 5.765 | 9.442 | |
| $Mn_2O_3$ | 9091 | cubic | Ia-3 | 206 | 9.415 | | | |
| $MnCoO_3$ | 31854 | trigonal | R-3 | 148 | | 5.385 | | 54.52 |
| $Mn_2CoO_4$ | 39197 | tetragonal | I41/amd | 141 | | 5.784 | 9.091 | |

Table 3.2: Lattice parameters (a, a', c, $\alpha$), mean crystallite size (<D>), and microstrain (M.S.) values obtained from XRD Rietveld analysis on $Co_3O_4$–$Mn_3O_4$ mixtures for different milling time:

| Sample | Milling time | $Co_3O_4$ | | | $Mn_3O_4$ | | | | $Mn_xCo_{3-x}O_4$ | | | $Mn_{2-y}Co_yO_3$ | | | $Co_{1-z}Mn_{1+z}O_3$ | | | | Rwp |
|---|---|---|---|---|---|---|---|---|---|---|---|---|---|---|---|---|---|---|---|
| | | a Å | <D> nm | M.S. % | a' Å | c Å | <D> nm | M.S. % | a Å | <D> nm | M.S. % | a Å | <D> nm | M.S. % | a' Å | $\alpha$ deg | <D> nm | M.S. % | |
| Mn1.5Co1.5 | 2.5 | 8.071 | 32 | 0.33 | 5.772 | 9.361 | 15 | 1.86 | | | | | | | | | | | 0.15 |
| | 5 | 8.074 | 26 | 0.62 | 5.791 | 9.225 | 15 | 2.01 | | | | | | | | | | | 0.14 |
| | 10 | 8.069 | 25 | 0.53 | 5.742 | 9.111 | 13 | 1.11 | 8.292 | 9 | 2.54 | 9.364 | 14 | 0.41 | | | | | 0.13 |
| | 20 | 8.086 | 27 | 0.62 | | | | | 8.298 | 10 | 2.5 | 9.331 | 27 | 0.45 | | | | | 0.11 |
| | 30 | 8.098 | 28 | 0.69 | | | | | 8.289 | 8 | 1.74 | 9.322 | 26 | 0.46 | | | | | 0.09 |
| | 45 | 8.11 | 27 | 0.71 | | | | | 8.269 | 9 | 1.36 | 9.318 | 32 | 0.41 | | | | | 0.09 |
| | 65 | | | | | | | | 8.272 | 10 | 1.28 | 9.353 | 39 | 0.43 | | | | | 0.09 |
| | 100 | | | | | | | | 8.276 | 10 | 1.22 | | | | 5.395 | 54.45 | 39 | 0.86 | 0.11 |
| MnCo2 | 2.5 | 8.073 | 31 | 0.63 | 5.807 | 9.3091 | 25 | 2.11 | | | | | | | | | | | 0.15 |
| | 5 | 8.078 | 32 | 0.64 | 5.702 | 9.2818 | 14 | 1.49 | 8.276 | 9 | 2.4 | | | | | | | | 0.12 |
| | 10 | 8.083 | 32 | 0.66 | | | | | 8.268 | 8 | 2.08 | | | | | | | | 0.11 |
| | 20 | 8.086 | 25 | 0.84 | | | | | 8.27 | 12 | 1.05 | | | | | | | | 0.08 |
| | 30 | 8.104 | 25 | 0.88 | | | | | 8.256 | 12 | 0.84 | | | | | | | | 0.13 |
| | 45 | 8.098 | 24 | 0.1 | | | | | 8.253 | 14 | 0.9 | | | | | | | | 0.13 |
| | 65 | | | | | | | | 8.247 | 14 | 0.88 | | | | | | | | 0.11 |
| | 100 | | | | | | | | 8.256 | 13 | 0.71 | | | | | | | | 0.1 |

### 3.1.2 Powder morphology

The morphology of the starting reactants is reported in figure 3.4. It can be observed that both precursors are composed of micrometric particles.

SEM analysis on the milled powder did not allow to observe significant morphological differences between the two observed composition. In figure 3.5 are reported SEM micrographs of MnCo2 milled powders obtained at different milling times as representative of both compositions. A milling treatment of 5 hours is enough to transform the starting micrometric oxides mixtures into micrometric aggregates composed of heterogeneously dispersed sub-micrometric particles. From 10 hours of milling on, all examined samples denote a higher degree of homogeneity with particles smaller than 100nm. 100h milled samples exhibit finally high homogeneity and particle size of about 20-30nm. Further information on particles morphology can be derived from nitrogen adsorption at 77K. Table 3.3 reports results of the BET analysis and the Specific Surface Area (SSA) as calculated by BET data obtained from selected samples. At 10 h of milling $22 m^2/g$ specific area values were obtained for both mixtures denoting that the comminution degree is scarcely dependent on the powders composition at the examined milling stage. The observed surface values correspond to mean equivalent spherical diameter of about 45nm, while a mean crystallite size of about 20nm is calculated from XRD Rietveld analysis (Table 3.2). Then, as confirmed by SEM observation, at 10 h milling the powders are composed of stable solid nanometric agglomerates containing smaller substructures. At 100 h milling mean BET particle size is halved with respect to that coming from 10 h milled powder ($\sim$50 $m^2/g$ vs $\sim$22 $m^2/g$), at the expense of a tenfold increase in milling time. The particle size diameter as obtained by applying the spherical equivalent model (19$\div$25nm), in comparison with SEM observations (see figure 3.5) and XRD crystallite mean sizes (see <D> in table 3.2) lead to conclude that also at 100 h milling, the samples are composed of stable solid agglomerates containing smaller substructures, both in nanometric range. The XRD and morphological evolution of powders during the mechanochemical treatment suggest that relatively short HEBM treatment ensures sufficient activation of the oxides. 10h milling are enough in fact to nanostructurate the powders and promote the nucleation of the mixed spinel phase. Considering the following casting and sintering procedure necessary to obtain a suitable interconnect coating, improvements in the morphological and structural properties do not justify prolonged milling times. Ten hours milled samples were then selected as suitable mixed spinel precursor and therefore investigated further by means of thermal analysis.

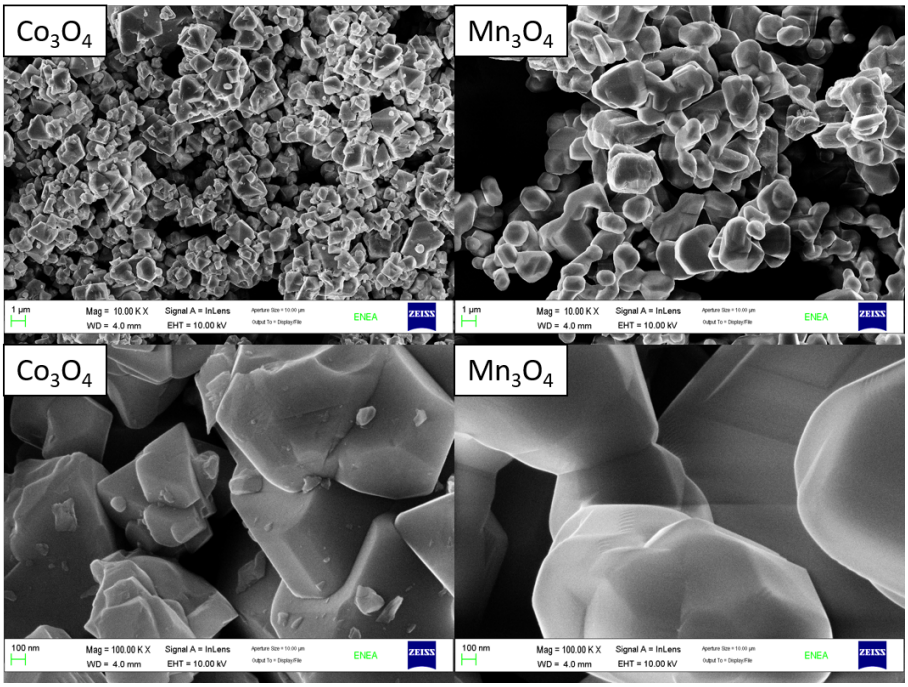



Figure 3.4: SEM micrographs of the $Co_3O_4$ and $Mn_3O_4$ precursors.

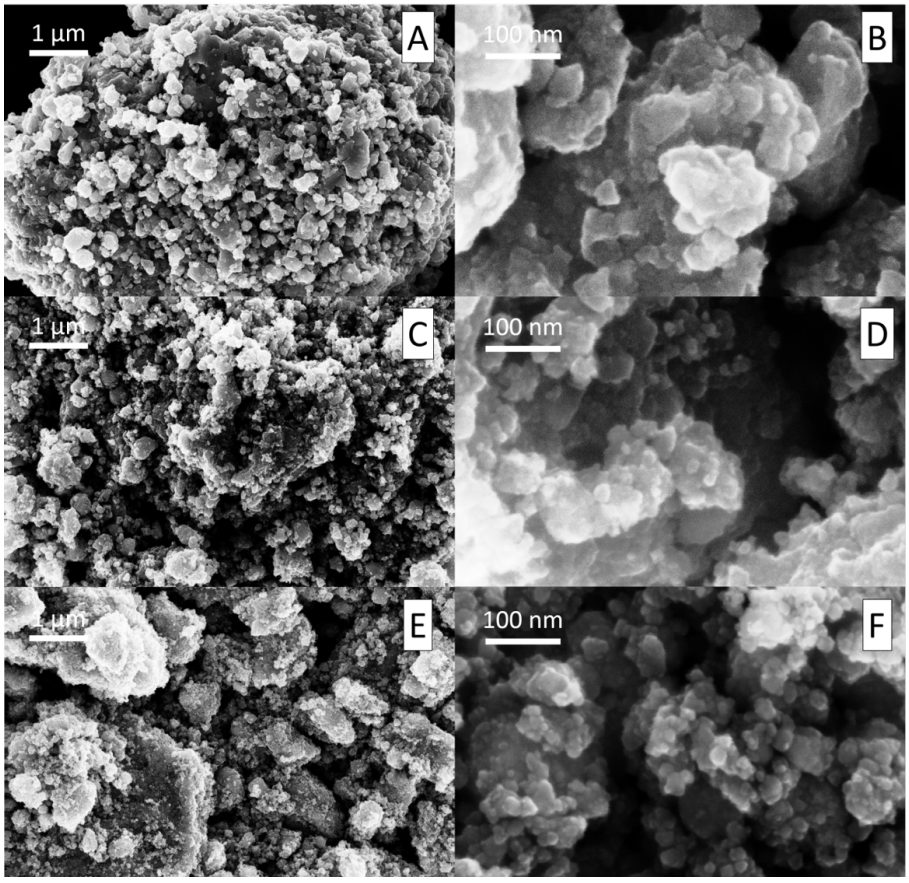



Figure 3.5: SEM micrographs of MnCo2 samples milled for different time: (A,B) 5h; (C,D) 10h; (E,F) 100h.

Table 3.3: BET specific surface area and particles size for different samples:

| Composition | Milling Time (hours) | BET Specific Surface Area ($m^2/g$) | BET Particles Size ($l$)* (nm) |
|---|---|---|---|
| Mn1.5Co1.5 | 10 | 22±1 | 47±1 |
| | 100 | 48±1 | 25±1 |
| MnCo2 | 10 | 22±1 | 46±1 |
| | 100 | 55±1 | 19±1 |

$*l = \frac{6}{A_{BET} \cdot \rho}$

### 3.1.3 High-temperature phase behaviour

In-situ high-temperature XRD measurements were performed in order to follow the thermally induced solid state synthesis process of the desired single cubic spinel phase from the 10 h milled samples. The obtained diffractograms are reported in figure 3.6a-b, while phase content evolution of the mixtures as a function of the applied temperature are shown in figure 3.7a-b.

Analysing the Mn1.5Co1.5 powder, heating initially promotes the crystallization of bixbyite and the growth of the cubic $Mn_xCo_{3-x}O_4$ spinel at the expense of the $Co_3O_4$ phase. At 600 °C the solid state synthesis of the cubic spinel has started, and it is complete at 700 °C, with the full consumption of starting reactants and bixbyite phase. During the successive cooling stage, the formed cubic lattice remains stable in the 800÷600°C range, while at 500 °C the expected decomposition of the high temperature spinel is observed, with nucleation of a tetragonal $Mn_{2-w}Co_2O_4$ spinel phase (JCPDS card No.18-0408). Successive cooling to ambient temperature does not lead to other structural changes. Analogously to the Co:Mn=1:1 case, thermal XRD patterns of the Co:Mn=2:1 mixture, reported in figure 3.6b show the $Mn_xCo_{3-x}O_4$ spinel synthesis occurring above 500 °C. The full conversion of the reactants in a single cubic spinel phase is almost complete at 700°C. The formed phase is stable upon cooling.

The above discussed study highlights once more the effectiveness of the HEBM process in the reactant activation; the HEBM treated powders evolve rapidly towards the expected equilibrium state (each measurement step requires about 20 minutes). On the contrary, pristine reactants (i.e. not subjected to HEBM) require long processing times to complete the solid state reaction at high temperature. In figure 3.8 is reported the high temperature XRD pattern of the pristine Co:Mn=1:1 reactants mixture collected at 800 °C after 7h of isothermal treatment. Despite the long reaction time, the powder pattern highlights presence of high quantities of secondary phases, namely the Co oxide precursors and a Mn rich oxide.

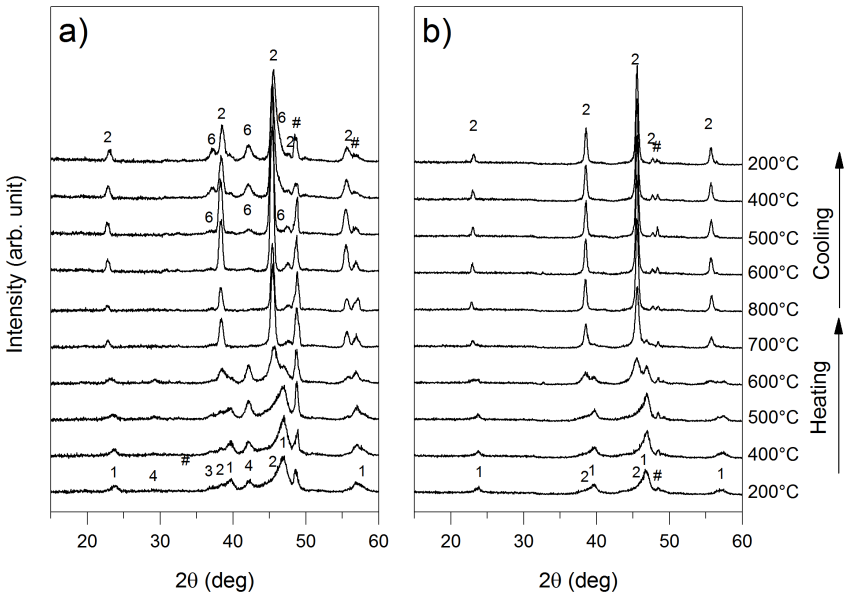



Figure 3.6: X-ray diffraction patterns (Fe source) of a) Mn1.5Co1.5 and b) MnCo2 samples milled for 10 hours collected at different temperatures (heating and cooling rates = 10 °C/min); (1) $Co_3O_4$, (2) $MnCo_2O_4$, (3) $Mn_3O_4$, (4) $Mn_{2-y}Co_yO_3$, (6) $Mn_{2-w}Co_2O_4$, (#) sample holder.

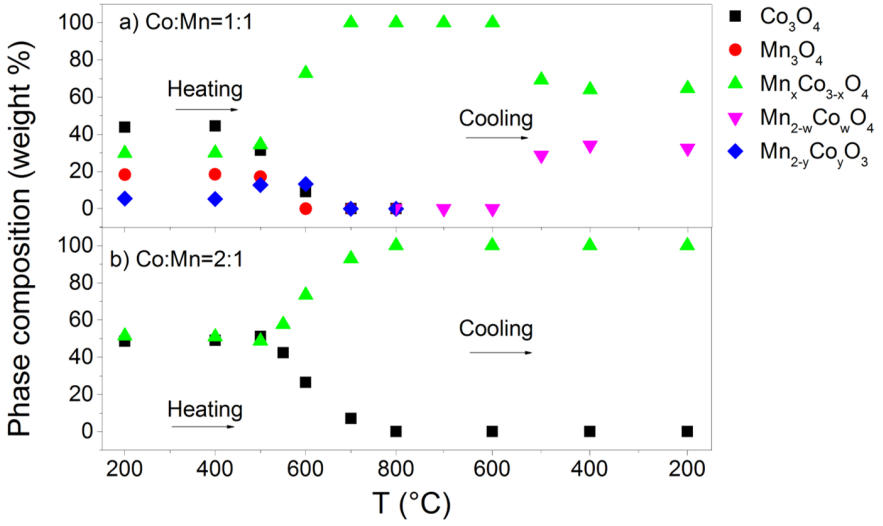



Figure 3.7: Phase content (weight %) of Mn1.5Co1.5 and MnCo2 10h ball milled samples samples versus temperature during heating and cooling stages, obtained from QPA of XRD data reported in figure 3.6.

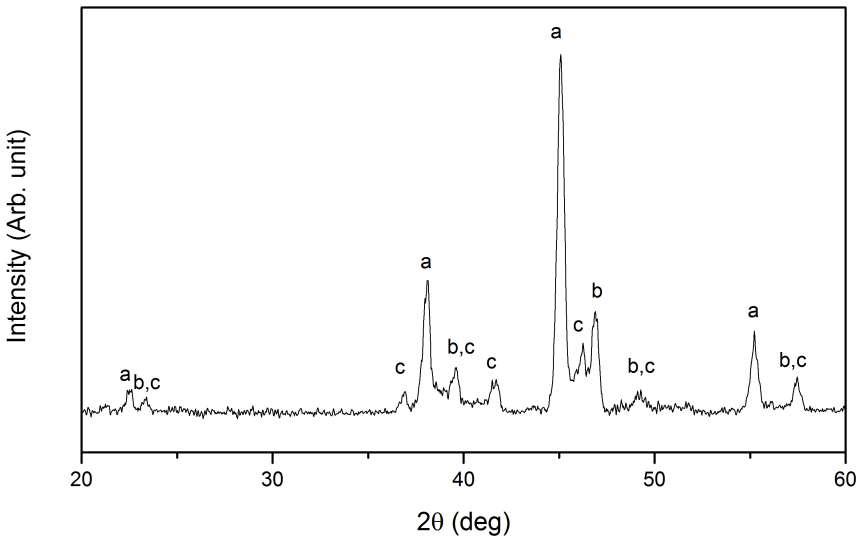



Figure 3.8: X-ray diffraction pattern (Fe source) of a $Co_3O_4$-$Mn_3O_4$ hand mixed mixture (Co:Mn=1:1) collected at 800°C after 7 hours of isothermal treatment: a) mixed Mn-Co cubic spinel; b) $Co_3O_4$ precursor; c) mixed Mn-Co tetragonal spinel originated by $Mn_3O_4$ decomposition and partial reaction.

## 3.2 Influence of the composition on processed powder properties

In view of large scale application, a relatively short milling treatment demonstrated to be highly effective in terms of comminution and activation degree. In fact, in situ thermal XRD analysis shows highly enhanced reaction kinetics: the processed powders subjected to thermal treatment evolve quickly toward thermodynamic equilibrium with rapid production of the expected phases. The synthesis method may be therefore effective to produce powder mixtures of opportune compositions to be applied through wet-powder deposition techniques. The desired high temperature phase would be then formed during the sintering treatments, without the need for powder calcination steps. Results reported in next section are therefore related to the evaluation of processed powders characterized by different chemical compositions. Compositional tailoring of the powders should in fact allow to optimize the material properties for the application, as described in section 1.3. Several compositions, reported in table 2.1, were therefore subjected to the short HEBM treatment and characterized by means of structural and processing variables, observing the influence of different Mn:Co ratio and metal doping (i.e. Cu, Fe) on room temperature and high temperature phase stability (section 3.2.1), sintering properties (section 3.2.2), thermal expansion (section 3.2.3) and electrical conductivity (section 3.2.4).

### 3.2.1 Chemico-physical characterization

After the mechanochemical treatment, fine black powders were collected for all the compositions. The XRD patterns of the 10 hours milled powders are reported in figure 3.9. All the examined samples are characterized by similar patterns, comparable with the spectra reported in figure 3.1, with significant peak broadening ascribable to nanostructuration of diffractive domains and lattice defectivity induced by the HEBM treatment. The three Mn-Co samples evidence the residual presence of the $Co_3O_4$ precursor phase (JCPDS card n. 42-1467). The observed asymmetry towards lower angles can be related to the nucleation of a mixed $MnCo_2O_4$ phase (JCPDS card n. 23-1237). Only the Mn1.5Co1.5 sample shows signals related to the $Mn_3O_4$ precursor phase (JCPDS card n. 24-0734).

Cu-containing samples show similar peak broadening. The Mn1.33Co1.17Cu0.5 pattern exhibits mainly reflections compatible with the $Co_3O_4$ phase, with the already observed asymmetry towards lower angles. Small broadened peaks at $2\Theta\sim45$ and $2\Theta\sim49$ degrees are ascribable to the presence of CuO phase (JCPDS card n. 48-1548). Raising Mn content, reflections related to $Mn_3O_4$ become evident, similarly to what was observed for the Mn-Co samples. In the samples characterized by lower Cu addition (i.e. 0.07 atomic ratio) clear evidences of CuO phase (JCPDS card n. 48-1548) are not observed, suggesting low stability of CuO structure during the HEBM treatment, most likely due to facile diffusion of small copper ions into the spinel lattice during the mechano-chemical treatment.

Regarding Fe addition, the small broadened peak at $2\Theta\sim48$ degrees is due to the presence of highly destructured $Fe_2O_3$ phase (JCPDS card n. 33-0664), and are more evident in the MnCo1.6Fe0.4 pattern, as expected due to the higher iron content. In the case of copper containing samples, instead, in the MnCo1.6Fe0.2Cu0.2 pattern, similar to what is observed for MnCo1.8Fe0.2 sample, features of a hematite phase are visible.

The higher stability exhibited by the cobalt precursor phase in comparison with to the Mn and Cu oxides with respect to the mechanochemical action is clearly evident from these results. The Mn1.5Co1.5 sample, composed by similar Co and Mn amounts, is characterized by $Mn_3O_4$ reflections scarcely visible with respect to the cubic $Co_3O_4$ phase peaks. Regarding copper oxide, it can be clearly observed from the pattern related to the Mn2.05Co0.45Cu0.5 sample, that also the CuO phase gets easily destructured during the milling, the CuO peaks being significantly lower and broader with respect to those of cobalt oxide. The observed phenomena can be ascribed to the difference in hardness of the materials, with Co spinel characterized by significantly higher hardness with respect to Haussmannite (Mohs hardness: 5.5)

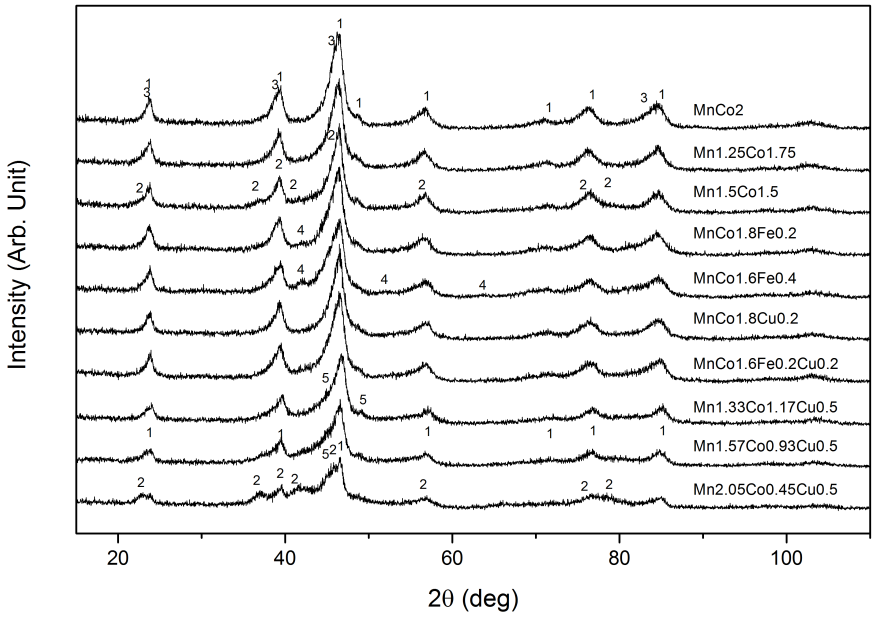



Figure 3.9: X-Ray Diffraction patterns (Fe surce) (Fe source) of the doped Mn-Co mixtures after 10 h of milling; (1) $Co_3O_4$, (2) $Mn_3O_4$, (3) $MnCo_2O_4$, (4) $Fe_2O_3$, (5) CuO reflections.

[117] and Tenorite (Mohs hardness: 3.5-4). The successive destructuration of the crystalline phases easily promotes interdiffusion of Mn and Cu atoms in the Co precursors phase or in the nucleating mixed spinel lattice.

Therefore, as shown in the XRD analysis, also in the case of the doped samples, the 10h HEBM treatment does not produce a single equilibrium spinel phase but some metastable mixture of metal oxides, similarly to what observed from QPA results reported in section 3.1.

To evaluate powders morphology and mean particle size, nitrogen adsorption measurements at 77 K were carried out. In table 3.4 BET specific surface area and calculated mean particle size are reported. All the samples exhibit comparable values, with Copper containing powders characterized by the lower BET area, suggesting that Copper addition promotes higher aggregation degree. Mean particle size ranges between 170 and 330 nm.

### High-temperature behaviour in air

In order to evaluate how the composition influences the high temperature properties of the samples, the milled powders were subjected to thermogravimetric analysis. In 3.10 the curves acquired in air are reported.

All samples show a weight loss step ascribable to the departure of adsorbed humidity. In the 200÷500 °C temperature range, a gradual weight increase can

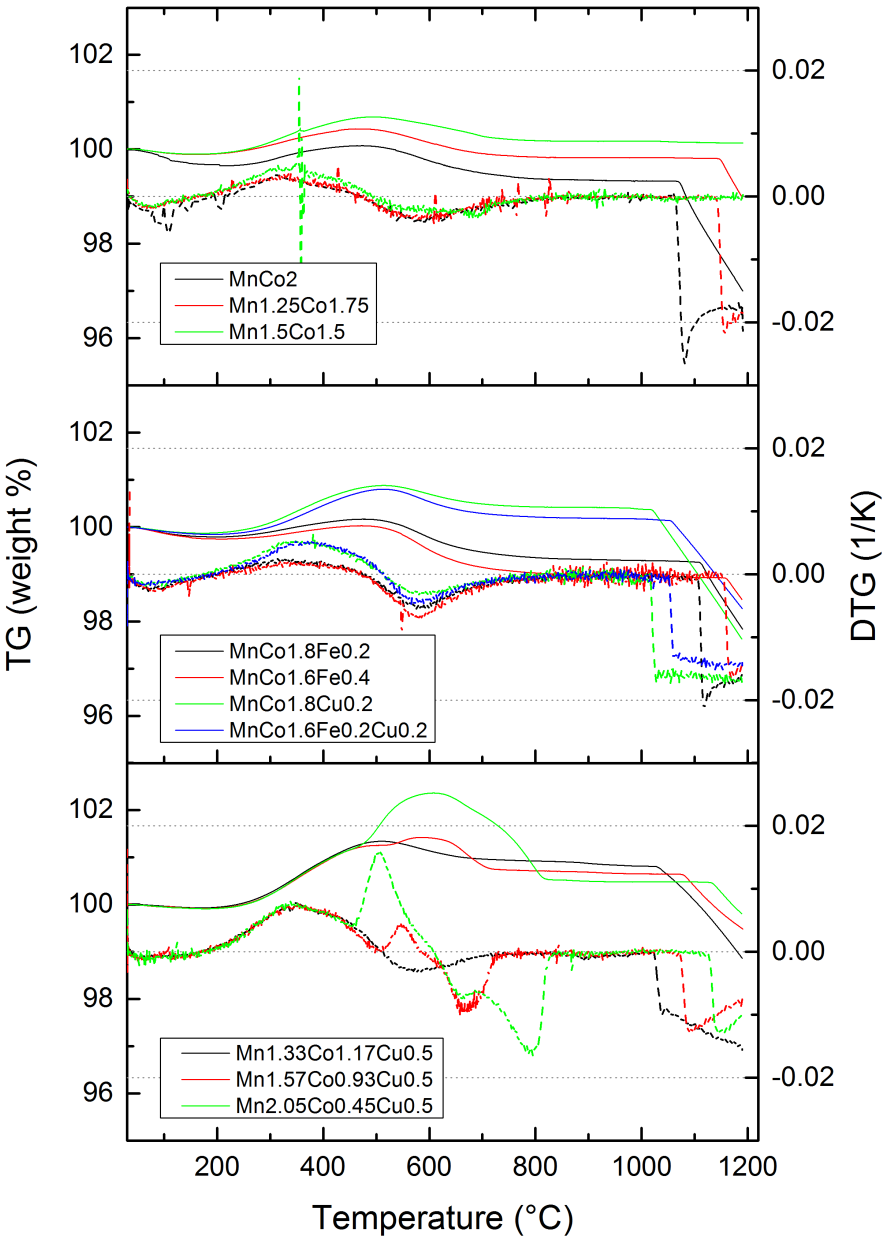



Figure 3.10: Thermogravimetric curves as a function of temperature for the different samples acquired in air; solid lines represent weight% change, dotted lines the derivative.

Table 3.4: BET specific surface area and particles size for different samples:

| Sample | BET Specific Surface Area ($m^2/g$) | BET Particles Size ($l$)* (nm) |
|---|---|---|
| MnCo2 | 6.2±0.3 | 176±9 |
| Mn1.25Co1.75 | 5.7±0.3 | 195±10 |
| Mn1.5Co1.5 | 4.5±0.2 | 255±12 |
| MnCo1.8Fe0.2 | 6.0±0.3 | 182±9 |
| MnCo1.6Fe0.4 | 6.8±0.3 | 163±8 |
| MnCo1.8Cu0.2 | 3.3±0.2 | 323±20 |
| MnCo1.6Fe0.2Cu0.2 | 3.8±0.2 | 287±16 |
| Mn1.33Co1.17Cu0.5 | 4.2±0.2 | 265±13 |
| Mn1.57Co0.93Cu0.5 | 3.5±0.2 | 325±15 |
| Mn2.05Co0.45Cu0.5 | 4.1±0.2 | 293±13 |

$l = \frac{6}{A_{BET} \cdot \rho}$

be observed for all compositions. This phenomenon can be related to the powder comminution and activation induced by the HEBM, carried out in Ar atmosphere. Highly reactive new surfaces are produced during the mechano-chemical treatment that interacts with oxygen already at low temperature giving rise to the oxidation phenomena observed during the thermal treatment. Moreover, the HEBM treatment induces a high degree of interdiffusion of the precursor oxides with solid state reactions at the new interfaces, most likely with the formation of highly anion defective lattices, due to the milling atmosphere. Subsequent filling of the oxygen vacancies may therefore occur when exposed to air at moderate temperatures. The occurrence of similar weight gain phenomena and the existence of metastable non-stoichiometric mixed valence spinels has been observed for similar systems and ascribed to high reactivity due to high nanostructuration of the compounds [118], and it is supposed that similar mechanisms occur here, due to the defectivity induced by the HEBM treatment. Regarding the influence of the composition of $MnCo_{2-y-z}Fe_yCu_z$ on this weight gain step, it can be observed that the magnitude of the weight gain increases following the order: MnCo1.6Fe0.4 <MnCo1.8Fe0.2 < MnCo2 <MnCo1.6Fe0.2Cu0.2 <MnCo1.8Cu0.2. This can be related to the initial powder composition: $Co_3O_4$ precursor is substituted with species characterized by different oxygen content (i.e. $Fe_2O_3$ and CuO), and it is likely to suppose that, with Fe and Cu ions presence in the spinel lattice due to the mechano-chemical treatment, the oxygen uptake of the metastable spinels will be inversely related to the initial oxygen content.

Raising the temperature, in the 500÷700 °C temperature range, the Mn-Co, $MnCo_{2-y-z}Fe_yCu_z$ and Mn1.33Co1.17Cu0.5 samples show a similar gradual weight

loss, reaching a plateau for higher temperatures. In this temperature range, for the Mn-Co samples the reaction between the activated precursors is expected [see figure 3.6]. The release of the extra oxygen content acquired during the previous weight acquisition step, followed by an interval of weight stability, is compatible therefore with the reorganization of the metastable oxidized lattices to form high temperature stable phases. Also in this weight change step a relationship between the weight loss and the material composition of $MnCo_{2-y-z}Fe_yCu_z$ samples can be observed: in particular, the weight loss increases following the order: MnCo1.8Cu0.2 <MnCo1.6Fe0.2Cu0.2 <MnCo2 <MnCo1.8Fe0.2 <MnCo1.6Fe0.4. The samples characterized by the higher initial oxygen content show therefore the higher mass loss. The substitution of the Co2+/Co3+ precursor with higher or lower oxidation state species, respectively Fe3+ from $Fe_2O_3$ and Cu2+ from CuO, affects the oxidation behaviour of the milled powder both during the formation of the metastable spinels and during the homogenization reaction that produce equilibrium compounds. In section 3.1 we observed that during mechano-chemical treatment of Mn and Co oxides the reaction proceeds through nucleation and growth of mixed phases rather than through interdiffusion phenomena of the starting oxides. Observing how the thermal behaviour of the doped powders is influenced by the initial composition, it is likely to suppose that also in the case of the Fe, Cu doped compounds the formation of Fe and Cu doped phases occurs already during the milling step with a similar reaction mechanism involved.

The Mn richest samples, i.e. Mn1.57Co0.93Cu0.5 and Mn2.05Co0.45Cu0.5, undergo a further weight acquisition step before exhibiting weight loss. In section 3.1 - figure 3.6 we had observed how the presence of Mn-rich unreacted spinels could lead to the oxidation of $Mn_3O_4$to $Mn_2O_3$ during heating, and it is likely to ascribe this weight gain to a similar phenomenon. Raising further the temperature, the oxidized compound reacts with the existing spinels, resulting in weight loss and formation of spinel phases. The behaviour of the Cu-doped samples will be further investigated in the next section by means of the outcome of in-situ high temperature XRD analysis.

Further heating over 1000 °C leads to an additional weight loss phenomenon for all samples except Mn1.5Co1.5. Regarding Mn-Co samples, it is known that at high temperature, a multi-phase boundary between spinels and reduced MeII oxide phases exists for Co-Mn oxide mixtures [119], with equilibrium temperature increasing with Mn content. The absence of the weight loss phenomena for the sample Mn1.5Co1.5 indicates for this composition a phase boundary temperature beyond 1200 °C. In the case of Cu addition, a similar behaviour can be supposed, with a dual phase region also for the mixed Cu-Mn-Co oxides. Unlike Mn-Co samples, the weight loss is observed for all the compositions. Considering that the Mn2.05Co0.45Cu0.5

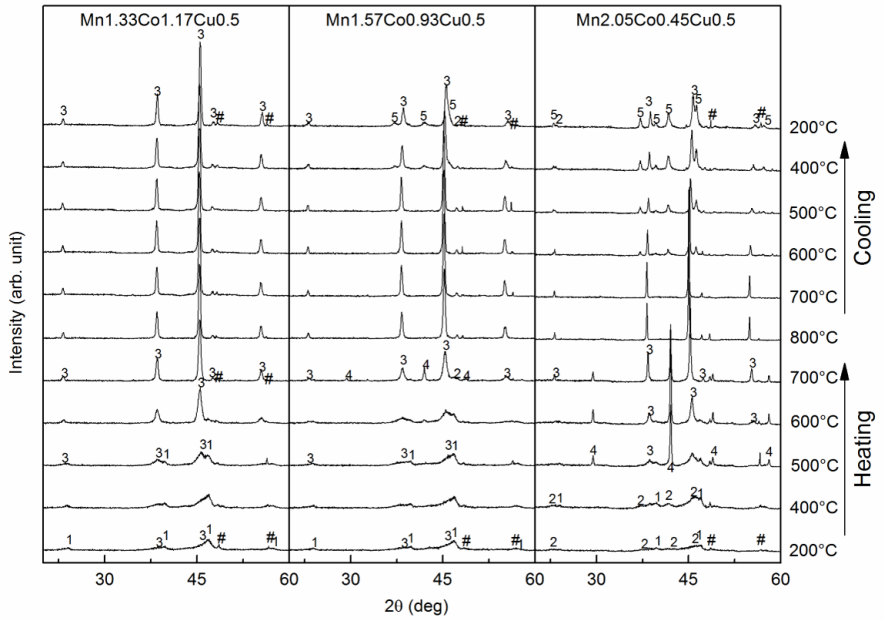



Figure 3.11: In situ X-ray diffraction patterns (Fe source) of a) Mn1.33Co1.17Cu0.5, b) Mn1.57Co0.93Cu0.5 and c) Mn2.05Co0.45Cu0.5 samples milled for 10 hours collected at different temperatures (heating rate = 10°C/min); 1) $Co_3O_4$, 2) $Mn_3O_4$, 3) $MnCo_2O_4$, 4) $Mn_2O_3$, 5) Tetragonal mixed spinel phase, #) sample holder.

sample is characterized by an approximate 4:1 Mn:Co ratio, it is evident that copper lowers significantly the dual phase region boundary temperature. Co substitution with Fe appears to extend instead the spinel stability region.

During the successive cooling stage, the weight loss associated to the high temperature phase transition is recovered for all the stoichiometries, compatibly with spinel stability at intermediate temperature. In the case of the MnCo1.8Cu0.2 sample, weight gain occurs in two steps, suggesting a multiple oxidation process that could be due to multiple high temperature dual-phase regions, as observable in the Cu-Co oxides phase diagram [120].

To further investigate the behaviour of the Cu doped samples upon heating, high temperature in situ diffraction analyses were carried out on the ball-milled powders. The patterns are reported in figure 3.11.

Starting from the Mn1.33Co1.17Cu0.5 sample, the pattern collected at 400 °C is substantially similar to that acquired at room temperature, confirming that the oxidation phenomena observed with TGA measurements do not involve reactions or significant nucleation of new phases. The reaction between the activated precursors is instead evident at 500 °C, where the nucleation of a cubic spinel phase occurs. Heating further, the reaction between the remaining precursors carries on, forming a single cubic spinel phase. The weight loss observed in the 500÷700 °C by thermogravimetric measurements can be associated therefore to the rearrangement of

the metastable oxidized lattice, resulting in the nucleation of the high temperature spinel. During cooling, no structural changes are evident, showing that the examined composition is characterized by a single phase nature in the room temperature ÷800 °C temperature range.

The initial evolution of Mn1.57Co0.93Cu0.5 sample is similar, with the nucleation of a cubic spinel phase in the 400÷500 °C interval. At 600 °C reflections ascribable to the $Mn_2O_3$ phase (JCPDS card n. 24-0508) are visible, explaining the thermogravimetric weight gain occurring in the 600÷700 °C range. The growth of the spinel phase carries along with it the increase of peaks related to this Mn-rich phase up to 700 °C. Between 700 °C and 800 °C the rising spinel phase and $Mn_2O_3$ react, and the pattern collected at 800 °C is ascribable to the presence of a single spinel phase. During cooling, this phase is stable down to 500 °C. At 400 °C, reflections ascribable to a tetragonal spinel phase similar to Mn2CoO4 (JCPDS 48-1548) appear, indicating the decomposition of the high temperature cubic phase with the formation of a dual phase compound.

Regarding the Mn2.05Co0.45Cu0.5 sample, coherently with thermogravimetric results, nucleation of large amounts of the oxidized $Mn_2O_3$ phase occur already at 500 °C, along with the formation of a cubic spinel phase. The transformation of $Mn_3O_4$ and $Co_3O_4$ precursor phases occurs between 500 °C and 700 °C, where only $Mn_2O_3$ and the spinel phase are visible. Raising the temperature, $Mn_2O_3$ and the spinel phase react, and at 800 °C the spinel phase formation is almost complete. Similarly to what was observed for the Mn1.57Co0.93Cu0.5 sample, during cooling the segregation of a tetragonal spinel phase is observed at a temperature value between 700 °C and 600 °C.

### High temperature behaviour in reducing/reoxidizing conditions

Transition metal spinels undergo in fact through several reduction steps when subjected to reducing conditions at high temperature, with spinel structure decomposition and segregation of metals and oxides. Such phenomena have been identified clearly in literature (e.g. [50]) and exploited to promote powders sintering but, to the best of my knowledge, never investigated deeply in their mechanisms. To evaluate the powders behaviour when exposed to a reducing treatments, and the influence of composition on the occurring phenomena, the milled samples were subjected to thermogravimetric analysis in $Ar/H_2(5\%)$ atmosphere. The thermogravimetric curves are reported in figure 3.12.

During heating in reducing atmosphere, reduction of transition metal spinels to form $Me^{2+}$ oxides and metals is expected. As reported for similar systems, man-

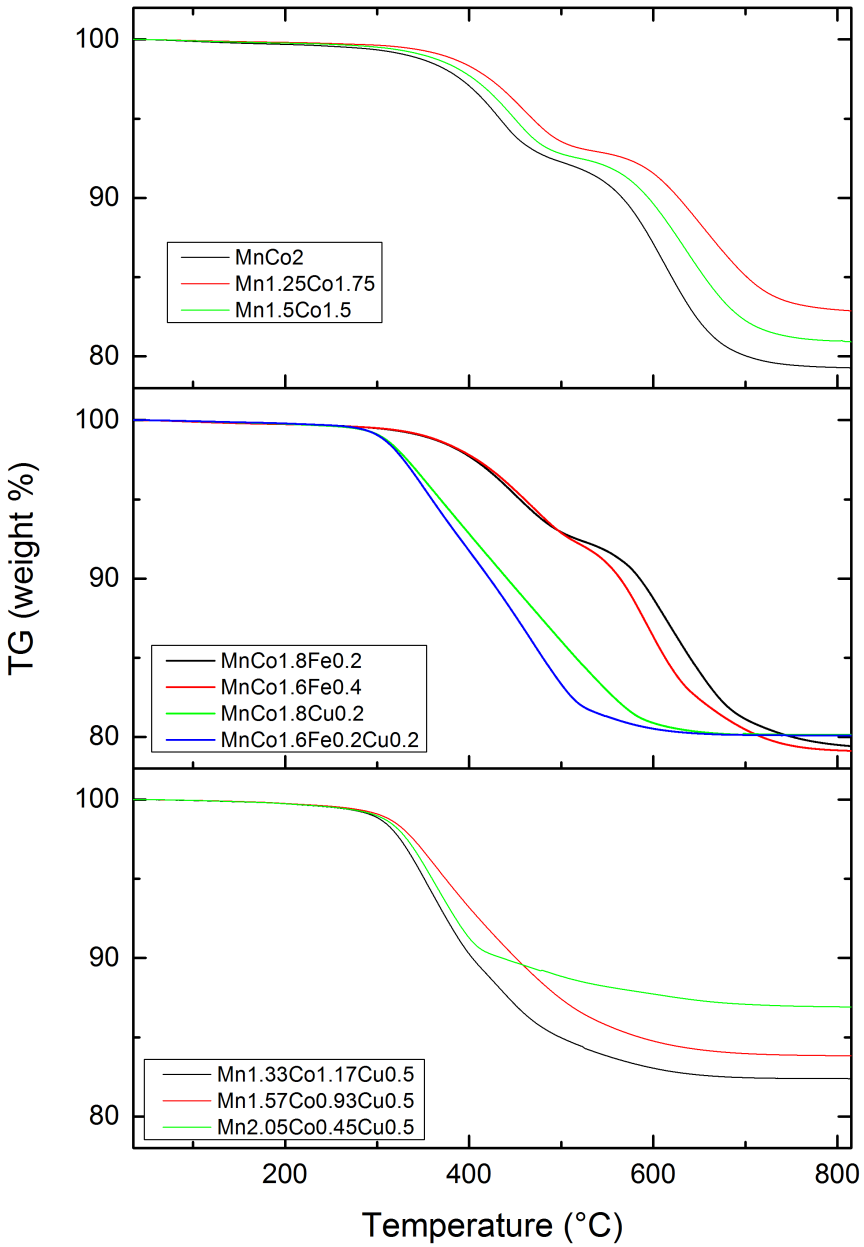



Figure 3.12: Thermogravimetric curves as a function of temperature for the different samples acquired in $Ar/H_2(5\%)$ atmosphere.

ganese complete reduction does not occur [50], while complete reduction to metals of cobalt or copper has been reported [50, 60] and is expected for iron. The overall reaction is reported in equation (3.1):

$$Mn_{3-x}(Co,Fe,Cu)_xO_4 + (1+x)H_{2(gas)} \rightarrow \frac{x}{3}MnO + x(Co,Fe,Cu) + (1+x)H_2O \tag{3.1}$$

The weight loss calculated following equation (3.1) is reported in table 3.5 in comparison with the experimental weight loss measured after 1 h of dwell time at 800°C. It can be observed that for all samples a good agreement between calculated and measured experimental results is found, suggesting that for all compositions complete reduction of Co,Fe,Cu and partial reduction of Mn to MnO occurs at 800°C.

Table 3.5: Calculated weight loss as reported in equation (3.1) and experimental data for TGA in reducing atmosphere:

| sample | theoretical weight loss (%) | Experimental weight loss (%) |
|---|---|---|
| MnCo2 | 20.3 | 20.6 |
| Mn1.25Co1.75 | 18.7 | 19.1 |
| Mn1.5Co1.5 | 17.0 | 17.1 |
| MnCo1.8Fe0.2 | 20.3 | 20.6 |
| MnCo1.6Fe0.4 | 20.4 | 20.8 |
| MnCo1.8Cu0.2 | 20.2 | 19.7 |
| MnCo1.6Fe0.2Cu0.2 | 20.2 | 19.7 |
| Mn1.33Co1.17Cu0.5 | 18.0 | 17.4 |
| Mn1.57Co0.93Cu0.5 | 16.4 | 16.1 |
| Mn2.05Co0.45Cu0.5 | 13.3 | 12.9 |

Regarding the shape of the thermogravimetric curves, several weight change steps can be observed. Starting from the Mn-Co samples, two weight losses are visible, respectively in the 400÷500 °C and in the 550÷700 °C range. It is likely therefore to suppose that the spinel reduction occurs through an intermediate step as represented in equation (3.2) and (3.3):

$$Mn_{3-x}(Co,Fe,Cu)_xO_4 + H_{2(gas)} \rightarrow \frac{x}{3}MnO + x(CoO+FeO+CuO) + H_2O_{(gas)} \tag{3.2}$$

$$\frac{x}{3}MnO + x(CoO+FeO+CuO) + xH_{2(gas)} \rightarrow \frac{x}{3}MnO + x(Co+Fe+Cu) + xH_2O_{(gas)} \tag{3.3}$$

The two weight loss steps would therefore be ascribed respectively to the loss of 1 mol of oxygen due to the reduction of the spinel to $Me^{2+}$ oxides and to CoO

reduction to metallic cobalt. It can be furthermore observed that a higher Mn:Co ratio increases reduction temperature of both phenomena.

Regarding Fe containing samples, the curves are similar to Mn-Co compositions, with a noticeable broadening of the second phenomenon at high temperatures, most likely ascribable to iron reduction reaction.

Cu containing samples exhibit instead significantly different features: The reaction onset temperature is significantly lower, suggesting that copper addition modify the spinel stability in reducing conditions as well as in air. MnCo1.8Cu0.2 sample is characterized by a large and broad weight loss in the 300÷600 °C range, similarly to the MnCo1.6Fe0.2Cu0.2 sample, exhibiting the weight loss phenomena in the 300÷500 °C range. Raising further Cu doping and Mn:Co ratio, the transition onset and the curve shape remain similar, with differences in the weight loss magnitude due to the different compositions: Mn2.05Co0.45Cu0.5 sample for example, shows most of the weight loss in a steep step between 300 and 400 °C, corresponding to the $Me_3O_4$-MeO reduction, an a slow weight loss for higher temperature, ascribable to the final Co and Cu reduction.

To further investigate the reduction phenomena, mathematical evaluation of DTG peaks was carried out, simulating a single peak for $Me_3O_4$ →MeO reduction, and separate peaks for Co, Cu and Fe reductions. In figure 3.13 the experimental DTG curves are reported in comparison with the calculated fits, while in table 3.6 is reported the theoretical and calculated weight losses and the corresponding peak temperatures.

Starting from Mn-Co samples, the fit with two single peaks is quite straightforward, and a good match between the theoretical and calculated peak ratio is obtained. In $MnCo_{2-y}Fe_y$ samples, the broadening of the second peak may be ascribed to the iron reduction phenomenon, as suggested by the fits. However, in the MnCo1.8Fe0.2 sample, the calculated area of the Fe peak suggests that part of iron reduction occurs at lower temperatures.

Regarding copper containing samples, starting from MnCo1.8Cu0.2 curve, the two principal peaks are highly overlapped, with the second peak ascribed to metallic cobalt formation shifted to lower temperature with respect to MnCo2 curve, suggesting a faster metal reduction from the $Me^{2+}$ oxide during its formation. The asymmetry of the metallic cobalt reduction peak can be fitted with a minor peak, with area compatible with copper reduction and segregation from the MeO phase. When cobalt is substituted simultaneously with iron and copper (MnCo1.6Fe0.2Cu0.2 sample), the cobalt reduction peak is further shifted to lower temperature, and the asymmetry at higher temperature can be fitted with two peaks with area compatible with iron and copper reduction phenomena. To verify the peaks assignation,

MnCo1.6Fe0.2Cu0.2 sample was selected to evaluate in details phase formations through high temperature XRD analysis carried out in reducing conditions. The last set of samples ($Mn_{2.5-z}Co_zCu_{0.5}O_4$) shows again significant overlap of the weight loss phenomena. In the case of the Mn2.05Co0.45Cu0.5 composition, the values obtained for simulated peaks area suggest that part of the Cu and Co to metals reduction is occurring concurrently with the first reduction phenomena.

The good match between the simulated peaks and the experimental curves and between the theoretical and calculated weight losses suggests that for all the compositions the reduction mechanism is due to the formation of $Me^{2+}$ oxides and to the subsequent reduction of Co, Fe and Cu from this phase. To further investigate this phenomena, selected compositions (MnCo2, MnCo1.6Fe0.4, MnCo1.6Fe0.2Cu0.2, Mn1.33Co1.17Cu0.5) were subjected to high temperature XRD analysis carried out in reducing atmosphere. The XRD patterns are reported in figure 3.14.

Starting from MnCo2 sample, no evolution is evident up to 300 °C. At 400 °C, spinel decomposition has occurred, with the appearance of broad peaks ascribable to a single phase unidentified from literature. This phase is however an intermediate between CoO and MnO, that share che same cubic structure with different cell parameters (MnO = 4.445 Å - CoO = 4.261 Å), suggesting that a mixed single (Mn,Co)O phase is formed. Raising the temperature, at 500 °C a peak ascribable to Co metallic phase is observable, along with the shift to higher angles of the mixed MeO phase due to the growth lattice parameter related to cobalt segregation. This phenomenon continues raising the temperature, and at 700 °C the pattern is ascribable to a mixture of MnO and Co. No significant changes are visible upon cooling.

Regarding the MnCo1.6Fe0.4 pattern, the initial evolution is similar. Between 500 and 600 °C reduction of iron occurs. Segregation of Co from the MeO phase occurs with the formation of a face centered cubic Co-rich phase, while segregation of Fe occurrs through the formation of a body centered cubic (BCC) Fe-Co alloy. The reduction is completed at 700 °C, as suggested by the absence of shift f MnO peaks position between 700 °C and 800 °C. An evolution between the Co-rich and Fe-Co phases is observable at high temperature: while at 600 °C FCC Cobalt represents the main metallic phase, at 700 °C we have an abundance of BCC Fe-Co phase, again reverted at 800 °C. Minor changes occur at high temperature and upon cooling, and are highlighted in detail later in the text (section 3.2.2). The comparison between HT-XRD and DTG analysis suggests that cobalt reduction is promoted by Fe presence, through the formation large amounts of Fe-Co. When the reduction reaction has been completed, the phase ratio reverts to the equilibrium values, in agreement with Fe-Co phase diagrams, characterized the existence of a

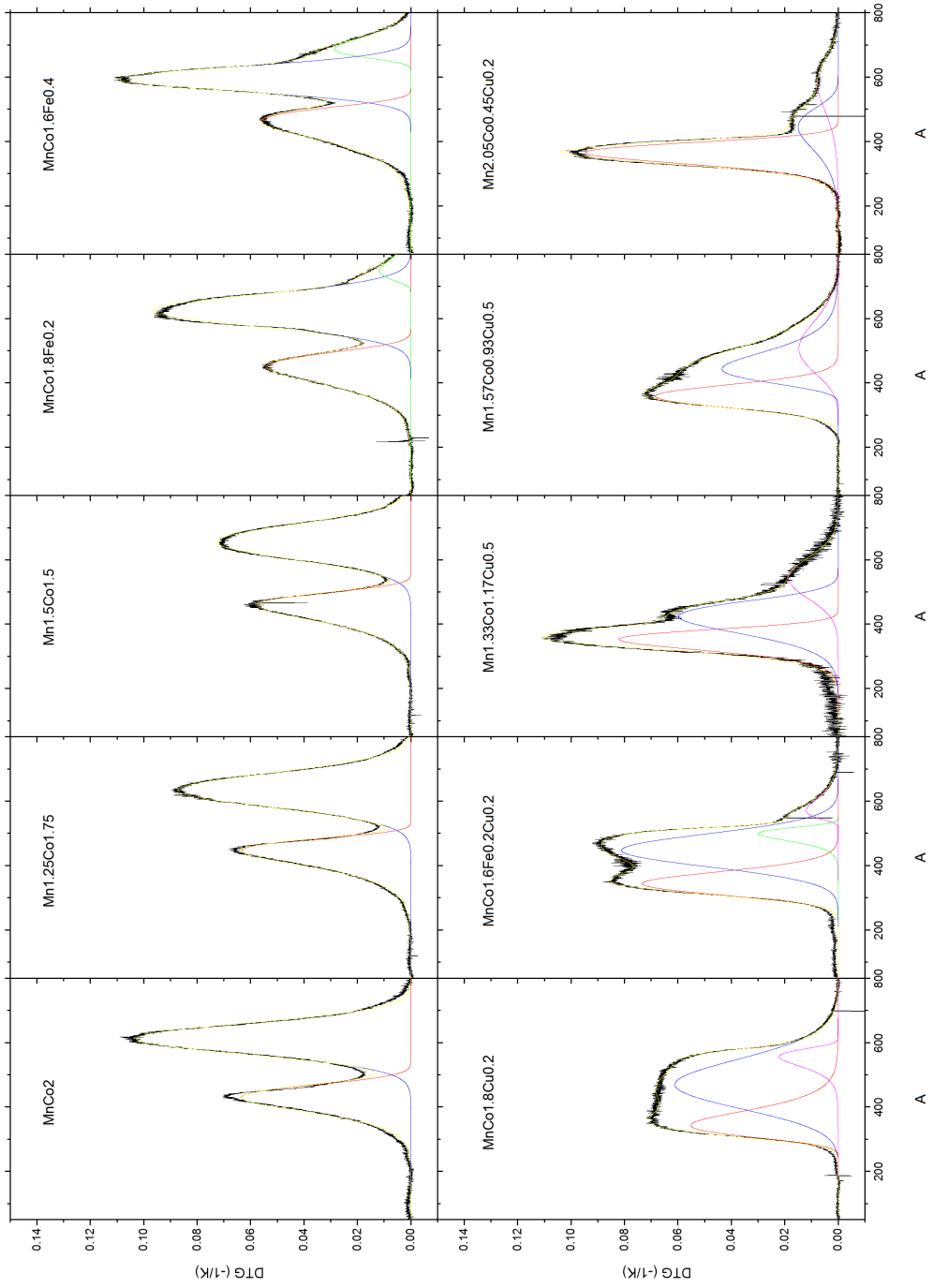



Figure 3.13: Experimental (black) and simulated (colours) DTG curves acquired in $Ar/H_2(5\%)$ atmosphere for the different samples (see text and figure 3.12).

Table 3.6: Calculated weight losses and maximum peak temperatures for fits reported in figure 3.13:

| sample | weight loss | $Me_3O_4$-MeO | CoO-Co | FeO-Fe | CuO-Cu |
|---|---|---|---|---|---|
| MnCo2 | teoretical (%) | 33 | 67 | | |
| | calculated (%) | 35 | 65 | | |
| | Temperature (°C) | 430 | 610 | | |
| Mn1.25Co1.75 | teoretical (%) | 36 | 64 | | |
| | calculated (%) | 38 | 62 | | |
| | Temperature (°C) | 445 | 635 | | |
| Mn1.5Co1.5 | teoretical (%) | 40 | 60 | | |
| | calculated (%) | 39 | 61 | | |
| | Temperature (°C) | 460 | 655 | | |
| MnCo1.8Fe0.2 | teoretical (%) | 33 | 60 | 7 | |
| | calculated (%) | 34 | 61 | 5 | |
| | Temperature (°C) | 450 | 625 | 745 | |
| MnCo1.6Fe0.4 | teoretical (%) | 33 | 53 | 13 | |
| | calculated (%) | 36 | 52 | 12 | |
| | Temperature (°C) | 470 | 595 | 680 | |
| MnCo1.8Cu0.2 | teoretical (%) | 33 | 60 | | 7 |
| | calculated (%) | 31 | 61 | | 8 |
| | Temperature (°C) | 340 | 485 | | 565 |
| MnCo1.6Fe0.2Cu0.2 | teoretical (%) | 33 | 53 | 7 | 7 |
| | calculated (%) | 34 | 53 | 8 | 5 |
| | Temperature (°C) | 340 | 470 | 510 | 550 |
| Mn1.33Co1.17Cu0.5 | teoretical (%) | 37 | 44 | | 19 |
| | calculated (%) | 39 | 44 | | 17 |
| | Temperature (°C) | 345 | 380 | | 450 |
| Mn1.57Co0.93Cu0.5 | teoretical (%) | 41 | 38 | | 21 |
| | calculated (%) | 42 | 38 | | 20 |
| | Temperature (°C) | 355 | 460 | | 480 |
| Mn2.05Co0.45Cu0.5 | teoretical (%) | 51 | 23 | | 26 |
| | calculated (%) | 65 | 14 | | 21 |
| | Temperature (°C) | 370 | 600 | | 490 |

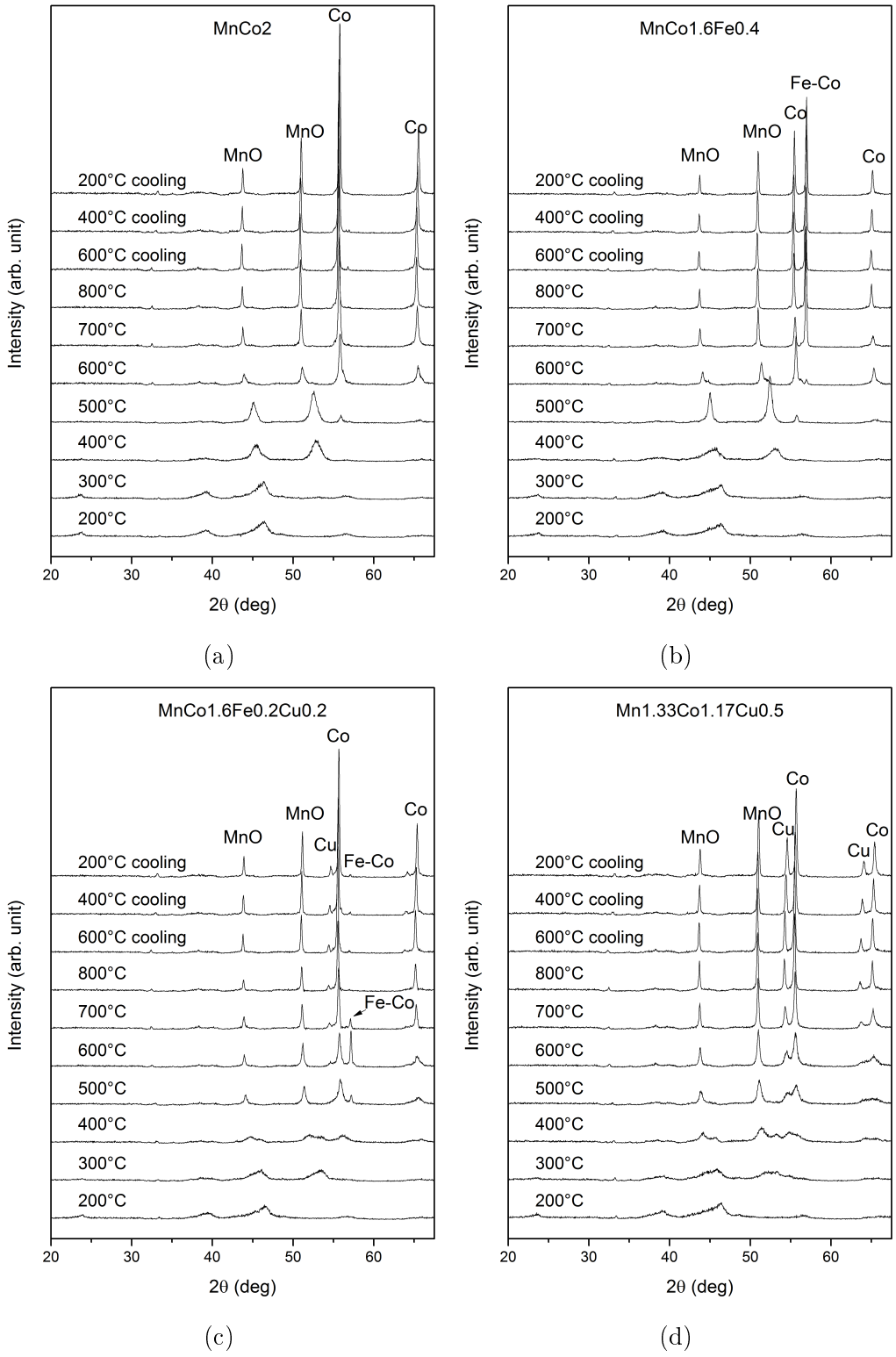



Figure 3.14: In situ high temperature X-ray diffraction patterns (Fe source) of a) MnCo2, b) MnCo1.6Fe0.4, c) MnCo1.6Fe0.2Cu0.2, d) Mn1.33Co1.17Cu0.5 samples milled for 10 hours collected at different temperatures in $He/H_2(5\%)$ atmosphere (heating rate = 10°C/min).

dual BCC-FCC phase region for Co-rich compositions at intermediate temperature [121].

In the MnCo1.6Fe0.2Cu0.2 sequence, metal reduction (Fe,Co) occurs already at 400 °C along with the spinel decomposition. The same Co-Fe reduction phenomena observed for the MnCo1.6Fe0.4 composition is visible in the 500÷700 °C temperature range. Copper reduction is clearly evident only at 600 °C, confirming the DTG peaks assignation of table 3.6. At 800 °C the peak related to the Fe-Co phase is almost vanished, suggesting that almost complete solubility of Fe in the FCC-Co phase occurs. Lowering the temperature, the Fe-Co phase is segregated again, in agreement with the Fe-Co phase diagram [121].

The Mn1.33Co1.17Cu0.5 sequence shows the appearance of Cu and Co after 300 °C, along with the spinel reduction, supporting the results obtained by DTG analysis. The spinel reduction is completed at 600 °C, with no significant evolution for higher temperatures and during cooling.

The reducing treatment is considered crucial in the sintering process of Mn-Co spinels coatings to obtain high densities at low temperature [56]. After the reduction treatment, the compound is oxidized in air (potentially in situ after the first sintering step) to form again the spinel phase stable in operating environment. To study the compounds behaviour during a re-oxidation process, TGA in air of reduced powders was carried out, and TG and DTG curves are reported in figure 3.15. All thermograms show slow oxidation phenomena occurring up to 500 °C followed by a significant weight gain phenomenon up to 800 °C. In all cases, the significant broadening of the DTG peaks corresponding the main weight gain suggests the occurrence of several overlapped steps.

As follows from the reduction step evaluation, the overall reaction should proceed as reported in equation (3.4):

$$\frac{x}{3}MnO + x(Co, Fe, Cu) + (1+x)O \rightarrow Mn_{3-x}(Co, Fe, Cu)_xO_4 \qquad (3.4)$$

In table 3.7 the comparison between the calculated weight gain and the weight gain measured after 1 h of isotherm at 800 °C is reported. The good overall match confirms the formation of spinel oxides after reoxidation of all the compositions.

To observe in detail the oxidation mechanism, in situ HT XRD analysis was carried out on MnCo2 and MnCo1.6Fe0.2Cu0.2 sample. The acquired patterns are reported in figure 3.16. Regarding MnCo2 sample, it can be observed that at 400 °C traces of CoO suggest the occurring oxidation of Co. At 500 °C oxidation of MnO to $Mn_2O_3$ and of cobalt to Co and $Co_3O_4$ is clearly evident. Disappearance of Mn and Co oxides peaks proceeds with the appearance of $MnCo_2O_4$ reflections,

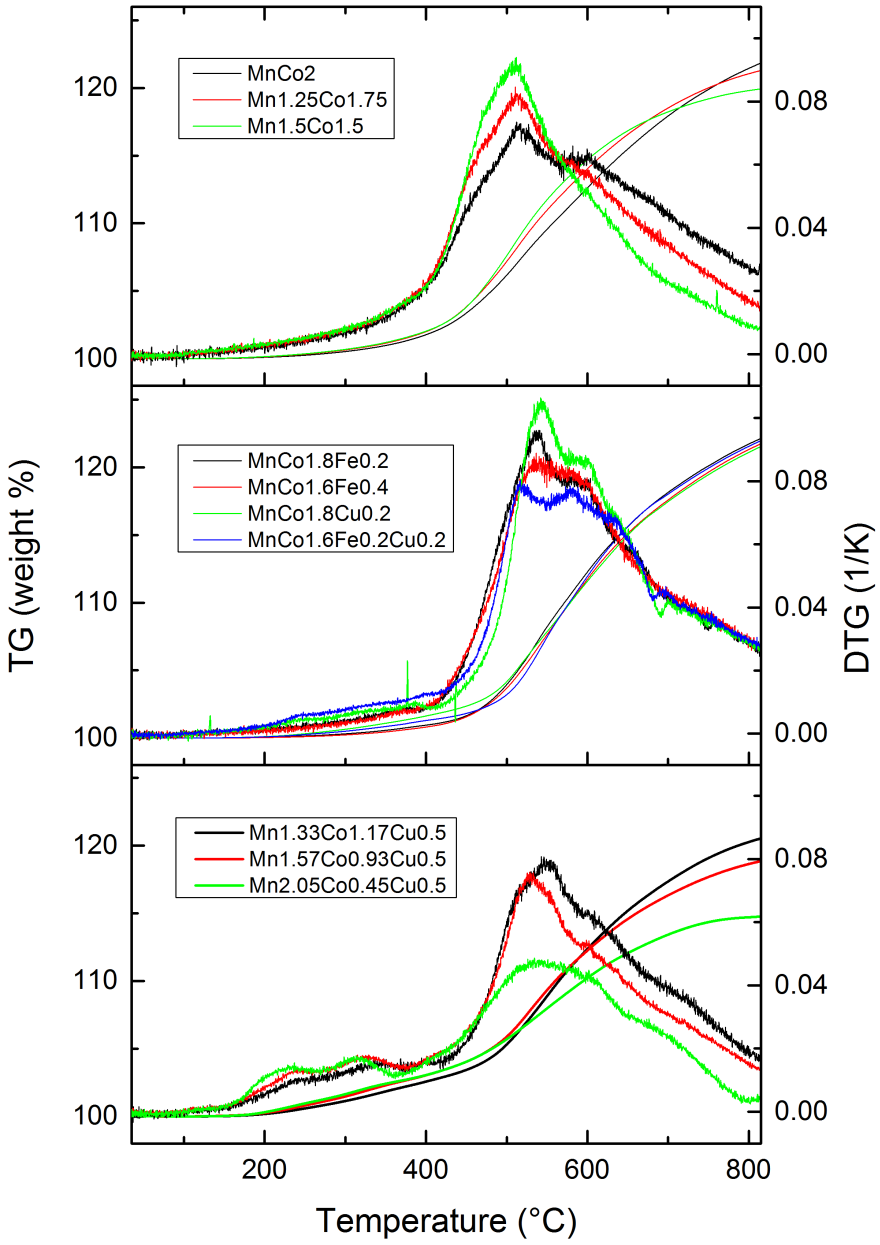



Figure 3.15: Thermogravimetric curves as a function of temperature for the different samples acquired in Air on reduced samples; solid lines represent weight% change, dotted lines the derivative.

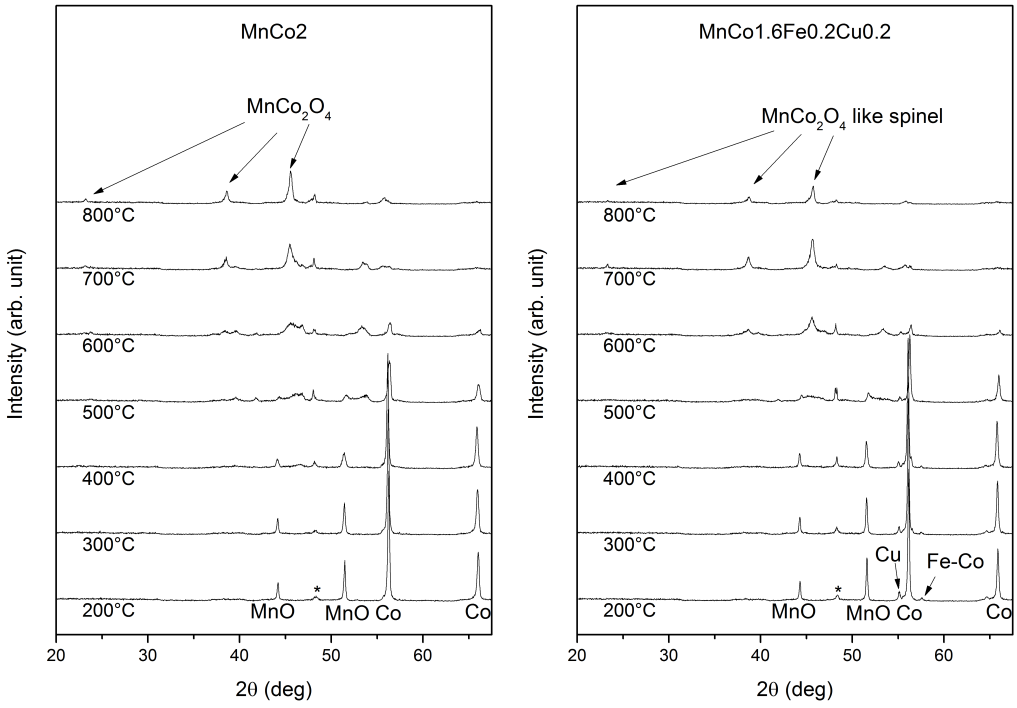
Table 3.7: Calculated weight loss as reported in equation (3.1) and experimental data for TGA analysis carried out on reduced powder in air:

| sample | theoretical weight gain (%) | Experimental weight gain (%) |
|---|---|---|
| MnCo2 | 25.4 | 24.4 |
| Mn1.25Co1.75 | 22.9 | 22.7 |
| Mn1.5Co1.5 | 20.5 | 20.8 |
| MnCo1.8Fe0.2 | 25.5 | 24.6 |
| MnCo1.6Fe0.4 | 25.6 | 24.6 |
| MnCo1.8Cu0.2 | 25.3 | 24.3 |
| MnCo1.6Fe0.2Cu0.2 | 25.4 | 24.6 |
| Mn1.33Co1.17Cu0.5 | 21.9 | 22.0 |
| Mn1.57Co0.93Cu0.5 | 19.6 | 20.0 |
| Mn2.05Co0.45Cu0.5 | 15.3 | 15.5 |

complete at 800 °C.

Regarding the MnCo1.6Fe0.2Cu0.2 sample, the reaction mechanisms seem similar, with the faster reaction towards the spinel phase possibly ascribable to iron presence. Copper seems to remain in its metallic state up to 600°C and oxidises and diffuses in the formed spinel phase at higher temperature.

The similarities during the reoxidation treatment observed in the TG analysis and HT-XRD patterns suggest that similar oxidation behaviour is obtained for all the samples. This is not surprising, since after the reduction treatment all the samples are composed of the same phases (MnO and metals). The metals oxidation phenomena will occur therefore in similar ways for all the compositions, and the spinel phase will be formed through solid state reaction of the oxides at interfaces.




(a) (b)

Figure 3.16: In situ high temperature X-ray diffraction patterns (Fe source) of a) MnCo2, b) MnCo1.6Fe0.2Cu0.2 samples milled for 10 hours and treated at 800°C in reducing atmosphere collected at different temperatures in air flow (heating rate = 10°C/min); (*) sample holder reflection.

### 3.2.2 Sintering Behaviour

The effectiveness of spinel protective coatings is related to their density: the presence of open porosity will inhibit in fact its effectiveness, allowing the alloy to be exposed in the oxidizing ambient. For wet-powder deposition method, density is connected to an effective sintering step. In particular, high densification (i.e. closure of open pores) must be achieved at temperatures that do not affect the alloy stability or cause an excessive growth of its thermal oxide scale. For ferritic stainless steel, this threshold could be identified in approximately 900°C. In this work, the evaluation of sintering behaviour was carried out on consolidated pellets prepared by uniaxial cold pressing. To compare sintering properties meaningfully, and ascribe differences to chemistry rather than to morphology of the powders, comparable green density is crucial. The geometric green densities are reported in table 3.8: similar values are obtained for all the different samples, as expected from the processing of morphologically similar powders.

#### Sintering in air

The consolidated pellets were subjected to dilatometric measurements between room temperature and 1200°C, with a 5°C/min heating rate. Shrinkage curves are reported in figure 3.17.

No significant differences can be observed among Mn-Co and Mn-Co-Fe samples, with sintering temperatures of about 1040-1060°C and maximum densification rates at approximately 1150°C. Copper addition greatly enhances sintering behaviour: sintering temperatures are lowered below 1000 °C and the shrinkage extent is greatly increased with respect to Mn-Co samples. High temperature dilatation phenomena are however visible in Mn1.33Co1.17Cu0.5 and Mn1.57Co0.93Cu0.5 curves. To fur-

Table 3.8: Green densities of the pelletized samples:

| Sample | Green density % |
|---|---|
| MnCo2 | 66±1 |
| Mn1.25Co1.75 | 67±1 |
| Mn1.5Co1.5 | 67±1 |
| MnCo1.8Fe0.2 | 66±1 |
| MnCo1.6Fe0.4 | 66±1 |
| MnCo1.8Cu0.2 | 65±1 |
| MnCo1.6Fe0.2Cu0.2 | 65±1 |
| Mn1.33Co1.17Cu0.5 | 65±1 |
| Mn1.57Co0.93Cu0.5 | 64±1 |
| Mn2.05Co0.45Cu0.5 | 65±1 |

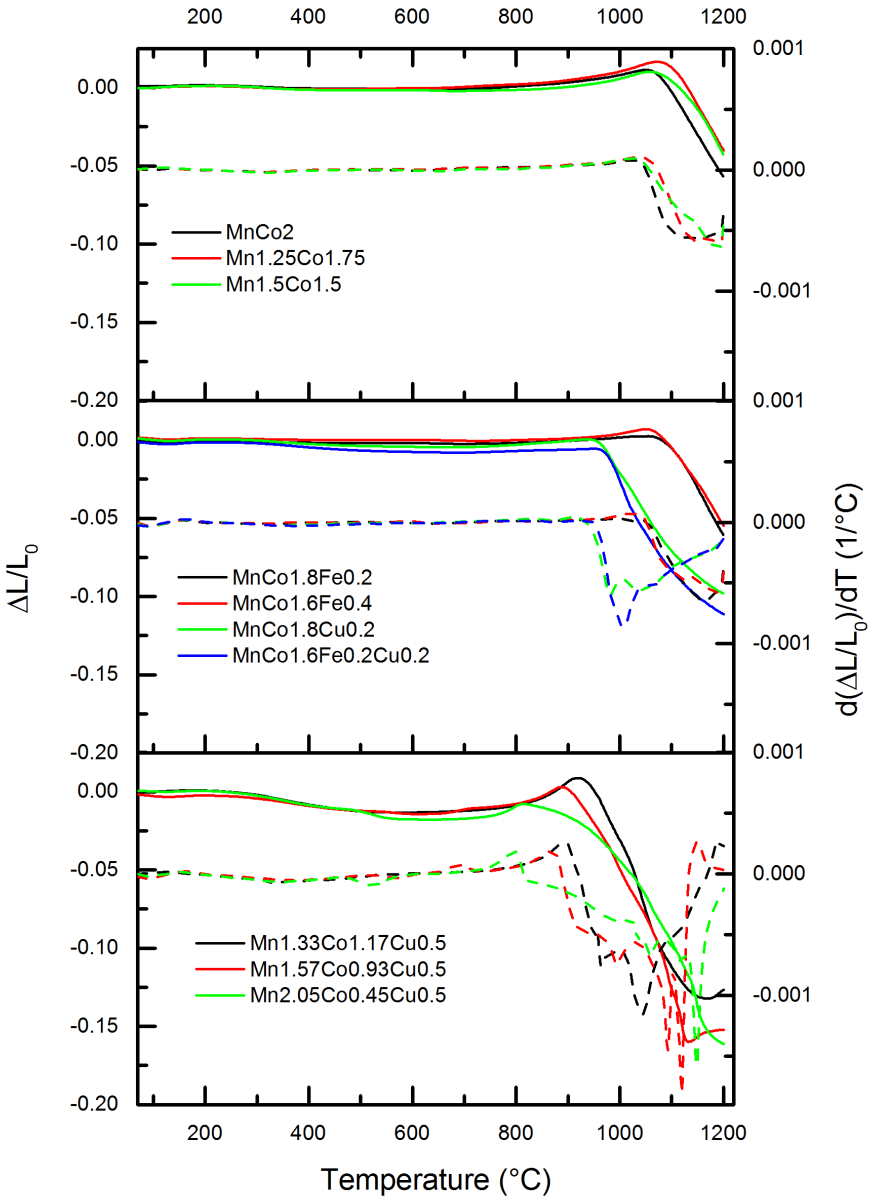



Figure 3.17: Dilatometric curves of the different samples acquired in air atmosphere: solid lines represent the shrinkage ratio, dotted lines the derivative.

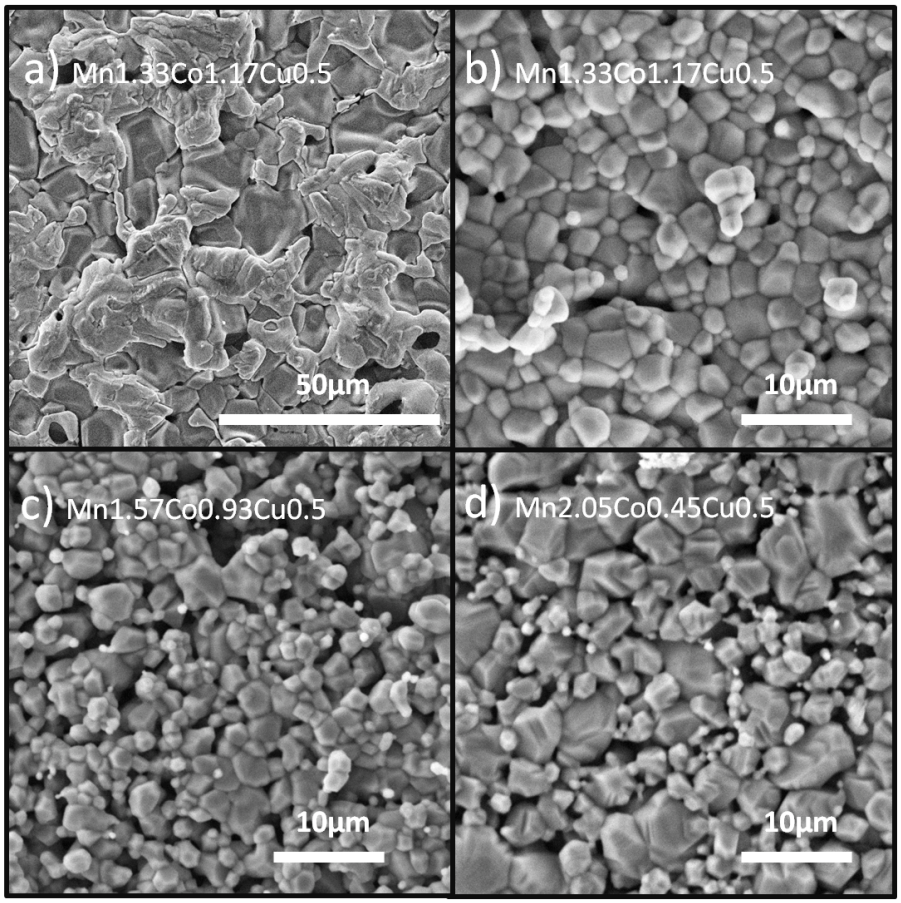



Figure 3.18: SEM images of samples sintered at (a) 1200 °C and (b,c,d) 1000 °C [see text for details].

ther investigate this phenomenon, a pellet obtained by pressing Mn1.33Co1.17Cu0.5 powder was heated in furnace at 1200°C for 10 minutes and slowly cooled. The SEM image is reported in figure 3.18a. Significant grain growth and can be observed, as well as the presence of an irregular and corrugated Cu-rich phase. The observation of the samples clearly suggests a liquid phase sintering at high temperature, most likely due to segregation and melting of the Cu-rich phase, that could result in swelling phenomena [122]. The contemporary release of oxygen gas, as observed by thermogravimetric analysis, when occurring in a highly packed structure could furthermore enhance the expansion phenomena.

In figure 3.19 a summary of sintering and maximum shrinkage temperature of the different samples is reported. Evaluating figure 3.19 no significant differences can be observed in the sintering temperature of Mn-Co and Mn-Co-Fe samples, while all Cu containing samples are characterized by significant enhancements. In figure 3.19b it can be observed that an increase in maximum shrinkage temperature is obtained raising manganese content, as evidenced also in the case of Cu-doped samples. Iron addition as well produces an increase in this property, lowered on the other hand by

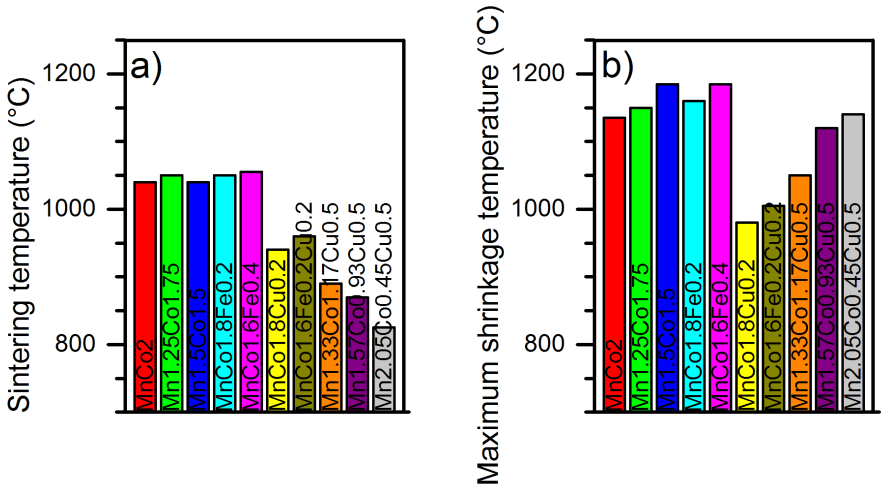



Figure 3.19: (a) Sintering temperature and (b) maximum shrinkage temperature for the different samples.

cobalt/copper substitution.

XRD analysis of the pellets after dilatometric measurements demonstrated in most cases secondary phases in addition to the spinel. This is most likely due to high packing and higher crystals growth, limiting oxygen diffusion and avoiding the single spinel phase recovery during cooling.

The undesired phase segregation upon sintering at high temperature is an issue to precisely determine CTE and electrical properties of the material. Therefore, the sintering treatment of the pellets needed for dilatometry and Van der Pauw experiments was tailored. In the case of Mn-Co samples, it was not possible to reduce the temperature to avoid secondary phase formation, but a second dwell at lower temperature (i.e. 800°C) was successfully introduced to facilitate the spinel recovery. For MnCo2 sample a further annealing (16h at 1000°C) was required to achieve single phase pellets, as observed for similar samples prepared with other synthesis routes [49]. For Cu containing samples instead, the lower sintering temperature, as observed in dilatometric measurements, allowed to reduce the thermal treatment to 1000°C, avoiding segregation of Cu-rich phases and still obtaining sufficiently dense pellets. In figure3.18b-d SEM images of the Mn1.33Co1.17Cu0.5, Mn1.57Co0.93Cu0.5 and Mn2.05Co0.45Cu0.5 samples after sintering at 1000°C are reported. A homogeneous morphology can be observed, characterized by significantly lower crystal growth with respect to the 1200°C thermal treatment. In table 3.9 a summary of the performed thermal treatments and the geometrical density measured after sintering is reported. It can be noted that Cu addition leads to densities comparable to Mn-Co samples even with a 200 K reduction in sintering temperature.

In figure 3.20 X-Ray diffraction patterns of the sintered samples are reported.

Table 3.9: Summary of sintering treatment details (see text for details) and sintered densities:

| Sample | Sintering treatment | Sintered density % |
|---|---|---|
| MnCo2 * | | 93±1 |
| Mn1.25Co1.75 | | 93±1 |
| Mn1.5Co1.5 | 4 h @1200 °C + 4 h @800 °C | 95±2 |
| MnCo1.8Fe0.2 | | 92±1 |
| MnCo1.6Fe0.4 | | 90±1 |
| MnCo1.8Cu0.2 | | 97±1 |
| MnCo1.6Fe0.2Cu0.2 | | 95±1 |
| Mn1.33Co1.17Cu0.5 | 4 h @1000 °C + 4 h @800 °C | 97±1 |
| Mn1.57Co0.93Cu0.5 | | 97±2 |
| Mn2.05Co0.45Cu0.5 | | 97±2 |

* 16h @ 1000 °C post sintering to recover single phase spinel structure

MnCo2 and Mn1.25Co1.75 show a pattern ascribable to a single cubic phase, with small shifts due to different Mn:Co ratio, while Mn1.5Co1.5 exhibits a mixture of tetragonal and cubic spinels. As reported in chapter 1.3, these results are in agreement with the Mn-Co oxides phase diagram at room temperature. A single cubic phase is stable for high Co content (Co:Mn>1.3), a single tetragonal phase is obtained for high Mn content (Co:Mn<0.5), while for intermediate compositions, depending on the synthesis and cooling method, a mixture of the two phases or a single metastable tetragonal phase is observed. All $MnCo_{2-x-y}Fe_xCu_y$ samples exhibit a single cubic spinel phase, with peak shifts due to the different metal content. In particular, due to the different size of dopants ionic radius with respect to the substituted cobalt [123], Fe-Co substitution promotes the enlargement of the lattice, differently from Cu-Co substitution that, due to similar ionic radii, does not induce significant changes in the cell parameter. Regarding the highly Cu doped samples, as observed by HT-XRD, Mn1.33Co1.17Cu0.5 is characterized by a single cubic phase, while raising Mn content peaks ascribable to a tetragonal spinel phase appear. Copper addition enhances therefore the cubic phase stability region at room temperature, while $Mn_2CoO_4$ compound is characterized by a single tetragonal phase [45], the Mn2.05Co0.45Cu0.5 sample shows a mixture of cubic and tetragonal phases.

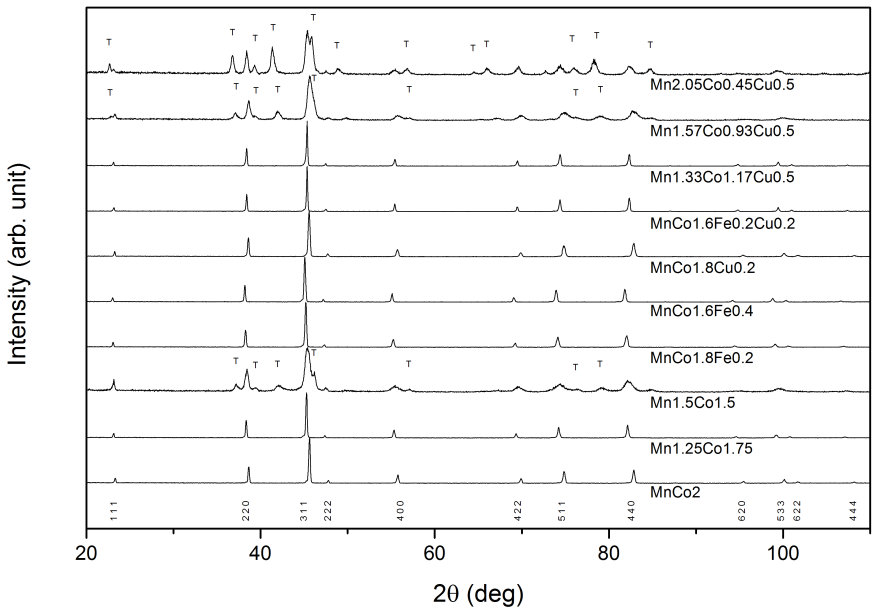



Figure 3.20: X-Ray Diffraction patterns (Fe surce) of samples sintered as described in table 3.9; crystallographic planes indicate cubic spinel reflections, while T indicates peaks ascribable to tetragonal spinels.

### Sintering in reducing atmosphere

As observed in the previous section and reported in literature, Mn-Co spinels are characterized by high sintering temperature, raising issues regarding the steel mechanical properties or the growth of thick chromia scales at such temperatures. Reactive sintering methods are therefore exploited, consisting in a heat treatment carried out in reducing atmosphere, to promote the spinel reduction and exploit the superior sintering properties of the reduced species, and a reoxidizing treatment, to form again the protective spinel coatings [50]. Although this method has been applied to produce most of the slurry coatings reported in literature, few studies have studied in depth the sintering mechanism. In particular, results reported in [56] show for example that great shrinkage is obtained through the reduction treatment.

In this study, to evaluate how the composition affects the shrinkage phenomena in reducing atmosphere, dilatometric analyses were carried out simulating a theoretical sintering treatment, consisting of heating up to 800 °C at 10°C/min and 2 h of dwell time. In figure 3.21 the dilatometric curves are reported.

All samples show length growth phenomena at intermediate temperatures. In particular, for Mn-Co and Mn-Co-Fe samples, the growth maximum is observed in the 500 ÷ 550 °C range, while for Cu-doped samples the maximum is observed below 400 °C. It is therefore likely to ascribe this length increase to the spinel phase demixing observed with TGA and XRD measurements.

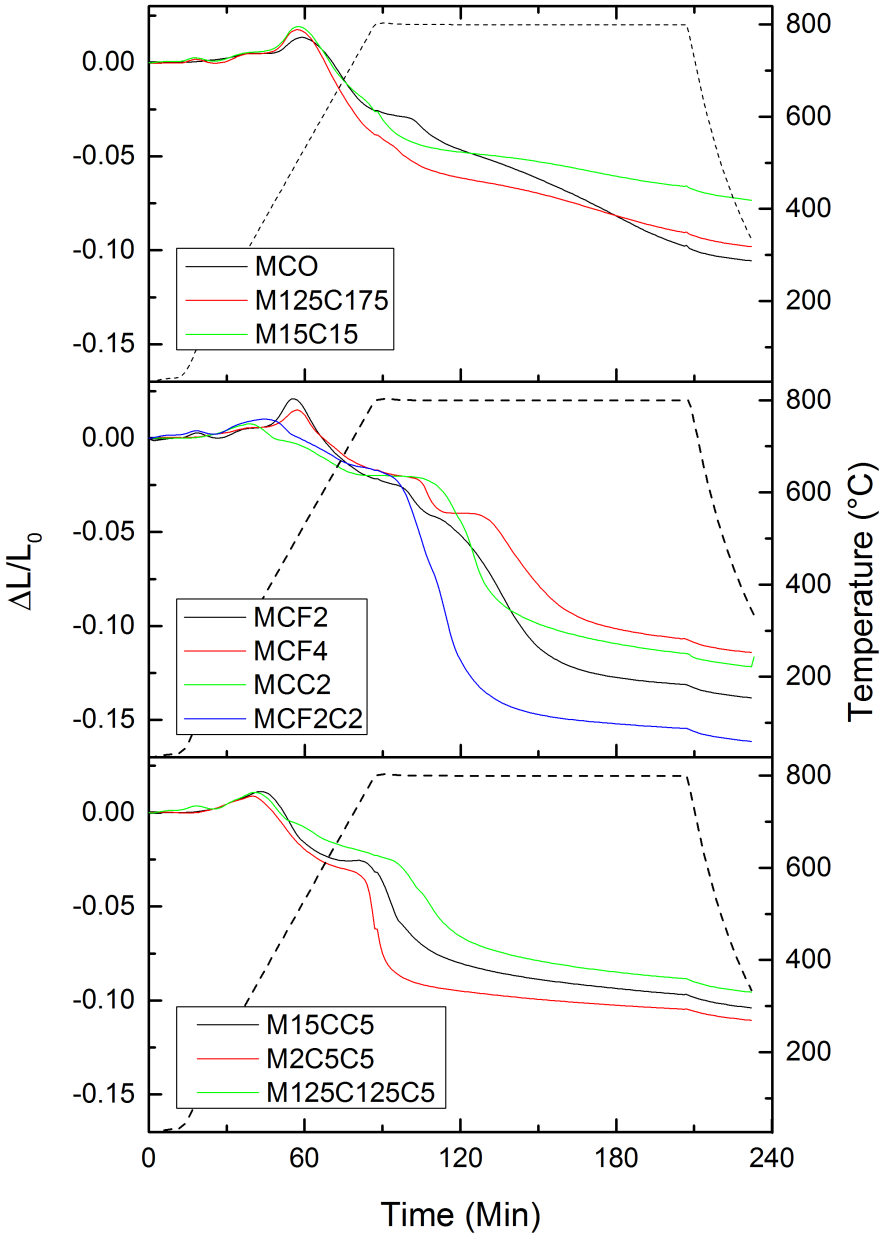



Figure 3.21: X-Ray Diffraction patterns (Fe surce) of samples sintered as described in table 3.9.

At higher temperature shrinkage phenomena can be observed, with variable onsets depending on the samples. For most of the samples, however, a large part of the shrinkage occurs during the isothermal step. Differently from TGA and HT-XRD analyses, carried out on powders, the dilatometric analysis evaluated compacted pellets. In this condition gas flow towards the centre of the pellets may be hindered, resulting in slow reduction phenomena, with sintering occurring mostly after complete reduction of the samples. This hypothesis is further corroborated observing for example among the Mn-Co samples that the sintering onset time grows with cobalt content, as expected by the higher amount of cobalt to be oxidized.

Furthermore, in some compositions (i.e. MnCo1.8Fe0.2 and MnCo1.6Fe0.4) several shrinkage steps can be observed. To explain these phenomena, in figure 3.22 are reported the high temperature patterns acquired on a MnCo1.6Fe0.4 sample during heating and dwell at 800 °C in reducing atmosphere. As commented in the previous section, reduction of Co and Fe proceeds through the formation of large amounts of Fe-Co phase (evident in the 700 °C pattern), while at 800 °C growth of Co phase over the Fe-Co phase is observed. During the dwell, the relative intensity of Fe-Co and Co phase peaks changes, suggesting a Co phase growth. The occurring reaction between metal phases could be accounted for shrinkage or dilatation phenomena, giving rise to the multiple steps observed in the MnCo1.8Fe0.2 and MnCo1.6Fe0.4 samples curves. This phenomenon is scarcely evident in the Mn1.6Fe0.2Cu0.2 composition, characterized by a faster Co and Fe reduction with the formation of a single Co phase, as shown from TGA and HT-XRD analyses, and not evident in Mn-Co-Cu samples, due to the scarce reciprocal solubility of Co and Cu.

XRD patterns of the samples after the reduction treatment are reported in 3.23. In all cases, after the sintering treatment a mixture of MnO and Co, Fe and Cu metals can be observed, as indicated by TGA measurements for powder samples.

To evaluate how shrinkage is affected by the composition, in figure 3.24 the final shrinkage of the different samples is reported. Starting from the Mn-Co samples, it is clear how a higher Mn:Co ratio promotes higher shrinkage. Fe doping improves shrinkage behaviour, with both Fe-doped samples characterized by higher shrinkage than the MnCo2 sample. The higher contraction observed for the MnCo1.8Fe0.2 sample suggests however that higher results are achieved with limited amounts. MnCo1.8Cu0.2 sample is characterized by a higher shinkage with respect to MnCo2, suggesting that limited amounts of copper may act as sintering aid also in reducing conditions as well. The $Mn_xCo_yCu0.5$ samples shows a trend opposite to the Mn-Co samples, with higher shrinkage for Mn-rich samples. Finally, a remarkable enhancement with respect to the undoped MnCo2 composition is observed when cobalt is substituted simultaneously by Co and Fe.

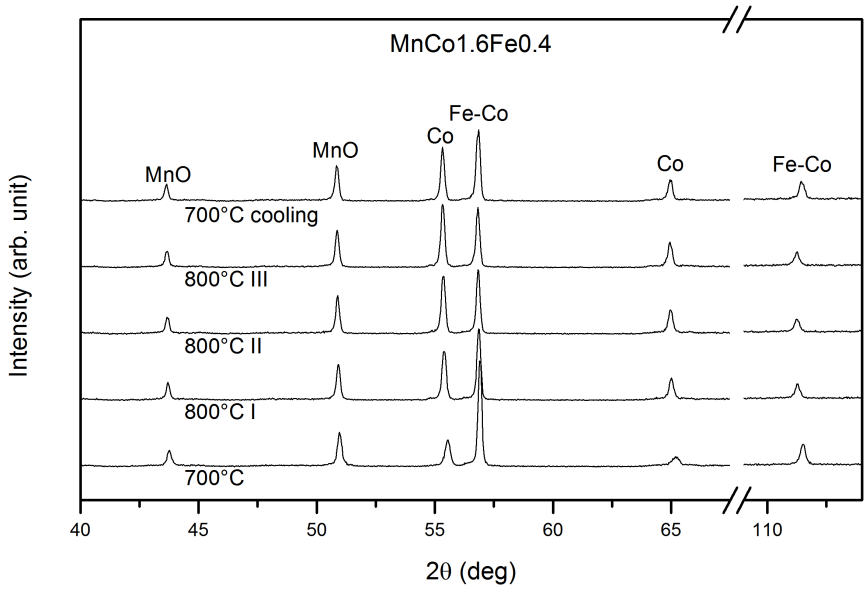



Figure 3.22: In situ high temperature X-Ray Diffraction patters (Fe source) of sample MnCo1.6Fe0.4 acquired in reducing atmosphere at 700°C, 800 °C after respectively 5, 25 and 45 minutes (800 °C I, II and III) and during cooling at 700 °C.

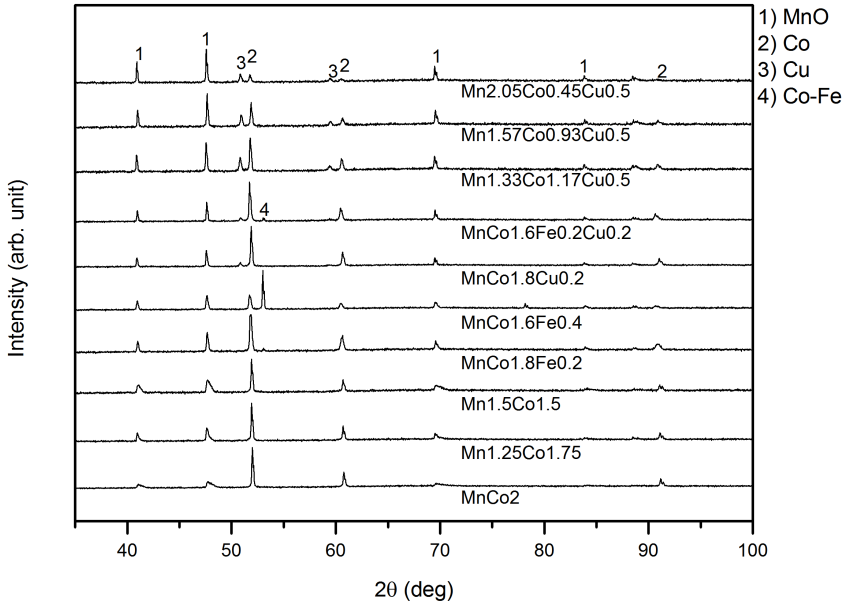



Figure 3.23: X-Ray Diffraction patters (Co source) of the different samples after the dilatometric analysis carried out in $N_2/H_2(5\%)$ up to 800 °C.

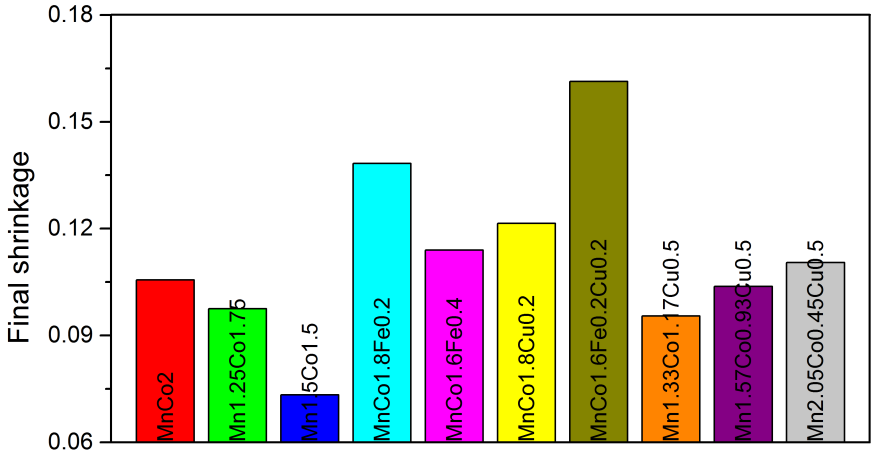



Figure 3.24: Shrinkage measured for the different samples after the sintering treatment in reducing atmosphere.

SEM micrographs of reduced pellet surfaces are reported in figure 3.25. Despite the large shrinkage, it can be observed that the samples show a porous morphology. Metal-rich samples (i.e. MnCo2 and MnCo1.6Fe0.2Cu0.2) samples are composed of a skeleton structure formed by rounded metal particles with dispersed faceted Mn-rich crystals. Raising Mn content, the situation reverses, as clearly visible by the Mn2.05Co0.45Cu0.5 sample, formed by aggregates of regularly edged Mn oxide crystals and rounded dispersed metal particles.

Observing these micrographs it can be suggested that most of the shrinkage observed with dilatometric experiments is due to the spinel reduction and sintering of the majority phase (e.g. metal, oxide) without however approaching high densities. In the $Mn(Co,Fe,Cu)_2O_4$ compositions, after the reduction has occurred sintering of the metal phase takes place. In the Mn-rich composition Mn2.05Co0.45Cu0.5 sintering of the MnO phase takes place driving the densification phenomenon. In the intermediate samples, sintering of the similar phases is hindered and lower shrinkage is observed.

To evaluate the length change phenomena occurring during the re-oxidation steps, MnCo2 and MnCo1.6Fe0.2Cu0.2 reduced pellets where subjected to dilatometric analysis in air. The curves are reported in figure 3.26. It can be observed that a dilatation phenomenon is evident in both cases between 400 and 750 °C, and ascribable to the oxidation of the metallic phases, followed by a slight contraction. No significant changes are observable during the dwell time. Furthermore, the overall length change is quite limited, if confronted with the shrinkage occurred during the reducing step.

To check morphology and phase composition of the re-oxidized pellets, reduced pellets of all the compositions were subjected to a furnace thermal treatment of 2h at

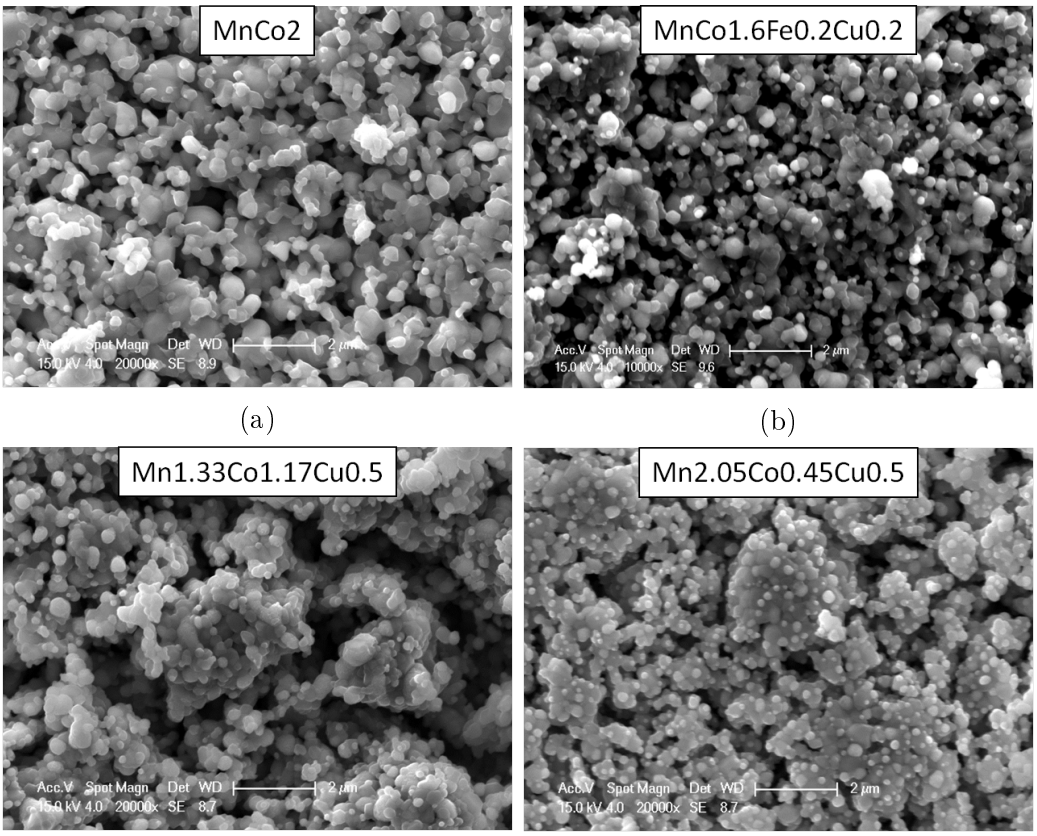



Figure 3.25: SEM images of pellets surface after the dilatometer reducing treatment.

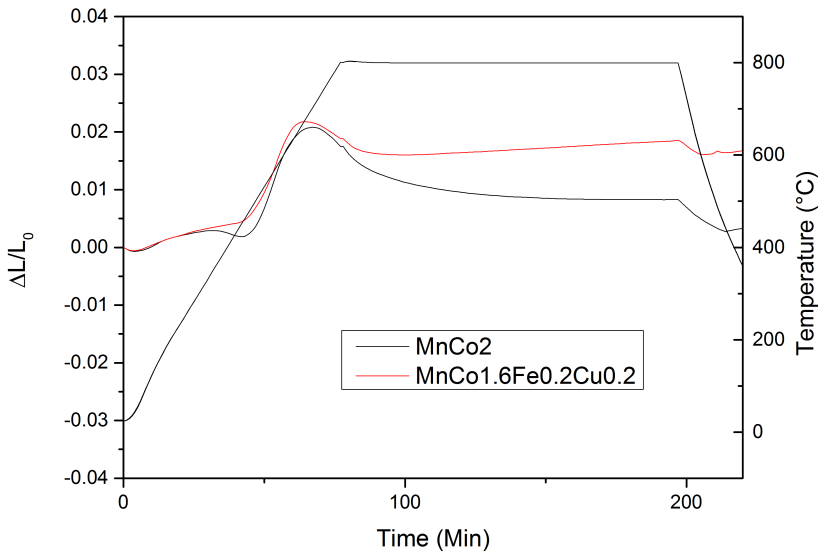
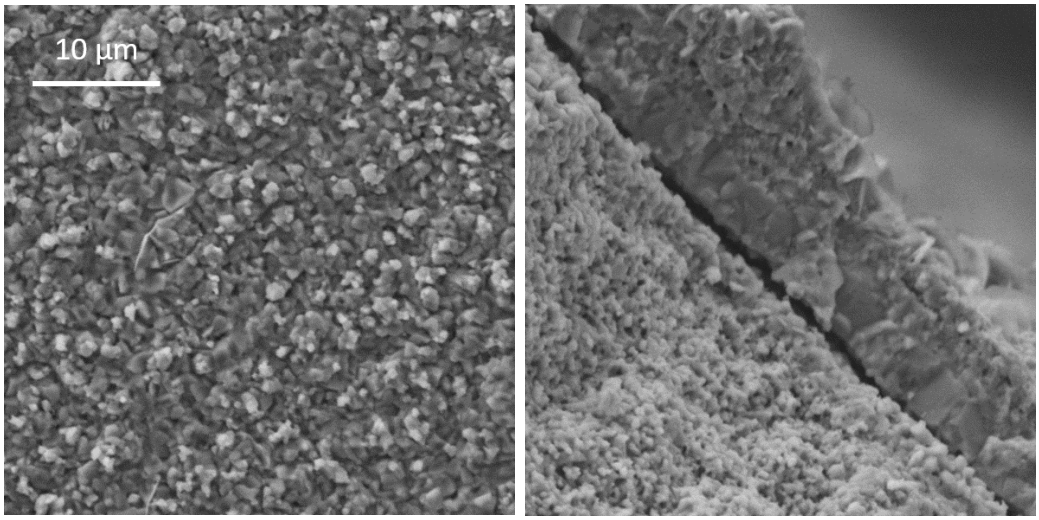



Figure 3.26: Dilatometric curves acquired in air on MnCo2 and MnCo1.6Fe0.2Cu0.2 reduced pellets.




(a) (b)

Figure 3.27: SEM images of MnCo1.6Fe0.2Cu0.2 pellets (a) surface and (b) fracture after the reduction-reoxidation treatment.

800 °C. In all cases no significant dilatation was observed (i.e. $\frac{\Delta L}{L_0} < 1\%$), suggesting that while significant shrinkage without major densification is achieved during the reducing step, the re-oxidation step brings little dimensional change but promotes significant densification due to the increase in weight. XRD analyses showed however the presence of secondary phases, due to incomplete oxidation and reaction: the formation of compact surface spinel layers hinders oxygen diffusion in the pellets core, as expected due to the protective effect of the Mn-Co spinels, limiting the weight recovery of the loss occurred during the reducing step. This phenomenon is clearly visible in figure 3.27, where SEM micrographies of a MnCo1.6Fe0.2Cu0.2 sample after the reduction-reoxidation treatment are reported. The surface shows a dense and compact morphology, and the fracture image shows a compact surface layer with a porous structure beneath.

Therefore, to simulate the effective density achievable through the reactive sintering process, theoretical sintered density was calculated based on the dimensional changes observed during the reactive sintering treatment, with the assumption that full weight was recovered during the re-oxidation process (i.e. as observed with TGA and as expected to occur in thin deposited layers). In table 3.10 the calculated densities are reported. Taking aside the singular result related to the MnCo1.6Fe0.2Cu0.2, characterized by the higher shrinkage during the reducing conditions, it can be observed that calculated density values are significantly higher than green densities, suggesting an effective densification occurred during the process, whereas sintering in air at 800 °C would not have produced significant shrinkage (see figure 3.17).

Regarding morphology, in figure 3.28 fractures of re-oxidized pellets are reported.

Table 3.10: Relative shrinkage achieved in reducing-reoxidizing condition and theoretical calculated sintered density (see text for details):

| Sample | relative shrinkage | sintered density (%) |
|---|---|---|
| MnCo2 | 0.10±0.01 | 90±3 |
| Mn1.25Co1.75 | 0.09±0.01 | 88±3 |
| Mn1.5Co1.5 | 0.06±0.01 | 81±3 |
| MnCo1.8Fe0.2 | 0.13±0.01 | 99±3 |
| MnCo1.6Fe0.4 | 0.10±0.01 | 91±3 |
| MnCo1.8Cu0.2 | 0.11±0.01 | 93±3 |
| MnCo1.6Fe0.2Cu0.2 | 0.15±0.01 | 100** |
| Mn1.33Co1.17Cu0.5 | 0.09±0.01 | 85±3 |
| Mn1.57Co0.93Cu0.5 | 0.09±0.01 | 86±3 |
| Mn2.05Co0.45Cu0.5 | 0.10±0.01 | 90±3 |

It can be observed a dense surface structure with closed porosity, confirming the theoretical density calculation.

Therefore, the reduction-reoxidation treatment was clearly effective in promoting sintering at temperatures compatible with the ferritic alloys substrates (i.e. 800 °C) for all the samples. Furthermore, the dilatometric analyses clearly show a dependence of the composition on the final shrinkage , enhanced by:

- The formation of high quantities of a majority phase at high temperature, i.e. high amounts of Co, Co-Fe or Mn;
- Appropriate Fe or Cu doping (e.g. 5-10 wt%);
- Simultaneous Fe and Cu doping.

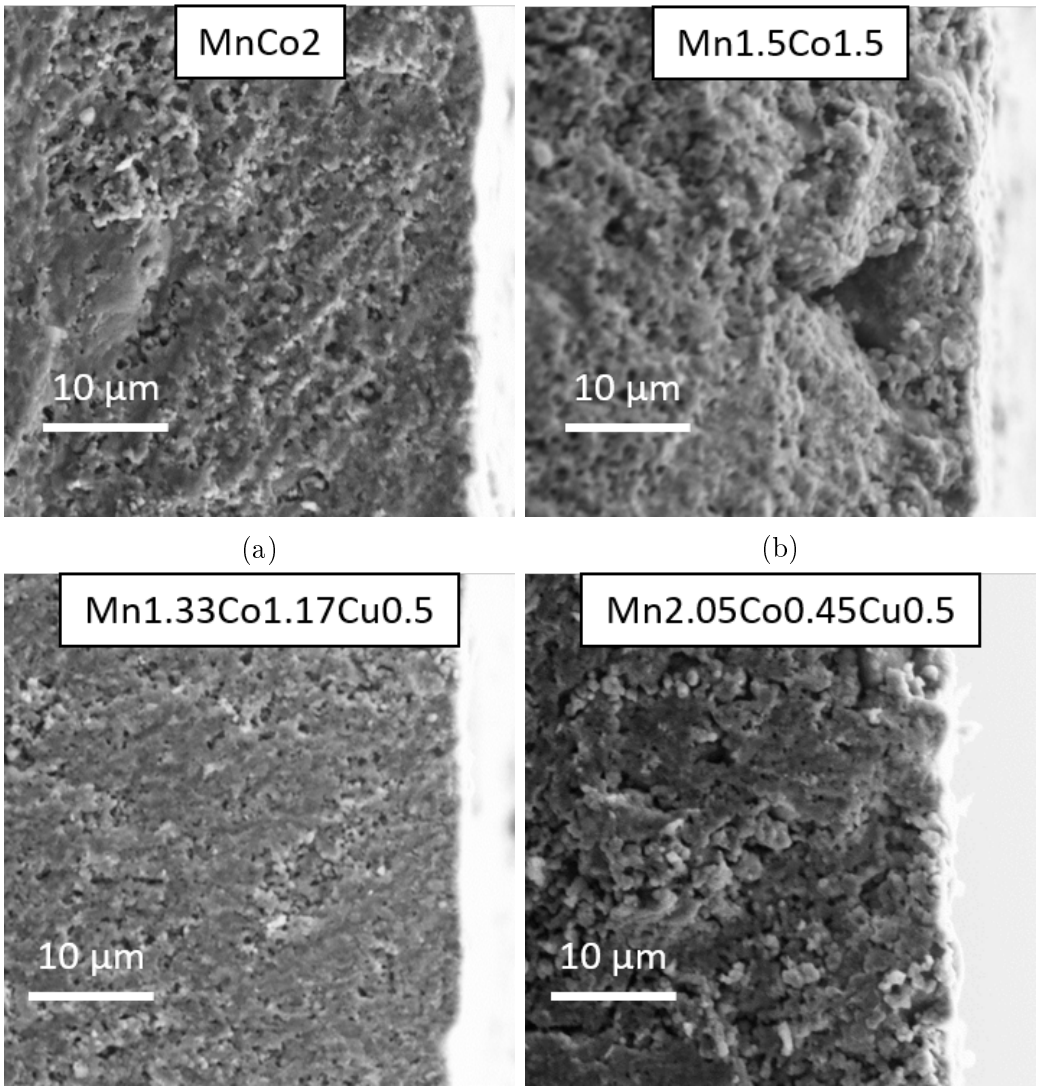



Figure 3.28: SEM images of pellets fracture of reduced pellets after reoxidation in furnace.

### 3.2.3 Thermal expansion

A good match between the thermal expansion behaviour of the alloy and of the coating is required to avoid detachment and spallation phenomena during thermal cycling. CTE of commmon commercial ferritic stainless steels is in the $11 \div 13 \text{cot}\, 10^{-6}\text{K}^{-1}$ [22], and the evaluation of the influence of the coating material composition on the CTE could allow to tune opportunely the material to precisely match the alloy. To evaluate the CTE of the different compositions, the pellets sintered in air as reported in table 3.9 were subjected to dilatometric analyses. The obtained curves are reported in figure 3.29.

Regarding Mn-Co samples, it can be observed that higher Co content induces higher thermal expansion. MnCo2 and Mn1.25Co1.75 samples, characterized by a single phase in the whole examined temperature range, show a linear behaviour. Mn1.5Co1.5 curve shows instead a discontinuity in the 500-600 °C temperature range, ascribable to the dual phase – single phase transition. $MnCo_{2-x-y}Fe_xCu_yO_4$ compositions and Mn1.33Co1.17Cu0.5 sample, similarly characterized by a single phase through the whole examined temperature range, show a linear behaviour. Dual-phase Cu samples exhibit instead a discontinuity in the 450-600 °C temperature range and in the 600-750 °C for the Mn1.57Co0.93Cu0.5 and Mn2.05Co0.45Cu0.5 samples respectively, most likely related to the dual-single phase transition occurring in these temperature intervals.

Average CTE values have been calculated between room temperature and 800 °C, and are reported in table 3.11. Considering thermal expansion of ferritic stainless steels ($11\text{-}13 \cdot 10^{-6}\text{K}^{-2}$ [22]), Mn1.33Co1.17Cu0.5, MnCo1.8Cu02 and Mn2.05Co0.45Cu0.5 exhibit the lesser compatibility.

To evaluate how the different Mn:Co ratio and dopant addition influence CTE, in figure 3.30 the CTE values at 800 °C are reported versus the cobalt content for the different samples.

Regarding Mn-Co composition, a clear linear trend can be observed between the composition and CTE values. Also for MnxCoyCu0.5 doped samples an analogue behaviour can be observed when changing Mn:Co ratio, and Cu addition does not affect significantly this trend but rather induces a shift of the curve toward higher CTEs. Furthermore, It can be observed a clear negative trend between CTE value and iron content, while similar enhancements are observed with the Cu-Co substitution in the MnCo2-MnCo1.8Cu0.2 and MnCo1.8Fe0.2-MnCo1.6Fe0.2Cu0.2 cases. Therefore, consistently with the single metal doped samples, the combined effect is obtained in the MnCo1.6Fe0.2Cu0.2 compound, the CTE of which is ranged between those of MnCo1.8Fe0.2 and MnCo1.8Cu0.2. This result suggests that the CTE of

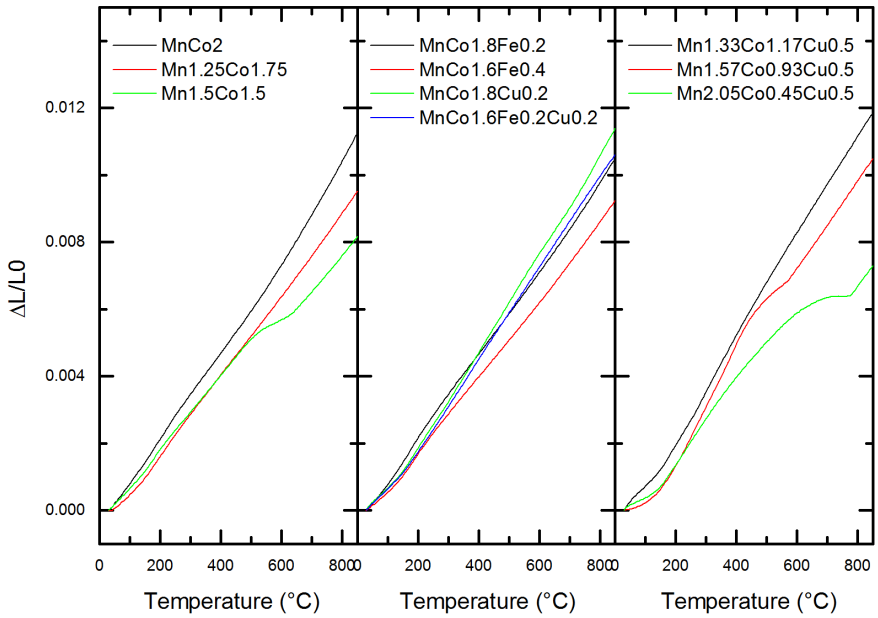



Figure 3.29: Dilatometric curves of sintered samples.

Table 3.11: Thermal expansion coefficient measured between room temperature and 800 °C for the different samples.:

| Sample | CTE @800 °C ($\cdot 10^{-6}K^{-1}$) |
|---|---|
| MnCo2 | 13.5±0.1 |
| Mn1.25Co1.75 | 11.5±0.1 |
| Mn1.5Co1.5 | 9.7±0.1 |
| MnCo1.8Fe0.2 | 12.7±0.1 |
| MnCo1.6Fe0.4 | 11.1±0.1 |
| MnCo1.8Cu0.2 | 13.7±0.1 |
| MnCo1.6Fe0.2Cu0.2 | 12.9±0.1 |
| Mn1.33Co1.17Cu0.5 | 14.5±0.1 |
| Mn1.57Co0.93Cu0.5 | 12.7±0.1 |
| Mn2.05Co0.45Cu0.5 | 8.5±0.1 |

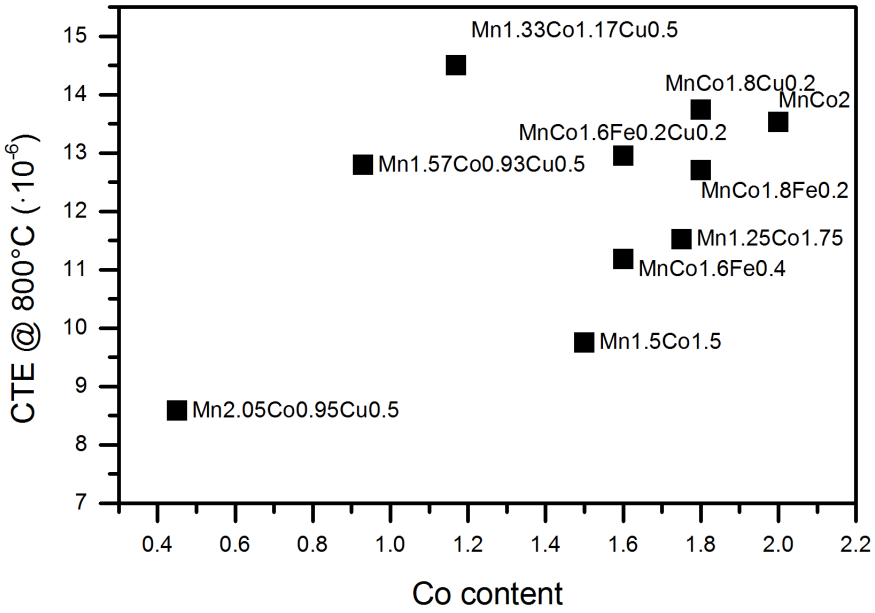



Figure 3.30: CTE of the different samples as a function of Co content $x$ in the $Me_{3-x}Co_xO_4$ spinel.

Mn-Co spinels can be tuned in the examined range by compositional tailoring, as the effect of the cobalt substitution with copper and iron on CTE is retained with the simultaneous doping.

The obtained results are in agreement with previous studies that suggest the occurrence of a relation between CTE and the different occupations and valence states in the spinel lattice [124]. In particular, thermal expansion of mixed metal spinels can be related to the composition principally via the occupation of octahedral sites, where compounds characterized by high valence differences possess higher CTE.

As previously introduced, $Mn_{3-x}Co_xO_4$ spinels characterized by an occupation of tetrahedral sites by $Co^{2+}$ atoms, while $Co^{2+}$, $Co^{III}$, $Mn^{3+}$ and $Mn^{4+}$ occupy octahedral sites, with $Co^{2+}$ and $Mn^{4+}$ amounts related to electro-neutrality constraints. In the $1<x<2$ compositional range, the increase of Co promotes an increase of $Co^{2+}$, $Co^{III}$ and $Mn^{4+}$ species at the expense of $Mn^{3+}$ atoms [48]. Increasing Co content in this composition range will theoretically cause higher valence inhomogeneity, raising CTE, in agreement with our results. The substitution of Co with Fe occurs with $Fe^{3+}$ species occupying preferentially octahedral sites in place of Co atoms [49], reducing the amount of octahedral $Co^{2+}$ and therefore the amount of species characterized by different valences, and lowering CTE, as observed here. In mixed Cu-Co-Mn compounds instead, $Cu^{1+}/Cu^{2+}$ species tend to occupy tetrahedral sites preferentially over $Co^{2+}$ atoms, leading to an enrichment of $Co^{2+}/Co^{III}$ pairs in octahedral

sites [125]. Furthermore, the presence of $Cu^{1+}$ atoms promotes $Mn^{3+}$ oxidation to $Mn^{4+}$ to maintain charge neutrality. Valence differences are therefore increased with copper doping, enhancing CTE. When Co is substituted by both Fe and Cu, the enhancement of CTE due to $Cu^{1+}$ and $Cu^{2+}$ introduction on tetrahedral sites is counterbalanced by the CTE decrease induced by the $Fe^{3+}$ presence in octahedral sites, and, with Fe and Cu ions not being competitors for lattice sites occupation in the examined composition range, the overall CTE change can be considered as limited to the sum of the single dopants contributions.

### 3.2.4 Electrical conductivity

Electrical conductivity measurement was carried out by means of the Van der Pauw method in the temperature range 500-800 °C. In figure 3.31 the Arrhenius plots are reported.

Similarly to thermal expansion, the samples characterized by a single phase in the examined range exhibit a linear trend, while samples exhibiting a dual-single phase transformation show slope changes at temperatures coherent with the discontinuities observed in dilatometric measurements. From the single-phase region of the Arrhenius plots, activation energies were calculated and are reported in Table 5. Mn-Co, Fe and 0.2 Cu doped samples exhibit comparable values of about 0.5eV, while significant Cu addition (i.e. 15 at% ) lowers significantly the activation energy to about 0.3eV.

To better evaluate how Mn:Co ratio and Cu addition affect electrical properties, in figure 3.32 the conductivity values measured at 800 °C are reported versus cobalt content.

The MnCo2 sample is characterized by a conductivity value of about 80S/cm, and a decreasing trend can be observed increasing Mn content. A similar decrease in conductivity with Mn content can be observed for the 05Cu doped samples as well. Cu addition increases electrical conductivity, with the Mn1.33Co1.17Cu0.5 sample characterized by a conductivity value of about 125S/cm. Regarding the substitution of Co with Fe, a clear decreasing trend can be observed, with conductivity of about 51 S/cm and 36 S/cm for MnCo1.8Fe0.2 and MnCo1.6Fe0.4 samples respectively. Finally, similar enhancements are observed when cobalt is substituted in the reference material (Mn1.8Co1.8Cu0.2 versus MnCo2O4) or in the iron doped sample (MnCo1.6Fe0.2Cu0.2 versus Mn1Co1.8Fe0.2) as observed for CTE.

In such spinel systems, the conductivity behaviour is usually ascribed to a small polaron hopping mechanism between mixed valence elements on octahedral sites, and in Mn-Co oxides it is usually related to $Co^{2+}/Co^{III}$ and $Mn^{3+}/Mn^{4+}$ pairs [35,

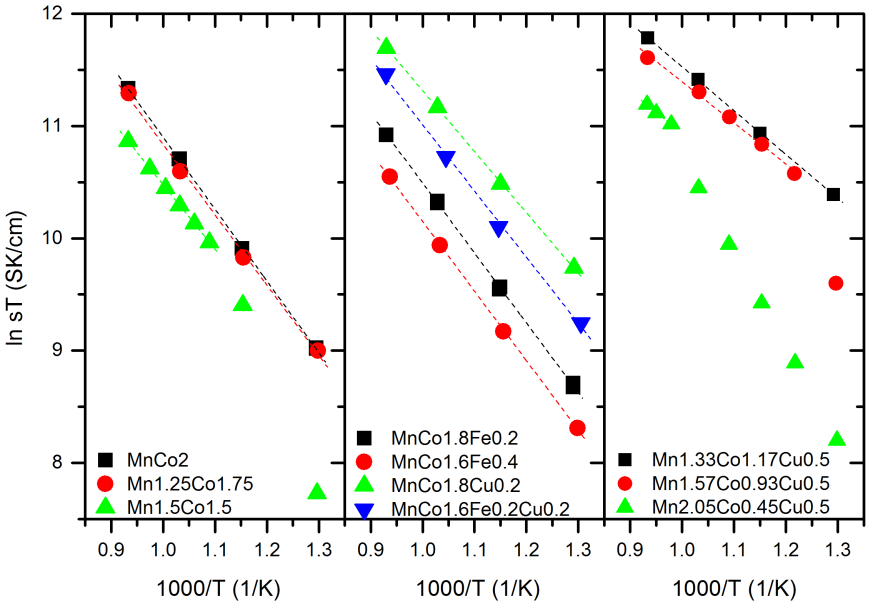



Figure 3.31: Arrhenius plots of electrical conductivity measured (dots) for the different samples and linear fits in the single phase linear regions (dashed lines).

Table 3.12: Activation energy calculated from the Arrhenius plot of the different samples:

| Sample | Temperature range ( °C) | Activation energy (eV) |
|---|---|---|
| MnCo2 | 500-800 | 0.55±0.02 |
| Mn1.25Co1.75 | 500-800 | 0.54±0.04 |
| Mn1.5Co1.5 | 650-800 | 0.49±0.02 |
| MnCo1.8Fe0.2 | 500-800 | 0.54±0.02 |
| MnCo1.6Fe0.4 | 500-800 | 0.53±0.02 |
| MnCo1.8Cu0.2 | 500-800 | 0.46±0.02 |
| MnCo1.6Fe0.2Cu0.2 | 500-800 | 0.50±0.02 |
| Mn1.33Co1.17Cu0.5 | 500-800 | 0.34±0.02 |
| Mn1.57Co0.93Cu0.5 | 600-800 | 0.32±0.03 |
| Mn2.05Co0.45Cu0.5 | 750-800 | 0.32±0.04 |

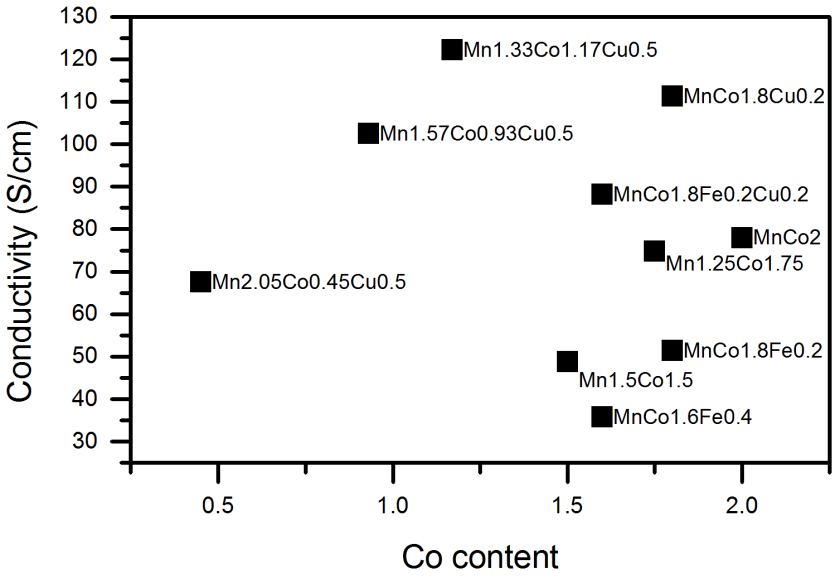



Figure 3.32: Conductivity measured at 800 °C for the different sintered samples as a function of Co content $x$ in the $Me_{3-x}Co_xO_4$ spinel.

48, 126]. The $Co^{2+}/Co^{III}$ and $Mn^{3+}/Mn^{4+}$ concentration ratio affects therefore significantly conductivity properties. The observed trend for Mn-Co samples is in agreement with previous findings, and is related to the maximum concentration of $Co^{2+}$ and $Mn^{4+}$ species for compositions with Mn:Co$\sim$2:1 [31]. The similar increasing trend here observed for the 05Cu-doped samples suggests that similar phenomena can be accounted for also in Cu-Mn-Co samples. The significant increase of conductivity in Cu samples with respect to Mn-Co compounds can be instead due to multiple mechanisms. Copper addition in mixed Mn-Co spinels occurs with preferential occupation of tetrahedral sites of the spinel lattice by $Cu^{1+}$ and $Cu^{2+}$ species, that promotes $Mn^{3+}$ oxidation to $Mn^{4+}$ to maintain charge neutrality. As a consequence, Cu introduction increases active pairs concentration and therefore electrical conductivity [125]. Tetrahedral Cu ions could furthermore contribute indirectly to electrical conductivity, through mediation of charge transfer mechanisms between near but not adjacent Mn atoms, as observed in Ni-Cu manganite spinels [127]. The observed decrease in conductivity with Fe substitution is instead related to the preferential occupation of octahedral sites by $Fe^{3+}$ atoms, not involved in polaron formation, limiting the charge carrier density [49]. Similarly to what was observed for CTE, without competition for lattice site occupation among the dopants, the effect of the simultaneous substitution is limited to the sum of the single factors.

# Chapter 4

# La-Fe perovskite coatings by chemical conversion of interconnect steels

La-based perovskites could represent an interesting alternative to spinel-base coatings thanks to their high stability at the operating temperatures. Among the factors limiting their application, high sintering temperatures and low obtained densities, limited mechanical adhesion, and possible kinetic instability in the presence of high chemical or electrical gradients must be overcome.

The molten carbonate conversion coating technique described in section 1.4 proved to be effective in the production of dense and adherent La-Fe base perovskite coatings on austenitic and low chromium ferritic stainless steels. Different growth mechanisms arise depending on the bath composition: a dissolution-precipitation mechanism, with the production of thick passivation coatings, and a template conversion mechanism, with the formation of thin layers. With significant coating effectiveness observed in molten carbonate fuel cells environments [8], the technique application to high chromium ferritic stainless steels, suitable for SOFCs, may represent a viable strategy to produce low cost and effective coating also in SOFC technology.

In this chapter the findings related to the application of the passivation process to several ferritic stainless steel are reported, with the evaluation and optimization of the experimental variables to produce both thick and thin coatings.

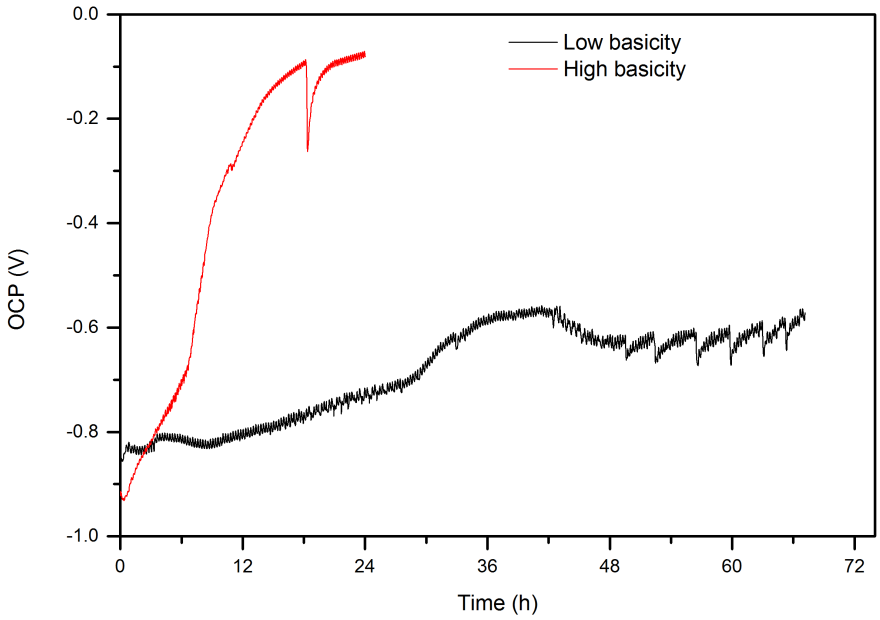



Figure 4.1: OCP curves of K41 steel samples electrode processed at 600 °C in salts characterized by different basicity.

## 4.1 Thick coatings

The salt composition plays obviously a key role in the passivation process, in particular the melt basicity, related to the presence of active oxygen ions. It has been shown that melt basicity of lithium-sodium carbonates is significantly increased by rare earth elements addition [91]. Furthermore, as basicity regulator, magnesium oxide was added to the melt [90]. Two levels were evaluated, as described in section 2. The initial experimental temperature was fixed at 600 °C, safe for what concerns salt stability [128] and sufficiently high to promote the perovskite structuration [76].

As previously described, the increase of the steel electrodes OCP towards more noble values is ascribable to the passivation of the steel surface. Considering the perovskite coating process, this phenomenon takes place in two successive steps: initial formation of lithium-iron oxides and growth of lanthanum-iron perovskite on the oxide sublayer [76]. In figure 4.1, the OCP curves of K41 steel samples exposed in different conditions, namely higher and lower basicity, are reported. it can be clearly observed the faster passivation occurring in the salt characterized by the higher basicity.

The XRD patterns of these samples are reported in figure 4.2. Both samples are characterized by similar patterns, with the presence of peaks ascribable to $LaFeO_3$ (JCPDS card N. 37-1493) as main phase, and secondary phases ascribable to the presence of a Fe-rich spinel or to salt residues (* peaks). Perovskite peaks are

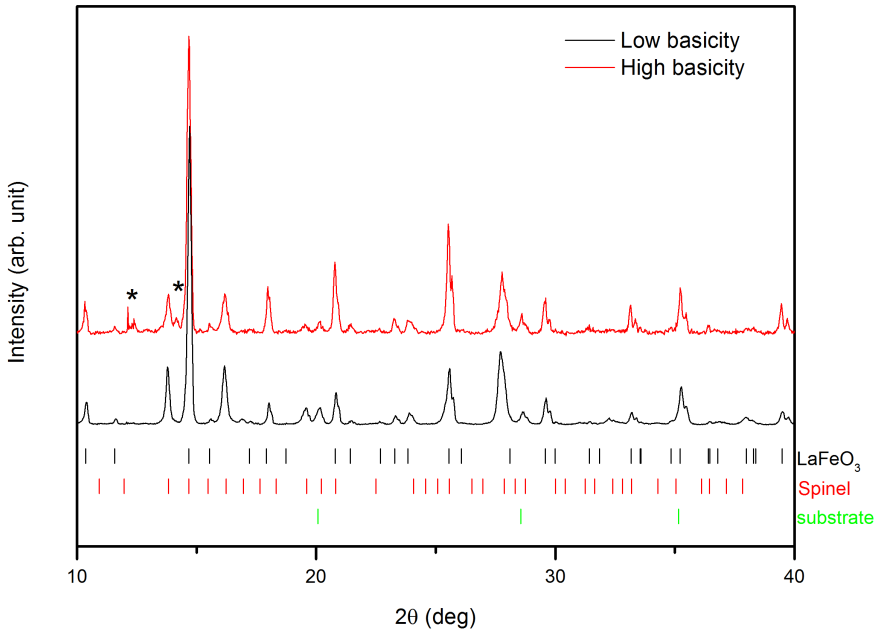



Figure 4.2: X-Ray Diffraction patterns (Mo surce) of K41 steel samples subjected to the passivation treatment at 600 °C in new salts characterized by different basicity.

sharp and well defined, suggesting high crystallinity and homogeneity. Regarding the spinel phase, excluding nanostructuration of crystallites as broadening source due to high temperature and long processing time, broadening of diffraction peaks suggests that the reflections may arise from multiple spinel phases characterized by different compositions and therefore lattice parameters. This is in agreement with the corrosion mechanism of ferritic stainless steels described in section 1.4.1, involving the formation of a superficial Fe-rich oxide and an inner Fe-Cr spinel. In particular, peak position is compatible with the presence of several Fe-rich spinels, such as magnetite ($Fe_3O_4$ - JCPDS card N. 19-629), lithiated iron spinel ($LiFe_5O_8$ - JCPDS card N. 17-114) or chromium-iron spinels ($FeCr_2O_4$ - JCPDS card N. 34-140).

In figure 4.3, SEM images of the samples exposed for 72 h at 600 °C in baths characterized by different basicity are reported. The low basicity samples is characterized by zones where well crystallized La-Fe oxide crystals are visible and zones where a more defective crystalline structure is observable. In the case of the high basicity sample, instead, the surface is homogeneously covered by large and highly definite cubic shaped crystals, corresponding to perovskite crystals.

These results suggest therefore that the different basicity levels considered do not give rise to different reaction mechanisms, but rather that higher basicity promotes the growth of the perovskite phase. Given these first results, it was decided to focus on the high basicity conditions, proceeding to investigate factors related to the

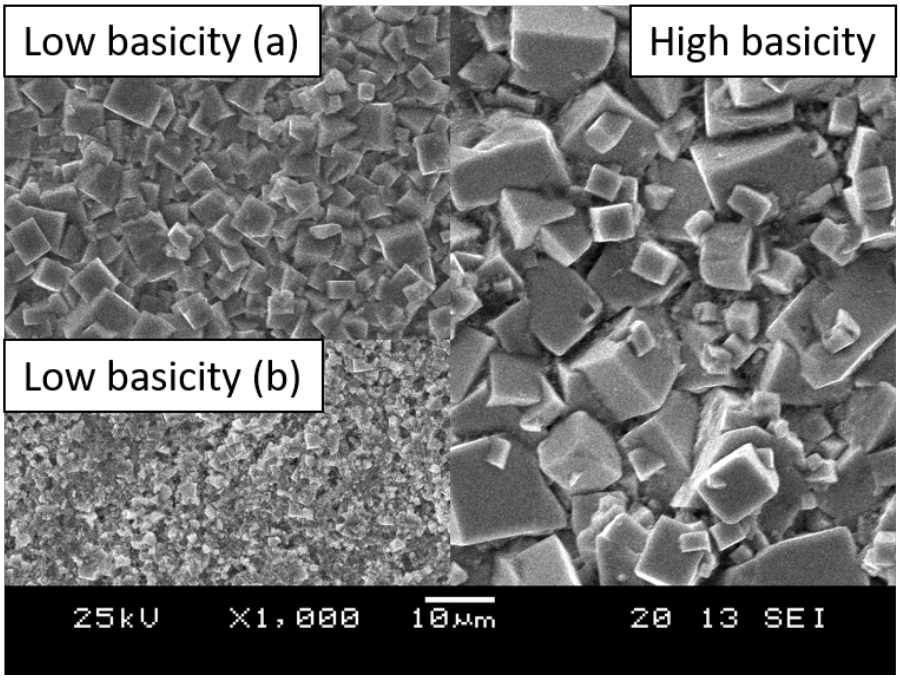



Figure 4.3: SEM images of K41 steel samples subjected to the passivation treatment at 600 °C in new salts characterized by different basicity.

experimental set-up that may induce spurious variability, and have to be identified and controlled to grant reproducibility of results and to identify the variable related to the physico-chemical interactions and processes.

The gas flow was promptly identified as a crucial factor. A $CO_2$ rich (and $O_2$ poor) atmosphere can be useful in fact to mitigate the oxidizing power of the melt, to avoid precipitation of additives or decomposition of the salt. In figure 4.4 are reported results related to the passivation of Crofer 22H in two different gas flowing conditions, namely sparging over the melt and bubbling inside the salt.

It can be observed from the OCP measurement that the sample C, immersed in gas bubbling conditions, reaches rapidly neutral OCP values, indicating a fast surface passivation. On the contrary, samples processed in gas sparging conditions show a slower growth of the OCP, suggesting slower passivation kinetics, that increase after the gas flow is immersed in the melt.

Results of XRD analysis performed on samples processed in the different conditions are reported in figure 4.5. The pattern of sample C is characterized by peaks ascribable to $LaFeO_3$ (JCPDS card N.37-1493), constituting the main phase, and secondary reflection ascribable to the iron rich spinel phases. The sample processed with the gas sparging over the melt, on the contrary, is characterized by lower presence of perovskite phase and higher reflections of spinel phases.

A further processing variable evaluated is the salt ageing. During the passivation,

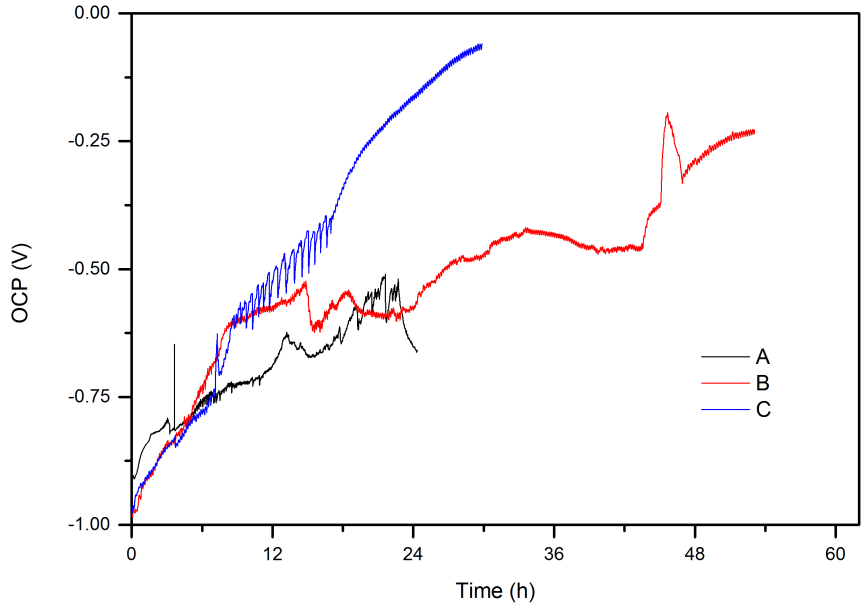



Figure 4.4: OCP curves of Crofer 22H steel samples processed in different gas flow conditions: A) 60 ml/min $CO_2$ flowing over the melt ; B) 60 ml/min $CO_2$ sparging over the melt for the first 24 hours and bubbling in the salt for the rest of the experiment ; C) 60 ml/min $CO_2$ bubbling in the melt.

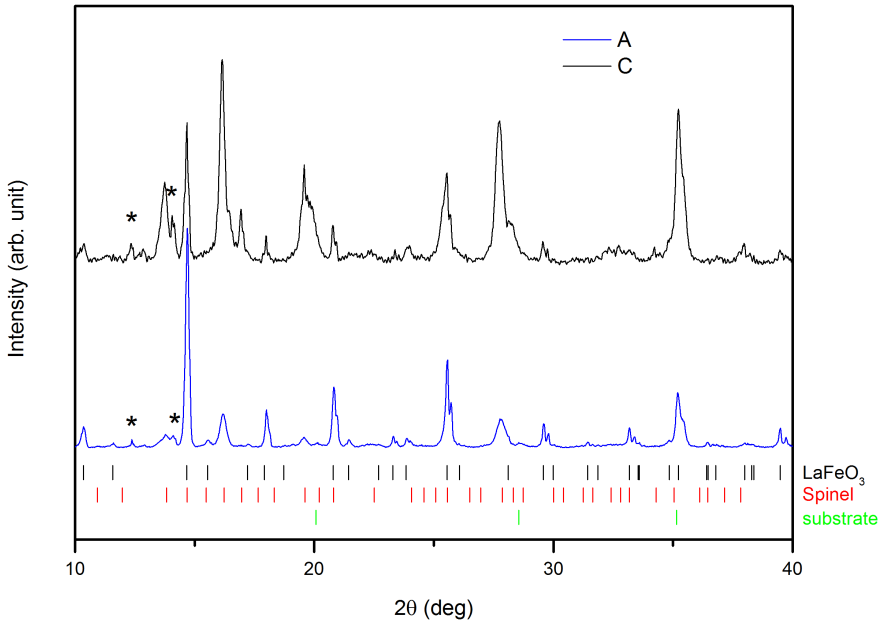



Figure 4.5: X-Ray Diffraction patterns (Mo source) of Crofer 22H steel samples processed in different gas flow conditions: A) 60 ml/min $CO_2$ flowing over the melt ; C) 60 ml/min $CO_2$ bubbling in the melt; (*) indicates reflections ascribable to salt residues.

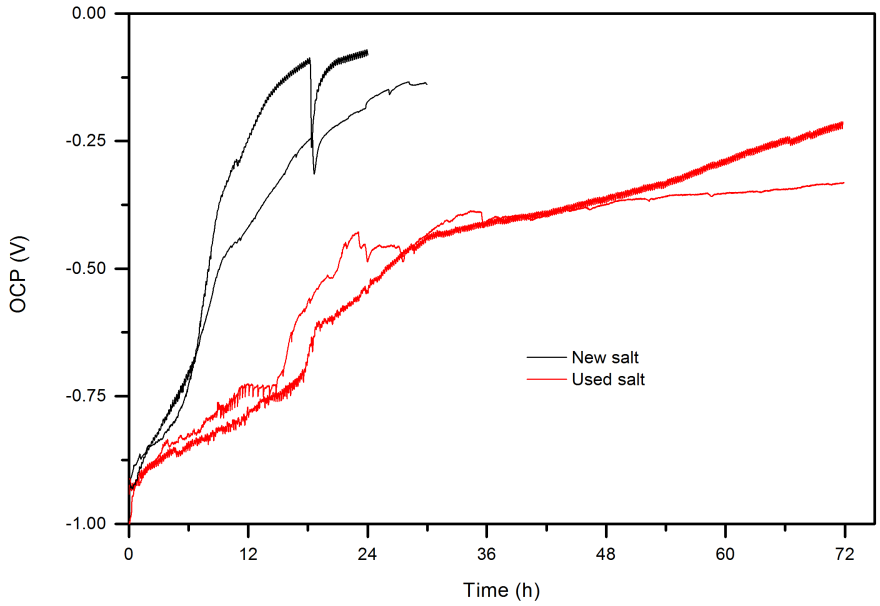



Figure 4.6: OCP curves of K41 steel samples processed in new and used 10Mg salts.

in fact, dissolution of steel elements occurs, with possible evolution of the bath properties. In figure 4.6 the OCP curves related to the processing of K41 samples in different batches of identical salt are reported, to highlight the difference between the first passivation experiment and following tests. It can be observed that the new salt promotes a significantly faster passivation of the steel.

SEM images of samples processed in new and old salts are reported in figure 4.7. In both cases, the sample surface is completely covered by La-Fe oxide crystals of regular cubic shape, that form the perovskite coating layer. A similar morphology is observed in both samples, despite larger grains are present in the used salt sample most likely due to higher growth allowed by the longer process time. The mechanism of passivation does not seems therefore to be altered in the two conditions. After the significant difference in the passivation kinetics observed between the experiments carried out in new and used salts, no significant differences were observed after the first evolution on several repeated experiments. This suggests that after the initial conditioning no profound changes to the bath properties occur with time, and the salt is characterized by high stability in the selected conditions.

To evaluate how temperature influences the passivation phenomena, experiments carried out on Crofer 22H steel samples at 600 °C and 650 °C have been carried out and compared. From the evaluation of the OCP curves reported in figure 4.8 an increase in the passivation kinetic with temperature can be observed.

SEM analysis results of the two samples are reported in figure 4.9, and show no significant difference between the two samples. However, observing the limited

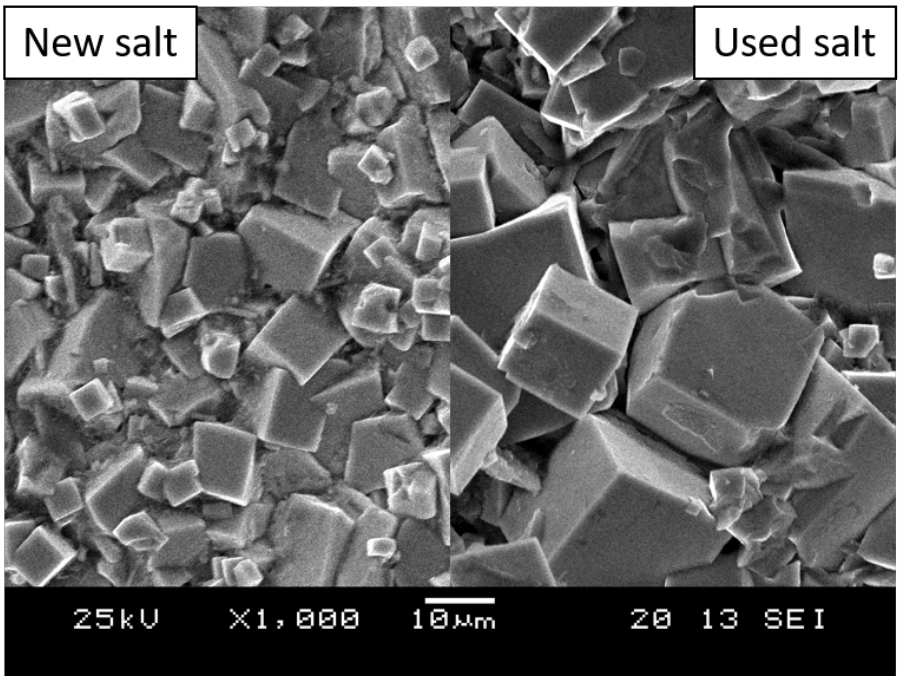



Figure 4.7: SEM images of K41 steel samples processed in new and used 10Mg salts.

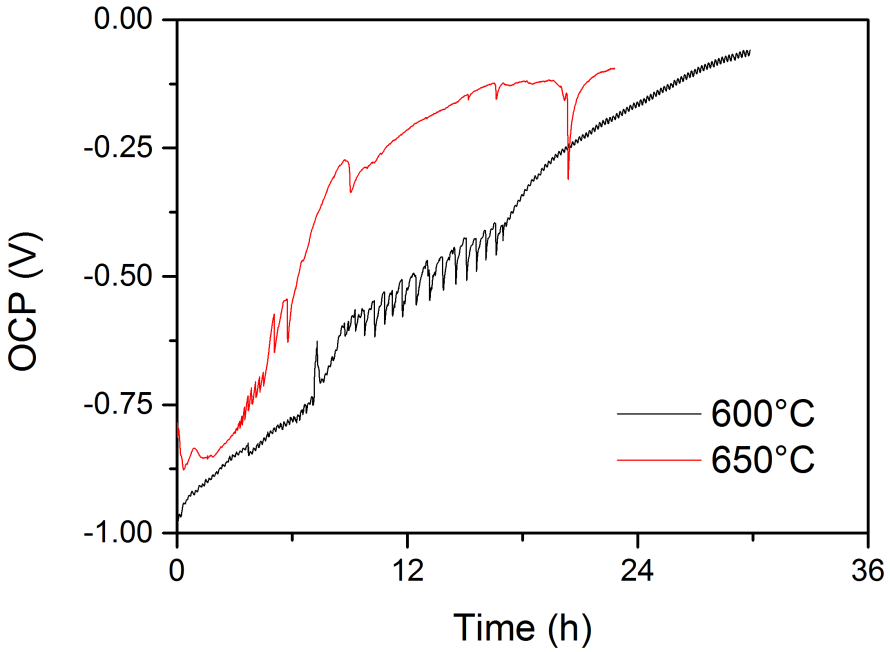



Figure 4.8: OCP curves of Crofer 22H steel samples processed at 600 °C and 650 °C.

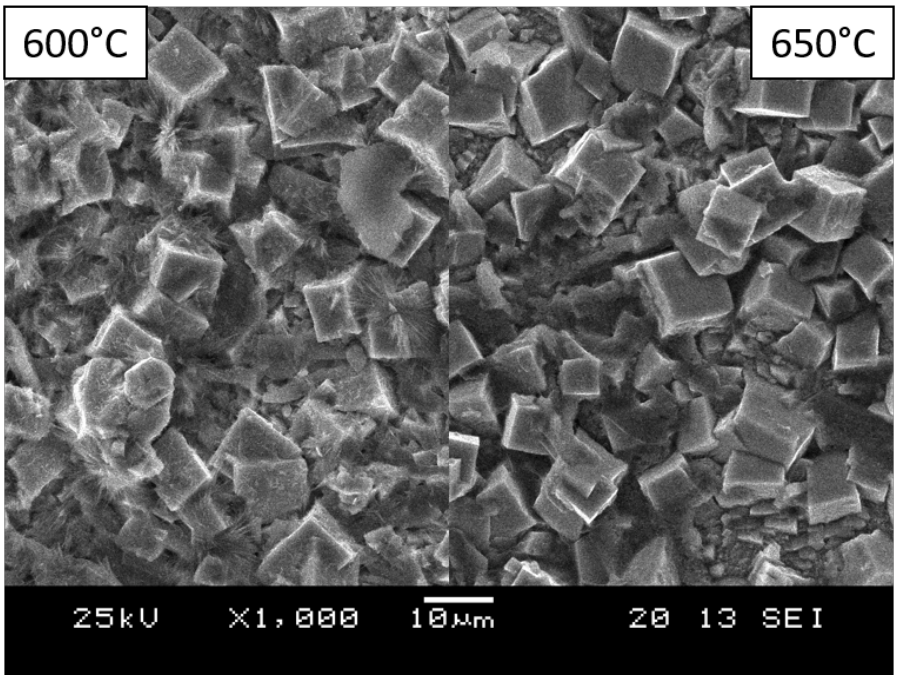



Figure 4.9: SEM images of Crofer 22H steel samples processed at 600 °C and 650 °C.

advantage, to ensure higher stability to the molten salt, avoiding possible decomposition occurring at high temperature, it was decided to limit the processing temperature to 600 °C.

The technique is therefore suitable to produce La-Fe perovskite layers on the surface of high chromium ferritic stainless steels. In view of the application, despite interesting results had been obtained on both Crofer 22H and K41 steels, it was decided to focus on the cheaper K41 steel and further investigate the coating structure and functionality.

In figure 4.10 is reported the XRD pattern of a K41 electrode subjected to the passivation treatment for 72 hours at 600 °C in a used salt. It can be observed the presence of $LaFeO_3$ perovskite as main phase, with low intensity peaks ascribable to a spinel phase.

SEM analysis of the coated sample surface, reported in figure 4.11, shows that the highly packed regular perovskite crystals cover the steel sample.

In figure 4.12 the SEM image of the sample section is depicted, with EDX maps results superimposed. In table 4.1 the EDX point analysis results related to the points indicated in figure 4.12 are reported. From the section it can be observed that the passivated steel possesses a multi-layer structure, with overall thickness between 35÷50 µm. Regarding the coating composition, starting from the steel (point 5), a first Fe-Cr oxide interfacial layer (point 4) approx. 5 µm thick can

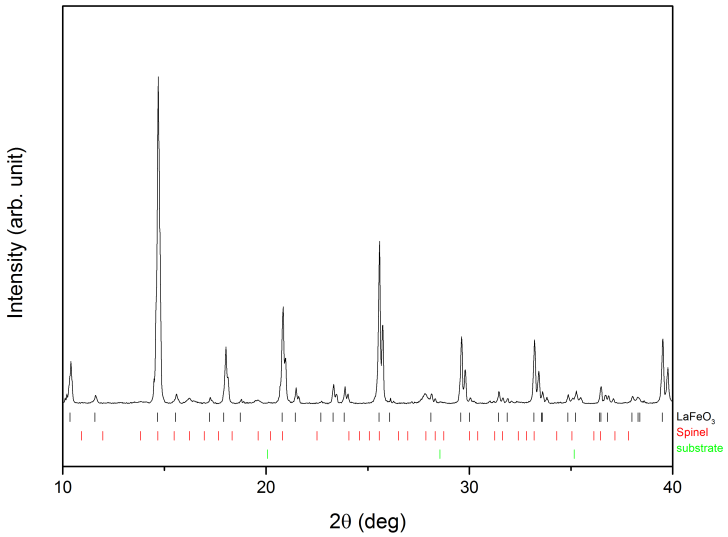



Figure 4.10: X-Ray Diffraction pattern (Mo source) of a K41 steel electrode after 72 hours of exposure in the 10Mg salt at 600 °C.

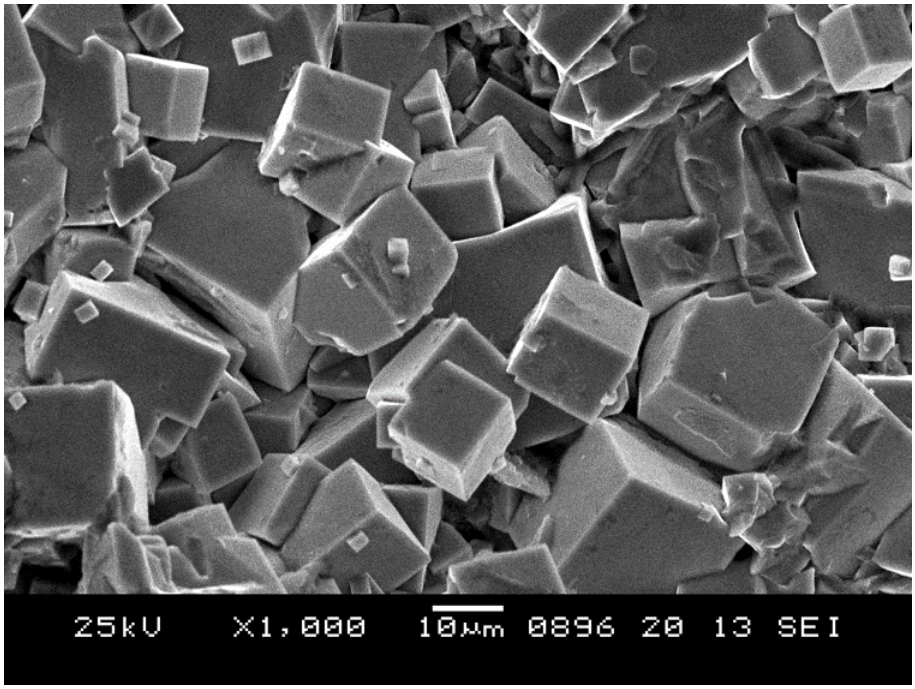



Figure 4.11: SEM images of a K41 steel electrode surface after 72 hours of exposure in the 10Mg salt at 600 °C.

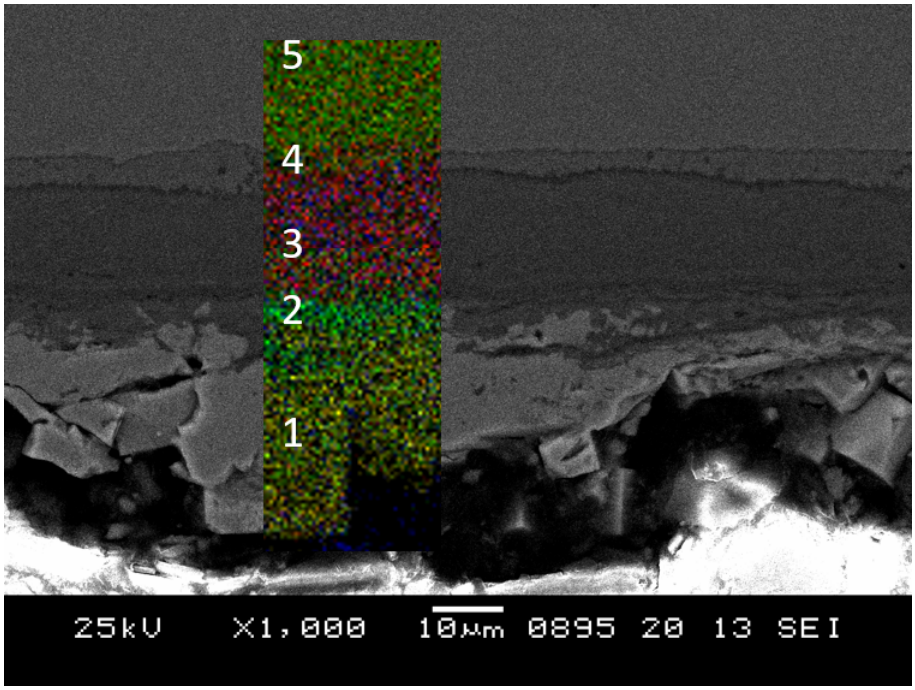



Figure 4.12: SEM image of the section of a K41 steel electrode section after 72 hours of exposure in the 10Mg salt at 600 °C with superimposed EDX map for Fe (green) Cr(red) La (yellow) and O (blue) and positions of EDX point analysis reported in table 4.1.

be observed. Below this interface, a second Fe-Cr oxide layer is formed (point 3), approx. 15µm thick. Furthermore, an iron-rich oxide is evident (point 2), possessing a homogeneous interface with the Fe-Cr oxide and an irregular interface with the perovskite crystals (point 1) evident on the sample surface.

Table 4.1: Results of EDX analysis from points collected in figure 4.12:

| Point | Element (Wt%) | | | |
|---|---|---|---|---|
| | La | Fe | Cr | O |
| 1 | 63.2 | 17.1 | 0.0 | 19.7 |
| 2 | 0.7 | 61.0 | 0.6 | 37.8 |
| 3 | 0.4 | 35.3 | 26.4 | 37.9 |
| 4 | 0.2 | 56.8 | 20.3 | 22.7 |
| 5 | 0.2 | 78.8 | 17.3 | 3.7 |

To produce steel samples suitable for oxidation stability tests, the process was scaled up as reported in chapter 2. The XRD pattern acquired on a K41 sample processed for 48 hours in the molten salt is reported in figure 4.13. Peaks ascribable to the $LaFeO_3$ phase are evident, with the perovskite constituting the main phase. Minor reflections ascribable to Fe-rich spinel phases are visible, as well as peaks ascribable to the substrate. No major differences are evident in comparison with

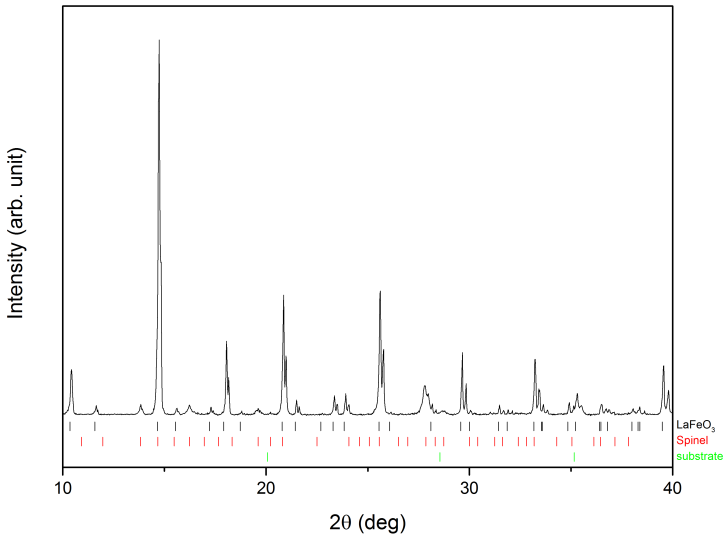



Figure 4.13: XRD pattern (Mo source) of a K41 steel foil processed for 48 hours in the 10Mg molten carbonate salt at 600 °C.

the pattern of the electrode reported in 4.10, suggesting that the process scale up did not affect significantly the passivation mechanism.

SEM images of the K41 foil coated sample are reported in figure 4.14. From the surface analysis it can be observed that the sample is homogeneously coated with tens of micron sized La-Fe perovskite grains, with surface morphology significantly similar to the preliminary experiment electrode reported in figure 4.11.

From the section analysis, reported in figure 4.15, it can be observed as well a similar morphology, with the multi-layer coating structure already observed. EDX results reported in table 4.2 confirm the presence of the perovskite layer as surface coating, and three Fe/Fe-Cr/Fe-Cr oxides sublayers with composition similar to the preliminary experiment sample. With respect to the latter, however, the perovskite layer is thinner, as expected by the decreased exposition time.

Table 4.2: Results of EDX analysis from points collected in figure 4.15:

| Point | Element (Wt%) | | | |
|---|---|---|---|---|
| | La | Fe | Cr | O |
| 1 | 68.3 | 17.5 | | 14.1 |
| 2 | 0.3 | 60.8 | 0.5 | 38.3 |
| 3 | 0.3 | 36.7 | 26.8 | 36.2 |
| 4 | 0.3 | 47.7 | 26.1 | 26.0 |
| 5 | 0.1 | 80.6 | 16.6 | 2.6 |

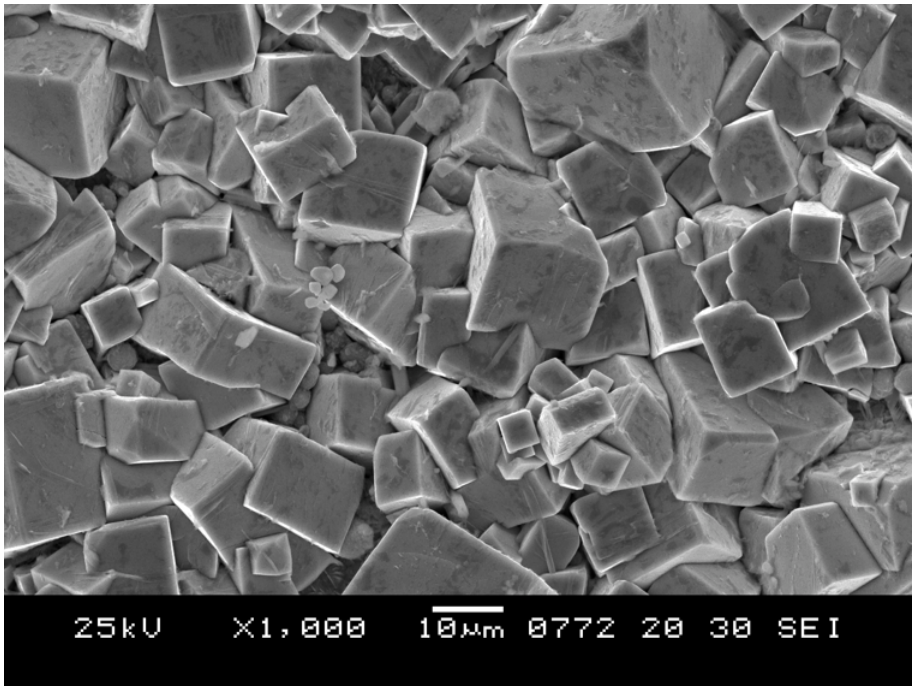



Figure 4.14: SEM images of a K41 steel foil surface after the molten carbonate treatment carried out for 48 hours at 600 °C in the 10Mg salt.

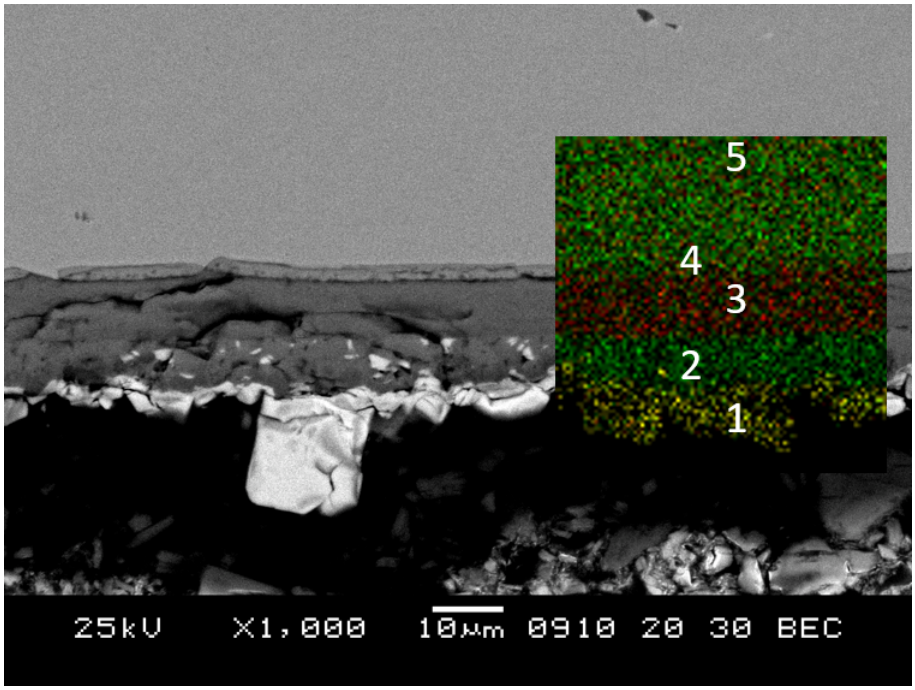



Figure 4.15: SEM image of the section of a K41 steel foil after 48 hours of exposure in the 10Mg salt at 600 °C with superimposed EDX map for Fe (green) Cr(red) La (yellow) and positions of EDX point analysis reported in table 4.2.

### 4.1.1 Considerations on the formation mechanism of thick perovskite coatings

The corrosion potential as a function of time can represent a useful indicator of corrosion layer formation. The corrosion potential is determined by the mixed potential of metal oxidation and reduction of the oxidising agents. Generally, in molten carbonate exposure of stainless steels, the first potential shift is associated with the initial formation of the oxides. Chromium oxides dissolve in the melt as soluble chromates, leaving a layer of iron oxide on the surface, that is lithiated in the lithium carbonate to lithium ferrite. This outer layer separates the inner oxide from the aggressive molten carbonate and prevents the inner oxide from further dissolution reaction.

The presence of lithiated Fe-rich spinel phases suggested by XRD analysis and the dual nature sublayer under the perovskite crystals, with a Fe-rich oxide as first sublayer [lithium is not detected by EDX analysis] as observed by SEM cross section analysis, is compatible with this corrosion mechanism. Regarding the nature of the formed lithiated oxide, $LiFeO_2$ is generally reported as corrosion product in common molten carbonates. Formation of $LiFe_5O_8$ spinel phases has been reported to occur however for austenitic stainless steels in $CO_2$ rich Li/Na carbonates below 600 °C [101], conditions matching quite well the ones used in this work. It is therefore likely to suppose that a similar behaviour is maintained for ferritic stainless steel.

In the experiments here reported, a recurring tendency observed in most samples is the slope change of the OCP curves occurring at approx. -0.7 V, suggesting the occurrence of transition between two evolution mechanisms. Among the possible electrochemical equilibria of Fe-species in molten carbonates, lithiation and oxidation of magnetite reported in equation (4.1) is characterized by a standard potential $E^0$ = -0.67 V

$$4Fe_3O_4 + 0.5Li_2O + O_2 \rightleftharpoons 2.4LiFe_5O_8 \tag{4.1}$$

It may therefore be supposed that in the adopted experimental conditions oxidation of the surface to a Fe-Cr spinel phase occurs in the first hours, followed by dissolution of Cr and leaving an iron rich spinel phase on the surface. Lithiation of the Fe oxide and therefore oxidation of $Fe^{2+}$ to $Fe^{3+}$ could therefore proceed as reported in equation (4.1). This process could be considered finished when the transition observable in the OCP curves occurs. The surface would be then rich in $Fe^{3+}$ ions, required for the reaction with lanthanum ions to form the perovskite oxide, with the dissolution-precipitation mechanism reported in [76]. The ennoblement of

the surface suggested by the OCP growth towards neutral values is therefore the effect of a mixed potential, with the perovskite presence driving the potential towards neutral values. However, as evident in the K41 electrodes processed for 72 h in the 10Mg salt, even with the complete coverage of the surface with perovskite crystals a neutral OCP is not obtained. It is likely to suppose therefore that the sublayer has an influence in the OCP response of the steel in the molten carbonate salt, not limited to the perovskite phase contribution.

Considering the above mentioned corrosion/passivation mechanism, the differences observed between the K41 and the Crofer 22H samples are expected. In particular, the faster passivation kinetic for the 22Cr steel may be ascribed to the faster formation of a complete $Fe^{3+}$ surface due to the different chemical composition of the steel. Furthermore, Crofer 22H electrodes tend to higher OCP values than the K41 samples, suggesting therefore higher effectiveness of the perovskite-spinel coating in the molten carbonate environment.

The difference in passivation kinetic observable between samples exposed in new and used salts may be ascribable to multiple phenomena, such as the dissolution of chromates in the melt, leading to the saturation of the salt with chromate species and therefore to the deceleration of chromium dissolution for the sequent samples, or to the precipitation of suspended additives induced by an external perturbation (the sample introduction). The formation of precipitates, and the existence of solute/precipitate equilibria with the subsequent diffusion kinetics from the bottom of the alumina crucible is suggested by the thickness difference observable between the electrode and the foil processed in the 10Mg salt, exposed respectively in the small and in the scaled-up experimental setup. It is in fact unlikely to ascribe the significant differences in the scale thickness ($\sim$2X) just to the increase in exposure time, suggesting that the electrode was subjected to an environment characterized by higher oxidizing power. This would be compatible with a precipitate rich in oxidizing species (i.e. La, Mg oxides): upon consumption of the reacting species on the sample surface, diffusion of reactants from the bottom of the crucible towards the steel would be in fact easier in the small crucible due to the shorter diffusion pathway.

A further interesting element that can be evaluated from the comparison between the electrode and the foil, is the difference in the depth of the perovskite layer: in the 48 h exposed sample, the perovskite layer is constituted by the coalescence of large crystals grown almost epitaxially on the thick Fe-rich oxide (figure 4.15). After 72 h of treatment, the perovskite crystals extend almost to the interface between the Fe-Cr oxide and the Fe-rich oxide figure (4.12). This suggests that after the complete coverage of the surface by perovskite crystals, lanthanum ions diffuse towards the

bulk - most likely at grain boundaries - and react with the internal iron oxide, with an inward growth mechanism of the already formed perovskite grains.

## 4.2 Thin coatings

The salt composition can be modified, through the addition of further additives, to promote the perovskite formation through a template conversion mechanism of the precursor layer. With this approach, thinner coatings are formed with faster passivation times with respect to the nucleation and growth mechanism [8].

The OCP curves of K41 electrodes exposed in different salts formulated to produce a thin coating are reported in figure 4.16 in comparison with the thick 10Mg formulation. It is clearly observable how the passivation kinetic is significantly increased with the additive addition. Both the 10Mg0.10X and 10Mg0.25X curves are in fact characterized by a steep growth from the initial exposure time, with neutral values obtained already after 8 hours and a plateau for exposure time superior to 12 hours for the 10Mg0.25X formulation, with the 10Mg0.10X curve reaching neutral values after 24 h.

To evaluate how salt basicity and temperature influenced the passivation process in presence of the additive, experiments were carried out on a medium basicity salt (6Mg0.25X) evaluating Crofer22H steel samples behaviour at different temperatures. The OCP curves are reported in figure 4.17 in comparison with a curve related to a 10Mg0.25X formulation at 575 °C. It can be observed how fast passivation kinetics are retained in these conditions down to 560 °C. The curve acquired at 550 °C is characterized by the slower growth, suggesting an inhibited passivation kinetic in this condition. The comparison between the 575 °C curves shows that also in the presence of the additive X the passivation kinetic is increased at higher melt basicity.

In figure 4.18 are reported the XRD patterns of K41, SSHT and Crofer 22H samples exposed for 48 hours in salts tailored to promote the formation of thin coatings. In all cases, peaks ascribable to a $LaFeO_3$ perovskite phase are evident, confirming the occurred growth of the perovskite layer. Reflections ascribable to the substrate are clearly observable in all cases, suggesting limited thickness of the coating. Regarding the K41 steel, in all cases the patterns highlight the presence of a Fe-rich spinel phase. Furthermore, haematite reflections are visible in the higher temperature (600 °C) patterns. Comparing the 10Mg0.10X 550 and 600 °C spectra, it can be observed that the temperature increase promotes perovskite and haematite growth. Comparing the patterns acquired on the 10Mg0.10X 600 °C and 10Mg0.25X 600 °C samples it can be observed how the higher additive content promotes the

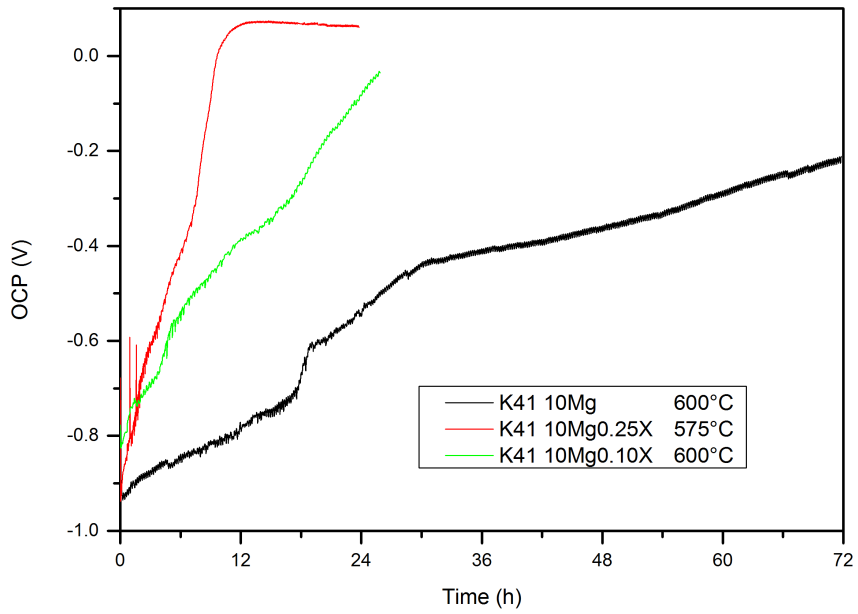



Figure 4.16: OCP curves of K41 steels processed at 600 °C in different salt formulations.

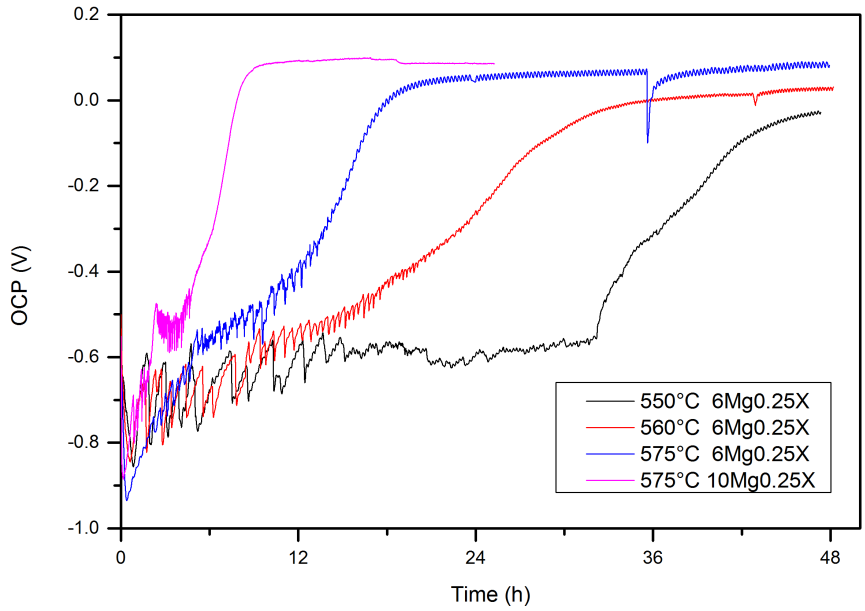



Figure 4.17: OCP curves acquired during the exposure of Crofer 22H samples in thin formulation salt characterized by medium basicity (salt D) at different temperatures in comparison with the high basicity salt C.

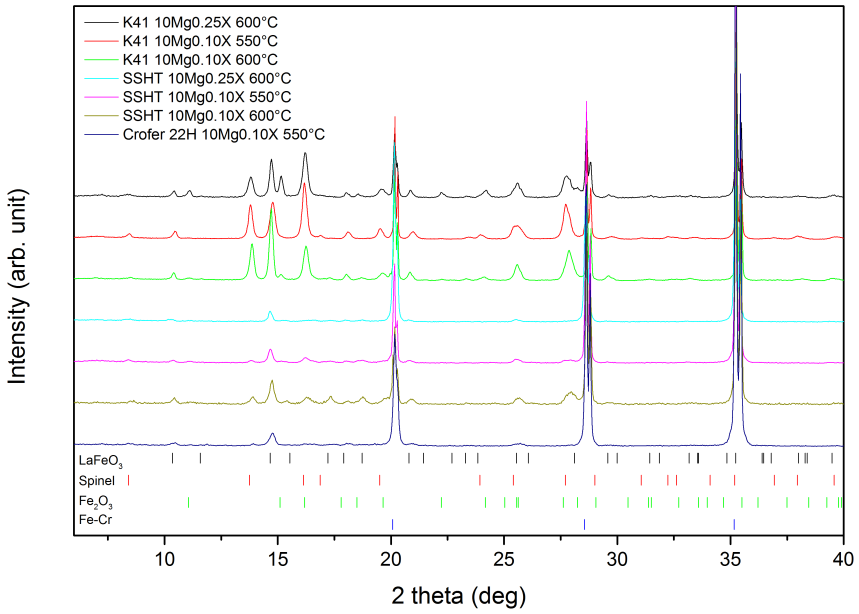



Figure 4.18: X-Ray Diffraction patterns (Mo surce) of the steel samples exposed in different conditions for 48 hours

haematite and spinel growth at the expense of the perovskite phase. Observing the SSHT patterns related to samples processed in the 10Mg0.10X salt at 550 °C and 600 °C it can be observed how also in this case higher temperature enhances oxide formation. However, differently with respect to the K41 sample, the pattern related to the SSHT steel sample exposed in the 10Mg0.25X salt shows the perovskite phase as main oxide phase, suggesting that limited oxidation of the steel occurs in these conditions. In the case of the reported Crofer 22H pattern, the perovskite represents the only oxide phase. Comparing the three different steels processed in identical conditions (10Mg0.25X-600 °C), it can be observed how oxide growth is clearly more pronounced in the K41 steel, the cheapest steel, and almost completely inhibited on the Crofer 22H sample, specifically designed to withstand highly oxidizing SOFC conditions and exhibiting excellent oxidation resistance properties in the used molten carbonate baths as well.

The SEM images of the three steels after 48 hours of treatment are reported in figure 4.19.

Starting from the K41 sample processed in the 10Mg0.10X salt at 600°C, the surface is characterized by the presence of a smooth oxide layer. The high magnification image (figure 4.19b) shows that the smooth layer is composed of small and well-defined crystals. Lowering the temperature, in the sample processed at 550 °C, the oxide layer is smoother, with the absence of a visible crystalline structure, with some iron-rich oxide globular particles visible on the oxide layer. The

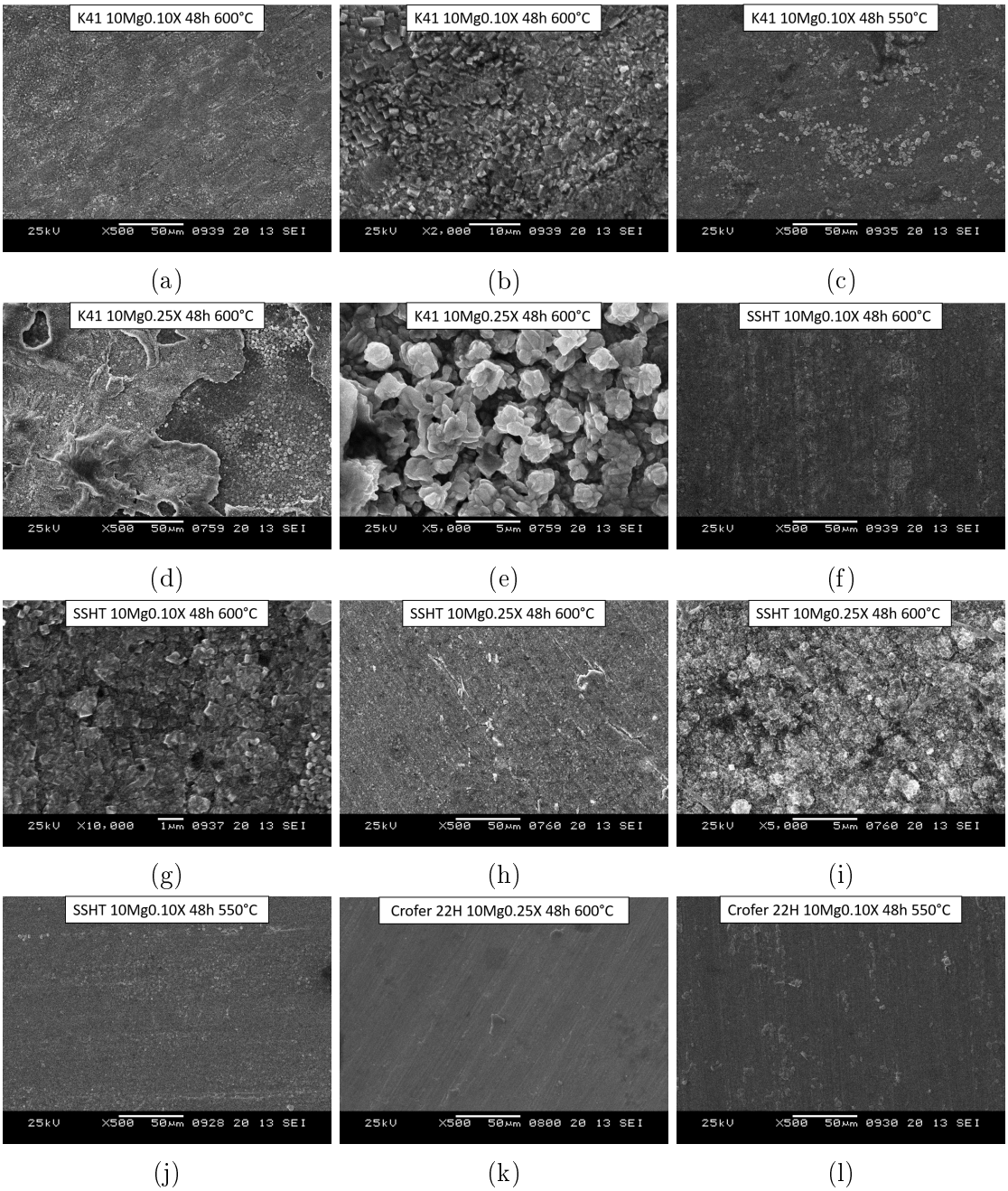



Figure 4.19: SEM images of different foil samples passivated in different conditions.

sample processed in the 10Mg0.25X salt at 600 °C is instead characterized by the presence of large and irregular oxide scales and globular aggregates of oxide particles, highlighted in figure 4.19e, suggesting that the high temperature and additive concentration led to an undesired overgrowth of the oxide layer.

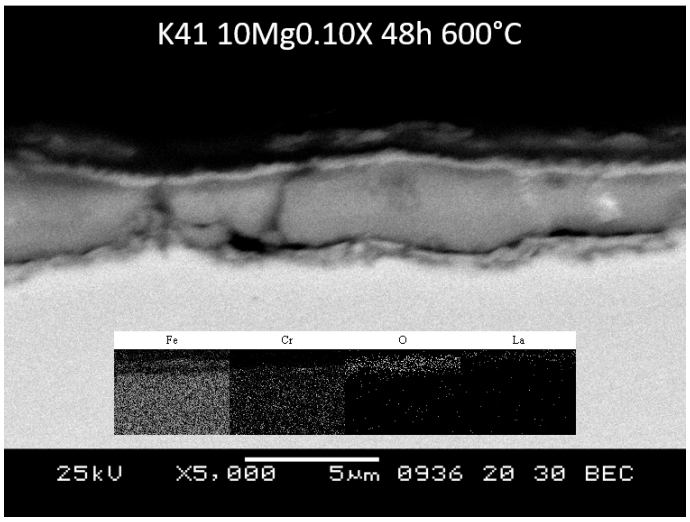
Regarding the SSHT steel, all the samples are characterized by a smooth oxide surface layer. The high magnification images show the presence of well defined crystals in the samples processed at 600 °C, with minor differences observable between the two salt compositions. Similarly to the K41, the sample processed in the 10Mg0.10X salt at 550 °C exhibits a smooth surface oxide layer with no evident crystalline structure.

Regarding Crofer 22H, the SEM analysis shows the presence of a smooth oxide layer, with parallel marks ascribable to the steel surface finish, highlighting the thin nature of the passivation layer. As for the SSHT sample, no significant changes in morphology are evident between the sample exposed in the 10Mg0.25X salt at 600 °C and in the 10Mg0.10X salt at 550 °C, that correspond to the extreme conditions of the experimental design investigated in this work, confirming the high stability of the Crofer 22H steel in the used molten salts: the passivation layer formed on the Crofer 22H in presence of the additive is in fact independent on the bath conditions inside the explored experimental domain.

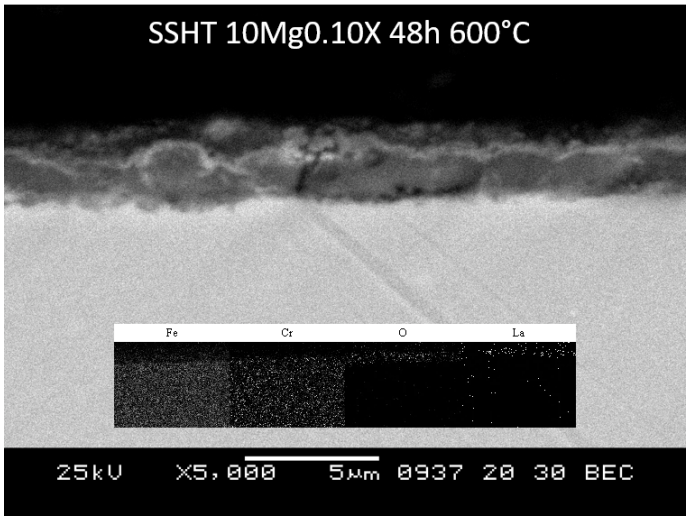
To further investigate the different passivation behaviours between the steels, sections of selected samples were prepared and analysed by SEM. In figure 4.20 the micrographs and corresponding EDX maps for K41 passivated in 10Mg0.10X salt at 600 °C and SSHT passivated in 10Mg0.10X and 10Mg0.25X salts at 600 °C are reported.

The K41 image shows an oxide scale on the sample surface of approx. 3 μm thickness. The EDX map shows that the scale is consituted by a chromium-iron oxide at the steel interface, and an iron-rich oxide towards the surface. Lanthanum seems confined at the coating surface, and combining the EDX data with the backscattered electron SEM image and XRD data is likely to identify the clear thin layer as the perovskite phase, with an iron-rich oxide, corresponding to the haematite, and an iron-chromium oxide, corresponding to the spinel phase, as sublayers. The section of the SSHT steel passivated in the identical conditions shows similar features, with a thinner oxide layer. In both cases the perovskite thickness is limited to less than a micron, with a considerable difference with the thick coatings reported in section 4.1. Raising the additive concentration, the thickness of the oxide sublayer is drastically reduced, and in the 10Mg0.25X processed sample a sub-micrometric oxide layer is formed.

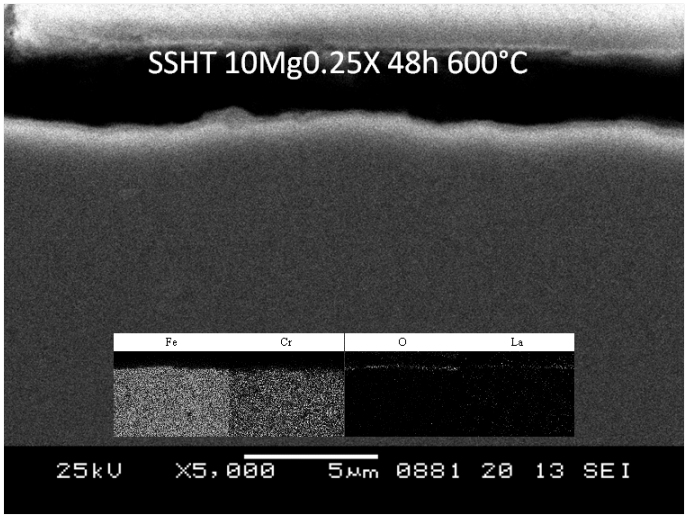
These preliminary experiments showed therefore that the bath can be tailored to




(a)




(b)




(c)

Figure 4.20: SEM images of K41 and SSHT steel samples section after a passivation treatment carried out for 48 hours at 600 °C and corresponding EDX maps for Fe, Cr, O and La.

promote the growth of thin coating layers through a template conversion mechanism also in the case of high chromium ferritic steels. The passivation kinetic is enhanced by additive concentration, temperature, and salt basicity. Higher temperature promotes as well the structuration of crystalline perovskite structures and enhances haematite formation.

Regarding the effect of the alloy, no significant differences are observed on the perovskite, limited for all the steels to thin sub micrometric layers. The cheap and less noble K41 shows instead the tendency to form thicker oxide sublayers. Furthermore, with high additive additions at high temperature (e.g. 10Mg0.25X at 600°C), the K41 samples show an overgrowth of the oxide scale, not observed in the case of the noble SSHT and Crofer 22H steels, that are characterized in the same conditions by sub micrometric passivation layers.

Further studies and evaluation of the coating structure of high chromium steels were focused on the K41 alloys, to produce coated foils for oxidation experiments. Similarly as for thick coatings reported in section 4.1, K41 was chosen due to its lower cost and readier availability for mass production with respect to the higher chromium steels. Regarding the experimental conditions, the 10Mg0.25X salt was selected, due to the faster passivation kinetics, carrying out the coating process at 600 °C and limiting the exposure time to avoid the overgrowth of the oxide scale.

In figure 4.21 the XRD pattern of a K41 foil sample subjected to the passivation treatment in the the 10Mg0.25X salt at 600 °C for 8 hours is reported. Apart from the substrate reflections, peaks ascribable to $LaFeO_3$ perovskite, a Fe-rich spinel and haematite can be observed. Differently from the 48 hours exposed sample perovskite constitutes the main oxide phase, and the high intensity of the substrate reflections suggest that a limited growth of the surface layer occurred.

The surface morphology of the K41 sample is reported in figure 4.22. After the passivation treatment, the steel is coated by a homogeneous oxide layer, with the presence of small globular particles apparently well adherent to the sublayer. The decrease of the processing time is therefore effective to limit the oxide overgrowth observed on the 48 hours samples, and furthermore represents a technological advantage.

In figure 4.23 results of the section SEM analysis are reported. The image shows the presence of an approx. 2 μm thick oxide layer on the steel surface. EDX maps show that chromium is confined on the internal section, while lanthanum presence is more evident on the surface. EDX spot analysis results, reported in table 4.3, show a decreasing trend of lanthanum concentration with depth, and an increase in chromium content. Comparing this results with the reported backscattered electron SEM image and the data from the EDX map analysis, similarly as observed for the

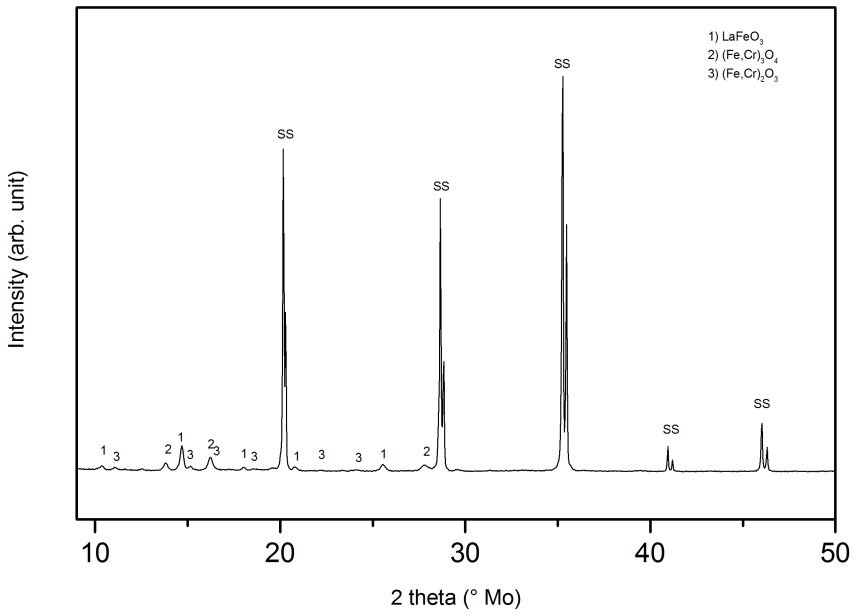



Figure 4.21: XRD pattern (Mo source) of a K41 steel foil after 8 hours of exposure in the 10Mg0.25X salt at 600 °C.

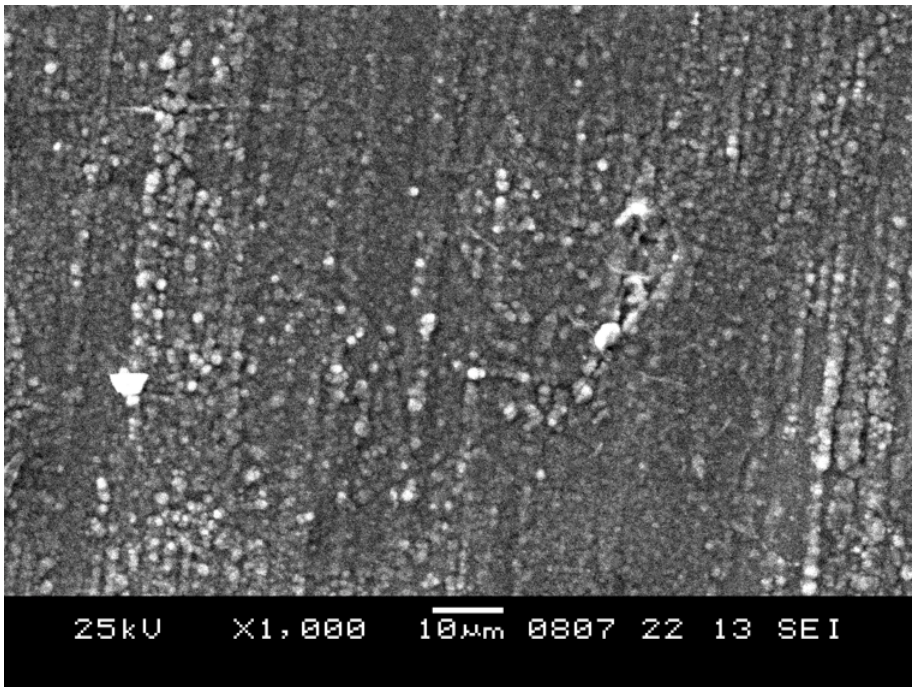



Figure 4.22: SEM image of the surface of a K41 steel foil after 8 hours of exposure in the 10Mg0.25X salt at 600 °C.

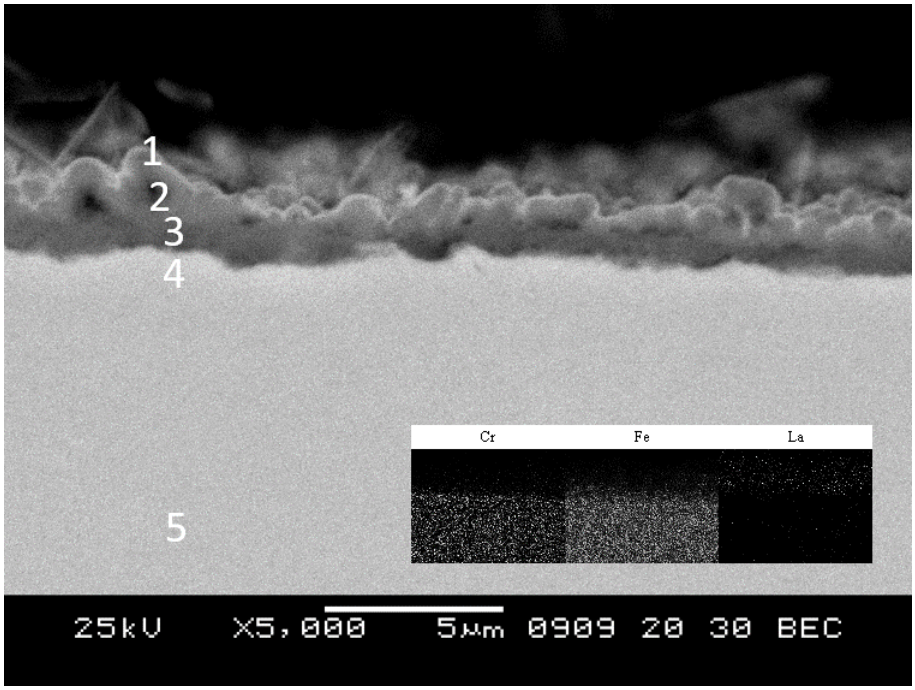



Figure 4.23: SEM image of the section of a K41 steel foil after 8 hours of exposure in the 10Mg0.25X salt at 600 °C, EDX maps for Cr, Fe and La and EDX spots (see table 4.3).

micrographies reported in figure 4.20, it is likely to ascribe the perovskite presence to the thin and homogeneous clear layer visible in the SEM image, grown on iron-rich oxide particles supported on a Fe-Cr spinel interface layer.

Table 4.3: Results of EDX analysis from points collected in figure 4.23:

| Point | Element (Wt%) | | | |
|---|---|---|---|---|
| | La | Fe | Cr | O |
| 1 | 16.6 | 28.1 | 2.3 | 53 |
| 2 | 5.9 | 39.2 | 3.9 | 50.9 |
| 3 | 1.2 | 44.8 | 9.1 | 44.9 |
| 4 | | 50.2 | 16.4 | 33.3 |
| 5 | | 80.3 | 16.8 | 2.9 |

In addition to the high chromium stainless steels, SS405 samples have been processed to obtain fully coated samples for oxidation experiments, as reported in chapter 2. The SS405 steel may represent a low cost alternative to high chromium alloys, and furthermore constitutes an opportune benchmark for the coating behaviour due to its low corrosion resistance in typical SOFC environments [129]. In figure 4.24 the XRD pattern of a SS405 steel sample passivated for 48 h at 600 °C in the 10Mg0.25X salt in reported. The pattern is ascribable to a mixture of $LaFeO_3$

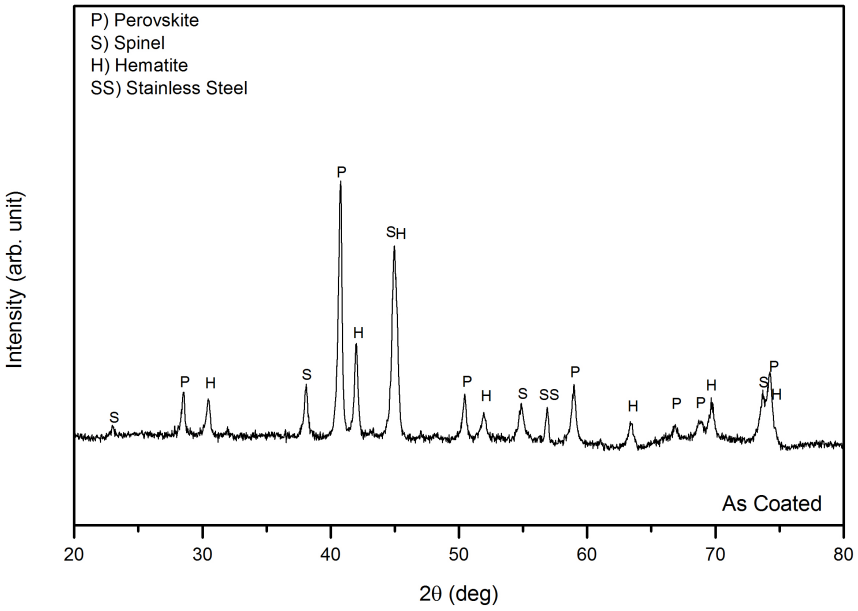



Figure 4.24: X-Ray Diffraction patterns (Fe surce) of SS405 steel samples passivated for 48 h in

perovskite phase, Fe-rich spinel phase and iron oxide ($Fe_2O_3$).

Results of SEM analysis are reported in figure 4.25. It appears that the conversion coating process resulted in the formation of a microcrystalline structure with high uniformity and total layer continuity (4.25a). The higher magnification image (4.25b) provides further details on the coating microstructure. The conversion coating consists of a continuous layered structure (zone A in 4.25b) and of three-dimensional islands formed of coating particles merging into crystallite agglomerates on the top (zone B in 4.25b).

The continuity of the obtained coating is also evident from the SEM cross-section image of 4.25c. A continuous, dense and adherent coating structure characterized by thickness lower than 5 μm and virtual absence of a corrosion scale beneath the coating layer is clearly observable. 4.25d shows a cross-section image of a coating region covered with a particle agglomerate, where, similarly to 4.25b, zone A corresponds to the inner perovskite layer and the zone B consists of micrometre-sized discrete particle agglomerates. Presence of La and Fe elements is found across the coating, suggesting that $LaFeO_3$ perovskite is the main constituent of the particle agglomerate surface and of the underlying layered coating regions.

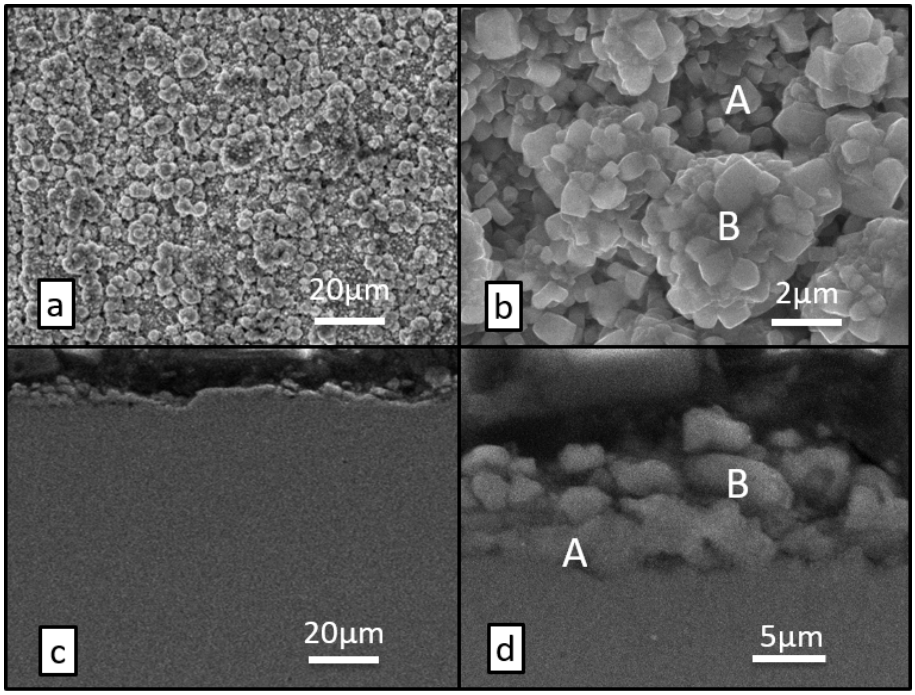



Figure 4.25: SEM image of surface (a and b) and section (c and d) at different magnification of the 13Cr steel after the molten carbonate coating treatment.

### 4.2.1 Considerations on the formation mechanism of thin perovskite coatings

The growth of the perovskite coating through the previously reported template conversion mechanism [8] occurs through the substitution of lithium ions in an opportune template oxide by lanthanum ions. This results in the formation of thin coatings, and obviously requires the formation and presence of the template layer. Lithiated iron oxides, in particular rock-salt structured compounds (i.e. $LiFeO_2$), are known to act as suitable templates, forming the perovskite oxides through metathesis reactions [130]. The experiments conducted in the 10Mg0.10X, 10Mg0.25X and 6Mg0.25X suggest that in all of these melts the right compromise between oxidizing power and basicity to promote the formation of the template layer is obtained.

The "classical" molten carbonate corrosion mechanism of ferritic stainless steels is composed of oxide formation, chromium dissolution in the outer layer and subsequent formation of lithiated iron oxides. The occurrence of such process in the reaction melts is suggested by the structure observed on SS405 and K41 steels, suggesting that oxidation phenomena occur to a greater extent in the less noble steels (i.e. SS405, K41) before the formation of a passive layer. As a further element, structural and morphological analysis of the less noble alloys show that just a thin layer of the iron oxide is lithiated and converted to the perovskite, as suggested by the

presence of both a Fe-Cr spinel and the unlithiated haematite phases in the K41 and SS405 steel sublayers. The absence of secondary phases, other than the perovskite, observed for the Crofer 22H passivated samples and, in selected circumstances, for the SSHT steel suggest instead that on these alloys a significantly thinner corrosion layer is formed, lithiated and converted to the perovskite.

Evaluating these evidences, it is also likely to suppose that the precursor formation constitutes the kinetically limiting step in the coating formation process. A thin perovskite layer could be in fact formed also in the case of a fast lithiation step coupled to a slow perovskite formation reaction. However, upon the hypothesis of a slow iron oxide lithiation and a fast conversion to perovskite, then presence of hematite could be easier to explain. Fast conversion of a slow-forming lithiated iron to perovskite could in fact lead to a stop in the lithiation process - due to the presence of the protective perovskite - leaving the thin perovskite layer structure on the haematite phase, as observed by cross-sectional SEM analyses. This hypothesis is in agreement with the occurrence of metathesis reactions, assumed to take place in the examined case [8], commonly promoted by large reactions enthalpies and characterized by fast kinetics [131, 132] .

## 4.3 Economic evaluation of the passivation method

Conversion coatings appear as promising strategies to passivate stainless steels at low manufacturing costs. Well-established industrial practices exist for conversion treatments applied to low corrosion-resistant substrates (i.e., Al, Mg alloys, carbon and low-alloyed steels). Surface conversion methods are usually identified by industry as an inexpensive treatment, requiring minimal surface preparation or consolidation post treatments. Large capital investments can also be avoided as these passivation treatments are prevalently realised through simple one-pot, one-step processes.

The economic evaluation reported in this section does not claim to be exhaustive for all the possible expenses, but rather to give a rough estimate evaluating material and energy requirements, without assessing capital and labor costs. Obtaining high running costs on this first evaluation, with SECA DOE target for the coating deposition process well below 10$/interconnect, would clearly raise doubts about further development of the technique.

Some assumptions were carried out for the evaluation of the process cost:

- The interconnect production process (usually consisting in several forming, cutting and soldering steps) should allow to coat the desired parts before the final assembly, therefore not requiring the application of masks during the

molten carbonate process;

- Direct scale up of the energy and $CO_2$ consumption observed in the large lab-scale experiments was carried out to evaluate the related costs. It is likely to hypothesize that this assumption gives rise to an overestimation of the consumed energy and gas with respect to purposely designed furnace systems;
- During large lab-scale experiments, successful depositions have been carried out on the same salt batch for up to approx. 1 month of operation. The salt bath lifespan is therefore estimated in 30 days. This assumption as well should represents a highly conservative approximation, due to the notably high stability of molten carbonates [128];
- With maximum $\sim$0.4 $m^2_{steel}/kg_{salt}$ of foils (double sided) processed simultaneously in the large-scale experiments, the cost of the salt was calculated considering an amount of 50 kg for every square metre of steel;
- 48 and 8 h were considered as processing time for respectively thick and thin coatings, allowing respectively 15 and 90 sets of samples to be processed in each salt batch during its lifetime;
- An average perovskite thickness of 5µm and 0.5µm, respectively for thick and thin coatings, was considered to assess the lanthanum amount consumed during the conversion process;
- The price of the chemicals taken as reference for the estimate of the salt cost is reported in table 4.4.

Table 4.4: Summary of prices for analytical grade chemicals to be used for the molten bath (Alfa Aesar):

| compound | price (€/kg) |
|---|---|
| $Na_2CO_3$ | 15 |
| $Li_2CO_3$ | 45 |
| MgO | 170 |
| $La_2O_3$ | 350 |
| total | 47 |

The summary of the running costs related to the molten carbonate conversion process is reported in table 4.5. The result shows that the passivation method may be characterized by appealing costs, in particular in the case of thin coatings. The differences between the two coating morphologies is mainly due to the different

processing time, allowing to passivate a lesser number of pieces during the foreseen salt life. Among the different cost items, large part of the cost would be ascribable to the salt ($\sim$ 75%). Longer exploitation of the salt and use of cheaper technical grade chemicals could therefore lead to a significant reduction in the process cost.

Table 4.5: Summary of materials and energy cost for the molten carbonate conversion coating process:

| | thick coating | thin coating |
|---|---|---|
| energy (€/m$^2$) | 42 | 7 |
| $CO_2$ (€/m$^2$) | 3.6 | 0.6 |
| salt* (€/m$^2$) | 156 | 26 |
| Lanthanum (€/m$^2$) | 8 | 0.8 |
| tot (€/m$^2$) | 208 | 34 |
| cost per interconnect coating** (€) | 2.08 | 0.34 |

*=$\frac{amount[\mathrm{kg/m^2}] \cdot price[€/\mathrm{kg}]}{lifespan[days] \cdot samples[\#/days]}$

**=10X10cm area

The values here reported are therefore promising, as comparable or relatively cheap with respect to common strategies adopted for deposition of spinel or perovskite coatings [133–135], suggesting the economical validity of the chosen approach and justifying to further develop the technique.

# Chapter 5

# Metal decorated perovskite composite coatings

Taking advantage of the reported high solubility of certain metal oxides in basic molten carbonates, as introduced in section 1.4, it is likely to suppose that is possible the tailoring of the reaction media to exploit opportune galvanic couples in the molten carbonate process. This could result in an enhancement of the sublayer oxidation phenomena due to the galvanic corrosion reactions (i.e. introducing a metal nobler than iron) and a simultaneous coating functionalization by the correspondent metal reduction. The production of two-phase composites may represent a suitable approach to tune the coating properties (see section 1.4).

This strategy has been here evaluated considering three different metals in the production of thick perovskite coatings: copper, nickel and silver. As reported in table 1.3, the elements were chosen as representing three different electrochemical conditions: nickel, slightly nobler with respect to iron; copper, with an electrochemical potential considerably higher than iron but not reaching neutrality with respect to the $CO_2/O_2$/Au electrode; silver, possessing a positive highly oxidizing electrochemical potential.

## 5.1 Copper-dispersed composite

In Figure 5.1 the OCP curves measured for K41 steel electrodes in 3Mg2Cu and 3Mg4Cu salts are reported in comparison with a curve acquired in the 3Mg salt. For all the curves some similarities can be observed: an initial slow potential increase is followed by a sharp growth starting approximately at the OCP value of -0.7V. An enhancement of the passivation kinetics can be observed with the increase of copper content, with the curves related to 3Mg2Cu and 3Mg4Cu characterized by faster

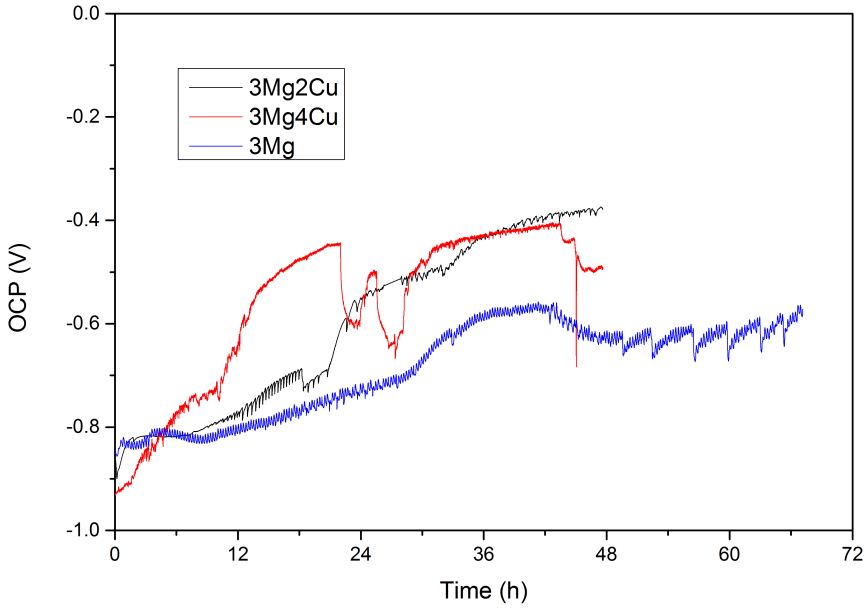



Figure 5.1: OCP curves of K41 steel samples electrode processed at 600 °C in salts characterized by different Cu content.

transition onsets, respectively after 20 h and 12 h, with final OCP values of approx. -0.4V after 48 h.

For both the Cu-added salts, the final OCP value is compatible with the presence on the sample surface of metallic Cu. The copper oxide reduction reaction, reported in table 1.3, is in fact characterized by a standard potential versus the oxygen electrode $E^0 = -0.4$V.

In figure 5.2 the XRD patterns of electrode samples processed in the different salts and for different times are reported. The samples exhibit similar features to the samples passivated in the undoped salt reported in section 4.1. Perovskite constitutes the main phase, with secondary peaks ascribable to the presence of Fe-rich spinels. However, peaks ascribable to the presence to metallic copper (Cu - JCPDS card N. 4-836) are evident. It is noteworthy to observe that copper is evident only as metal phase, with no trace of copper oxides observable in the XRD patterns. This suggests the occurrence of galvanic coupling reactions involving copper oxide reduction on the electrode surface, most likely coupled to iron oxidation from the oxide sublayer. A difference in copper signal intensity is observable between the samples treated in salt A for 26 hours and 48 hours. This suggests that re-dissolution of the metallic copper takes place for excessive immersion time. Although the copper re-dissolution mechanism is still not entirely understood, it could be related to cessation of the galvanic coupling effect with iron. When the passivation of the steel surface is completed, in fact, there is no further iron available for cathodic

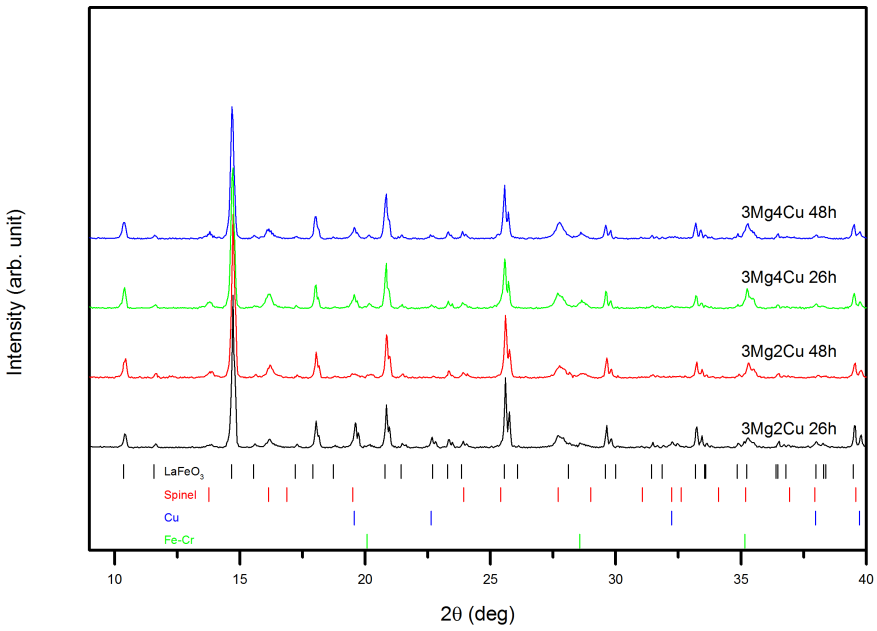



Figure 5.2: X-Ray Diffraction patterns (Mo surce) of K41 steel samples subjected to the passivation treatment at 600 °C in salts characterized by different Cu content for different time intervals.

protection of the metallic copper leading to copper oxidation and its re-dissolution. Such significant difference cannot be observed in the case of 3Mg4Cu salt samples, where both patterns are characterized by a similar intensity of Cu peaks, suggesting that the higher content of copper in the melt may inhibit the copper re-dissolution phenomena.

In figure 5.3 SEM images of electrodes processed in 3Mg2Cu and 3Mg4Cu salts for 26 and 48 hours are reported. Starting from the sample exposed for 26 hours in the 3Mg2Cu salt, it can be observed that cubic perovskite grains have grown on top of a plain Fe-Cr oxide layer. Furthermore, the presence of rounded and irregular copper metal particles partly grown inside the perovskite grains and partly directly deposited on the oxide sublayer can be observed. The SEM image of the sample subjected to the 48 h treatment in the same salt formulation shows a complete surface coverage by the perovskite crystals, but with a significantly lower copper presence. In particular, large number of hollow and defected crystals can be observed, confirming XRD data and suggesting that dissolution of the previously deposited metallic copper occurs between 26 and 48 h in the 3Mg2Cu salt. Evaluating samples subjected to the treatment in the 3Mg4Cu salt, it can be observed that a full coverage by perovskite grains can be obtained after 26 h immersion. This suggests that a higher copper content in the carbonate bath may promote the perovskite formation, as visible also by in-situ electrochemical analyses. Furthermore, defected perovskite

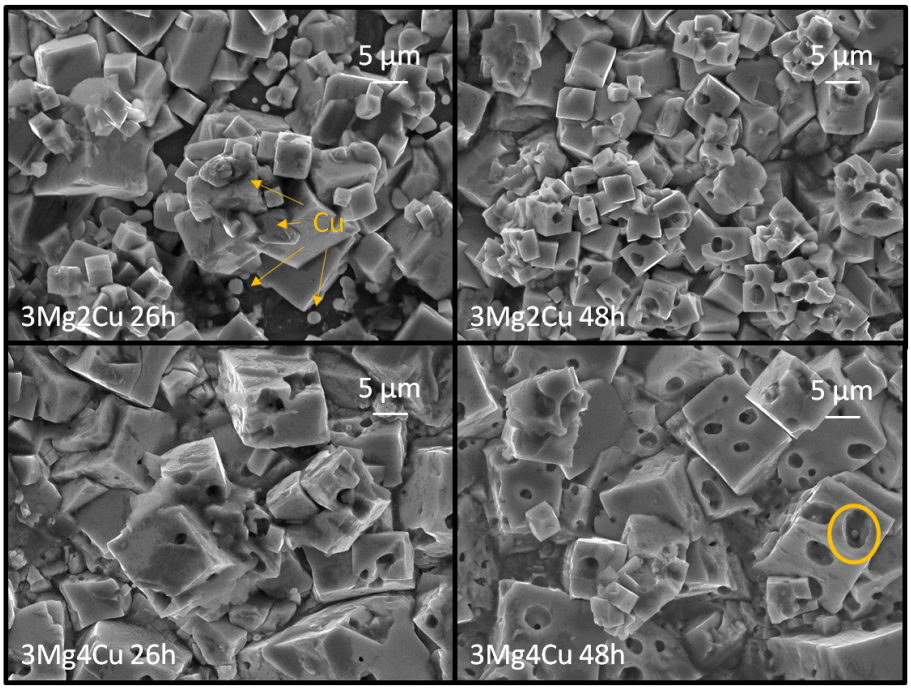



Figure 5.3: SEM images of K41 steel samples surface after the passivation treatment at 600 °C in salts characterized by different Cu content for different time intervals.

grains are already visible, suggesting that the metallic copper re-dissolution is already taking place after 26 h treatment in this salt composition. No significant changes in morphology are observable for longer exposure time: after 48 hours, the perovskite cubic crystals are characterized by more definite edges, meaning that a complete structuration is obtained for longer exposure time, but similar cavities and defects are observable. In the 48 h 3Mg4Cu SEM image, a cavity containing a small copper residue is highlighted. The presence of small copper particles inside perovskite cavities furthermore supports the hypothesis that crystal voids are originated by the dissolution of previously deposited copper.

To scale-up the process and to prepare passivated steel samples for the oxidation experiments, 3Mg4Cu salt was chosen to minimize the process time, due to the faster kinetics promoted by the higher copper content. The evaluation of the OCP curves and of the different morpho-structural properties of the treated samples can allow to identify the optimal passivation treatment time. A minimum time of approx. 18 hours is suggested by the end of the sharp OCP growth. On the other hand, the exposure time should be limited to avoid copper dissolution phenomena. Therefore, considering that after 26 hours of exposure copper re-dissolution was already observed, the process time was limited to 24 hours.

In Figure 5.4 the XRD pattern of a passivated steel foil is reported. The La-Fe perovskite constitutes the main phase, with further reflections ascribable to the

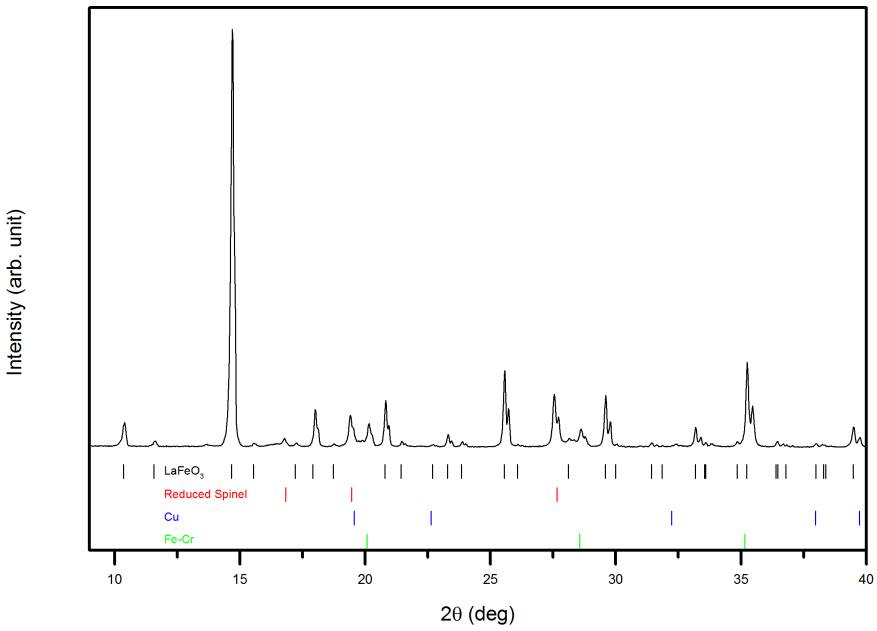



Figure 5.4: X-Ray Diffraction patterns (Mo surce) of a K41 steel foil subjected to the passivation treatment at 600 °C in the 3Mg4Cu salt for 24 h.

substrate and to a Li-rich Fe spinel (Li5Fe5O8 – JCPDS card N. 40-943). Small halos ascribable to metallic copper presence are also visible. From the comparison with the small crucible experiments, some differences can be observed. In particular, a reduced spinel phase is formed on the steel foil samples. This may be related to different oxygen activity in the molten salt contained in small and large crucibles, as suggested already in section 4.1.1. The presence of the La-Fe perovskite phase as main constituent of the sample surface suggests however that the scale up had limited effect on the perovskite coating formation process.

SEM analyses of surface and cross-section of the K41 coated foil sample are reported in Figure 6. It can be observed that the treatment promotes the homogeneous coverage of the whole surface with cubic perovskite grains and rounded embedded metal copper particles. From EDX analysis an overall surface atomic ratio Fe:Cu 7:1 was calculated.

The analysis of the cross-section shows a multi-layer structure approximately 10 µm thick. As evident from the EDX map and the EDX results reported in table 5.1, the La-Fe perovskite is concentrated in the outer layer (point 5), grown on an iron-rich oxide (point 4). Below this iron oxide, a Fe-Cr oxide (point 3) is formed. Furthermore, a narrow interfacial oxide layer between the Fe-Cr oxide and the steel (point 1) is observable and reported as point 2. From the analysis of EDX results, negligible amount of copper was detected in the perovskite phase or in the spinel sublayer. This suggests that copper ions in the melt are not taking part in

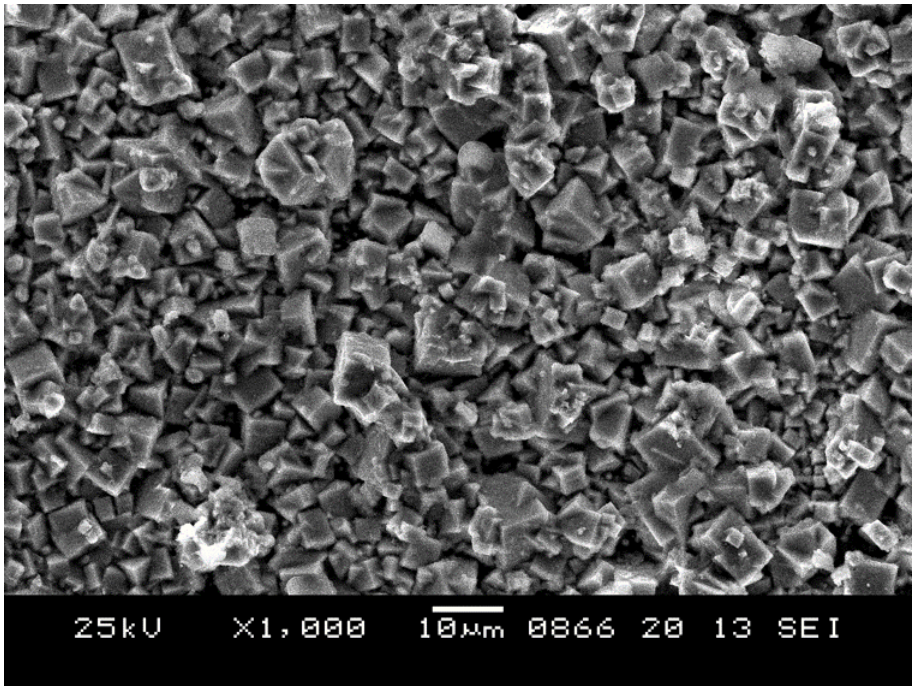



Figure 5.5: SEM image of the surface of a K41 sample after the passivation treatment carried out for 24 h in the 3Mg4Cu salt at 600 °C

the perovskite or in the spinel formation reactions. The presence of copper in the coating is therefore exclusively due to the galvanic deposition of the metallic phase with no significant copper doping phenomena of the perovskite or of the spinel oxide phases observed during the passivation process.

Table 5.1: Results of EDX analysis from points collected in figure 5.6:

| Point | Element (Wt%) | | | | | |
|---|---|---|---|---|---|---|
| | La | Fe | Cr | Cu | Mn | O |
| 1 | 60.3 | 16.4 | | | | 23.3 |
| 2 | 1.1 | 58.7 | 1.0 | | | 39.3 |
| 3 | 1.3 | 27.3 | 27.7 | | 0.3 | 43.4 |
| 4 | 0.4 | 37.5 | 28.5 | | 0.4 | 33.2 |
| 5 | 0.3 | 78.9 | 17.3 | | 0.3 | 3.2 |

The difference observed between the 3Mg4Cu electrode and the scaled up 3Mg4Cu foils, although not significant in the mechanism evaluation, are most likely ascribable to the experimental setup, allowing to highlight a new experimental variable as suggested section 4.1.1. In particular, the electrodes treated in the 3Mg, 3Mg2Cu and 3Mg4Cu salts were processed at the bottom of the alumina crucibles, while the foils treated in the 3Mg4Cu were suspended. This is likely to confirm therefore the effect of the precipitate in the molten salt, and its influence on the local basicity.

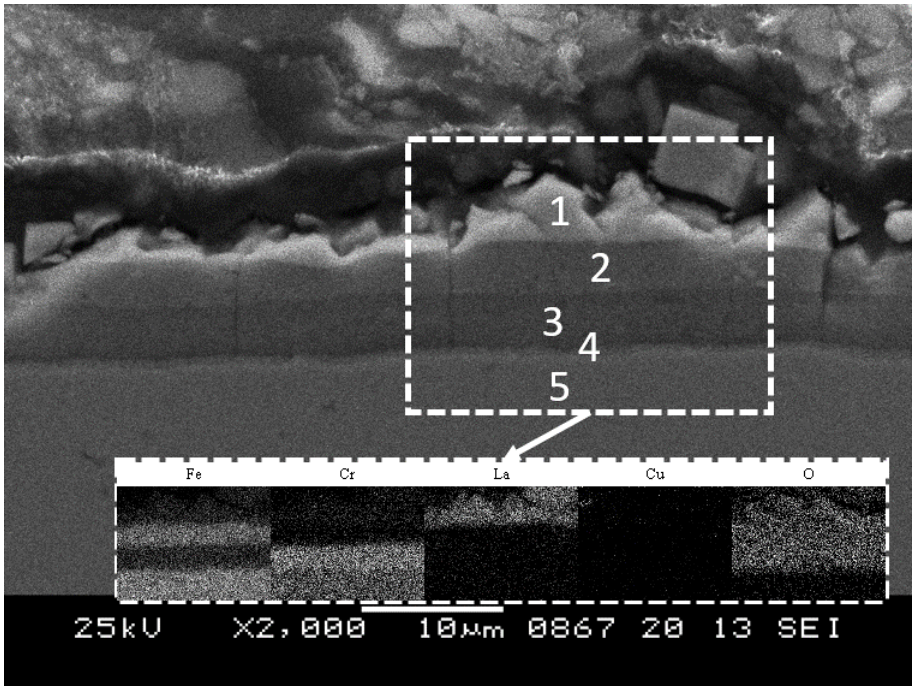



Figure 5.6: SEM image of the section of a K41 sample after the passivation treatment carried out for 48 h in the 3Mg4Cu salt at 600 °C with EDX maps for Fe, Cr, La, Cu and O and the position of EDX analysis reported in table 5.1.

To further evaluate the influence of copper addition, further experiments were carried out suspending the electrodes at approx. 1 cm of height from the crucible bottom, as carried out for the 10Mg samples in section 4.1. The effect of bath basicity was furthermore evaluated carrying out the experiments at a high bath basicity level (i.e. 10% mol MgO).

In figure 5.7 the OCP curves of different K41 electrodes passivated in a 10Mg1Cu salt are reported in comparison with the undoped salt curve. The curves are characterized by a slow initial growth, followed by a sharp transition, and a plateau at approx. -0.4 V. In comparison with the 10Mg curve a significant enhancement in passivation kinetics cannot be observed, suggesting that the acceleration of the perovskite growth induced by the copper addition may be higher in low basicity conditions. An evident difference between the doped and undoped condition is represented by the final OCP values. While in the 10Mg salt the OCP tends to grow towards neutral values, in the 10Mg1Cu salt the OCP reaches approx. -0.4 V and remains constant. This may be ascribed to the presence of metallic copper on the sample surface.

The XRD patterns of K41 electrodes processed for 22 h, 72 h and 120 h in the 10Mg1Cu salt are reported in figure 5.8. After 22 h of exposure, the pattern is ascribable to a mixture of Fe-rich spinels, $LaFeO_3$ and metallic copper. Increasing

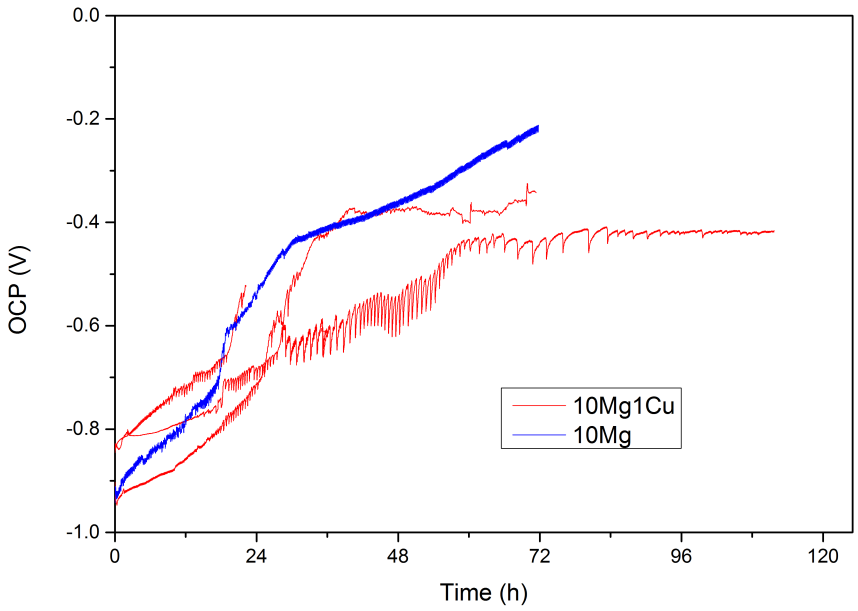



Figure 5.7: OCP curves of K41 steel electrodes exposed at 600 °C in the 10Mg1Cu salt for different processing time.

the exposure time, after 72 h perovskite and copper reflections are more intense, at the expense of spinel and substrate reflections. The pattern related to 120 h of exposure is characterized by features similar to the 72 h with a lesser presence of copper. The evolution of copper peaks suggests that also in these conditions dissolution phenomena of the deposited copper take place after the complete perovskite formation.

In figure 5.9 the surface SEM micrographs and corresponding EDX maps for Fe, Cu and La are reported. After 22 h of exposure, the surface is covered by a smooth Fe-rich oxide that acts as sublayer for small rounded copper particles and cubic perovskite grains. Copper deposition occurs, similarly as observed in the Cu doped 3Mg salt, on the perovskite grains as well. After 72 h the whole surface is homogeneously covered by the perovskite, with large rounded copper particles deposited. Raising further the exposure time no significant difference can be observed regarding the perovskite crystals, while is evident the occurrence of copper re-dissolution: the surface copper content (Wt%) of the 120 h sample is in fact 1/3 with respect to the 72 h sample.

The comparison of the 72 h sample processed in the 10Mg1Cu and 10Mg (figure 4.11) salts shows how in the presence of copper smaller crystals are grown. This may be due to a faster nucleation rate promoted by the galvanic reaction occurring in presence of copper.

Results of the SEM section analysis of the K41 electrode processed for 72 h at

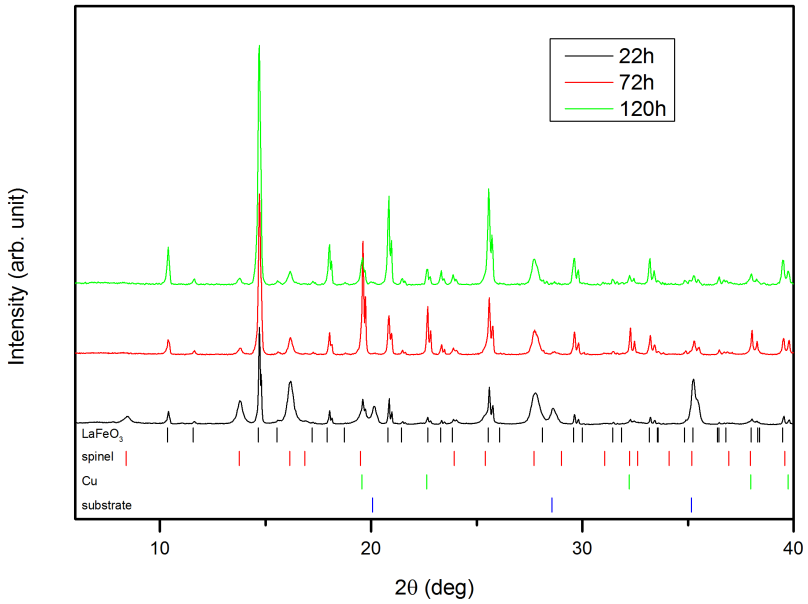



Figure 5.8: X-Ray Diffraction patterns of K41 steel electrodes exposed at 600 °C in the 10Mg1Cu salt for different processing time.

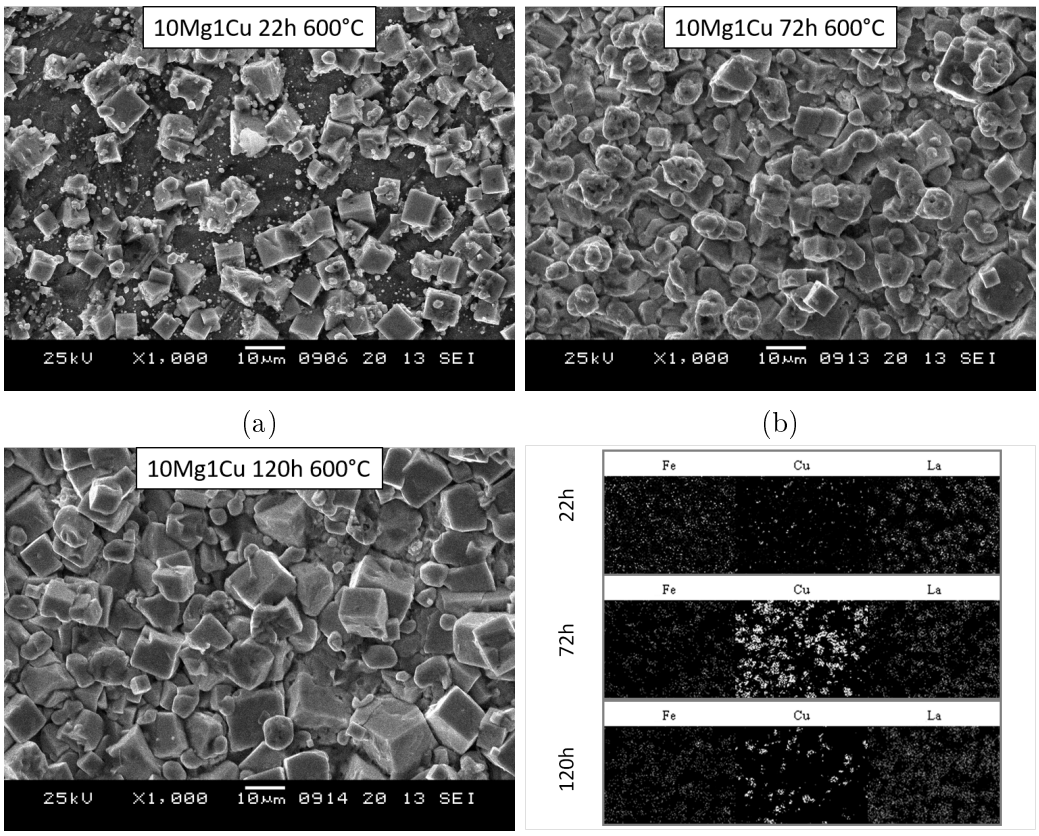



Figure 5.9: SEM images K41 steel electrodes surface exposed at 600 °C in the 10Mg1Cu salt for different processing time (a,b,c) and corresponding EDX maps for Fe,Cu and La (d).

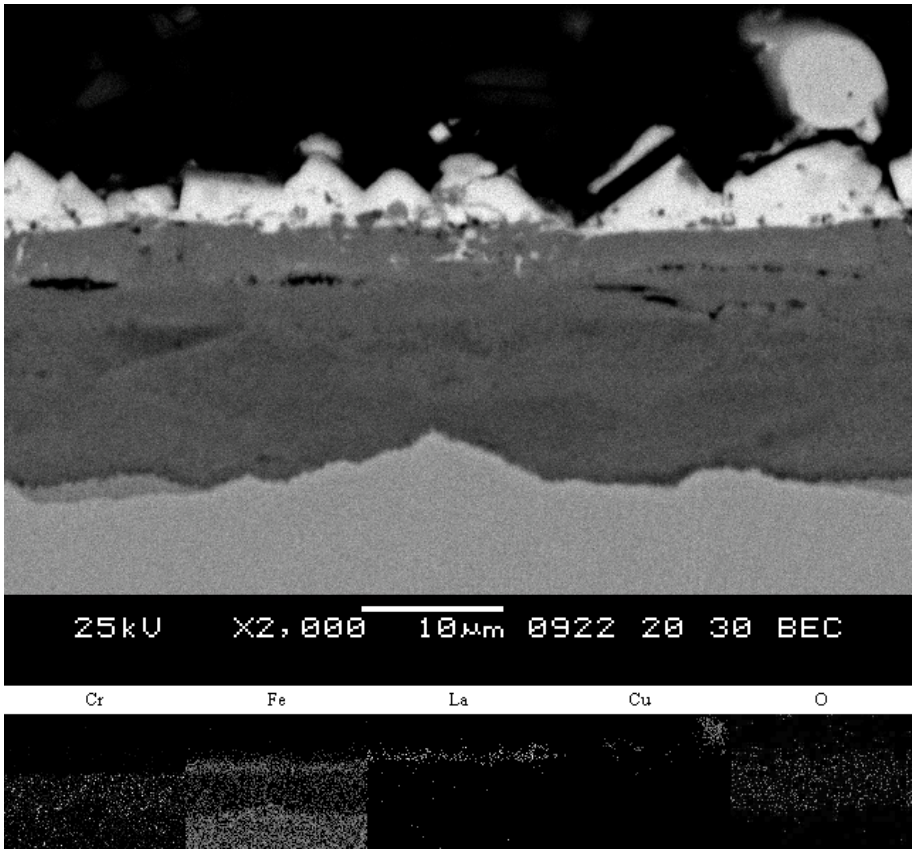



Figure 5.10: SEM image of the section of a K41 steel electrode exposed at 600 °C in the 10Mg1Cu salt for 72 h and corresponding EDX maps for Cr, Fe, La, Cu and O.

600 °C in the 10Mg1Cu salt is reported in figure 5.10. The electrode surface is characterized by the presence of an approx. 20 µm thick oxide scale. A multi-layer structure can be observed, composed by a discontinuous oxide scale at the steel-coating interface, a chromium-iron rich oxide, an iron-rich oxide and the perovskite grains. Large copper particles can be observed on the surface, while minor copper inclusions can be observed at the iron oxide-perovskite interface, most likely originated by the coverage of the small metallic copper particles observed in the 22 h sample by perovskite grains. Comparing with the electrode processed in similar conditions in the 10Mg salt (figure 4.12), it can be observed that copper addition promotes the growth of a thinner oxide layer

## 5.2 Nickel-dispersed composite

As second case-study metal, to confirm that the formation of the copper-perovskite composite coating is due to the occurrence of generic electrochemical reactions occurring in molten salt, and not to a phenomenon limited to copper oxide reduction,

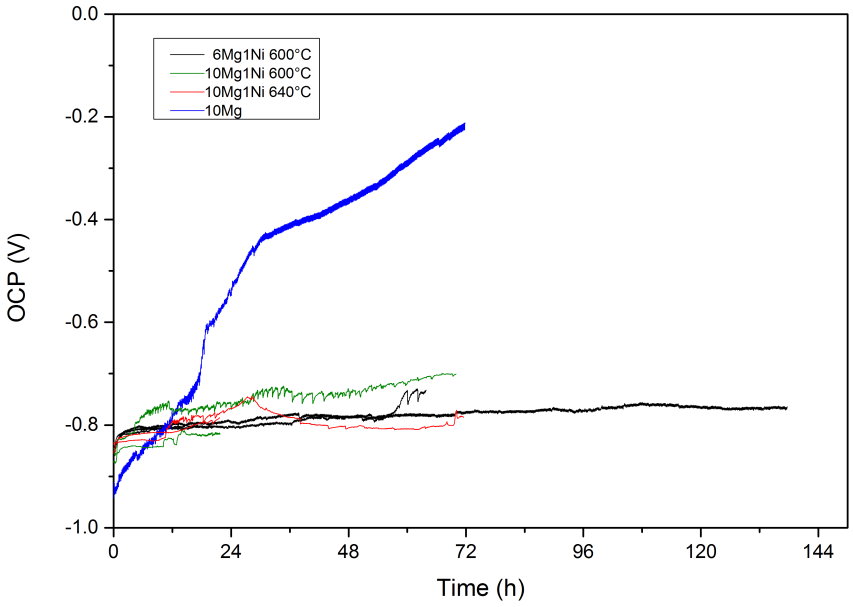



Figure 5.11: OCP curves acquired during the exposition of K41 steel electrodes in different nickel containing salts.

the addition of nickel to the molten bath was evaluated. To study the formation mechanism in presence of nickel, salt basicity and temperature were varied as well. In this section are therefore described the results obtained with the 10Mg1Ni and 6Mg1Ni salts described in chapter 2.

In 5.11 the OCP curves of K41 steel sample processed in different conditions are reported. It can be observed that in all cases the OCP remains constant at approx. 0.8 V, compatibly with the electrochemical redox potential of nickel as reported in table 1.3.

The XRD patterns of K41 electrodes processed in different conditions are reported in figure 5.12. The sample processed in the 10Mg1Ni salt for 22 h at 600 °C is characterized by the presence of multiple Fe-rich oxide phases and minor traces of perovskite growth. No clear signs of nickel deposition are visible. Raising the exposure time, the pattern suggests the structuration of the perovskite phase. Raising the temperature, the perovskite phase constitutes the main oxide phase already after 22 h, suggesting that a faster perovskite growth occurs. The samples processed in the 10Mg1Ni salt do not show however peaks ascribable to nickel.

Lowering the salt basicity in the presence of nickel seems to favour the formation of metallic nickel and perovskite: the pattern of the sample exposed for 20 h in the 6Mg1Ni salt is characterized in fact by perovskite as the main oxide phase, and metallic nickel peaks well evident. Raising the exposure time, structuration of Fe-rich spinel phases occurs, while nickel content decreases significantly, with the

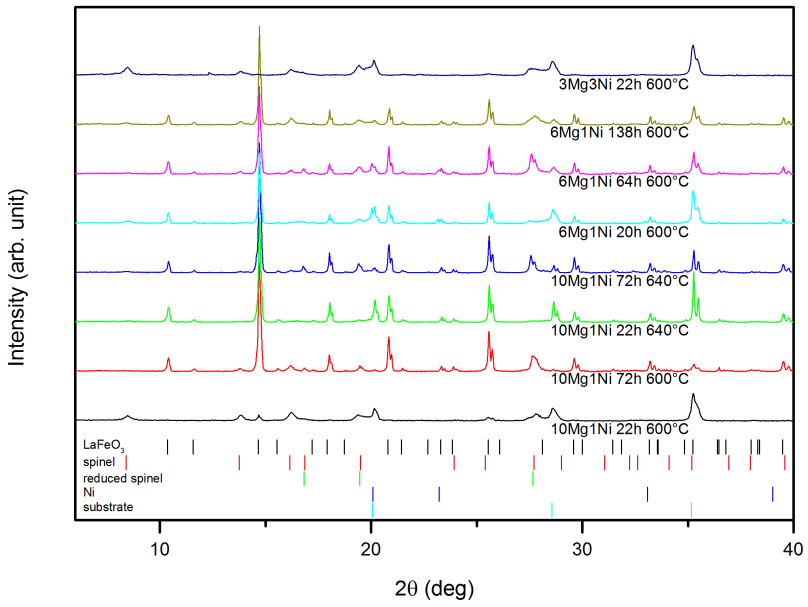



Figure 5.12: X-Ray Diffraction patterns of K41 steel electrodes exposed in nickel containing salts.

sample exposed for 138 h characterized by the absence of reflections ascribable to the metal.

SEM micrographs of the samples surface is reported in figure 5.13. After 72 h in the 10Mg1Ni salt at 600 °C the surface is almost completely covered by perovskite crystals of heterogeneous dimension. With respect to the undoped salt, the perovskite grains are characterized by smaller size. Raising the temperature up to 640 °C, the perovskite growth process seems inhibited, with the appearance of several zones characterized by small and irregular crystals. This morphology is observable both after 22 h of exposure and after 72 h, with a coarsening and growth of the crystalline structure occurring between 22 h and 72 h.

The samples treated in the 6Mg1Ni salt show instead different morphologies. After 20 h of exposure, the sample surface characterized by the presence of a homogeneous layer of Fe-rich oxide partially covered by perovskite crystals. Similarly as in the Cu-doped salts, nickel particles are embedded in the perovskite grains and small nickel nuclei are deposited on the oxide sublayer. Increasing the processing time dimensional growth of the perovskite crystals occurs, without however a complete perovskite coverage, along with disappearance of nickel particles.

The SEM section analysis of the sample processed for 72 h at 600 °C in the 10Mg1Ni salt is reported in figure 5.14. The sample is characterized by an oxide scale approx. 15 μm thick. The coating possesses once again a multi-layer structure similar to the one observed in the 10Mg and 10Mg1Cu samples, with a first Cr-rich

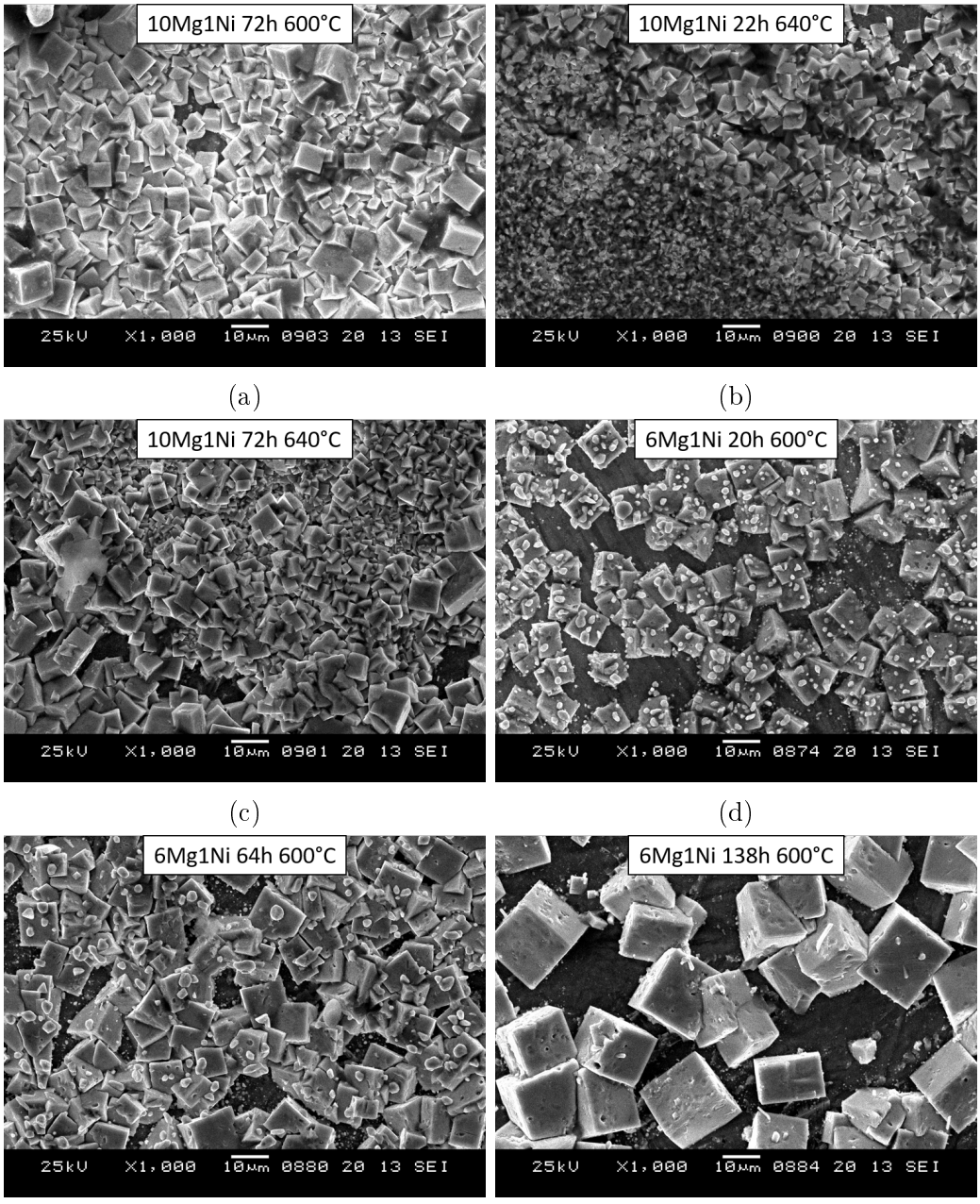



Figure 5.13: SEM images of K41 steel electrodes processed in nickel containing salts.

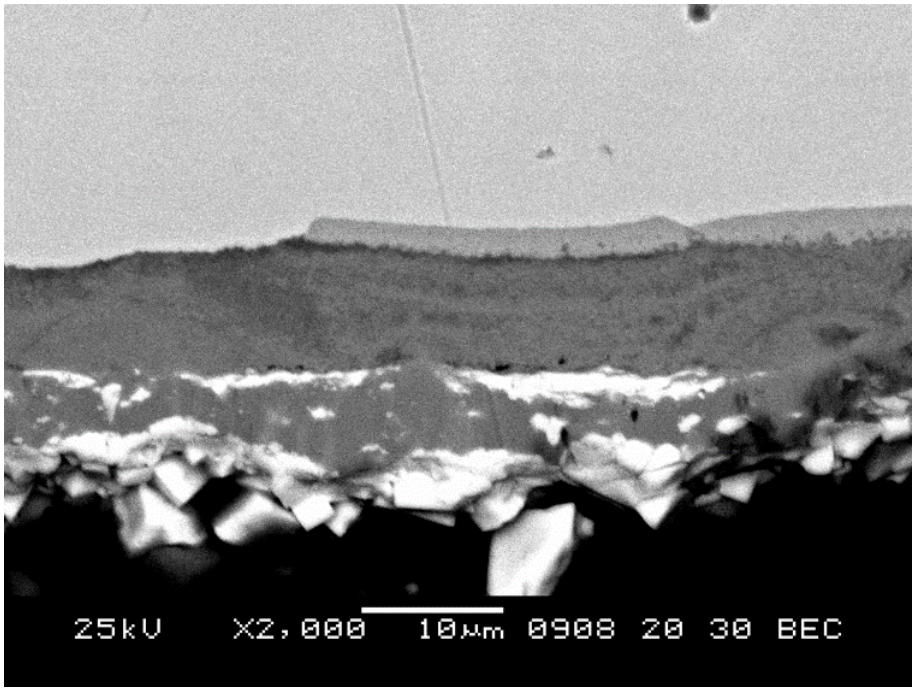



Figure 5.14: SEM image of the section of a K41 steel electrode exposed at 600 °C in the 10Mg1Ni salt for 72 h.

interfacial layer, covered by a Fe-Cr oxide layer, a Fe oxide layer and the perovskite grains. However, differently from the above mentioned cases, the presence of large domains of La-Fe rich oxide - most likely perovskite - at the interface between the Fe and the Fe-Cr oxides (the clear phase evident at the center of the oxide scale) is noteworthy.

## 5.3 Silver-dispersed composite

The third metal chosen to assess the mechanism of metal-perovskite composite formation was silver, as a noble metal easily obtainable in oxide form and characterized by appreciable solubility in molten alkali carbonates.

The OCP curves of K41 electrode treated at 600 °C are reported in figure 5.15. The curves acquired in the Ag doped bath are characterized by shape similar to the reference undoped bath, with fast passivation kinetics: neutral OCP values are reached after approx. 26 hours of exposure, compatibly with the presence of silver on the surface (see $E^0$ in table 1.3).

The XRD patterns of samples processed in the 10Mg1Ag salt for 22 h and 72 h are reported in figure 5.16. In both cases the spectra are ascribable to a mixture of perovskite, as main oxide phase, Fe-rich spinel, metallic silver and substrate contributions.

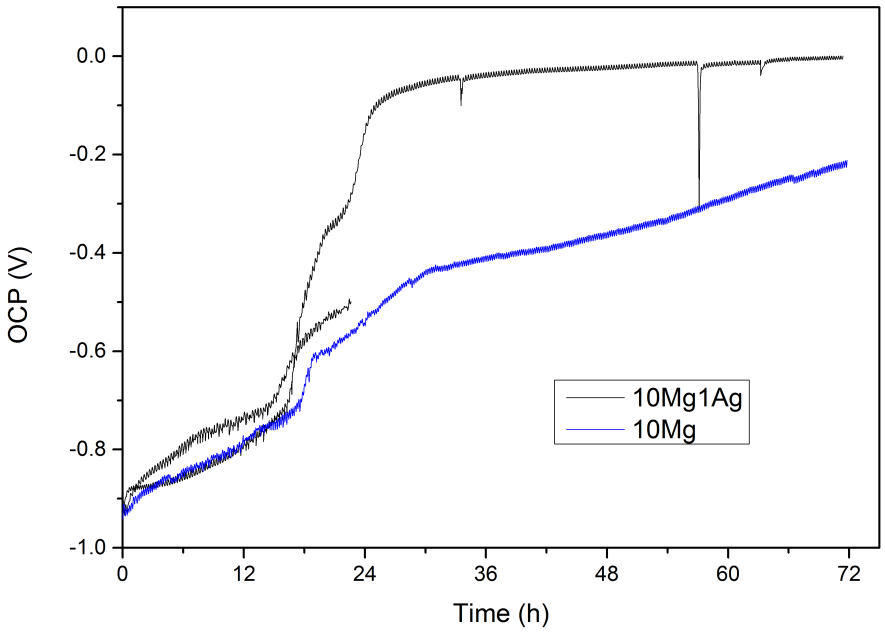



Figure 5.15: OCP curves acquired during the exposition of K41 electrodes at 600 °C in the 10Mg1Ag salt.

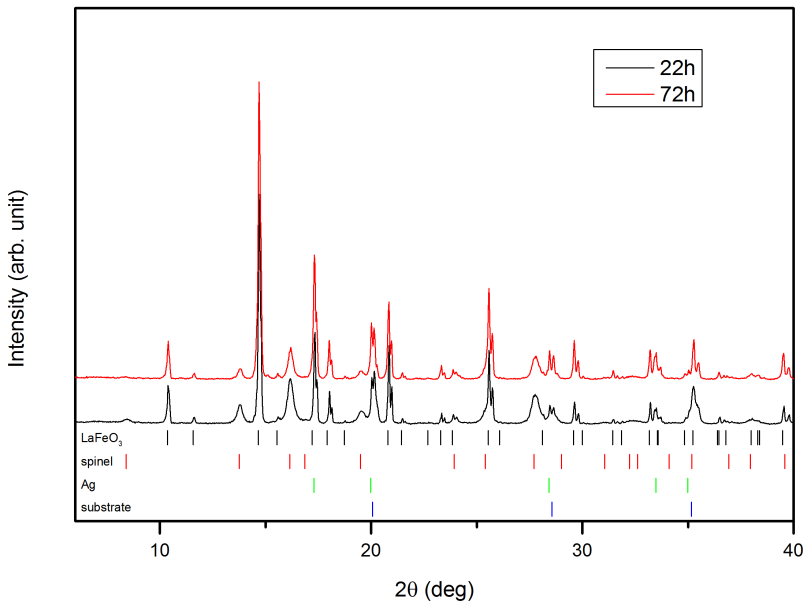



Figure 5.16: X-Ray Diffraction patterns of K41 steel electrodes exposed at 600 °C in the 10Mg1Ag salt for 22 h and 72 h.

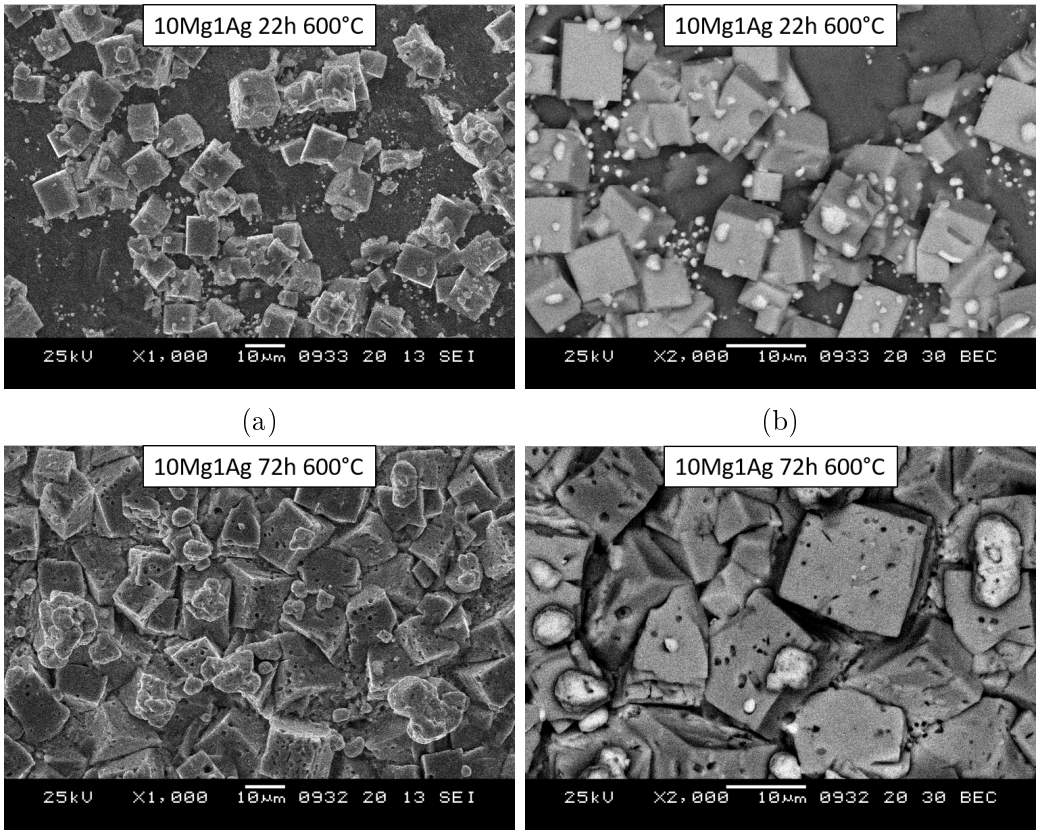



Figure 5.17: SEM images of K41 steel electrodes exposed at 600 °C in the 10Mg1Ag salt for 22 h and 72 h; (a,c) secondary electrons images, (b,d) backscattered electrons images.

In figure 5.17 the surface SEM micrographs are reported. After 22 h of exposure, the surface is covered by a smooth Fe-rich oxide that acts as sublayer for cubic perovskite grains and small rounded silver particles deposited on the sublayer and embedded in the perovskite crystals. The surface morphology is remarkably similar to the sample exposed to the 10Mg1Cu salt, suggesting that the same growth mechanisms are involved. After 72 h the whole surface is homogeneously covered by the perovskite, with large irregular silver particles deposited. The perovskite grains exhibit diffuse pits, most likely originated by the dissolution of small silver particles embedded in the perovskite. The silver particles as well are characterized by a porous surface, suggesting that the dissolution phenomenon hypothesized for the small particles is occurring for the larger aggregates as well.

Results of the SEM section analysis of the sample processed for 72 h in the 10Mg1Ag salt is reported in figure 5.18. As in the case of the undoped, Cu and Ni salts, the coating if composed by a multilayer structure, with Fe-Cr oxides at the steel interface and iron oxides towards the perovskite crystals. The porous

structure of silver particles deposited on the perovskite grains is clearly evident, confirming the evidence obtained through surface SEM analysis. With respect to the 10Mg1Cu and 10Mg samples exposed in similar conditions, the thickness of the coating (in particular of the sublayer) is reduced to approx. 10 μm, confirming the faster passivation suggested by the OCP curves.

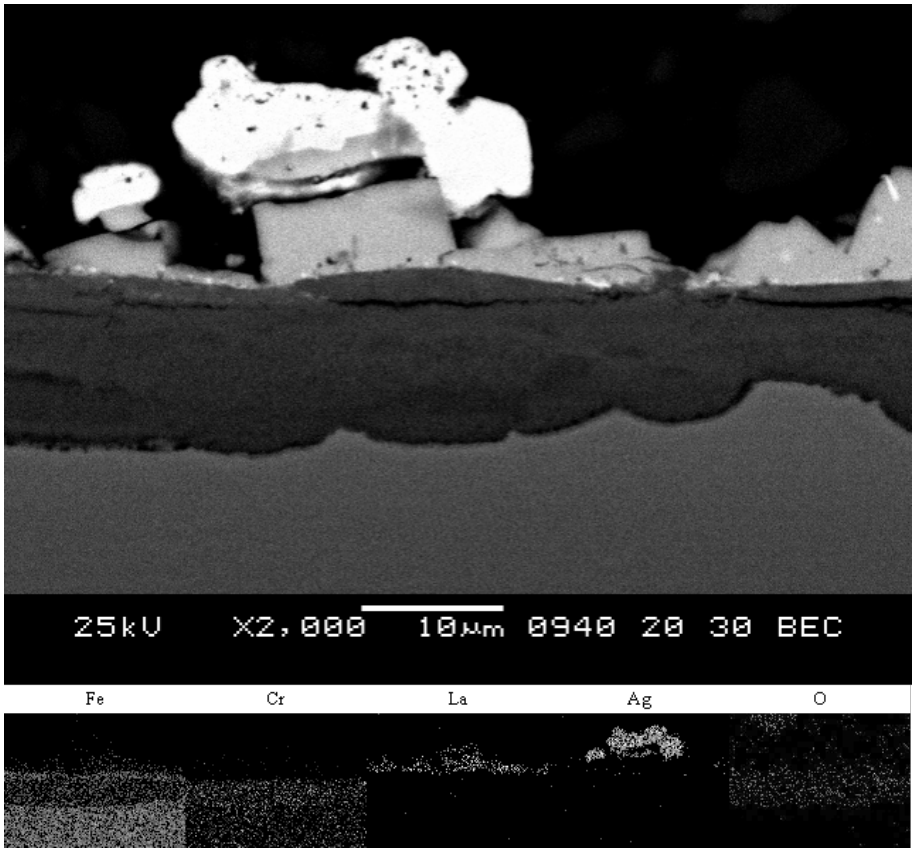



Figure 5.18: SEM image of the section of a K41 steel electrode exposed at 600 °C in the 10Mg1Ag salt for 72 h and corresponding EDX maps for Cr, Fe, La, Ag and O.

In figure 5.19 a detail of the coating structure is reported. The presence of small clear silver particles embedded in the perovskite grain at the sublayer interface confirm that silver deposition has already occurred at the initial stages of the perovskite formation. Furthermore, the interpenetration of the metal inside the perovskite crystal is observable in certain points. This suggests that the perovskite grain growth proceeds around silver nuclei, and that the large silver particles evident on the sample surface are originated by silver deposition both simultaneously and after the complete perovskite growth. Evaluating instead the interface between surface silver particles and perovskite grains, the metal particle does not seem adherent to the oxide grain, suggesting that no chemical interfacial layer between the metal and the perovskite exists. However, the observed interpenetration is most likely associated

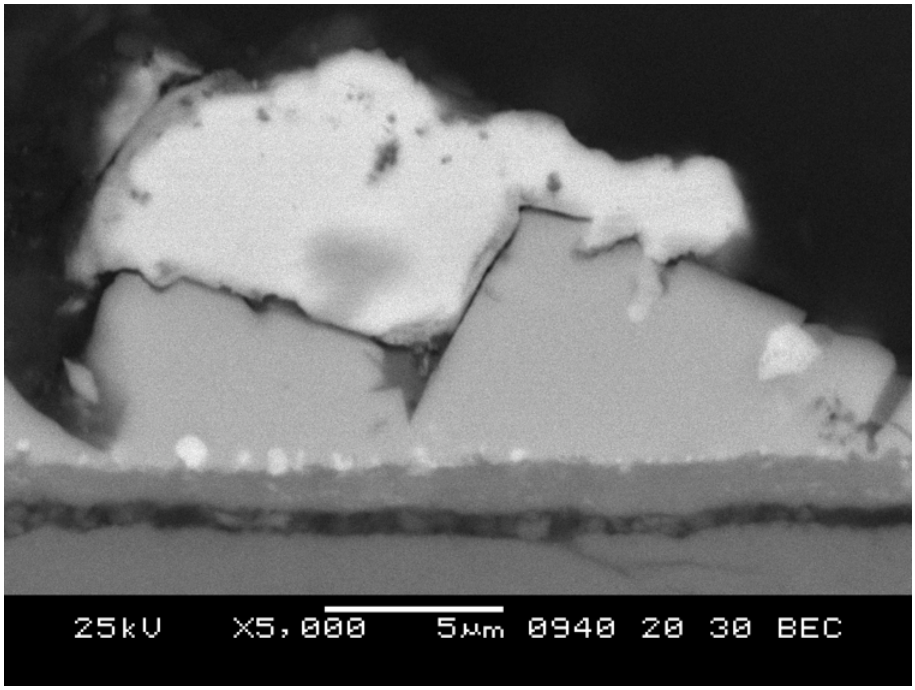



Figure 5.19: SEM image of the section of a K41 steel electrode exposed at 600 °C in the 10Mg1Ag salt for 72 h depicting the detail of a silver particle (clear, top) deposited on perovskite grains (medium gray, center) grown on the Fe-rich oxide sublayer (dark grey, bottom). Clear small silver particles can be observed ad the interface between the sublayer and the perovskite.

to high mechanical adhesion of the metal particles to the coating layer.

## 5.4 Formation mechanism of metal-perovskite composite coatings

The enhancements of the oxidizing power of the melt promotes the structuration of the perovskite layer, as reported in section 4.1. The introduction of oxide species that may act as oxidant for $Fe^{2+}$ ions should be therefore beneficial for the passivation process, in particular in low basicity formulations - as observed in the 3Mg4Cu and 3Mg2Cu salts in comparison with the undoped salt. In higher basicity salts (i.e. 10% mol MgO in the melt), despite not observing significant enhancement in the initial process kinetic, the addition of oxidizing species results in the growth of thinner oxide layers, as evident comparing the electrodes processed in the 10Mg salt (figure 4.11) with 10Mg1Cu (figure 5.10) and 10Mg1Ag (figure 5.18) salts. A faster formation of efficient passivation layers is therefore likely to occur: in particular, significantly thinner Fe-oxide sublayers are obtained, suggesting that less chromium dissolution takes place when Cu and Ag are added to the high basicity salt.

The experiments carried out with the addition of nickel highlights further interesting elements. When nickel is added to the high basicity salt, scarce metal deposition is obtained and the perovskite growth seems inhibited. When the basicity is lowered, significant metal reduction is observed during the first hours of experiment, and the deposited metal amount significantly decreases for high processing time, without however observing a full perovskite coverage.

Comparing the equilibrium potential, nickel should represent an oxidant for metallic iron, but could ensure cathodic protection towards the oxidation of $Fe^{2+}$ to $Fe^{3+}$ ions when occurring through the mechanism supposed in section 4.1. Nickel is therefore likely to be reduced on the surface at the expense of Fe atoms, but is likely to be readily oxidized protecting $Fe^{2+}$ ions from further oxidation. The presence of reduced spinel phases (i.e. $Li_5Fe_5O_8$), rich in $Fe^{2+}$ ions, in the XRD patterns of samples treated in the Ni-doped salts for long exposure times (e.g. 72h) confirms this hypothesis.

Furthermore, nickel re-oxidation could subtract oxide ions needed for the perovskite formation. The development of defective and irregular perovskite grains, as observed in low basicity undoped salts (see figure 4.3), suggests thus the reduction of the overall oxidizing power of the melt in presence of nickel. The absence of an effective passivation layer is clearly evident in the cross sectional image reported in figure 5.14: the presence of the perovskite at the Fe-Cr oxide/Fe oxide interface suggests the inward growth of perovskite crystals, most likely occurring at the $LaFeO_3$/Li-Fe oxide grain boundary interfaces, connected to inward lanthanum and outward lithium ions diffusion and denoting the absence of an effective passivation behaviour of the perovskite phase.

The results related to the lower basicity salt 6Mg1Ni show that in the first hours of experiment significant nickel deposition occurs. It is likely that in this salt, characterized by lower oxidizing power, a higher contribution for the initial steel oxidation is due to nickel/iron galvanic coupling, promoting higher nickel reduction. After this first phenomenon, it is likely that the lower oxidizing power of the melt can not promote the fast nickel re-oxidation observable in the 10Mg1Ni salt, leading to slower solubilization kinetics. However, nickel can still act as cathodic protection for further iron oxidation, inhibiting complete coverage of the sample surface by the perovskite.

The experimental evidences reported in this work and the evaluation of corrosion mechanisms of stainless steels in common molten carbonates, described in section 1.4.1, and of the formation of La-Fe perovskite layers by dissolution-precipitation reactions [8, 76] allow to propose a formation mechanism for the metal-perovskite composite coatings, schematically reported in figure 5.20:

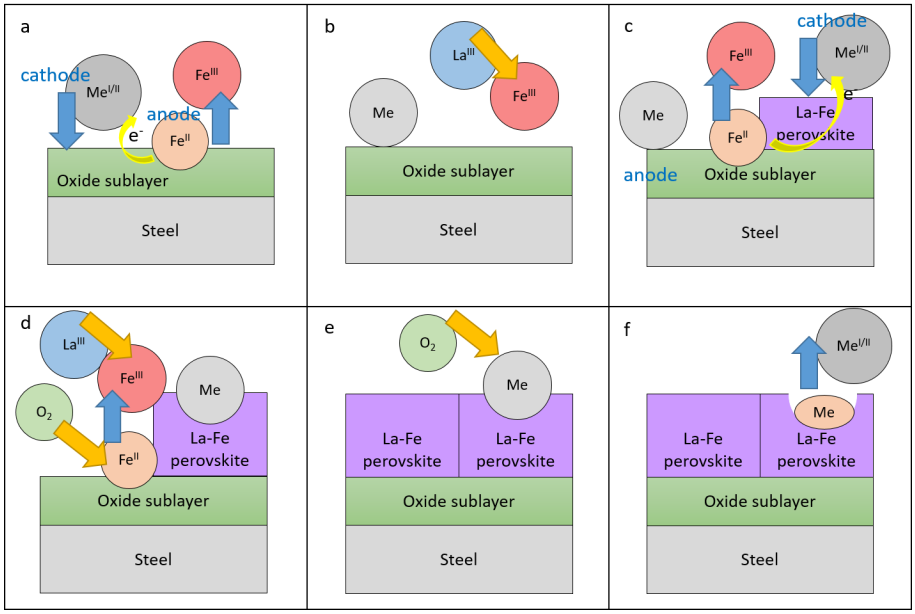



Figure 5.20: Schematic representation of the proposed metal-perovskite composite coating formation mechanism described in section 5.4.

**a** The oxidizing metal ions dissolved in the melt interact with the steel and give rise to the formation of a galvanic couple with iron, promoting its oxidation and the precipitation of the oxidizing metal on the sample surface;

**b** $Fe^{3+}$ oxidized species react with lanthanum oxides in the melt to form the perovskite phase;

**c** The galvanic coupling of the nobler metal can occur also through the perovskite oxide, acting as electronic conductor, resulting in the deposition of the metal on the growing perovskite crystals;

**d** The formation of the perovskite phase clearly occurs also in the absence of the galvanic coupling. Common mechanisms of iron oxidation, carried out by dissolved oxide ions, and its reaction with lanthanum oxides give rise to the formation of perovskite crystals as in undoped melts;

**e** Once the surface is completely covered by the perovskite oxide, the conditions for galvanic coupling of the oxidant metal with iron cease to exist (i.e. no ionic medium contact). Without galvanic protection given by the iron oxidation, the reduced metal species are oxidized by oxide ions in the melt;

**f** The oxidized metals dissolve in the melt, with mechanism and kinetics dependent on their nature, leaving hollow perovskite crystals.

# Chapter 6

# Evaluation of the high temperature stability of coated steels

To evaluate if the La-Fe perovskite based conversion coatings could be suitable for the application in SOFC technology, passivated samples were subjected to exposure tests in simulated SOFC environments to evaluate the stability of the coating layer in the selected conditions. The experiments were carried out at 700 °C, as representative of IT-SOFC operating temperature. Different alloys and coating structure combinations were evaluated to assess the effectiveness of the different synthetic strategies evaluated in chapter 4 and 5. The 13Cr SS405 alloy was selected for several reasons: this alloy may in fact constitute a low cost alternative to high chromium ferritic stainless steels, and due to its poor oxidation resistance in simulated operating conditions [129] it represents a suitable benchmark for a protective layer. The 18Cr K41 ferritic stainless steel was selected instead as a common SOFC interconnect material readily available and relatively cheap (with respect to highly alligated high chromium ferritic alloys), to evaluate the oxidation response of the different La-Fe perovskite based conversion coatings.

A summary of the tested samples is reported in table 6.1.

Table 6.1: Summary of the coated steels and perovskite structures combination subjected to oxidation experiments reported in this chapter:

| Steel | Coating | Morphology | Section |
|---|---|---|---|
| SS405 | La-Fe | thin perovskite layer | 6.1 |
| K41 | La-Fe | thick perovskite layer | 6.2.1 |
| K41 | La-Fe thin | thin perovskite layer | 6.2.2 |
| K41 | Cu/La-Fe | thick composite layer | 6.2.3 |

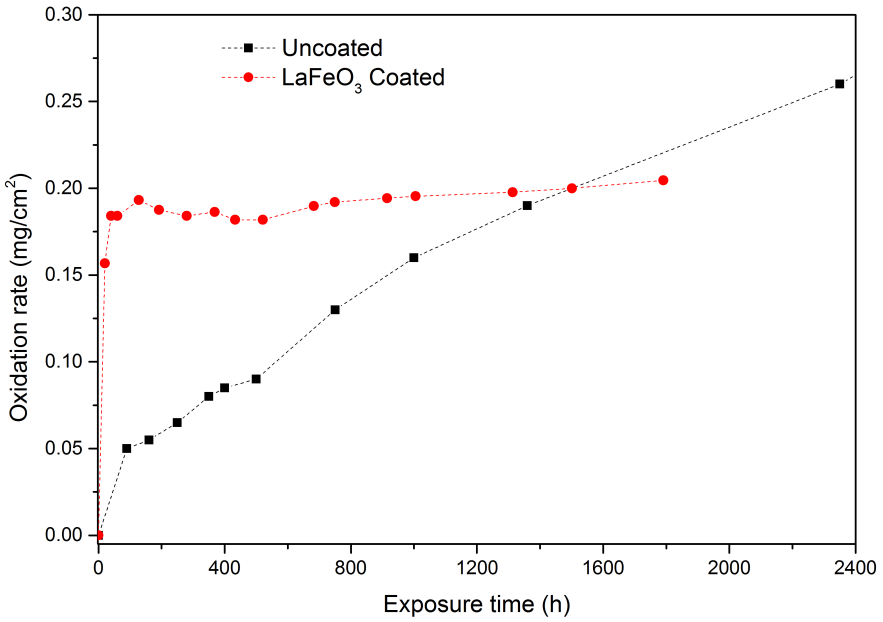



Figure 6.1: Weight change of uncoated and $LaFeO_3$ coated SS405 samples during discontinuous oxidation experiments at 700°C in humid air (3%).

## 6.1 Oxidation behaviour of La-Fe perovskite coated SS405 steel

The effect of the perovskite coating on the long-term oxidation behaviour in air at 700 °C of the 13Cr steel is illustrated in figure 6.1. The uncoated steel follows a slow quasi-linear rate of oxidation. The $LaFeO_3$ perovskite coated steel is instead characterized by a different behaviour: an initial abrupt weight gain is observed in the first 200 h exposure, and after this time the coated steel presents no further appreciable weight gain over long time exposure. No visible yellowish colour changes of alumina supports, ascribable to Cr release, were observed for the coated samples.

The initial fast oxidation of the coated samples can be explained by assuming that oxygen-deficient oxides constitute the coating layer, formed in the oxygen-lean molten salt bath. Thus, the initial weight gain should indicate the occurrence of a rapid oxygen uptake to form more stoichiometric oxide phases. After the initial oxidation period, the protective effect of the coating becomes evident as testified by the very low weight gain, suggesting the absence of further significant oxygen uptake.

In figure 6.2 the XRD patterns of the samples exposed for 1000 hours and 1800 hours are reported in comparison with the as-coated sample. Growth of haematite and spinel phase is visible in the oxidized samples pattern. Small peak shifts of the

iron-rich spinel phase towards higher 2Θ values, as clearly evident from the 2Θ∼74° peak, could be due to a change in lattice parameter induced by Cr enrichment of the spinel phase, most likely occurring during the first hours of test as suggested by the similarity observable between the 1000 h and the 1800 h pattern. The minor peak observable at 2Θ∼39° could not be unambiguously assigned, although it could indicate the formation of lanthanum silicates or lanthanum/lithium silicates (e.g. LiLaSiO4 - JCPDS card n. 48-0006) most likely structured during the high temperature exposure.

Silicates are known to be highly soluble in molten carbonate salts [136]. Silicon extraction from the steel could lead to the presence of silicon rich residuals on the coating surface after the passivation treatment. The washing procedure carried out in water most likely does not remove efficiently the deposited silicates, scarcely soluble in water solutions. However, lanthanum silicates and lithium silicates are commonly characterized by high ionic conductivity [137, 138]. The formation of discrete particles on the coating surface should therefore not represent a threat for the coating effectiveness in term of electric properties.

Furthermore, removal of silicon from SOFC interconnect steels is recognized as an important issue in order to avoid formation of electrically insulating silica beneath the chromia surface [139]. Since conventional surface treatments used for Si removing from steels are in general very costly, the molten carbonate treatment can be seen also as a convenient and easy way for production of silicon-free steel interfaces for SOFC applications.

Surface microstructure evolution of coated steel samples as a function of exposure time is shown in figure 6.3. No significant differences can be observed in the sample surface morphology, suggesting that $LaFeO_3$ conversion coatings possess high stability and protective and diffusion barrier properties in these conditions. Only a tiny growth of the particle agglomerate sizes can be discerned after 1000 h exposure, most likely occurring in the first hours of test. The relative proportion of Fe and La in the two characteristic zones of the perovskite coating is reported in table 6.2, in terms of Fe/La atomic ratio. The results suggest that the molten carbonate conversion process resulted in the formation of a non-stoichiometric $LaFeO_3$ perovskite coating with a large excess of Fe cations. Furthermore, the Fe/La ratio significantly increases in the particle agglomerate region with increasing exposure time suggesting that a gradual structural surface change is taking place in the perovskite structure due to some Fe surface segregation phenomena. This should be not unexpected, since description of surface Fe segregation in non-stoichiometric $LaFeO_3$ perovskites with a Fe/La ratio $>1$ is a phenomenon already described in literature [140]. According to the proposed structural model, perovskite maintains its structural stability

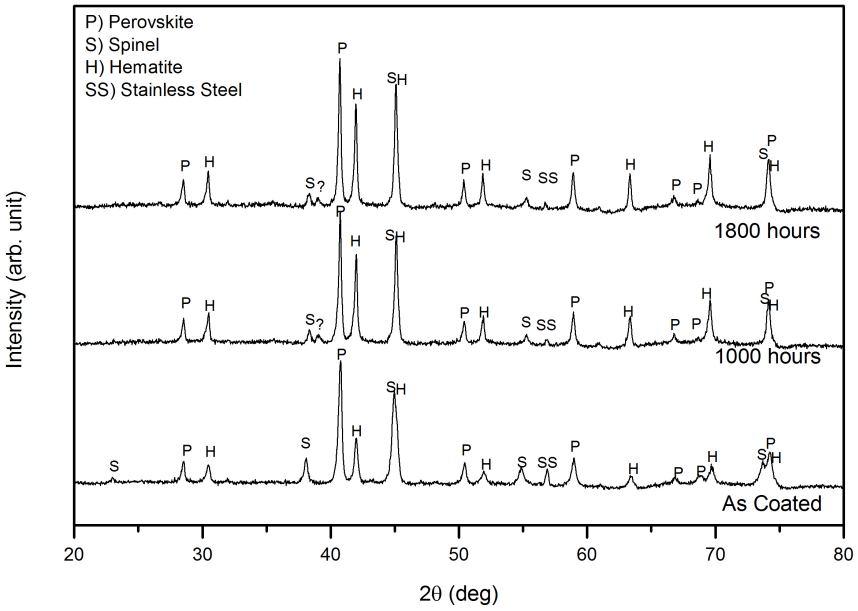



Figure 6.2: X-Ray diffraction patterns (Fe source) of the coated SS405 samples after different exposure intervals at 700°C in humid air (3%)

by accommodating the Fe excess in surface layers composed of $FeO_6$ octahedra. In agreement with our results, the stability of such non-stoichiometric perovskite structures has been reported to degrade significantly only above 800 °C, when the surface defects, i.e. the $FeO_6$ octahedra, collapse into a separated haematite phase.

Table 6.2: Perovskite chemical composition (Fe/La ratio) of smooth coating areas and particles clusters as reported in figure 6.3:

| As Coated | | 1000 hours | | 1800 hours | |
|---|---|---|---|---|---|
| Smooth layer (A) | Particle cluster (B) | Smooth layer (A) | Particle cluster (B) | Smooth layer (A) | Particle cluster (B) |
| 4 | 6 | 6 | 10 | 6 | 12 |

Results of surface and cross-section SEM analyses of the coated 13Cr steel after 1800 hours of exposure in air at 700 °C are reported in figure 6.4. The low magnification surface image (6.4(a)) clearly shows that no apparent spallation and detachment phenomena occurred during the exposure experiment, the steel surface still being homogeneously and completely covered by the perovskite coating. The morphology of the smooth sublayer (zone A) and of the particle agglomerates (zone B) observed at high magnification (6.4(b)) is comparable with what is observed on the initial coated sample denoting no apparent chemical or thermo-mechanical degradation mechanism of the perovskite coating structure under the selected ex-

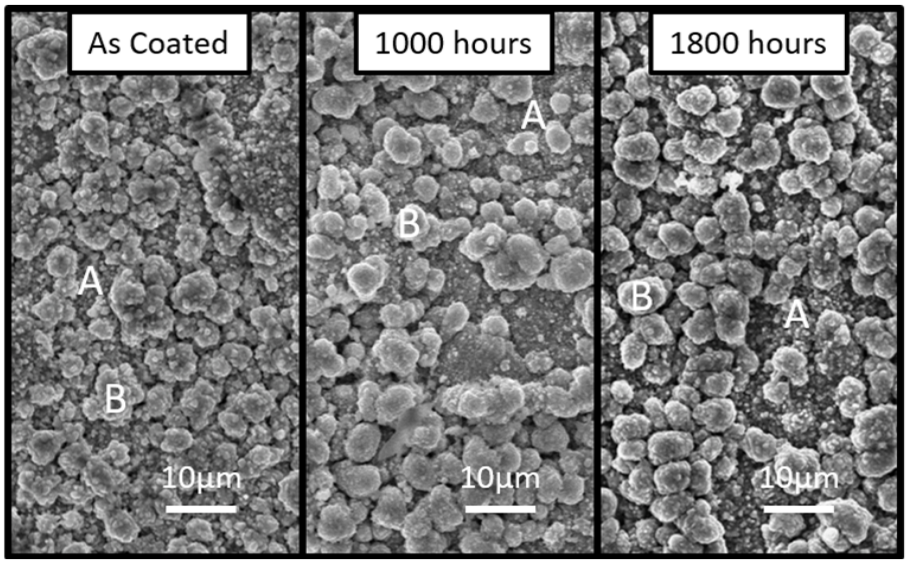



Figure 6.3: SEM images of the coated SS405 samples after different exposure intervals at 700°C in humid air (3%)

perimental conditions. Examination of the cross-section coating (6.4(c,d,e)) allowed to reveal some slight changes in the coating structure, but not in the thickness. A denser appearance of the perovskite coating and notably of the particle agglomerate structure is clearly observable indicating that exposure led to compacting or sintering of the coating structure. The EDX maps (6.4(e)) show only lanthanum and iron as metallic elements in the external coating layer, while a thin and constrained chromium rich oxide layer is clearly observable beneath the perovskite coating, suggesting that the $LaFeO_3$ layer behaves as an effective Cr diffusion barrier.

To evaluate the behaviour of uncoated and coated samples in highly demanding dual atmosphere environments (i.e. Air on the cathode side and $H_2$ on the anode side), the uncoated and coated steel were subjected to exposure tests as indicated in chapter 2.

Figure 6.5 reports the results of the ASR conductivity experiments carried out in dual-atmosphere conditions at 700 °C. The uncoated stainless steel shows a gradual degradation of surface electrical performances up to approximately 700 hours. After this period a significant ASR evolution is observed, indicating that a severe degradation mechanism is occurring on the oxidized steel surface. The coated sample shows a similar behaviour, with breakaway occurring after 500-600 hours. In both cases the contact resistance abruptly increases towards the ohm value range in just a few hours from the start of the breakaway event, suggesting that the surface degradation process should be similar in both the samples.

This was a somewhat unexpected result since the perovskite coating exhibited a significantly higher oxidation resistance in single atmosphere tests. It is also

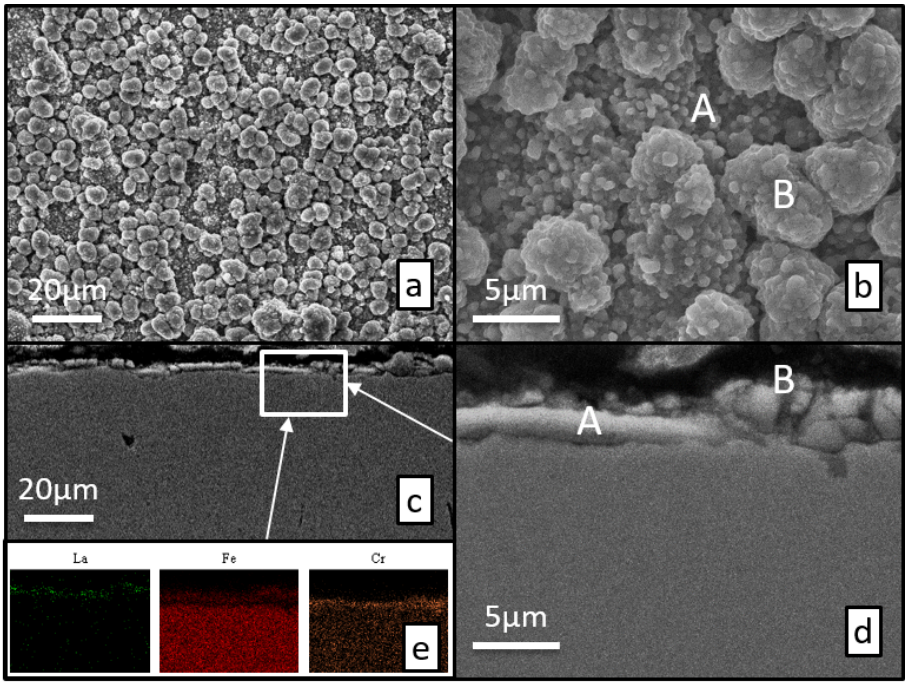



Figure 6.4: SEM images of the coated SS405 steel surface (a and b) and section (c and d) after 1800 h of exposure in air at 700 °C with the high magnification cross-sectional image incorporating the EDX mapping of La, Fe, and Cr elements (e)

important to note that, before the breakaway event, the $LaFeO_3$ conversion coating resulted in ASR values comparable to the uncoated steel. Much more accurate ASR values on the uncoated 13Cr steel were reported in previous studies by using contact paste methods [129]. Acceptably low ASR values, much below 50 $m\Omega \cdot cm^2$, were obtained at 700 °C and under single air atmosphere, suggesting that a comparable contact resistance behaviour would be expected also for the $LaFeO_3$ coating.

The XRD patterns of the samples after dual atmosphere testing are reported in figure 6.6. In the case of the uncoated steel, only peaks ascribable to haematite phase are observable, indicating that the abrupt growth of electrical resistance could be due to massive growth of $Fe_2O_3$ on the sample surface. The pattern related to the coated sample is ascribable to a mixture of haematite and Fe-Cr spinel phases, with the perovskite phase peaks no longer visible.

The surface microstructure of the steel coupons after 750 h exposure in dual atmosphere oxidation conditions is reported in figure 6.7 and figure 6.8, where surface and cross-section micrographs of the uncoated and coated steel samples are respectively reported. Starting with the uncoated sample, figure 6.7(a) shows that the steel surface is completely covered by a homogeneous layer rich in iron oxide. The oxide scale, represented in section in figure 6.7(b) appears very thick, although

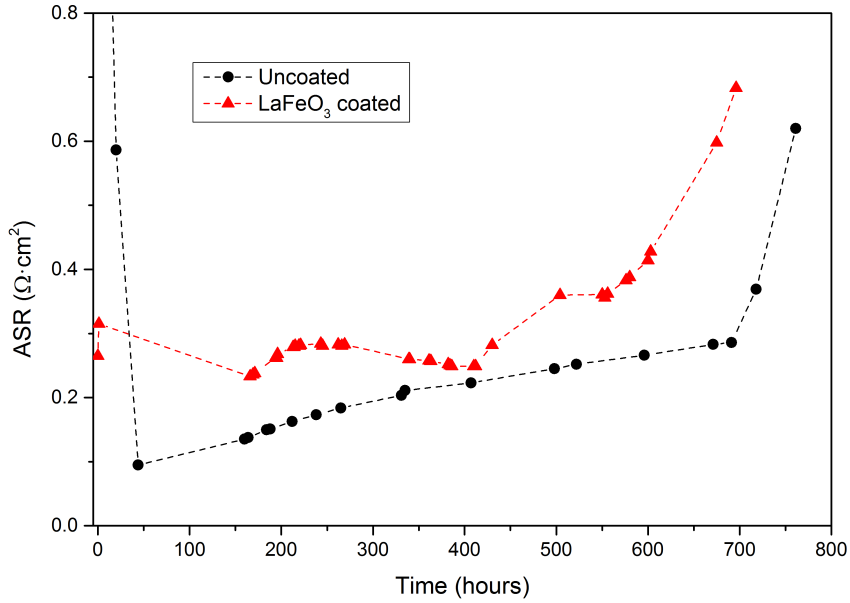



Figure 6.5: ASR curves acquired at 700 °C in dual-atmosphere ($H_2$/air) conditions for the coated and uncoated SS405 steel

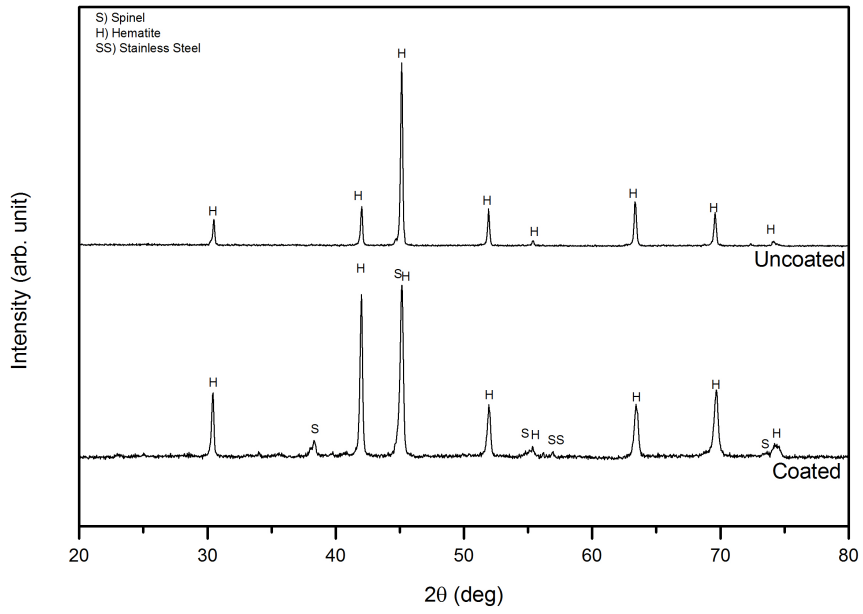



Figure 6.6: X-Ray diffraction patterns of the air-side steel surfaces after oxidation experiments carried out at 700 °C in dual-atmosphere ($H_2$/air).

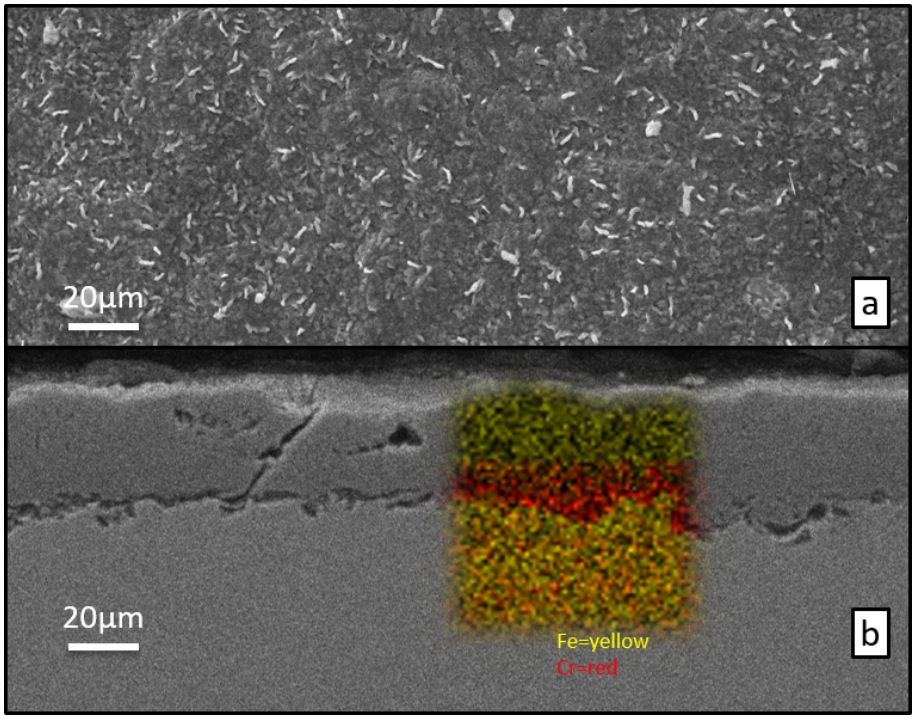



Figure 6.7: SEM images of the air-side steel surface (a) and section (b) of the uncoated SS405 steel after oxidation in dual atmosphere at 700 °C and over imposed SEM/EDX map of Fe and Cr elements.

a good general morphology is apparently preserved in terms of scale density, adherence and compactness. A dual layer nature is clearly observable being the iron oxide (i.e., haematite) concentrated on the outer surface, whereas the innermost layer is made up of a mixed Fe-Cr oxide.

In marked contrast with the uncoated steel sample, the perovskite coated sample surface, depicted in figure 6.8(a), shows a damaged structure compatible with a localized nodule attack. The surface shows, in fact, a characteristic buckled appearance, with presence of numerous protruding haematite nodules. The haematite nodules appear to be separated by more uniform regions of layered haematite, and nodules and layered haematite regions cover almost completely the sample surface. By way of example, the cross-section of figure 6.8(b) shows the morphology of a number of oxides nodules at different stage of growth lying over highly porous (Fe,Cr)-rich regions (oxidation spots). Furthermore, only some fragment remnants of the initial perovskite coating can be observed, mostly present in those surface regions that are far away from the iron oxide nodules. Coating detachment losses could also explain the absence of $LaFeO_3$ peaks in the XRD spectra of figure 6.6.

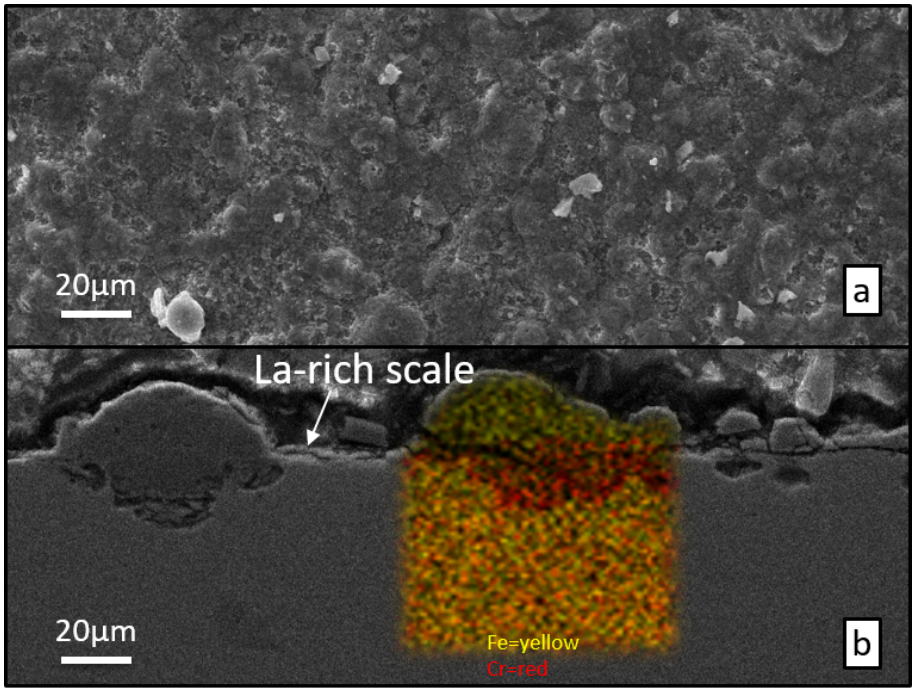



Figure 6.8: SEM images of the air-side steel surface (a) and section (b) of the $LaFeO_3$ coated SS405 steel after oxidation in dual atmosphere at 700 °C and over imposed SEM/EDX map of Fe and Cr elements.

### 6.1.1 Corrosion mechanism in dual-atmosphere oxidation environments

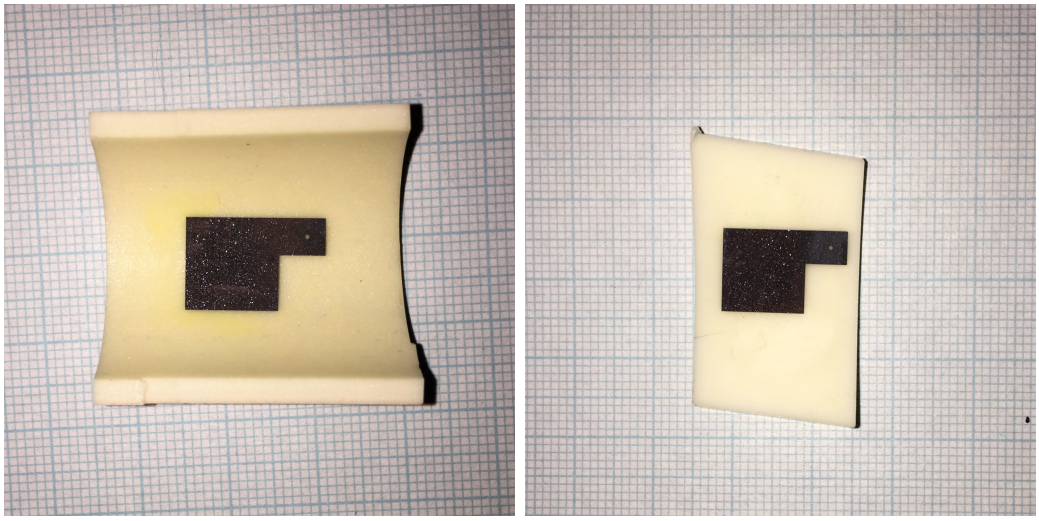
Hematite formation in dual atmosphere oxidation experiments should not be surprising since several studies have already described that similar phenomena take place in stainless steels as a consequence of a localized disruption (breakaway) of the initially-formed protective oxide layer [141–145]. Studies on breakaway corrosion in SOFC-relevant oxidizing conditions focus however on high Cr ferritic stainless steels (18Cr and higher) since they easily form a continuous, self-healing and thin chromia layer, at least in simple oxidizing atmospheres, which is needed for a good corrosion protection in SOFC interconnect applications. Breakaway corrosion on high Cr ferritic steels usually occurs as a non-uniform type of attack via a nodular growth corrosion mechanism. According to a prevalent view, haematite-rich nodules initially form at some small defects present in the protective chromia layer due to enhanced Fe cation mobility in hydrogen-containing atmospheres, resulting in a gradual conversion of chromia into a much less protective (Fe,Cr) oxide spinel. With a sufficiently long exposure lateral growth of haematite nodules may eventually cause the build-up of a continuous and thick haematite layer. However, according to figure 6.7(b), any strong oxidation spot beneath the layered oxide scale that could indicate a localized

initiation site for a haematite nodule formation could be not seen on the uncoated 13Cr steel sample. Moreover, the corrosion scale appears highly uniform with a very limited porosity development and absence of characteristic bumps or nodules over the whole sample surface (figure 6.7(a)). All these features do not seem consistent with a classical breakaway corrosion mechanism via a localized nodule attack. In this respect, previous studies indicate that uncoated 13Cr steels form (Fe,Cr) spinel oxides rather than the more protective chromia layers when exposed to air at 700 °C in single oxidation atmosphere experiments [129]. Relevant to this, it has been also reported that the Fe tracer diffusion coefficient is about 3 orders of magnitude higher than Cr in $(Cr_xFe_{1-x})_{3-\delta}O_4$ spinels over a wide range of oxygen activity and cationic composition [146], thereby suggesting that a poor dual atmosphere corrosion resistance of 13Cr steels in comparison to high Cr steels can be expected due to a much more rapid Fe cation transport through a (Fe,Cr) spinel layered surface. The growth process of haematite is likely to be controlled by fast lattice diffusion of Fe cations within the (Fe,Cr) spinel layer leading to uniform growth of haematite layers (layer-by-layer mechanism) in place of a localized corrosion attack. As a further support to the proposed mechanism, it may be worth mentioning that formation of continuous thick layers of haematite has been sometimes reported also on high Cr steels [144]. In particular, Rufner et al. [143] observed the growth of a thick and continuous Fe-rich oxide layer in a 18Cr (type 441) ferritic stainless steel exposed for 300 h at 800 °C [143] in dual air / 97$H_2$-3$H_2O$ atmospheres. The authors suppose that the use of high $H_2$ concentrations at the anode side could have dramatically enhanced the formation of more and more localized Fe-rich nodules and their quick lateral growth over the whole steel surface leading to formation of a continuous and thick haematite layer. Consistent with the classical breakaway corrosion model, the corrosion layer was characterized by the presence of a porous haematite-rich surface layer and by strong tendency to scale spallation, which is very different from the compact and adherent corrosion scale that we have observed on the uncoated 13Cr steel.

Conversely, the degradation mechanism of the perovskite coated steel appears to be very different from that of the uncoated 13Cr steel. Like high Cr steels, the $LaFeO_3$ coated surface shows evident signs of a localized type of corrosion attack, although the degradation rate of the surface electrical properties appeared very similar to the uncoated 13Cr steel as per figure 6.5, thus suggesting some similarities in the breakaway mechanism at some later stage of reaction in both the cases. However, the initiation of the localized attack on the coated steel is not easy to explain, although it may be supposed that some structure or chemical heterogeneity in the surface coating could be a preferential site for initial attack. From this

viewpoint, a spatially heterogeneous coating surface defect could be originating from an uneven distribution of coating thickness. In particular, suppositions could be made if a corrosion model involving local thin coating areas as preferential sites for initial localized attack in dual oxidation atmospheres can be used to interpret our experimental findings.

As previously mentioned, overall stability of perovskite oxides can be generally considered as the sum of thermodynamic and kinetic stability properties. At the anode $H_2/H_2O$ gas ratio used in this work, the oxygen partial pressure on the anode side is in the order of $10^{-24}$ atm, which leads to a steep oxygen chemical gradient between the opposite sides of the steel coupon. On the other hand, the $LaFeO_3$ is a thermodynamically stable phase over a wide range of oxygen partial pressures. For instance, the decomposition oxygen pressure at 800 °C is around $10^{-22}$ atm [147], which could suggest that $LaFeO_3$ should retain its structure stability, according to thermodynamics, since it is unlikely that the oxygen partial pressure would be lower than $10^{-22}$ atm inside the coating material, at 700 °C. Although $LaFeO_3$ meets the criteria for thermodynamic stability at these conditions, influence of hydrogen on kinetic stability of the $LaFeO_3$ coating cannot be excluded due to the already mentioned tendency towards Fe segregation. Hydrogen diffusion in a steel lattice occurs in a relatively short time, if compared with the experiment scale [148]. Permeation from the anode side, occurring in the first hours of experiment, will induce a steep oxygen concentration gradient across the perovskite coating layer, which could enhance the Fe cation transport and its surface segregation in the thinnest parts of the perovskite coating, where kinetic demixing effects and oxygen chemical gradients are the highest. Consequently, since these areas are the most susceptible to phase degradation and decomposition they should also correspond to the preferential sites for localized haematite nodule attack. Once haematite nodules are formed, it is likely that mechanical failure of the perovskite coating under the influence of evolving stress between the growing nodules and adjacent coating regions will promote further propagation of the corrosive attack in a way similar to the uncoated 13Cr steel. In fact, coating detachment will leave exposed a (Fe,Cr) spinel sublayer with a chemical composition very similar to that naturally forming on the uncoated 13Cr steel. Fe cation transport through the surface regions covered only by the spinel layer should therefore raise to haematite formation in later stages of reactions through a more uniform growth mechanism similar to that discussed for the uncoated steel.



(a) as-coated → 200 h (b) 200 h → 400 h

Figure 6.9: Pictures of the K41 foil samples passivated with a thick La-Fe perovskite coating on the alumina supports after the indicated intervals of oxidation (air, 700 °C).

## 6.2 Oxidation behaviour of passivated K41 steel

### 6.2.1 Thick perovskite coating

K41 samples passivated with a thick La-Fe perovskite based coating, processed for 48 h in the 10Mg salt, were subjected to oxidation treatments in air to evaluate the coating stability.

In figure 6.9 the pictures of alumina supports used for the experiments are shown. After the first 200 h the support is stained with yellowish marks. Being chromate salts characterized by yellow colour, it is straightforward to identify the stains with chromate release from the exposed samples. When proceeding for further exposure time, samples were rinsed in distilled water after 200 h and processed on new supports. After the initial release phenomena, no stains were observed for the following exposure intervals, suggesting that the observed chromium release is a transient phenomenon, probably related to contaminated salt residues not removed despite the long washing procedure in boiling water (see section 2).

In figure 6.10 the XRD patterns of a K41 thick coated sample after exposure for different intervals up to 1000 h are reported in comparison with the as-coated sample.

During the first 200 h of exposure minor peaks (*) ascribable to a mixed $(Fe,Cr)_2O_3$ phase appear [$Cr_{1.3}Fe_{0.7}O_3$ - JCPDS card N. 35-1112], most likely ascribable to the structuration of thin chromia-like oxide at the steel interface. Furthermore, a

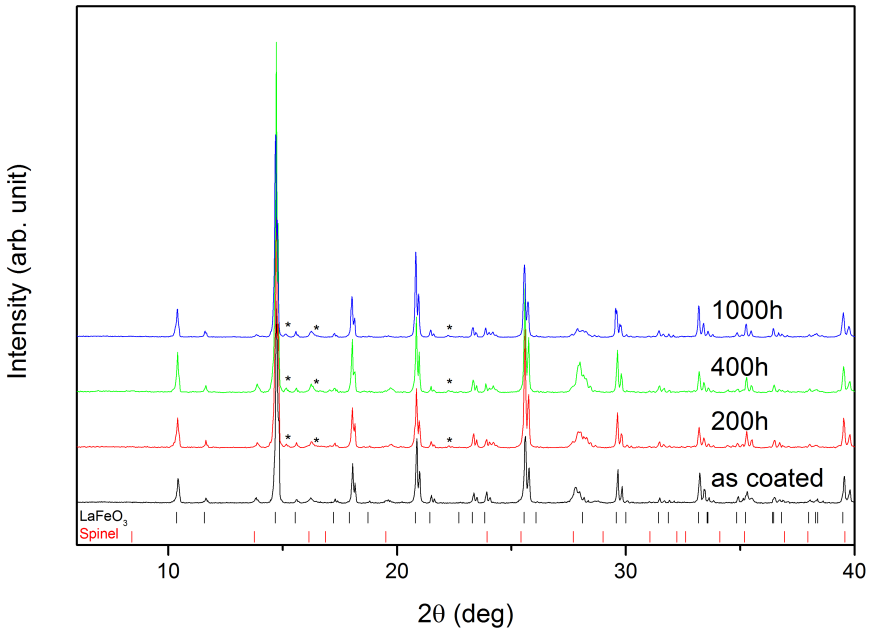



Figure 6.10: X-Ray Diffraction patterns (Mo surce) of the K41 steel samples passivated with a thick La-Fe perovskite coating after oxidation experiments carried out for different exposure time in air at 700 °C in comparison with the as-coated sample; (*) indicates reflections ascribable to a mixed $(Cr,Fe)_2O_3$ oxide.

slight shift of spinel peaks towards higher angles can be observed, probably due to chromium enrichment of the spinel oxide. After the first 200 h of experiment no significant changes are evident, suggesting high structural stability of the oxide phases for further processing time.

To evaluate the morphological changes induced by the oxidation treatment to the coated sample, in figure 6.11 is reported the SEM image of a coated sample after 200 h of experiment. The high temperature exposure promotes smoothing of the perovskite grains, but no other significant differences with respect to the as-coated sample are evident.

In figure 6.12 the results of cross section SEM analysis of the sample exposed for 200 h are reported. No significant growth of the oxide thickness can be observed. The coating retains the multi-layer morphology, with minor closed porosity originated in particular at the Fe oxide / Fe-Cr oxide interface. Slight detachment of the perovskite crystals highlight the fragility of the ceramic coating layer, and considering the overall compactness of the surface morphology are most likely due to the mechanical polishing procedure. Regarding the composition, EDX data reported in table 6.3 suggest the enrichment in iron of the perovskite layer and in chromium and manganese of the Fe-Cr oxide layer, suggesting slight element diffusion from the steel in the Fe-Cr oxide to form mixed Fe-Cr-Mn phases.

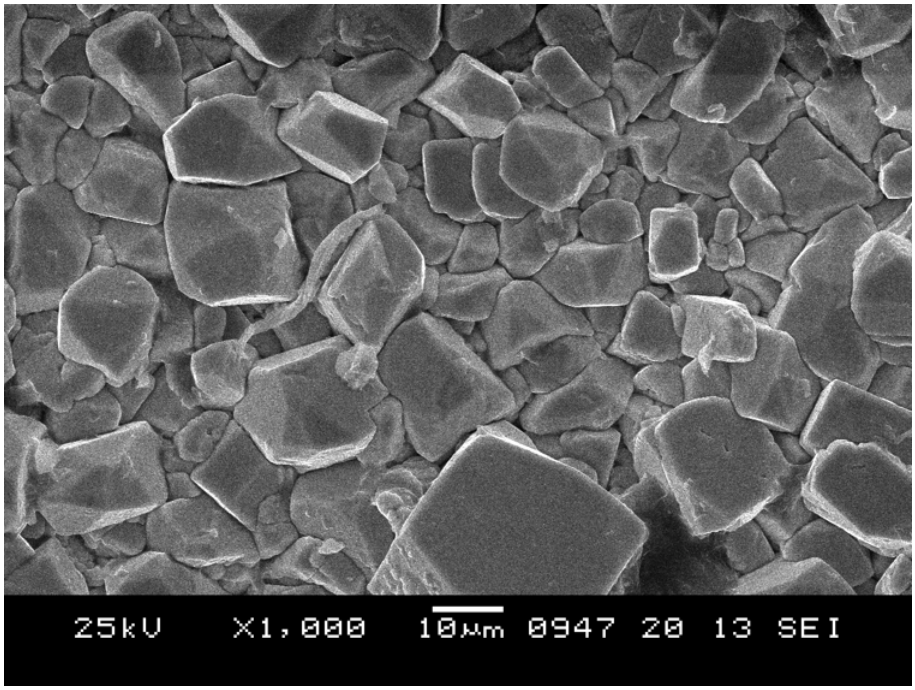



Figure 6.11: SEM image of the surface of a K41 sample passivated with a thick La-Fe perovskite coating after 200 h of oxidation in air at 700 °C.

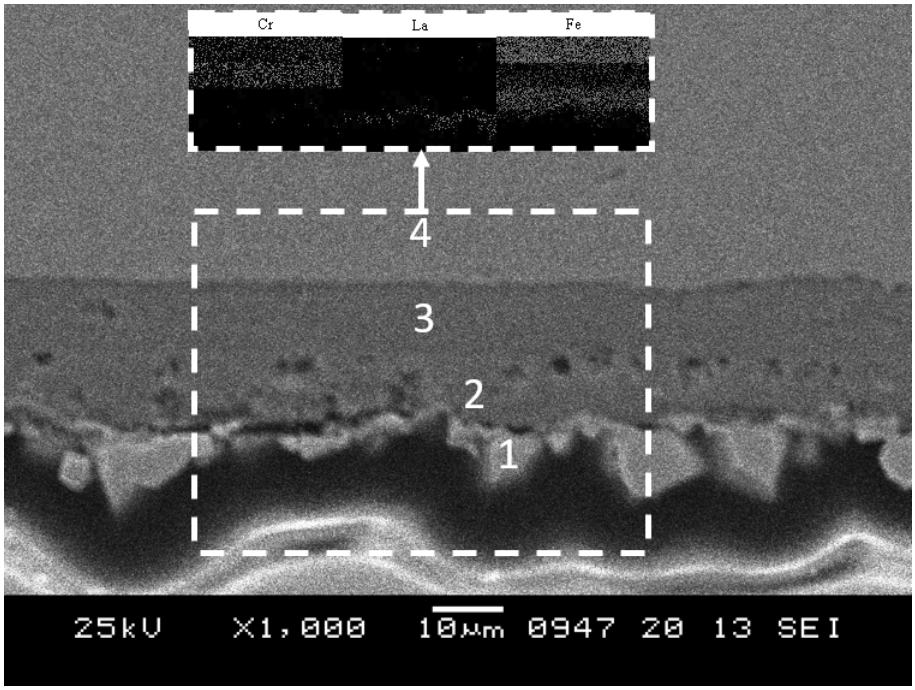



Figure 6.12: SEM image of the section of a K41 sample passivated with a thick La-Fe perovskite coating after 200 h of oxidation in air at 700 °C with EDX maps for Fe, Cr and La and the position of EDX analysis reported in table 6.3.

Table 6.3: Results of EDX analysis of the points indicated in figure 6.12:

| Point | Element (Wt%) | | | | |
|---|---|---|---|---|---|
| | La | Fe | Cr | Mn | O |
| 1 | 61.3 | 17.3 | | | 21.5 |
| 2 | 0.3 | 60.1 | 0.8 | | 38.8 |
| 3 | 0.2 | 29.5 | 25.0 | 0.3 | 45.0 |
| 4 | 0.2 | 82.2 | 14.5 | | 3.1 |

The surface morphology of a coated sample after 1000 h of oxidation is reported in figure 6.13. No major differences are observed with respect to the 200 h oxidized sample.

In figure 6.14 the SEM cross-sectional analysis of the 1000 h oxidized sample is reported. Again, the image suggests that the coating has retained its multi-layer structure with well defined interfaces, with the perovskite coating on top of an iron-rich layer, a Cr-Fe layer and a Cr-rich thin scale. Results from the EDX spot analysis, reported in table 6.4 suggest a slight further iron and oxygen enrichment of the perovskite layer and manganese and chromium enrichment of the Fe-Cr spinel intermediate layer. Remarkably, negligible presence of chromium is detected in the perovskite and in the Fe-rich spinel, suggesting that chromium is not incorporated in the perovskite phase or in the first sublayer, and that the coating acts as effective chromium barrier in the adopted experimental conditions.

Table 6.4: Results of EDX analysis of the points indicated in figure 6.14:

| Point | Element (Wt%) | | | | |
|---|---|---|---|---|---|
| | La | Fe | Cr | Mn | O |
| 1 | 57.8 | 19.7 | | | 22.4 |
| 2 | 0.3 | 59.7 | 0.8 | | 39.2 |
| 3 | 0.2 | 29.2 | 29.2 | 0.5 | 41.0 |
| 4 | | 80.2 | 17.2 | | 2.6 |

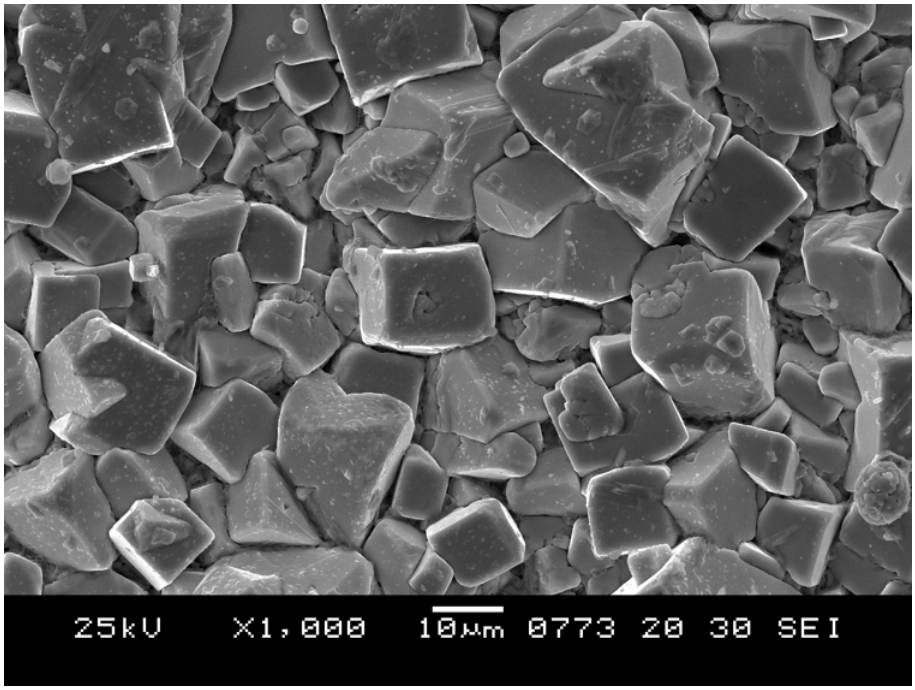



Figure 6.13: SEM image of the surface of a K41 sample passivated with a thick La-Fe perovskite coating after 1000 h of oxidation in air at 700 °C.

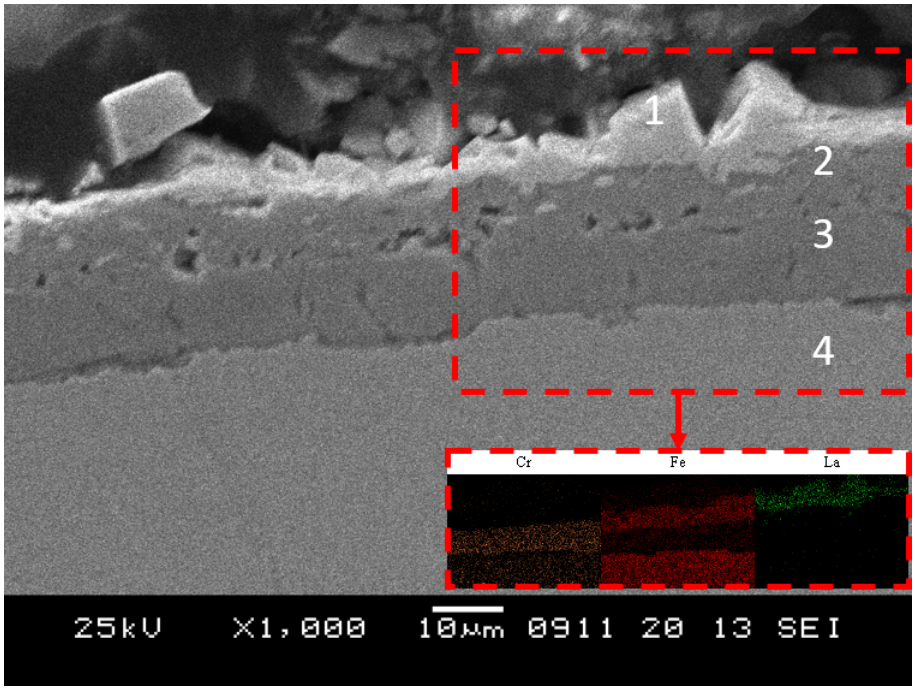



Figure 6.14: SEM image of the section of a K41 sample passivated with a thick La-Fe perovskite coating after 1000 h of oxidation in air at 700 °C with EDX maps for Fe, Cr and La and the position of EDX analysis reported in table 6.4.

### 6.2.2 Thin perovskite coating

Samples coated with a thin La-Fe perovskite layer, processed in the 10Mg0.25X salt for 8 h, were subjected to oxidation treatments in air similarly to thick-layer coated coupons. Differently from the thick coated samples, no yellow stains were observed on the alumina support after the high temperature oxidation experiments.

The XRD patterns reported in figure 6.15 allow to follow the structural evolution of the coated samples in air at 700 °C. During the first 200 h, growth of haematite and spinel phase occurs, similarly as observed in the SS405 case (see figure 6.2). Furthermore, minor reflections ascribable to the structuration of a La-rich silicate phase appear. Between 200 h and 400 h of exposure the growth of haematite and spinel phase proceeds, as well as the silicate phase structuration.

Differently to the thick La-Fe layer case, the thin coating is characterized therefore by a higher evolution during the first hours of test, similarly as the SS405 coated samples reported in section 6.1. This suggests that despite the difference in the substrate composition, similarities in the passivation layer morphology and structure promote the same oxidation phenomena.

The surface morphology of the surface after 200 h of oxidation is depicted in figure 6.16. No sign of spallation or cracks are detected, with the steel sample homogeneously covered. The oxidation treatment promotes the structuration of small crystals, and the smoothing of the globular particles seen on the as-coated sample. The appearance of fiber-like particles can be observed, most likely ascribable to the structuration of silicates.

The cross-sectional analysis image is reported in figure 6.17, with the EDX maps for Cr, Fe and La. The steel is covered by a dense oxide scale, with heavy elements (i.e. La) concentrated in a thin scale, as observed in the as-coated sample. With respect to the as-coated sample, characterized by irregular bumps due to the presence of small superficial iron oxide particles, smoothing of the surface occurred, with the oxidized sample characterized by a significantly more regular surface. Results of EDX spot analysis, reported in table 6.5, confirm the trend observed for the as-coated sample, with lanthanum signal decreasing with the coating depth. EDX data suggest furthermore Fe-Cr enrichment of the oxide scale, compatible with the structuration and growth of the spinel and haematite phase observed with XRD diffraction. Traces of Manganese are also detected at the interface, confirming the tendency of Mn to diffuse in the chromium-rich interface oxide layer, as observed in section 6.2.1.

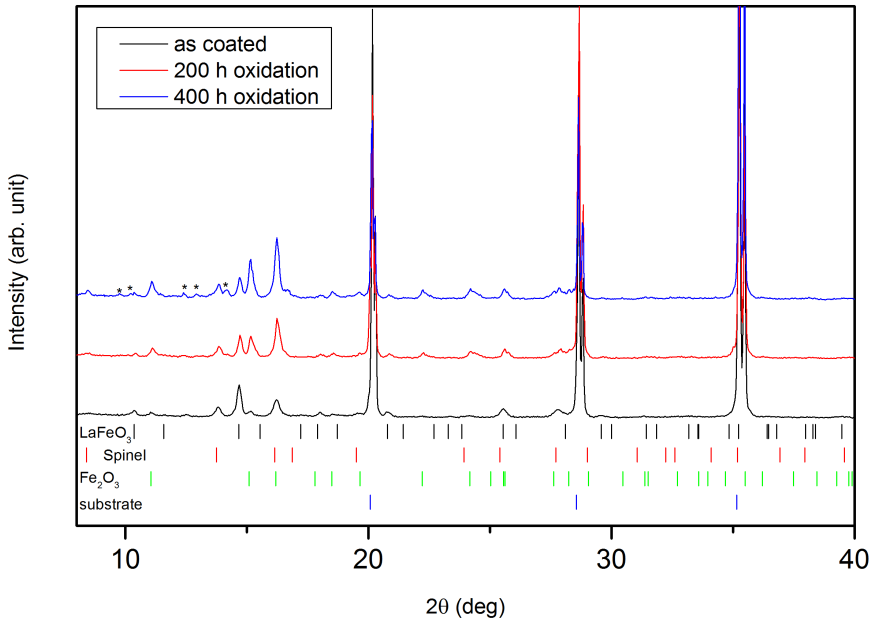



Figure 6.15: X-Ray Diffraction patterns (Mo surce) of the K41 steel samples passivated with a thin La-Fe perovskite coating after oxidation experiments carried out for different exposure time in air at 700 °C in comparison with the as-coated sample; (*) indicates reflections ascribable to a La-rich silicate phase.

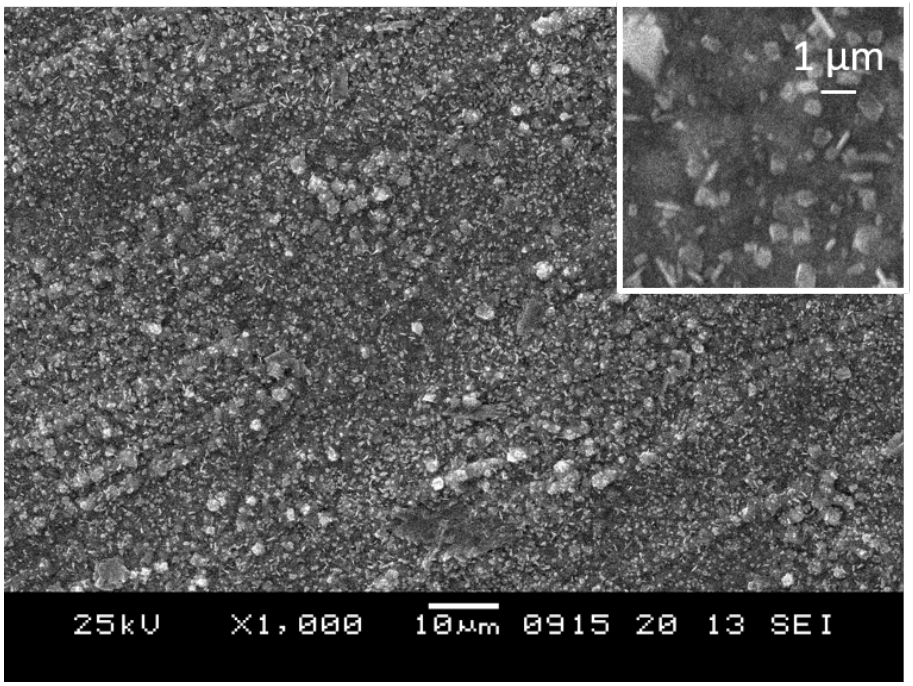



Figure 6.16: SEM image of the surface of a K41 sample passivated with a thin La-Fe perovskite coating after 200 h of oxidation in air at 700 °C.

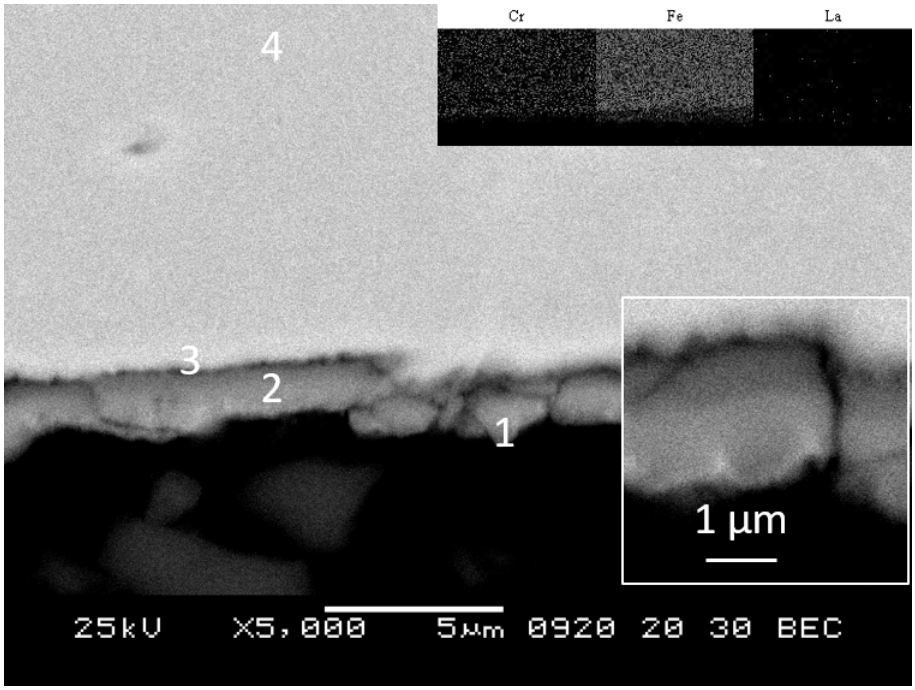



Figure 6.17: SEM image of the section of a K41 sample passivated with a thin La-Fe perovskite coating after 200 h of oxidation in air at 700 °C with EDX maps for Fe, Cr and La and the position of EDX analysis reported in table 6.5.

Table 6.5: Results of EDX analysis of the points indicated in figure 6.17:

| Point | Element (Wt%) | | | | |
|---|---|---|---|---|---|
| | La | Fe | Cr | Mn | O |
| 1 | 8.3 | 33.3 | 1.9 | | 56.6 |
| 2 | 2.9 | 43.8 | 8.5 | 0.4 | 44.4 |
| 3 | 0.8 | 36.1 | 26.4 | 1.5 | 35.2 |
| 4 | | 79.6 | 17.3 | 0.5 | 2.6 |

The surface after 400 h of exposure is reported in figure 6.18. The samples are still characterized by a dense appearance of the coating layer, with further structuration of the small crystals and fibrous particles observed after 200 h.

The cross-sectional analysis image is reported in figure 6.19, with the EDX maps for Cr, Fe and La. The steel is covered by a dense and adherent oxide scale. The coating shows high similarity to the 200 h exposed sample, with the surface richer in heavy elements (i.e. La). From the EDX maps, Cr seems confined in the interface layer. Results of EDX spot analysis, reported in table 6.6, confirm the observation carried out on the as-coated sample and on the 200 h exposed steel, suggesting that after the oxidation experiment the oxide scale is composed of the thin perovskite layer well adherent to an iron oxide layer, covering a mixed Fe-Cr oxide layer. Also in this case Mn presence can be detected at the interface, in amounts significantly

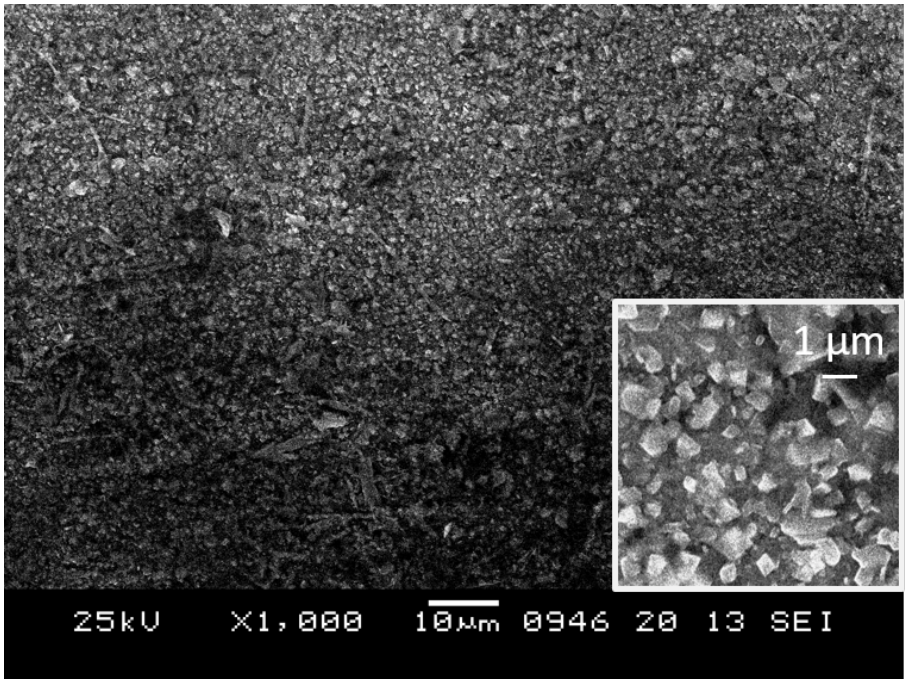



Figure 6.18: SEM image of the surface of a K41 sample passivated with a thick La-Fe perovskite coating after 400 h of oxidation in air at 700 °C.

higher than those detected in oxidized thick coatings. In the case of a thin protective layer, higher compositional gradients subsist: cationic mobility and evolution of the coating layer is therefore promoted, as testified also from the morphological evaluation. The absence of chromium-related stains on the alumina supports, and the chromium confinement by the perovskite layer observed with SEM/EDX analysis, suggests however that the phenomena is limited to the sublayer, and, as observed on the SS405 steel, also in the case of thin coatings grown on the K41 steel the perovskite acts as effective barrier to chromium release protecting the alloy from the oxidation.

Table 6.6: Results of EDX analysis of the points indicated in figure 6.19:

| Point | Element (Wt%) | | | | |
|---|---|---|---|---|---|
| | La | Fe | Cr | Mn | O |
| 1 | 22.0 | 16.1 | 1.8 | | 60.2 |
| 2 | 5.3 | 41.1 | 5.7 | | 47.9 |
| 3 | 1.2 | 26.7 | 26.1 | 2.7 | 43.2 |
| 4 | 0.3 | 81.1 | 15.3 | | 3.2 |

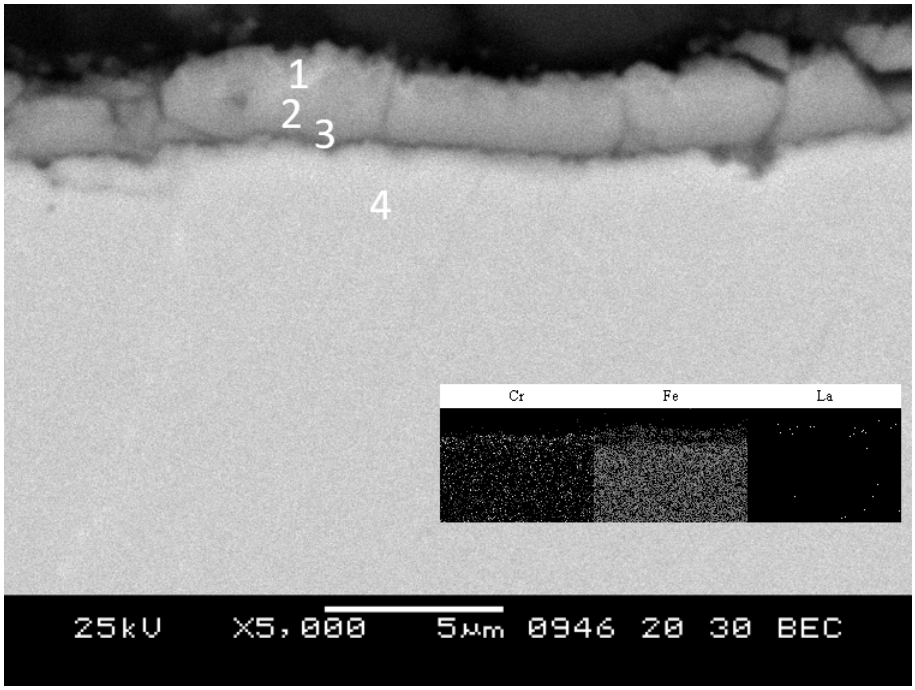
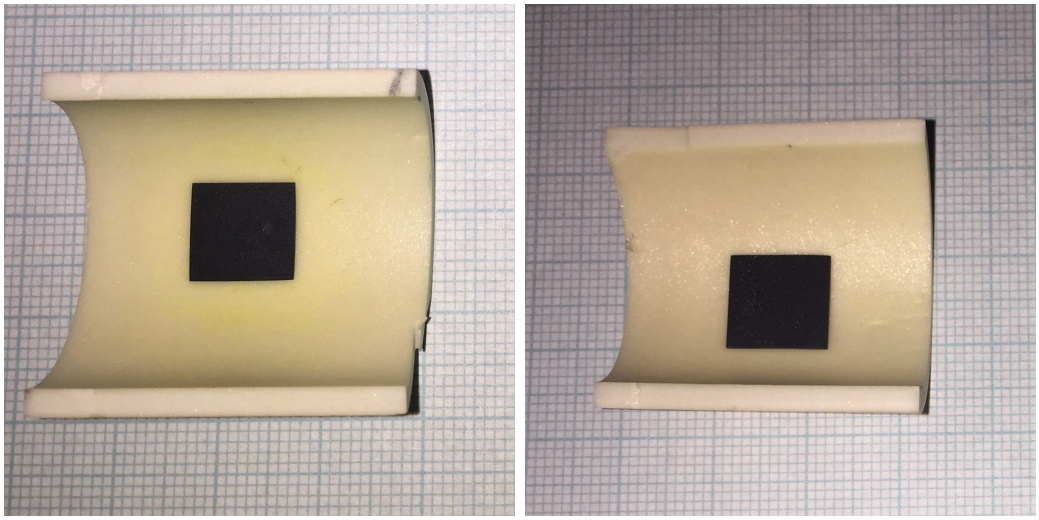



Figure 6.19: SEM image of the section of a K41 sample passivated with a thin La-Fe perovskite coating after 400 h of oxidation in air at 700 °C with EDX maps for Fe, Cr and La and the position of EDX analysis reported in table 6.6.

### 6.2.3 Cu-perovskite composite coating

The behaviour of the Cu-perovskite composite coating was evaluated with oxidation experiments in air at 700 °C similarly to the previous samples. As observable in figure 6.20a, after the first 200 h of test yellowish stains were visible on the alumina plate, as in the case of the thick La-Fe perovskite coated steel (figure 6.9). The samples exposed for further time, rinsed in distilled water after the first 200 h and exposed on new supports, do not show traces of contamination. This suggests that chromium release from thick La-Fe perovskite coatings obtained by the molten carbonate passivation method occurs as a transient phenomenon, most likely ascribable to the presence of contaminated salt residues.

In figure 6.21 the XRD patterns of the oxidized sample after different exposure times are reported. Similarly to the as-coated foil, the perovskite oxide constitutes the main phase, suggesting also in this case the high stability of the perovskite phase. Further reflections are ascribable to the substrate and to the presence of a Fe-rich spinel phase, similar to the one observed on the thick-coating oxidized samples described in section 6.2.1. A comparison with the as-coated pattern suggests that the high temperature exposure led therefore to the oxidation of the partially-reduced $Li_5Fe_5O_8$ spinel phase with the formation of the new spinel phase. No reflections ascribable to copper oxide or metallic copper are evident. Furthermore,



(a) as-coated → 200 h (b) 200 h → 400 h

Figure 6.20: Pictures of the K41 foil samples passivated with a Cu-perovskite composite composite on the alumina supports after the indicated intervals of oxidation (air, 700 °C).

the oxidized samples are characterized by the presence of minor peaks ascribable to a lanthanum-rich silicate phase (i.e. $LiLaSiO_4$), as previously observed on the thin oxidized perovskite coatings (section 6.1 and 6.2.2).

SEM images of the surface of a sample exposed for 200 h is reported in figure 6.22. Regarding the coating structure, the oxidation treatments promote a smoothing of the cubic grains, but no major differences can be observed with respect to the as-coated sample (figure 5.5). The evidence of aggregates of fibrous La-Si rich particles on the perovskite grains confirms the occurred structuration of lanthanum silicates during the high temperature exposure suggested by XRD analysis.

From the cross-section analysis, reported in figure 6.23, it can be observed that no significant evolution of the oxide layer occurs during the high-temperature exposure, although some closed porosity has developed in particular in the spinel sublayer. The outer layer shows minimal differences with respect to the as-coated sample, suggesting that also in this case the perovskite coating is characterized by high stability. Results of EDX spot analysis, reported in table 6.7, indicate an evolution of the sublayer composition but not of the perovskite outer layer. High-temperature exposure clearly promotes chromium diffusion. However, it is interesting to observe that chromium diffusion seems not directed outwardly, but from the Fe-Cr oxide layer towards the steel-coating interface, resulting in the formation of a chromium rich oxide layer (point 4, figure 6.23). Furthermore, it is interesting to observe the presence of copper in the iron-rich oxide (point 2), suggesting inward copper ion diffusion.

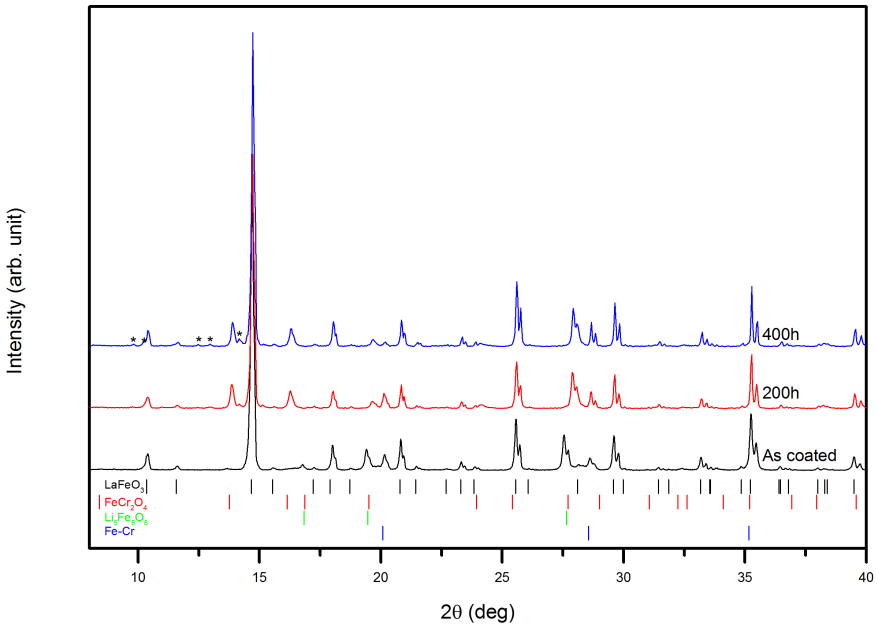



Figure 6.21: X-Ray Diffraction patterns (Mo surce) of the K41 steel samples passivated with a Cu-perovskite composite coating after oxidation experiments carried out for different exposure time in air at 700 °C in comparison with the as-coated sample.

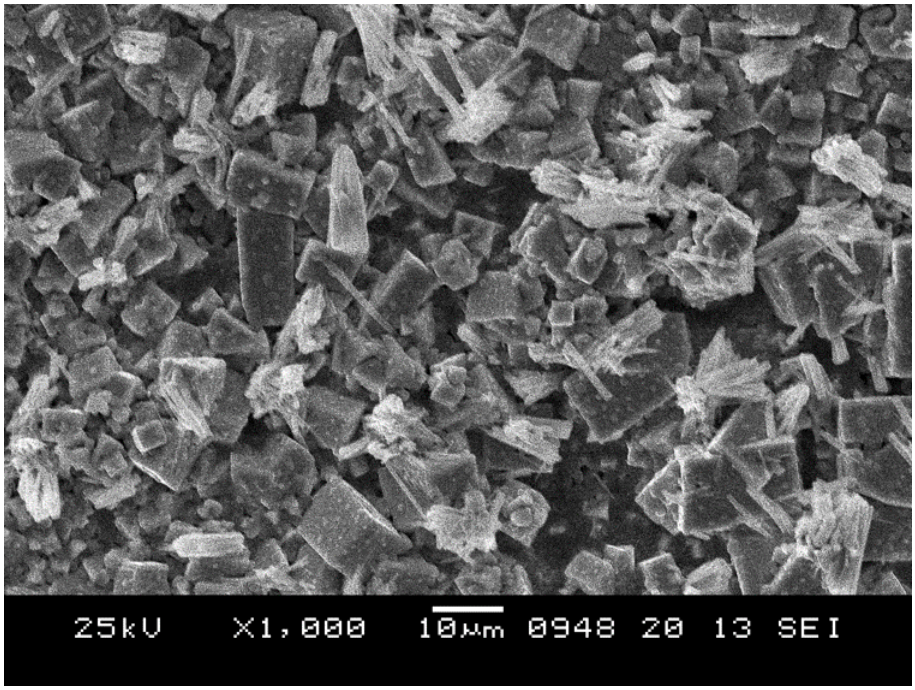



Figure 6.22: SEM image of the surface of a K41 sample passivated with a Cu-perovskite composite coating after 200 h of oxidation in air at 700 °C.

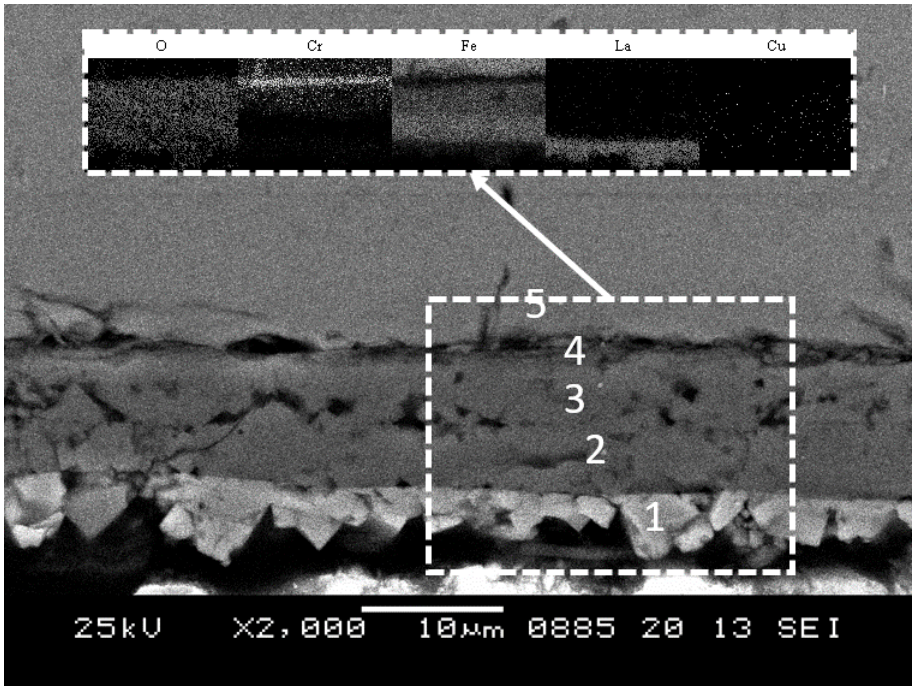



Figure 6.23: SEM image of the section of a K41 sample passivated with a Cu-perovskite composite coating after 200 h of oxidation in air at 700 °C with overimposed EDX maps and the position of EDX analysis reported in table 6.7

Table 6.7: Results of EDX analysis of the points indicated in figure 6.23:

| Point | Element (Wt%) | | | | | |
|---|---|---|---|---|---|---|
| | La | Fe | Cr | Cu | Mn | O |
| 1 | 63.6 | 17.1 | | | | 19.2 |
| 2 | 0.4 | 57.6 | 1.2 | 1.5 | | 39.3 |
| 3 | | 46.8 | 10.8 | | | 42.3 |
| 4 | | 24.0 | 39.9 | | 0.7 | 35.4 |
| 5 | | 87.6 | 9.8 | | | 2.5 |

The morphology of the surface of a sample exposed for 400 h is reported in figure 6.24. The surface is covered by a homogeneous crystalline layer, with the presence of some fibrous particles analogous to the one observed after 200 h of exposure. Regarding the perovskite phase, no significant differences can be observed in comparison to the as-coated sample apart from the smoothing of crystals edges, as observed in the La-Fe undoped thick coating.

Results of the SEM section analysis of a sample exposed for 400 h are reported in figure 6.25. From the morphological point of view, great similarity is observable with the as-coated sample (figure 5.6), suggesting that no significant evolution of the oxide scale occurs after 400 h at 700 °C. The EDX maps confirm the multi-layer structuration of the coating, with chromium gathering at the steel-coating

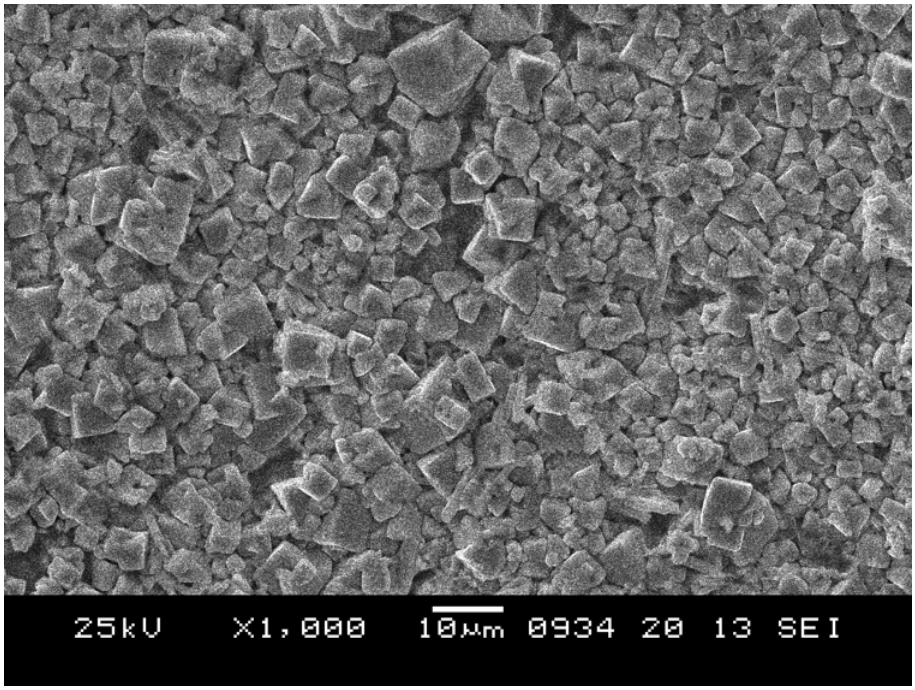



Figure 6.24: SEM image of the surface of a K41 sample passivated with a Cu-perovskite composite coating after 400 h of oxidation in air at 700 °C.

interface layer. Results of EDX spot analysis, reported in table 6.7, indicate that the evolution observed after the first 200 h of exposure is carrying on. Copper traces are still visible in the first Fe-rich oxide layer, but in minor amount. Furthermore, manganese concentration in the chromium rich layer suggests its diffusion toward the interface with the formation of mixed Cr-Fe-Mn spinels.

Table 6.8: Results of EDX analysis of the points indicated in figure 6.25:

| Point | Element (Wt%) | | | | | |
|---|---|---|---|---|---|---|
| | La | Fe | Cr | Cu | Mn | O |
| 1 | 59.6 | 16.3 | | | | 24.2 |
| 2 | 46.8 | 22.4 | 0.4 | 0.4 | | 30.0 |
| 3 | 2.2 | 44.1 | 9.3 | 0.4 | | 44.0 |
| 4 | 0.4 | 18.5 | 36.7 | | 0.7 | 43.8 |
| 5 | | 37.1 | 28.7 | | 1.3 | 32.9 |
| 6 | | 85.5 | 12.3 | | | 2.2 |

Regarding copper diffusion in the spinel sublayer, two hypotheses may be raised regarding its presence: migration from the coating surface, or oxidation and diffusion from the spinel/perovskite interface. The first possibility may be supported by the absence of large copper oxide clusters evident in the surface. However, if diffusion pathways that allow copper migration towards the bulk exist, it is likely to expect

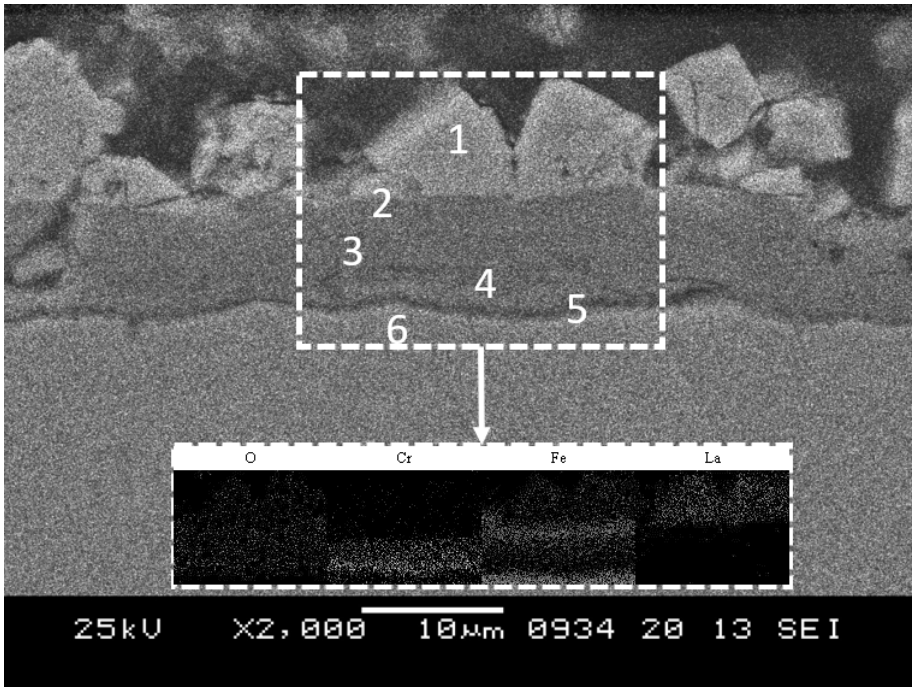



Figure 6.25: SEM image of the section of a K41 sample passivated with a Cu-perovskite composite coating after 400 h of oxidation in air at 700 °C with overimposed EDX maps and the position of EDX analysis reported in table 6.8.

chromium outward migration through the same paths, with its release not hindered by the coating layer: significant chromium diffusion across the first spinel sublayer and the perovskite layer should therefore be observed. This is in contrast with the visual inspection of the alumina supports, showing that after the initial chromate deposition no significant evolution is observed, and with the sectional analysis. The second option is deriving instead from the deposition mechanism. It was in fact clearly demonstrated in the case of silver-perovskite composite deposition, due to the opportune experimental response of Ag in backscattered electron images - causing it to light up with respect to the perovskite phase due to its high molecular weight - that small metal particles are encased in the perovskite grains at the sublayer-perovskite interface (see figure 5.19). Despite not being evident in the copper-perovskite composite layers evaluated with high temperature oxidation tests, due to the lower molecular weight of Cu, it is likely to suppose that similar trapping of metallic copper occurs during the deposition process. The traces detectable in the spinel sublayer could then be due to its presence at the perovskite/spinel interface prior to the exposure experiments as discrete metal particles, undergoing oxidation at high temperature and diffusing in the iron-rich sublayer.

## 6.3 Concluding remarks on the oxidation behaviour of coated steels

The results reported in this chapter allow to draw some conclusions on the oxidation behaviour of the coated steels. The perovskite-based coatings showed high stability, when oxidized in single environment experiments. The tests carried out on the SS405 steel, alloy characterized by poor corrosion resistance at 700 °C, showed a remarkable improvement of its oxidation behaviour, with an initial coating evolution during the first hours of exposure, ascribable to the oxygen-lean nature of the synthesis environment, followed by slight changes in the coating structure up to 1800 h. The comparison of these findings with the results reported for the uncoated steel show therefore that the thin perovskite based coating is highly effective in oxidizing conditions. The results related to the 18Cr K41 steel confirm the findings regarding the perovskite-based coating stability for both thin and thick coating layers, allowing to compare the different evolutions promoted by the different coating morphologies. In particular, while little morphological and compositional evolution can be observed in the case of thick layers (i.e. La-Fe and Cu/perovskite composite), the experiments conducted on thin coatings show higher chemico-physical evolution, with signs of cation diffusion phenomena most likely due to the higher chemical gradients derived by the reduced thickness.

Regarding chromium retention capability, a qualitative evaluation was performed observing the alumina supports used for the exposure tests. In the case of thick La-Fe and Cu-perovskite composite coatings, characterized by similar morphology, yellowish stains on the alumina supports were observed after the first 200 h of exposure in air. For further exposure time no signs were observed. Cross-sectional analysis of the thick coatings did not show chromium presence across the perovskite layer, suggesting that chromium release may be a transient phenomenon due to salt residues on the surface of the thick coating layers. This morphology could be therefore effective and suitable for the application if subjected to a pre-oxidation treatment to remove these residues. SS405 and K41 samples passivated with a thin perovskite based coating did not instead produce marks or stains on the support.

The evidences reported in this chapter can be compared with recent results related to thin La-Fe perovskite coatings grown as well with the molten salt method on 22Cr Crofer 22H and SSHT substrates [149]. The passivation layers reported in this work were characterized by limited thickness (e.g. figure 4.20c - less than 1 μm), and the oxidation behaviour of coated steels was evaluated by means of phase stability, electrical performances and chromium retention ability up to 1000 h. During

the oxidation test, significant evolution of the oxide layers was observed, including growth of spinel, haematite, silicate phases and degradation of the perovskite phase, much more evident on the thinner layer grown on the Crofer 22H steel. As expected from the occurrence of perovskite degradation phenomena, chemical analyses showed evidences of Cr diffusion into the simulated cathode layer: while minor amounts (i.e. 1-2 wt%) were detected after 1000 h in the cathode layer bulk for the SSHT coated steel, higher quantities (i.e. 5-7 wt%) were found for the Crofer 22H samples. This difference is most likely ascribable to higher instability and permeability associated to the latter's lower coating thickness. However, despite chromium diffusion occurrence, the ASR values could be considered suitable for the application ($<0.05\ \Omega \cdot cm^2$) through the whole examined period for both substrates, furthermore showing a decreasing trend.

Comparing these data with the results reported in this chapter, it is likely to suppose the existence of a coating thickness threshold to minimize the kinetic instability phenomena described in section 1.4 and avoid perovskite degradation and chromium release. The oxidation experiments carried out on the SS405 steel show in fact that the perovskite layer is remarkably stable up to 1800 h. The experiments carried out on the thin perovskite coated K41 alloy, despite the shorter duration, do not highlight significant evidences suggesting the occurrence of perovskite degradation phenomena. As reported in [149], thinner coatings deposited on much more noble steels undergo instead significant evolution. Therefore, the fact that the perovskite layer grown through the template conversion mechanism on different substrates possesses similar thickness, as shown in section 4.2, suggests that the contribution of the oxide sublayer in ensuring the perovskite stability can't be neglected. The presence of a sufficiently thick oxide sublayer, as grown on the K41 and SS405 alloys, will in fact give rise to lower oxygen and electrochemical gradients across the perovskite. With the opportune coating thickness, the driving forces for cation pumping in perovskite structures should be therefore minimized, avoiding cation segregation and kinetic demixing effects and ensuring long-term stability to the perovskite phase.

The experiments carried out in dual-atmosphere on the SS405 alloy show instead significant oxidative phenomena both on the coated and uncoated steel. Dual atmosphere exposure represents however a highly challenging environment. Results reported in recent years show in fact that significant and unexpected corrosion processes proceed also on high chromium steels, with mechanisms and possible solutions yet to be precisely identified [150, 151]. The difference in the corrosion morphology observed between the uncoated and coated steel in this work, a diffuse haematite growth in the first case and a localized attack in the latter, suggest however the positive effect of the coating layer. This leaves space to further optimization in terms of

microstructure, thickness and mechanical robustness to ensure effective protection also in the highly corrosive dual atmosphere environments.

# Conclusions and outlook

The aim of this thesis was the evaluation of cost-effective and environmentally friendly methods for the synthesis of coating materials and for the production of effective coating layers. The synthesis of Mn-Co spinels, currently representing the best compromise between processability and effectiveness among coating materials, was approached by means of cost-effective and environmentally friendly mechanochemical techniques. Furthermore, as an innovative approach, a novel molten salt passivation technique was applied to produce dense La-Fe perovskite based coatings on SOFC suitable alloys.

In particular, High Energy Ball Milling was evaluated to produce mixed Mn-Co and Fe-Cu doped Mn-Co spinels. The mechanochemical treatment of Mn-Co oxide mixtures promotes the solid-state reaction of the starting compounds, with the formation of nano-structured powders. Long term processing (e.g. 65 h) leads to the complete reaction: in the case of the Co-rich sample a single-phase spinel is formed, while in the Mn-rich sample a multi-phase mixture, with phases commonly not produced by traditional high temperature solid state techniques, is obtained. In view of the application, a relatively short milling treatment (e.g. 10h) proved effective in terms of comminution and activation degree, despite not promoting the formation of single-phase products. The short mechanochemical approach may be in fact effective to produce powder mixtures of opportune compositions to be applied through wet-powder deposition techniques. The high-temperature desired phase would be then formed during the sintering treatments, without the need for high-temperature single-phase powder calcination steps commonly adopted in ceramic powder synthesis.

To optimize the Mn-Co spinel composition, different Mn-Co, Cu-Mn-Co, Fe-Mn-Co and Fe-Cu-Mn-Co powders were synthesised through the short HEBM treatment in order to evaluate the effect of chemical composition on phase stability, sintering behaviour, thermal expansion and electrical conductivity. It was observed that high Mn:Co ratios and iron addition enhance spinel phase stability at high temperature, while copper addition decreases the spinel phase stability both in oxidizing and re-

ducing conditions. Sintering behaviour in air is greatly enhanced by copper addition; the doping did not however succeed in lowering the sintering temperature to levels suitable for the material. The reactive sintering route, consisting in a reducing and in an oxidizing step, was therefore studied. A significant shrinkage is obtained during the first step, most likely ascribable however to the spinel decomposition rather than to an effective densification. The oxidation step induces instead spinel recovery, without significant dimensional changes, leading to significant densification with high densities obtained at 800 °C. The composition influences this process, with Fe-Cu simultaneous doping significantly effective in enhancing final density. Furthermore, relations between the chemical composition and thermal expansion behaviour were found. In particular, CTE is raised by Co and Cu content, and lowered with Fe and Mn. This trend is retained in the case of multiple doping, allowing to hypothesize the tailoring of the composition ad hoc for the specific substrate alloy. A similar relation was observed also in the case of electrical conductivity.

Substitution of Co with Fe and Cu to obtain a Fe-Cu doped Mn-Co spinel proved therefore as a versatile approach to enhance sintering behaviour and electrical conductivity while retaining thermal expansion compatibility with ferritic stainless steels. This suggests that a multiple doping approach can represent an effective strategy to design cobaltite materials properly tailored to the application.

The application of a molten carbonate chemical surface conversion technique to high-chromium stainless steels, to produce dense and adherent La-Fe perovskite based coatings, was initially evaluated studying and optimizing the experimental variables and the bath composition. The method was subsequently successfully exploited to produce La-Fe perovskite based coatings characterized by tunable thickness, full density and high homogeneity. Furthermore, the occurrence of opportune galvanic coupling phenomena was supposed and verified in appropriately tailored small scale experiments after the introduction of metal oxides (i.e. Cu, Ni, Ag) in the melt. The reduction phenomenon of the nobler metal on the coating surface was exploited to promote the passivation layer formation and to obtain metal-perovskite composite structures.

The stability of the produced coatings was evaluated with high temperature (700 °C) exposure experiments. The oxidation experiments were carried out on different substrates and coating structure combinations. A first evaluation was carried out on a SS405 (13Cr) alloy, selected as low cost alternative to high chromium alloys and as suitable benchmark due to its poor high temperature oxidation resistance, coated with a thin La-Fe perovskite based coating. The experiments were carried out at 700 °C in air and in dual $H_2$/air atmosphere (3% $H_2O$-$H_2$ and 3% $H_2O$-air flow respectively at the simulated anode and cathode side). A remarkable improvement of

the corrosion resistance was noticed in air, with no chromium release or significant corrosion signs after 1800 h. Breakaway was instead observed in the more challenging dual atmosphere conditions, with the coated sample characterized however by reduced corrosion with respect to the uncoated steel.

Oxidation experiments carried out in air at 700 °C on K41 (18Cr) coated steels allowed to observe a remarkable stability of the coating layers in the case of thick perovskite and Cu-perovskite composite coatings, possessing similar morphology. Both samples were characterized by a transient chromium release phenomenon occurring in the first hours of experiment, most likely due to the decomposition of salt residues from the surface rather than to actual chromium diffusion through the coating layer: presence of chromium across the perovskite layer, suggesting its diffusion, was in fact not detected after the experiments. Samples coated with thin perovskite layers showed instead higher chemico-physical evolution, with signs of cation diffusion phenomena most likely driven by the higher chemical gradients derived by the reduced thickness. The thin perovskite layer deposited on the high chromium K41 steel proved however effective in protecting the alloy from corrosion, with no visible signs of chromium release.

The molten carbonate conversion coating technique seems therefore a suitable approach to produce dense La-Fe perovskite based coatings stable in SOFC simulated cathode environments. The development of the technique to produce the metal-perovskite coating, taking advantage of the galvanic coupling phenomena evidenced in this work, seems moreover a promising strategy to tailor the coating properties.

The results reported in this work highlight new research trends that could be pursued. In particular, deposition of the multiple (Fe-Cu) doped spinels through wet-powder techniques could be evaluated exploiting their enhanced sintering behaviour in order to obtain highly dense coating layers characterized by opportunely tailored CTE and high electrical conductivity.

# Bibliography


[1] R. Steinberger-Wilckens et al. “Benchmarking Protective Coatings for SOFC ferritic steel interconnects – The SCORED 2 : 0 Project”. In: *Proceedings of the 12th European SOFC & SOE Forum 2016*. 2016, pp. 41–50.

[2] M. Höök and X. Tang. “Depletion of fossil fuels and anthropogenic climate change - A review”. In: *Energy Policy* 52 (2013), pp. 797–809.

[3] K. Kaygusuz. “Energy for sustainable development: A case of developing countries”. In: *Renewable and Sustainable Energy Reviews* 16.2 (2012), pp. 1116–1126.

[4] J. Zheng et al. “Analysis of air pollution reduction and climate change mitigation in the industry sector of Yangtze River Delta in China”. In: *Journal of Cleaner Production* 114.2015 (2016), pp. 314–322.

[5] E. Tambo, W. Duo-quan, and X. N. Zhou. “Tackling air pollution and extreme climate changes in China: Implementing the Paris climate change agreement”. In: *Environment International* 95 (2016), pp. 152–156.

[6] H. M. Al-Maamary, H. A. Kazem, and M. T. Chaichan. “The impact of oil price fluctuations on common renewable energies in GCC countries”. In: *Renewable and Sustainable Energy Reviews* August (2016).

[7] N. Shaigan et al. “A review of recent progress in coatings, surface modifications and alloy developments for solid oxide fuel cell ferritic stainless steel interconnects”. In: *Journal of Power Sources* 195.6 (2010), pp. 1529–1542.

[8] S. Frangini, F. Zaza, and A. Masci. “Molten carbonate corrosion of a 13-Cr ferritic stainless steel protected by a perovskite conversion treatment: Relationship with the coating microstructure and formation mechanism”. In: *Corrosion Science* 62 (2012), pp. 136–146.

[9] B. C. H. Steele and A. Heinzel. “Materials for fuel-cell technologies”. In: *Nature* 414.6861 (2001), pp. 345–352.

[10] S. Mekhilef, R. Saidur, and a. Safari. “Comparative study of different fuel cell technologies”. In: *Renewable and Sustainable Energy Reviews* 16.1 (2012), pp. 981–989.

[11] H. Spacil. *Electrical Device including Nickel Containing Stabilized Zirconia Electrode. - Patent US3503809 A*. 1970.

[12] H.-H. Möbius. “On the history of solid electrolyte fuel cells”. In: *Journal of Solid State Electrochemistry* 1.1 (1997), pp. 2–16.

[13] A. Weber and E. Ivers-Tiffée. “Materials and concepts for solid oxide fuel cells (SOFCs) in stationary and mobile applications”. In: *Journal of Power Sources* 127.1-2 (2004), pp. 273–283.

[14] S. C. Singhal. “Solid Oxide Fuel Cells”. In: *The Electrochemical Society Interface* (2007), pp. 41–44.

[15] W. Zhu and S. Deevi. “Development of interconnect materials for solid oxide fuel cells”. In: *Materials Science and Engineering: A* 348 (2003), pp. 227–243.

[16] N. Sakai et al. “Lanthanum chromite-based interconnects as key materials for SOFC stack development”. In: *International Journal of Applied Ceramic Technology* 1.1 (2004), pp. 23–30.

[17] T. Akashi, T. Maruyama, and T. Goto. “Transport of lanthanum ion and hole in LaCrO3 determined by electrical conductivity measurements”. In: *Solid State Ionics* 164.3-4 (2003), pp. 177–183.

[18] T. Nakamura, G. Petzow, and L. Gauckler. “Stability of the perovskite phase LaBO3 (B = V, Cr, Mn, Fe, Co, Ni) in reducing atmosphere I. Experimental results”. In: *Materials Research Bulletin* 14.5 (1979), pp. 649–659.

[19] F. Tietz. “Components manufacturing for solid oxide fuel cells”. In: *Solid State Ionics* 152-153.DECEMBER 2002 (2002), pp. 373–381.

[20] W. A. Surdoval. “The Solid State Energy Conversion Alliance (SECA) - A US Department of Energy initiative to promote the development of mass customized solid oxide fuel cells for low-cost power”. In: *The 7th International Symposium on Solid Oxide Fuel Cells - Tsukuba*. Vol. 2001. 16. 2001, pp. 53–62.

[21] Z. Yang. “Recent advances in metallic interconnects for solid oxide fuel cells”. In: *International Materials Reviews* 53.1 (2008), pp. 39–54.

[22] Z. Yang et al. "Selection and Evaluation of Heat-Resistant Alloys for SOFC Interconnect Applications". In: *Journal of The Electrochemical Society* 150.9 (2003), A1188.

[23] L. Cooper et al. "The effect of surface treatment on the oxidation of ferritic stainless steels used for solid oxide fuel cell interconnects". In: *Journal of Power Sources* 184.1 (2008), pp. 220–228.

[24] B. Hua et al. "The electrical property of MnCo2O4 and its application for SUS 430 metallic interconnect". In: *Chinese Science Bulletin* 55.33 (2010), pp. 3831–3837.

[25] C. Lee and J. Bae. "Oxidation-resistant thin film coating on ferritic stainless steel by sputtering for solid oxide fuel cells". In: *Thin Solid Films* 516.18 (2008), pp. 6432–6437.

[26] S. P. Jiang and X. Chen. "Chromium deposition and poisoning of cathodes of solid oxide fuel cells - A review". In: *International Journal of Hydrogen Energy* 39.1 (2014), pp. 505–531.

[27] J. W. Fergus. "Metallic interconnects for solid oxide fuel cells". In: *Materials Science and Engineering: A* 397.1-2 (2005), pp. 271–283.

[28] H. B. Qi and D. G. Lees. "The Effects of Surface-Applied Oxide Films Containing Varying Amounts of Yttria , Chromia , or Alumina on the High-Temperature Oxidation Behavior of Chromia-Forming and Alumina-Forming Alloys". In: *Oxidation of Metals* 53.5-6 (2000), pp. 507–527.

[29] I. Belogolovsky et al. "Effects of Surface-Deposited Nanocrystalline Chromite Thin Films on the Performance of a Ferritic Interconnect Alloy". In: *Journal of The Electrochemical Society* 154.9 (2007), B976.

[30] H. Rashtchi, M. A. F. Sani, and A. M. Dayaghi. "Effect of Sr and Ca dopants on oxidation and electrical properties of lanthanum chromite-coated AISI 430 stainless steel for solid oxide fuel cell interconnect application". In: *Ceramics International* 39.7 (2013), pp. 8123–8131.

[31] R. Lacey et al. "Evaluation of Co and perovskite Cr-blocking thin films on SOFC interconnects". In: *Solid State Ionics* 181.27–28 (2010), pp. 1294–1302.

[32] L. T. Sagdahl, M.-A. Einarsrud, and T. Grande. "Sintering of LaFeO3 Ceramics". In: *Journal of the American Ceramic Society* 83.9 (2004), pp. 2318–2320.

[33] N. Orlovskaya et al. "Structural evolution of La–Cr–O thin films: Part I. Microstructure and phase development". In: *Thin Solid Films* 515.4 (2006), pp. 1741–1747.

[34] J. C. Mah et al. "Metallic interconnects for solid oxide fuel cell: A review on protective coating and deposition techniques". In: *International Journal of Hydrogen Energy* (2016), pp. 1–11.

[35] A. Petric and H. Ling. "Electrical Conductivity and Thermal Expansion of Spinels at Elevated Temperatures". In: *Journal of the American Ceramic Society* 90.5 (2007), pp. 1515–1520.

[36] B.-K. Park et al. "A Perovskite-Type Lanthanum Cobaltite Thin Film Synthesized via an Electrochemical Route and Its Application in SOFC Interconnects". In: *Journal of The Electrochemical Society* 162.14 (2015), F1549–F1554.

[37] J. Wilson, M. Pillai, and T. Armstrong. *Coatings for metal interconnects to reduce SOFC degradation - Patent US2013/0230792 A1*. US.

[38] J. Froitzheim et al. "Long term study of Cr evaporation and high temperature corrosion behaviour of Co coated ferritic steel for solid oxide fuel cell interconnects". In: *Journal of Power Sources* 220 (2012), pp. 217–227.

[39] S. Canovic et al. "Oxidation of Co- and Ce-nanocoated FeCr steels: A microstructural investigation". In: *Surface and Coatings Technology* 215 (2013), pp. 62–74.

[40] J. G. Grolig, J. Froitzheim, and J.-E. Svensson. "Effect of Cerium on the Electrical Properties of a Cobalt Conversion Coating for Solid Oxide Fuel Cell Interconnects – A Study Using Impedance Spectroscopy". In: *Electrochimica Acta* 184 (2015), pp. 301–307.

[41] E. Aukrust and A. Muan. "Phase Relations in the System Cobalt Oxide-Manganese Oxide in Air". In: *Journal of the American Ceramic Society* 46.10 (1963), pp. 511–511.

[42] Y. Golikov et al. "Phase diagrams of the Co-Mn-O system in air". In: *Journal of Physics and Chemistry of Solids* 46.5 (1985), pp. 539–544.

[43] R. Rojas and E. Vila. "Thermal behaviour and reactivity of manganese cobaltites Mn x Co 3–x O 4 (0.0 x 1.0) obtained at low temperature". In: *Journal of Materials Chemistry* (1994).

[44] J. L. M. de Vidales et al. "Thermal Behavior in Air and Reactivity in Acid Medium of Cobalt Manganese Spinels MnxCo3-xO4 (1< x<3) Synthesized at Low Temperature". In: *Chemistry of Materials* 7.9 (1995), p. 1716.

[45] E. Vila et al. "Structural and Thermal Properties of the Tetragonal Cobalt Manganese Spinels Mn x Co 3 - x O 4 (1.4 < x < 2.0)". In: *Chemistry of Materials* 8.5 (1996), pp. 1078–1083.

[46] A. Navrotsky and O. Kleppa. "The thermodynamics of cation distributions in simple spinels". In: *Journal of Inorganic and Nuclear Chemistry* 29.11 (1967), pp. 2701–2714.

[47] A. Navrotsky. "Thermodynamics of A3O4-B3O4 Spinel Solid Solutions". In: *J. Inorg. Nucl. Chem.* 31.1 (1969), pp. 59–72.

[48] H. Bordeneuve et al. "Structural variations and cation distributions in Mn3-xCoxO4 (0<x<3) dense ceramics using neutron diffraction data". In: *Solid State Sciences* 12.3 (2010), pp. 379–386.

[49] Y. Liu et al. "Crystal Structure, Chemical Stabilities and Electrical Conductivity of Fe-Doped Manganese Cobalt Spinel Oxides for SOFC Interconnect Coatings". In: *Journal of the Electrochemical Society* 160.11 (2013), F1316–F1321.

[50] Z. Yang et al. "Thermal Growth and Performance of Manganese Cobaltite Spinel Protection Layers on Ferritic Stainless Steel SOFC Interconnects". In: *Journal of The Electrochemical Society* 152.9 (2005), A1896.

[51] Z. Yang et al. "Fabrication of (Mn, Co) 3O4 Surface Coatings onto Alloy Substrates". In: March (2007).

[52] K. Wang, Y. Liu, and J. W. Fergus. "Interactions Between SOFC Interconnect Coating Materials and Chromia". In: *Journal of the American Ceramic Society* 94.12 (2011), pp. 4490–4495.

[53] Z. Yang et al. "(Mn,Co)3O4 spinel coatings on ferritic stainless steels for SOFC interconnect applications". In: *International Journal of Hydrogen Energy* 32.16 (2007), pp. 3648–3654.

[54] M. Y. Yoon et al. "Preparation and properties of a MnCo2O4 for ceramic interconnect of solid oxide fuel cell via glycine nitrate process". In: *Metals and Materials International* 17.6 (2011), pp. 1039–1043.

[55] S. R. Akanda, N. J. Kidner, and M. E. Walter. "Spinel coatings on metallic interconnects: Effect of reduction heat treatment on performance". In: *Surface and Coatings Technology* 253 (2014), pp. 255–260.

[56] S.-I. Lee et al. "Highly Dense Mn-Co Spinel Coating for Protection of Metallic Interconnect of Solid Oxide Fuel Cells". In: *Journal of the Electrochemical Society* 161.14 (2014), F1389–F1394.

[57] Y. Xu et al. "Cu doped Mn–Co spinel protective coating on ferritic stainless steels for SOFC interconnect applications". In: *Solid State Ionics* 192.1 (2011), pp. 561–564.

[58] B.-K. Park et al. "Cu- and Ni-doped Mn1.5Co1.5O4 spinel coatings on metallic interconnects for solid oxide fuel cells". In: *International Journal of Hydrogen Energy* 38.27 (2013), pp. 12043–12050.

[59] G. Chen et al. "Mn1.4Co1.4Cu0.2O4 spinel protective coating on ferritic stainless steels for solid oxide fuel cell interconnect applications". In: *Journal of Power Sources* 278 (2015), pp. 230–234.

[60] J. Xiao et al. "Oxidation of MnCu0.5Co1.5O4 spinel coated SUS430 alloy interconnect in anode and cathode atmospheres for intermediate temperature solid oxide fuel cell". In: *International Journal of Hydrogen Energy* 40.4 (2015), pp. 1868–1876.

[61] T. Brylewski et al. "Structure and electrical properties of Cu-doped Mn-Co-O spinel prepared via soft chemistry and its application in intermediate-temperature solid oxide fuel cell interconnects". In: *Journal of Power Sources* 333 (2016), pp. 145–155.

[62] Y. Liu, J. W. Fergus, and C. D. Cruz. "Electrical properties, cation distributions, and thermal expansion of manganese cobalt chromite spinel oxides". In: *Journal of the American Ceramic Society* 96.6 (2013), pp. 1841–1846.

[63] P. Baláž et al. "Hallmarks of mechanochemistry: from nanoparticles to technology". In: *Chemical Society Reviews* 42.18 (2013), p. 7571.

[64] H. Zoz et al. "Zoz GmbH , where and what". In: *High Energy Milling / Mechanical Alloying / Reactive Milling* (1997), pp. 1–65.

[65] A. Boschetto et al. "Kinematic observations and energy modeling of a Zoz Simoloyer high-energy ball milling device". In: *The International Journal of Advanced Manufacturing Technology* 69.9-12 (2013), pp. 2423–2435.

[66] N. Burgio et al. "Mechanical alloying of the Fe-Zr system. Correlation between input energy and end products". In: *Il Nuovo Cimento D* 13.4 (1991), pp. 459–476.

[67] F. Padella et al. "Mechanical alloying of the Pd-Si system in controlled conditions of energy transfer". In: *Journal of the Less Common Metals* 175.1 (1991), pp. 79–90.

[68] Z. Z. Fang and H. Wang. "17 - Sintering of ultrafine and nanosized particles". In: *Sintering of Advanced Materials - Fundamentals and Processes*. 2010, pp. 434–473.

[69] S.-S. Pyo et al. "Characteristic of (La0.8Sr0.2)0.98MnO3 coating on Crofer22APU used as metallic interconnects for solid oxide fuel cell". In: *International Journal of Hydrogen Energy* 36.2 (2011), pp. 1868–1881.

[70] D. Monceau et al. "Kinetic demixing of ceramics in an electrical field". In: *Solid State Ionics* 73.3-4 (1994), pp. 221–225.

[71] K. Szot et al. "Nature of the surface layer in ABO3-type perovskites at elevated temperatures". In: *Applied Physics A Materials Science & Processing* 62.4 (1996), pp. 335–343.

[72] J. F. Vente, W. G. Haije, and Z. S. Rak. "Performance of functional perovskite membranes for oxygen production". In: *Journal of Membrane Science* 276.1-2 (2006), pp. 178–184.

[73] C. Fu, K. Sun, and D. Zhou. "Effects of La0. 8Sr0. 2Mn (Fe) O3-$\delta$ Protective Coatings on SOFC Metallic Interconnects". In: *Journal of Rare Earths* 24.3 (2006), pp. 320–326.

[74] W. J. Shong et al. "Effects of lanthanum-based perovskite coatings on the formation of oxide scale for ferritic SOFC interconnect". In: *Materials Chemistry and Physics* 127 (2011), pp. 45–50.

[75] S. Frangini, A. Masci, and F. Zaza. *Procedimento Termochimico per la Produzione di Rivestimenti Ceramici Protettivi su Acciai Inossidabili. - Patent RM2010A000583*. 2010.

[76] S. Frangini, A. Masci, and F. Zaza. "Molten salt synthesis of perovskite conversion coatings: A novel approach for corrosion protection of stainless steels in molten carbonate fuel cells". In: *Corrosion Science* 53.8 (2011), pp. 2539–2548.

[77] H. Nagamoto et al. "Change of thermal expansion coefficient and electrical conductivity of LaCo1–xMxO3 (M = Fe, Ni)". In: *Journal of Materials Research* 8.12 (1993), pp. 3158–3162.

[78] A. V. Knyazev et al. "Crystal structure and thermal expansion of RbNaCaTh(Si8O20)". In: *Russian Journal of Inorganic Chemistry* 58.10 (2013), pp. 1172–1176.

[79] M. H. Hung, M. V. M. Rao, and D. S. Tsai. "Microstructures and electrical properties of calcium substituted LaFeO3 as SOFC cathode". In: *Materials Chemistry and Physics* 101.2-3 (2007), pp. 297–302.

[80] X. B. Yuan et al. "Large enhancement of room temperature magnetoresistance in Ag-added La 0.67(Ca0.65Ba0.35)0.33MnO 3". In: *Solid State Communications* 135.3 (2005), pp. 170–173.

[81] V. P. S. Awana et al. "Magneto-transport of high TCR (temperature coefficient of resistance) La2/3Ca1/3MnO3 : Ag polycrystalline composites". In: *Solid State Communications* 140.9-10 (2006), pp. 410–415. arXiv: `0609364 [cond-mat]`.

[82] X. B. Yuan et al. "Improvements of conductive property and room temperature magnetoresistance in Ag-Ti-added La0.67Ba0.33MnO3". In: *Sensors and Actuators, A: Physical* 133.1 (2007), pp. 104–109.

[83] N. V. Khiem et al. "Electrical properties of Ag-La0.7Ca0.3MnO3". In: *Materials Letters* 63.11 (2009), pp. 899–902.

[84] J. Miao et al. "Electrical transport and magnetoresistance in La2/3Ca1/3MnO3/CuO composites". In: *Materials Letters* 60.17-18 (2006), pp. 2214–2216.

[85] J. H. Miao et al. "Giant magnetoresistance in La0.67Ca0.33MnO3 granular system with CuO addition". In: *Materials Research Bulletin* 43.3 (2008), pp. 631–638.

[86] M. S. Anwar et al. "Impact of Co3O4 phase on the magnetocaloric effect and magnetoresistance in La0.7Sr0.3MnO3/Co3O4 and La0.7Ca0.3MnO3/Co3O4 ceramic composites". In: *Ceramics International* 41.1 (2014), pp. 631–637.

[87] B. K. Andersen. "Thermodynamic properties of molten alkali carbonates". Ph.D. thesys. Technical University of Lyngby, 1975.

[88] B. K. Andersen et al. "Thermodynamic Properties of the O2—O2(-)—O2(2-)—O(2-) System in Molten Alkali Carbonates." In: *Acta Chemica Scandinavica* 31a (1977), pp. 242–248.

[89] G. Moutiers et al. "Thermodynamic and voltammetric study of oxygen systems in molten Na2CO3-K2CO3 (56-44 mol.%) eutectic at 750°C". In: *Electrochimica Acta* 36.5-6 (1991), pp. 1063–1071.

[90] S. Frangini and S. Scaccia. "Thermal stability and oxidizing properties of mixed alkaline earth-alkali molten carbonates: A focus on the lithium-sodium carbonate eutectic system with magnesium additions". In: *Thermochimica Acta* 574 (2013), pp. 55–62.

[91] S. Frangini. "Lux-Flood Basicity of Mixed La2O3-Alkali Molten Carbonates Determined by Analysis of their Oxygen Solubility Properties". In: *The Open Physical Chemistry Journal* 3.1 (2009), pp. 1–7.

[92] R. A. Donado, L. G. Marianowski, and H. C. Maru. "Corrosion of the Wet-Seal Area in Molten Carbonate Fuel Cells." In: *Journal of the Electrochemical Society* 131.11 (1984), pp. 2535–2540.

[93] E. R. Hwang and S. G. Kang. "A study of a corrosion-resistant coating for a separator for a molten carbonate fuel cell". In: *Journal of Power Sources* 76.1 (1998), pp. 48–53.

[94] C. E. Baumgartner. "Metal Oxide Solubility in Eutectic Li/K Carbonate Melts". In: *Journal of the American Ceramic Society* 67.7 (1984), pp. 460–462.

[95] J. D. Doyon. "NiO Solubility in Mixed Alkali/Alkaline Earth Carbonates". In: *Journal of The Electrochemical Society* 134.12 (1987), p. 3035.

[96] M. L. Orfield. "Solubility of NiO in Molten Li2 CO 3, Na2 CO 3, K 2 CO 3, and Rb2 CO 3 at 910°C". In: *Journal of The Electrochemical Society* 135.7 (1988), p. 1662.

[97] Y. Ito et al. "Dissolution behaviour of copper and nickel oxides in molten Li2CO3/Na2CO3/K2CO3". In: *Journal of Power Sources* 23.4 (1988), pp. 357–364.

[98] L. Qingfeng. "Complex Formation during Dissolution of Metal Oxides in Molten Alkali Carbonates". In: *Journal of The Electrochemical Society* 146.7 (1999), p. 2449.

[99] H. Yokokawa, N. Sakai, and T. Kawada. "Chemical Potential Diagrams for Fe-Cr-Li-K-C-O System: Thermodynamic Analysis on Reaction Profiles Between Alloys and Alkali Carbonates". In: *Journal of The Electrochemical Society* 140.12 (1993), p. 3565.

[100] S. Mitsushima et al. "Corrosion Model for Iron in the Presence of Molten Carbonate". In: *Journal of The Electrochemical Society* 151.6 (2004), A825–A830.

[101] T. H. Lim et al. "Effects of temperature and partial pressure of CO2/O2 on corrosion behaviour of stainless-steel in molten Li/Na carbonate salt". In: *Journal of Power Sources* 89.1 (2000), pp. 1–6.

[102] C. L. Zeng, J. Li, and T. Zhou. "Galvanic corrosion in molten salts: A discussion of the corrosion mechanism of two-phase Ni-20Cr-20/30Cu alloys in eutectic (Li,K)2CO 3 at 650°C". In: *Oxidation of Metals* 64.3-4 (2005), pp. 207–218.

[103] H. M. Rietveld. "Line profiles of neutron powder-diffraction peaks for structure refinement". In: *Acta Crystallographica* 22.1 (1967), pp. 151–152.

[104] R. A. Young. *The Rietveld Method*. IUCr monographs on crystallography. Oxford University Press, 1995.

[105] L. Lutterotti and M. Bortolotti. "Rietveld texture analysis from diffraction images". In: *Zeitschrift fur Kristallographie Supplements* (2007).

[106] G. Bergerhoff and I. Brown. *Crystallographic Databases*. Chester: International Union of Crystallography, 1987.

[107] P. Scardi, L. Lutterotti, and P. Maistrelli. "Experimental determination of the instrumental broadening in the Bragg–Brentano geometry". In: *Powder Diffraction* (1994).

[108] I. C. Madsen et al. "Outcomes of the International Union of Crystallography Commission on Powder Diffraction Round Robin on Quantitative Phase Analysis: samples 1 a to 1 h". In: *Journal of Applied Crystallography* 34.4 (2001), pp. 409–426.

[109] S. Brunauer, P. H. Emmett, and E. Teller. "Adsorption of Gases in Multimolecular Layers". In: *Journal of the American Chemical Society* 60.2 (1938), pp. 309–319.

[110] M. Wojdyr. "Fityk : a general-purpose peak fitting program". In: *Journal of Applied Crystallography* 43.5 (2010), pp. 1126–1128.

[111] R. Svoboda and J. Málek. "Applicability of Fraser–Suzuki function in kinetic analysis of complex crystallization processes". In: *Journal of Thermal Analysis and Calorimetry* 111.2 (2013), pp. 1045–1056.

[112] L. J. van der Pauw. "A method of measuring the resistivity and Hall coefficient on lamellae of arbitrary shape". In: *Philips Technical Review* 20 (1958), pp. 220–224.

[113] S. Frangini and S. Loreti. "The role of alkaline-earth additives on the molten carbonate corrosion of 316L stainless steel". In: *Corrosion Science* 49.10 (2007), pp. 3969–3987.

[114] I. Novoselova et al. "High-temperature electrochemical synthesis of carbon-containing inorganic compounds under excessive carbon dioxide pressure". In: *Journal of Mining and Metallurgy, Section B: Metallurgy* 39.1-2 (2003), pp. 281–293.

[115] G. S. Frankel. "Fundamentals of Corrosion Kinetics". In: *Active Protective Coatings*. Springer Netherlands, 2016, pp. 17–32.

[116] European Commission. *SOFC Single Cell Performance and Endurance Test Modules TM SOFC 01-04LD/ 05-08HD*. Tech. rep. 2010.

[117] G. C. Wood and T. Hodgkiess. "The Hardness of Oxides at Ambient Temperatures". In: *Materials and Corrosion/Werkstoffe und Korrosion* 23.9 (1972), pp. 766–773.

[118] B. Gillot. "DTG Curves of Selective Oxidation of Submicrometer Mixed Valency Spinels: Data Table for the Oxidation Temperature of Transition Metals and Its Relation to the Cation-Oxygen Distance". In: *Journal of Solid State Chemistry* 113.1 (1994), pp. 163–167.

[119] E. Aukrust and A. Muan. "Thermodynamic properties of solid solutions with spinel type structure. The system Co3O4–Mn3O4". In: *Trans Metall Soc AIME* 230 (1964), pp. 378–382.

[120] L. a. Zabdyr and O. B. Fabrichnaya. "Phase equilibria in the cobalt oxide-copper oxide system". In: *Journal of Phase Equilibria* 23.2 (2002), pp. 149–155.

[121] I. Ohnuma et al. "Phase equilibria in the Fe-Co binary system". In: *Acta Materialia* 50.2 (2002), pp. 379–393.

[122] R. M. German, P. Suri, and S. J. Park. "Review: Liquid phase sintering". In: *Journal of Materials Science* 44.1 (2009), pp. 1–39.

[123] R. D. Shannon. "Revised effective ionic radii and systematic studies of interatomic distances in halides and chalcogenides". In: *Acta Crystallographica Section A* 32.5 (1976), pp. 751–767.

[124] G. Bayer. "Thermal expansion of oxide compounds with spinel structure". In: *Thermochimica Acta* 3.6 (1972), pp. 421–426.

[125] P. a. Wright et al. "Mixed-metal amorphous and spinel phase oxidation catalysts: characterization by x-ray diffraction, x-ray absorption, electron microscopy, and catalytic studies of systems containing copper, cobalt, and manganese". In: *Chemistry of Materials* 4.5 (1992), pp. 1053–1065.

[126] H. Bordeneuve et al. "Cation distribution in manganese cobaltite spinels Co3-x Mn x O4 ($0 < x < 1$) determined by thermal analysis". In: *Journal of Thermal Analysis and Calorimetry* 101.1 (2010), pp. 137–142.

[127] E. Elbadraoui. "Cation distribution and mechanism of electrical conduction in nickel-copper manganite spinels". In: *Solid State Ionics* 93.3-4 (1997), pp. 219–225.

[128] S. Frangini and A. Masi. "Molten carbonates for advanced and sustainable energy applications: Part I. Revisiting molten carbonate properties from a sustainable viewpoint". In: *International Journal of Hydrogen Energy* 41.41 (2016), pp. 18739–18746.

[129] S. Frangini et al. "Degradation behavior of a commercial 13Cr ferritic stainless steel (SS405) exposed to an ambient air atmosphere for IT-SOFC interconnect applications". In: *Materials Chemistry and Physics* 144 (2014), pp. 491–497.

[130] T. K. Mandal and J. Gopalakrishnan. "From rocksalt to perovskite: a metathesis route for the synthesis of perovskite oxides of current interest". In: *Journal of Materials Chemistry* 14.8 (2004), p. 1273.

[131] J. B. Wiley and R. B. Kaner. "Rapid solid-state precursor synthesis of materials." In: *Science (New York, N.Y.)* 255.5048 (1992), pp. 1093–7.

[132] I. P. Parkin. "Solid state metathesis reaction for metal borides, silicides, pnictides and chalcogenides: ionic or elemental pathways". In: *Chemical Society Reviews* 25.3 (1996), p. 199.

[133] M. Seabaugh et al. "Manufacturing Analysis of SOFC Interconnect Coating Processes". In: *11th Annual SECA Workshop* (2010).

[134] N. J. Kidner and Nextech Coatings. "Protective Coatings for Metallic SOFC Components". In: *13th annual SECA workshop* (2012).

[135] Battelle Memorial Institute. "Manufacturing Cost Analysis of 100 and 250 kW Fuel Cell Systems for Primary Power and Combined Heat and Power Applications". In: *DOE Report* January (2016).

[136] S. Licht and H. Wu. "STEP iron, a chemistry of iron formation without CO 2 emission: Molten carbonate solubility and electrochemistry of iron ore impurities". In: *Journal of Physical Chemistry C* 115.50 (2011), pp. 25138–25147.

[137] E. Béchade et al. "Synthesis of lanthanum silicate oxyapatite materials as a solid oxide fuel cell electrolyte". In: *Journal of the European Ceramic Society* 28.14 (2008), pp. 2717–2724.

[138] J. Du and C. H. Chen. "Structure and lithium ion diffusion in lithium silicate glasses and at their interfaces with lithium lanthanum titanate crystals". In: *Journal of Non-Crystalline Solids* 358.24 (2012), pp. 3531–3538.

[139] J. M. Rakowski. *Method for reducing formation of electrically resistive layer on ferritic stainless steels - Patent US2013/0266892 A1*. 2013.

[140] A. Delmastro et al. "Synthesis and characterization of non-stoichiometric LaFeO3 perovskite". In: *Materials Science and Engineering: B* 79.2 (2001), pp. 140–145.

[141] H. Falk-Windisch, J. E. Svensson, and J. Froitzheim. "The effect of temperature on chromium vaporization and oxide scale growth on interconnect steels for Solid Oxide Fuel Cells". In: *Journal of Power Sources* 287 (2015), pp. 25–35.

[142] A. W. Bredvei Skilbred and R. Haugsrud. "The effect of dual atmosphere conditions on the corrosion of Sandvik Sanergy HT". In: *International Journal of Hydrogen Energy* 37.9 (2012), pp. 8095–8101.

[143] J. Rufner et al. "Oxidation behavior of stainless steel 430 and 441 at 800°C in single (air/air) and dual atmosphere (air/hydrogen) exposures". In: *International Journal of Hydrogen Energy* 33.4 (2008), pp. 1392–1398.

[144] Y. Zhao and J. W. Fergus. "Oxidation of Alloys 430 and 441 in SOFC Dual Atmospheres: Effects of Flow Rate and Humidity". In: *Journal of the Electrochemical Society* 159.3 (2012), pp. C109–C113.

[145] G. R. Holcomb et al. "Dual-Environment Effects on the Oxidation of Metallic Interconnects". In: *Journal of Materials Engineering and Performance* 15.4 (2006), pp. 404–409.

[146] J. Töpfer, S. Aggarwal, and R. Dieckmann. "Point defects and cation tracer diffusion in (CrxFe1 - x)3 - $\delta$O4 spinels". In: *Solid State Ionics* 81.3-4 (1995), pp. 251–266.

[147] P. M. Price and D. P. Butt. "Stability and Decomposition of Ca-Substituted Lanthanum Ferrite in Reducing Atmospheres". In: *Journal of the American Ceramic Society* 98.9 (2015), pp. 2881–2886.

[148] S. K. Yen. "Critical Hydrogen Concentration for the Brittle Fracture of AISI 430 Stainless Steel". In: *Journal of The Electrochemical Society* 143.9 (1996), p. 2736.

[149] S. Frangini et al. "Thin film perovskite coatings and their application for SOFC ferritic steel interconnects". In: *Proceedings of the 12th European SOFC & SOE Forum 2016*. 2016, pp. 24–31.

[150] M. E. Leonard et al. "High-temperature (800 °C) dual atmosphere corrosion of electroless nickel-plated ferritic stainless steel". In: *International Journal of Hydrogen Energy* 39.28 (2014), pp. 15746–15753.

[151] P. Alnegren et al. "Severe dual atmosphere effect at 600 °C for stainless steel 441". In: *Journal of Power Sources* 301 (2016), pp. 170–178.

# List of Tables


1.1 Comparison of key properties of different alloy groups for SOFC applications [21]: . . . 9
1.2 Comparison of the various coating materials: . . . 14
1.3 Standard redox potentials for oxidation of various metals (vs. $CO_2/O_2/Au$ SRE electrode) at 873 K . . . 27

2.1 Sample nomenclature, metal composition, corresponding spinel composition and section of the thesis where the sample is described: . . . 30
2.2 Nominal composition of the ferritic alloys used in this work: . . . 32
2.3 Summary of salt names and additives introduced in the eutectic $LiCO_3$ - $NaCO_3$ with 1 mol% $La_2O_3$, targeted coating morphology, level of basicity (with respect to the salts used in this work), metal additions and thesis section where the application is described: . . . 33

3.1 Phases and crystallographic data of structural models used in Rietveld analysis: . . . 44
3.2 Lattice parameters (a, a', c, $\alpha$), mean crystallite size (<D>), and microstrain (M.S.) values obtained from XRD Rietveld analysis on $Co_3O_4$–$Mn_3O_4$ mixtures for different milling time: . . . 44
3.3 BET specific surface area and particles size for different samples: . . . 47
3.4 BET specific surface area and particles size for different samples: . . . 53
3.5 Calculated weight loss as reported in equation (3.1) and experimental data for TGA in reducing atmosphere: . . . 58
3.6 Calculated weight losses and maximum peak temperatures for fits reported in figure 3.13: . . . 62
3.7 Calculated weight loss as reported in equation (3.1) and experimental data for TGA analysis carried out on reduced powder in air: . . . 66
3.8 Green densities of the pelletized samples: . . . 68
3.9 Summary of sintering treatment details (see text for details) and sintered densities: . . . 72
3.10 Relative shrinkage achieved in reducing-reoxidizing condition and theoretical calculated sintered density (see text for details): . . . 80
3.11 Thermal expansion coefficient measured between room temperature and 800 °C for the different samples.: . . . 83
3.12 Activation energy calculated from the Arrhenius plot of the different samples: . . . 86

4.1 Results of EDX analysis from points collected in figure 4.12: . . . . . 98
4.2 Results of EDX analysis from points collected in figure 4.15: . . . . . 99
4.3 Results of EDX analysis from points collected in figure 4.23: . . . . . 111
4.4 Summary of prices for analytical grade chemicals to be used for the molten bath (Alfa Aesar): . . . . . 115
4.5 Summary of materials and energy cost for the molten carbonate conversion coating process: . . . . . 116

5.1 Results of EDX analysis from points collected in figure 5.6: . . . . . 122

6.1 Summary of the coated steels and perovskite structures combination subjected to oxidation experiments reported in this chapter: . . . . . 137
6.2 Perovskite chemical composition (Fe/La ratio) of smooth coating areas and particles clusters as reported in figure 6.3: . . . . . 140
6.3 Results of EDX analysis of the points indicated in figure 6.12: . . . . 151
6.4 Results of EDX analysis of the points indicated in figure 6.14: . . . . 151
6.5 Results of EDX analysis of the points indicated in figure 6.17: . . . . 155
6.6 Results of EDX analysis of the points indicated in figure 6.19: . . . . 156
6.7 Results of EDX analysis of the points indicated in figure 6.23: . . . . 160
6.8 Results of EDX analysis of the points indicated in figure 6.25: . . . . 161

# List of Figures


1.1 Schematic representation of a fuel cell. . . . . 2
1.2 Common fuel cells and corresponding fuels, charge transport ions and oxidizers [9]. . . . . 3
1.3 Schematic representation of a SOFC. . . . . 4
1.4 Oxygen reduction and diffusion mechanisms in pure electronic, ionic-electronic composite, mixed ionic-electronic conducting cathodes [13]. 5
1.5 Schematic representation of a tubular SOFC. . . . . 6
1.6 Schematic representation of a planar SOFC. . . . . 7
1.7 Trend of research and development on SOFC interconnect materials [16]. . . . . 8
1.8 Equilibrium vapor pressures of chromium–oxygen–hydrogen gas species at 800 ∘C [27]. . . . . 10
1.9 Schematic representation of the metallic interconnect coatings requirements. . . . . 11
1.10 Phase diagram of the Mn-Co oxide system in air (S=spinel, H=Haussmanite, R.S. = rock salt) [41, 42]. . . . . 16
1.11 Schematic representation of the HEBM energy transfer mechanism. . 18
1.12 Schematic representation of a HEBM treatment evolution depicted as surface area development during the process. . . . . 19
1.13 Schematic picture of the formation process of a La-Fe perovskite conversion coating by (a) dissolution-precipitation and (b) precursor-template processes [8]. . . . . 23

2.1 (a) Schematic view of the electrode samples processing geometry and pictures of (b) a steel electrode, (c) the sample cage used to obtain full coated steel samples and (d) steel foils after a passivation treatment. 34
2.2 Picture of the $Al_2O_3$ crucibles used for the small scale experiments (a, left) and scaled up passivation process (a, right), the latter depicted during operation (b) with the $Al_2O_3$ rods used to insulate the thermocouple and to provide gas flow. . . . . 35
2.3 Schematic representation of the experimental set-up used for the dual atmosphere ASR measurements. . . . . 37

3.1 X-Ray Diffraction patterns (Mo source) of the Mn1.5Co1.5 powder mixture subjected to different milling times. . . . . 40
3.2 X-Ray Diffraction patterns (Mo source) of the MnCo2 powder mixture subjected to different milling times. . . . . 41

3.3 Quantitative phase analysis results (weight%) of (a) Mn1.5Co1.5 and (b) MnCo2 samples as a function of milling time. . . . . 42
3.4 SEM micrographs of the $Co_3O_4$ and $Mn_3O_4$ precursors. . . . . 46
3.5 SEM micrographs of MnCo2 samples milled for different time: (A,B) 5h; (C,D) 10h; (E,F) 100h. . . . . 46
3.6 X-ray diffraction patterns (Fe source) of a) Mn1.5Co1.5 and b) MnCo2 samples milled for 10 hours collected at different temperatures (heating and cooling rates = 10 °C/min); (1) $Co_3O_4$, (2) $MnCo_2O_4$, (3) $Mn_3O_4$, (4) $Mn_{2-y}Co_yO_3$, (6) $Mn_{2-w}Co_2O_4$, (#) sample holder. . . . 48
3.7 Phase content (weight %) of Mn1.5Co1.5 and MnCo2 10h ball milled samples samples versus temperature during heating and cooling stages, obtained from QPA of XRD data reported in figure 3.6. . . . . 48
3.8 X-ray diffraction pattern (Fe source) of a $Co_3O_4$-$Mn_3O_4$ hand mixed mixture (Co:Mn=1:1) collected at 800°C after 7 hours of isothermal treatment: a) mixed Mn-Co cubic spinel; b) $Co_3O_4$ precursor; c) mixed Mn-Co tetragonal spinel originated by $Mn_3O_4$ decomposition and partial reaction. . . . . 49
3.9 X-Ray Diffraction patterns (Fe surce) (Fe source) of the doped Mn-Co mixtures after 10 h of milling; (1) $Co_3O_4$, (2) $Mn_3O_4$, (3) $MnCo_2O_4$, (4) $Fe_2O_3$, (5) CuO reflections. . . . . 51
3.10 Thermogravimetric curves as a function of temperature for the different samples acquired in air; solid lines represent weight% change, dotted lines the derivative. . . . . 52
3.11 In situ X-ray diffraction patterns (Fe source) of a) Mn1.33Co1.17Cu0.5, b) Mn1.57Co0.93Cu0.5 and c) Mn2.05Co0.45Cu0.5 samples milled for 10 hours collected at different temperatures (heating rate = 10°C/min); 1) $Co_3O_4$, 2) $Mn_3O_4$, 3) $MnCo_2O_4$, 4) $Mn_2O_3$, 5) Tetragonal mixed spinel phase, #) sample holder. . . . . 55
3.12 Thermogravimetric curves as a function of temperature for the different samples acquired in $Ar/H_2(5\%)$ atmosphere. . . . . 57
3.13 Experimental (black) and simulated (colours) DTG curves acquired in $Ar/H_2(5\%)$ atmosphere for the different samples (see text and figure 3.12). . . . . 61
3.14 In situ high temperature X-ray diffraction patterns (Fe source) of a) MnCo2, b) MnCo1.6Fe0.4, c) MnCo1.6Fe0.2Cu0.2, d) Mn1.33Co1.17Cu0.5 samples milled for 10 hours collected at different temperatures in $He/H_2(5\%)$ atmosphere (heating rate = 10°C/min). . . . . 63
3.15 Thermogravimetric curves as a function of temperature for the different samples acquired in Air on reduced samples; solid lines represent weight% change, dotted lines the derivative. . . . . 65
3.16 In situ high temperature X-ray diffraction patterns (Fe source) of a) MnCo2, b) MnCo1.6Fe0.2Cu0.2 samples milled for 10 hours and treated at 800°C in reducing atmosphere collected at different temperatures in air flow (heating rate = 10°C/min); (*) sample holder reflection. . . . . 67

3.17 Dilatometric curves of the different samples acquired in air atmosphere: solid lines represent the shrinkage ratio, dotted lines the derivative. . . . . 69
3.18 SEM images of samples sintered at (a) 1200 °C and (b,c,d) 1000 °C [see text for details]. . . . . 70
3.19 (a) Sintering temperature and (b) maximum shrinkage temperature for the different samples. . . . . 71
3.20 X-Ray Diffraction patterns (Fe surce) of samples sintered as described in table 3.9; crystallographic planes indicate cubic spinel reflections, while T indicates peaks ascribable to tetragonal spinels. . . . . 73
3.21 X-Ray Diffraction patterns (Fe surce) of samples sintered as described in table 3.9. . . . . 74
3.22 In situ high temperature X-Ray Diffraction patters (Fe source) of sample MnCo1.6Fe0.4 acquired in reducing atmosphere at 700°C, 800 °C after respectively 5, 25 and 45 minutes (800 °C I, II and III) and during cooling at 700 °C. . . . . 76
3.23 X-Ray Diffraction patters (Co source) of the different samples after the dilatometric analysis carried out in $N_2/H_2(5\%)$ up to 800 °C. . . . 76
3.24 Shrinkage measured for the different samples after the sintering treatment in reducing atmosphere. . . . . 77
3.25 SEM images of pellets surface after the dilatometer reducing treatment. 78
3.26 Dilatometric curves acquired in air on MnCo2 and MnCo1.6Fe0.2Cu0.2 reduced pellets. . . . . 78
3.27 SEM images of MnCo1.6Fe0.2Cu0.2 pellets (a) surface and (b) fracture after the reduction-reoxidation treatment. . . . . 79
3.28 SEM images of pellets fracture of reduced pellets after reoxidation in furnace. . . . . 81
3.29 Dilatometric curves of sintered samples. . . . . 83
3.30 CTE of the different samples as a function of Co content $x$ in the $Me_{3-x}Co_xO_4$ spinel. . . . . 84
3.31 Arrhenius plots of electrical conductivity measured (dots) for the different samples and linear fits in the single phase linear regions (dashed lines). . . . . 86
3.32 Conductivity measured at 800 °C for the different sintered samples as a function of Co content $x$ in the $Me_{3-x}Co_xO_4$ spinel. . . . . 87

4.1 OCP curves of K41 steel samples electrode processed at 600 °C in salts characterized by different basicity. . . . . 90
4.2 X-Ray Diffraction patterns (Mo surce) of K41 steel samples subjected to the passivation treatment at 600 °C in new salts characterized by different basicity. . . . . 91
4.3 SEM images of K41 steel samples subjected to the passivation treatment at 600 °C in new salts characterized by different basicity. . . . 92

4.4 OCP curves of Crofer 22H steel samples processed in different gas flow conditions: A) 60 ml/min $CO_2$ flowing over the melt ; B) 60 ml/min $CO_2$ sparging over the melt for the first 24 hours and bubbling in the salt for the rest of the experiment ; C) 60 ml/min $CO_2$ bubbling in the melt. . . . . 93
4.5 X-Ray Diffraction patterns (Mo source) of Crofer 22H steel samples processed in different gas flow conditions: A) 60 ml/min $CO_2$ flowing over the melt ; C) 60 ml/min $CO_2$ bubbling in the melt; (*) indicates reflections ascribable to salt residues. . . . . 93
4.6 OCP curves of K41 steel samples processed in new and used 10Mg salts. . . . . 94
4.7 SEM images of K41 steel samples processed in new and used 10Mg salts. . . . . 95
4.8 OCP curves of Crofer 22H steel samples processed at 600 °C and 650 °C. . . . . 95
4.9 SEM images of Crofer 22H steel samples processed at 600 °C and 650 °C. . . . . 96
4.10 X-Ray Diffraction pattern (Mo source) of a K41 steel electrode after 72 hours of exposure in the 10Mg salt at 600 °C. . . . . 97
4.11 SEM images of a K41 steel electrode surface after 72 hours of exposure in the 10Mg salt at 600 °C. . . . . 97
4.12 SEM image of the section of a K41 steel electrode section after 72 hours of exposure in the 10Mg salt at 600 °C with superimposed EDX map for Fe (green) Cr(red) La (yellow) and O (blue) and positions of EDX point analysis reported in table 4.1. . . . . 98
4.13 XRD pattern (Mo source) of a K41 steel foil processed for 48 hours in the 10Mg molten carbonate salt at 600 °C. . . . . 99
4.14 SEM images of a K41 steel foil surface after the molten carbonate treatment carried out for 48 hours at 600 °C in the 10Mg salt. . . . . 100
4.15 SEM image of the section of a K41 steel foil after 48 hours of exposure in the 10Mg salt at 600 °C with superimposed EDX map for Fe (green) Cr(red) La (yellow) and positions of EDX point analysis reported in table 4.2. . . . . 100
4.16 OCP curves of K41 steels processed at 600 °C in different salt formulations. . . . . 104
4.17 OCP curves acquired during the exposure of Crofer 22H samples in thin formulation salt characterized by medium basicity (salt D) at different temperatures in comparison with the high basicity salt C. . . 104
4.18 X-Ray Diffraction patterns (Mo surce) of the steel samples exposed in different conditions for 48 hours . . . . . 105
4.19 SEM images of different foil samples passivated in different conditions. 106
4.20 SEM images of K41 and SSHT steel samples section after a passivation treatment carried out for 48 hours at 600 °C and corresponding EDX maps for Fe, Cr, O and La. . . . . 108
4.21 XRD pattern (Mo source) of a K41 steel foil after 8 hours of exposure in the 10Mg0.25X salt at 600 °C. . . . . 110

4.22 SEM image of the surface of a K41 steel foil after 8 hours of exposure in the 10Mg0.25X salt at 600 °C. . . . . 110
4.23 SEM image of the section of a K41 steel foil after 8 hours of exposure in the 10Mg0.25X salt at 600 °C, EDX maps for Cr, Fe and La and EDX spots (see table 4.3). . . . . 111
4.24 X-Ray Diffraction patterns (Fe surce) of SS405 steel samples passivated for 48 h in . . . . . 112
4.25 SEM image of surface (a and b) and section (c and d) at different magnification of the 13Cr steel after the molten carbonate coating treatment. . . . . 113

5.1 OCP curves of K41 steel samples electrode processed at 600 °C in salts characterized by different Cu content. . . . . 118
5.2 X-Ray Diffraction patterns (Mo surce) of K41 steel samples subjected to the passivation treatment at 600 °C in salts characterized by different Cu content for different time intervals. . . . . 119
5.3 SEM images of K41 steel samples surface after the passivation treatment at 600 °C in salts characterized by different Cu content for different time intervals. . . . . 120
5.4 X-Ray Diffraction patterns (Mo surce) of a K41 steel foil subjected to the passivation treatment at 600 °C in the 3Mg4Cu salt for 24 h. 121
5.5 SEM image of the surface of a K41 sample after the passivation treatment carried out for 24 h in the 3Mg4Cu salt at 600 °C . . . . . 122
5.6 SEM image of the section of a K41 sample after the passivation treatment carried out for 48 h in the 3Mg4Cu salt at 600 °C with EDX maps for Fe, Cr, La, Cu and O and the position of EDX analysis reported in table 5.1. . . . . 123
5.7 OCP curves of K41 steel electrodes exposed at 600 °C in the 10Mg1Cu salt for different processing time. . . . . 124
5.8 X-Ray Diffraction patterns of K41 steel electrodes exposed at 600 °C in the 10Mg1Cu salt for different processing time. . . . . 125
5.9 SEM images K41 steel electrodes surface exposed at 600 °C in the 10Mg1Cu salt for different processing time (a,b,c) and corresponding EDX maps for Fe,Cu and La (d). . . . . 125
5.10 SEM image of the section of a K41 steel electrode exposed at 600 °C in the 10Mg1Cu salt for 72 h and corresponding EDX maps for Cr, Fe, La, Cu and O. . . . . 126
5.11 OCP curves acquired during the exposition of K41 steel electrodes in different nickel containing salts. . . . . 127
5.12 X-Ray Diffraction patterns of K41 steel electrodes exposed in nickel containing salts. . . . . 128
5.13 SEM images of K41 steel electrodes processed in nickel containing salts. 129
5.14 SEM image of the section of a K41 steel electrode exposed at 600 °C in the 10Mg1Ni salt for 72 h. . . . . 130
5.15 OCP curves acquired during the exposition of K41 electrodes at 600 °C in the 10Mg1Ag salt. . . . . 131

5.16 X-Ray Diffraction patterns of K41 steel electrodes exposed at 600 °C in the 10Mg1Ag salt for 22 h and 72 h. . . . . 131
5.17 SEM images of K41 steel electrodes exposed at 600 °C in the 10Mg1Ag salt for 22 h and 72 h; (a,c) secondary electrons images, (b,d) backscattered electrons images. . . . . 132
5.18 SEM image of the section of a K41 steel electrode exposed at 600 °C in the 10Mg1Ag salt for 72 h and corresponding EDX maps for Cr, Fe, La, Ag and O. . . . . 133
5.19 SEM image of the section of a K41 steel electrode exposed at 600 °C in the 10Mg1Ag salt for 72 h depicting the detail of a silver particle (clear, top) deposited on perovskite grains (medium gray, center) grown on the Fe-rich oxide sublayer (dark grey, bottom). Clear small silver particles can be observed ad the interface between the sublayer and the perovskite. . . . . 134
5.20 Schematic representation of the proposed metal-perovskite composite coating formation mechanism described in section 5.4. . . . . 136

6.1 Weight change of uncoated and $LaFeO_3$ coated SS405 samples during discontinuous oxidation experiments at 700°C in humid air (3%). . . 138
6.2 X-Ray diffraction patterns (Fe source) of the coated SS405 samples after different exposure intervals at 700°C in humid air (3%) . . . . . 140
6.3 SEM images of the coated SS405 samples after different exposure intervals at 700°C in humid air (3%) . . . . . 141
6.4 SEM images of the coated SS405 steel surface (a and b) and section (c and d) after 1800 h of exposure in air at 700 °C with the high magnification cross-sectional image incorporating the EDX mapping of La, Fe, and Cr elements (e) . . . . . 142
6.5 ASR curves acquired at 700 °C in dual-atmosphere ($H_2$/air) conditions for the coated and uncoated SS405 steel . . . . . 143
6.6 X-Ray diffraction patterns of the air-side steel surfaces after oxidation experiments carried out at 700 °C in dual-atmosphere ($H_2$/air). . . . 143
6.7 SEM images of the air-side steel surface (a) and section (b) of the uncoated SS405 steel after oxidation in dual atmosphere at 700 °C and over imposed SEM/EDX map of Fe and Cr elements. . . . . 144
6.8 SEM images of the air-side steel surface (a) and section (b) of the $LaFeO_3$ coated SS405 steel after oxidation in dual atmosphere at 700 °C and over imposed SEM/EDX map of Fe and Cr elements. . . . . 145
6.9 Pictures of the K41 foil samples passivated with a thick La-Fe perovskite coating on the alumina supports after the indicated intervals of oxidation (air, 700 °C). . . . . 148
6.10 X-Ray Diffraction patterns (Mo surce) of the K41 steel samples passivated with a thick La-Fe perovskite coating after oxidation experiments carried out for different exposure time in air at 700 °C in comparison with the as-coated sample; (*) indicates reflections ascribable to a mixed $(Cr,Fe)_2O_3$ oxide. . . . . 149
6.11 SEM image of the surface of a K41 sample passivated with a thick La-Fe perovskite coating after 200 h of oxidation in air at 700 °C. . . 150

6.12 SEM image of the section of a K41 sample passivated with a thick La-Fe perovskite coating after 200 h of oxidation in air at 700 °C with EDX maps for Fe, Cr and La and the position of EDX analysis reported in table 6.3. . . . . 150

6.13 SEM image of the surface of a K41 sample passivated with a thick La-Fe perovskite coating after 1000 h of oxidation in air at 700 °C. . 152

6.14 SEM image of the section of a K41 sample passivated with a thick La-Fe perovskite coating after 1000 h of oxidation in air at 700 °C with EDX maps for Fe, Cr and La and the position of EDX analysis reported in table 6.4. . . . . 152

6.15 X-Ray Diffraction patterns (Mo surce) of the K41 steel samples passivated with a thin La-Fe perovskite coating after oxidation experiments carried out for different exposure time in air at 700 °C in comparison with the as-coated sample; (*) indicates reflections ascribable to a La-rich silicate phase. . . . . 154

6.16 SEM image of the surface of a K41 sample passivated with a thin La-Fe perovskite coating after 200 h of oxidation in air at 700 °C. . . 154

6.17 SEM image of the section of a K41 sample passivated with a thin La-Fe perovskite coating after 200 h of oxidation in air at 700 °C with EDX maps for Fe, Cr and La and the position of EDX analysis reported in table 6.5. . . . . 155

6.18 SEM image of the surface of a K41 sample passivated with a thick La-Fe perovskite coating after 400 h of oxidation in air at 700 °C. . . 156

6.19 SEM image of the section of a K41 sample passivated with a thin La-Fe perovskite coating after 400 h of oxidation in air at 700 °C with EDX maps for Fe, Cr and La and the position of EDX analysis reported in table 6.6. . . . . 157

6.20 Pictures of the K41 foil samples passivated with a Cu-perovskite composite composite on the alumina supports after the indicated intervals of oxidation (air, 700 °C). . . . . 158

6.21 X-Ray Diffraction patterns (Mo surce) of the K41 steel samples passivated with a Cu-perovskite composite coating after oxidation experiments carried out for different exposure time in air at 700 °C in comparison with the as-coated sample. . . . . 159

6.22 SEM image of the surface of a K41 sample passivated with a Cu-perovskite composite coating after 200 h of oxidation in air at 700 °C. . . . . 159

6.23 SEM image of the section of a K41 sample passivated with a Cu-perovskite composite coating after 200 h of oxidation in air at 700 °C with overimposed EDX maps and the position of EDX analysis reported in table 6.7 . . . . . 160

6.24 SEM image of the surface of a K41 sample passivated with a Cu-perovskite composite coating after 400 h of oxidation in air at 700 °C. . . . . 161

6.25 SEM image of the section of a K41 sample passivated with a Cu-perovskite composite coating after 400 h of oxidation in air at 700 °C with overimposed EDX maps and the position of EDX analysis reported in table 6.8. . . . . 162